Holographic Experiments on Defects

by

Matthias Christian Wapler

A thesis
presented to the University of Waterloo
in fulfillment of the
thesis requirement for the degree of
Doctor of Philosophy
in
Physics

Waterloo, Ontario, Canada, 2009

I hereby declare that I am the sole author of this thesis. This is a true copy of the thesis, including any required final revisions, as accepted by my examiners.

I understand that my thesis may be made electronically available to the public.

Abstract

Using the AdS/CFT correspondence, we study the anisotropic transport properties of both supersymmetric and non-supersymmetric matter fields on (2+1)-dimensional defects coupled to a (3+1)-dimensional $\mathcal{N} = 4$ SYM "heat bath".

We address on the one hand the purely conformal defect where the only non-vanishing background field that we turn on is a "topological", parameter parametrizing the impact on the bulk. On the other hand we also address the case of a finite external background magnetic field, finite net charge density and finite mass.

We find in the purely conformal limit that the system possesses a conduction threshold given by the wave number of the perturbation and that the charge transport arises from a quasiparticle spectrum which is consistent with an intuitive picture where the defect acquires a finite width in the direction of the SYM bulk. We also examine finite-coupling modifications arising from higher derivative interactions in the probe brane action.

In the case of finite density, mass and magnetic field, our results generalize the conformal case. We discover at high frequencies a spectrum of quasiparticle resonances due to the magnetic field and finite density and at small frequencies a Drude-like expansion around the DC limit. Both of these regimes display many generic features and some features that we attribute to strong coupling, such as a minimum DC conductivity and an unusual behavior of the "cyclotron" and plasmon frequencies, which become correlated to the resonances found in the conformal case. We further study the hydrodynamic regime and the relaxation properties, in which the system displays a set of different possible transitions to the collisionless regime. The mass dependence can be cast in two regimes: a generic relativistic behavior dominated by the UV and a non-linear hydrodynamic behavior dominated by the IR. In the massless case, we also extend earlier results [49] to find an interesting duality under the transformation of the conductivity and the exchange of density and magnetic field.

Furthermore, we look at the thermodynamics and the phase diagram, which reproduces general features found earlier in 3+1 dimensional systems and demonstrates stability in the relevant phase [45].

Acknowledgements

I would like to thank first of all my advisor Rob Myers for sharing his vast knowledge with me and for his help, advice and comprehensive support throughout my graduate studies.

Furthermore I would like to thank Alexander Abanov, Mohammed Ansari, Cliff Burgess, Johanna Erdmenger, Jaume Gomis, Troels Harmark, Sean Hartnoll, Matt Headrick, Doug Hoover, Gary Horowitz, Matthias Kaminski, Pavel Kovtun, Per Kraus, Karl Landsteiner, David Mateos, Volodya Miransky, Markus Müller, Marta Orselli, Andrei Parnachev, Mukund Rangamani, Subir Sachdev, Sang-Jin Sin, Aninda Sinha, Kostas Skenderis, and Yidun Wan for helpful discussions and useful comments related to this thesis; and Rob Myers and Aninda Sinha also for proofreading parts of this thesis.

I would also like to thank Nemani Suryanarayana and Oscar Dias for very interesting, helpful and humerus discussions during earlier collaborations; Jordan Hovdebo, Mark Laidlaw, Peter Langenfelder and Susha Parameswan for interesting and helpful discussions at earlier stages of my PhD and Jaume Gomis, Robb Mann and Lee Smolin for their service on my supervisory committee and Anton Burkov, Johanna Erdmenger, Jaume Gomis, Michele Moska and Lee Smolin for their service on my examination committee.

Furthermore, I would also like to thank the Perimeter Institute for its hospitality and support during my PhD and the Kavli Institute for Theoretical Physics for its hospitality during my 8-months visit, which was the most enjoyable and productive period of my PhD and at the end of which this project was initiated.

Finally, I would like to greatly thank my friends for absorbing significant amounts of recoil and lifting my spirits during the many stressful phases of my PhD.

Research at the Perimeter Institute is supported in part by the Government of Canada through NSERC and by the Province of Ontario through MRI. This research is also supported from an NSERC Discovery grant and from the Canadian Institute for Advanced Research. Research at the KITP was supported in part by the NSF under Grant No. PHY05-51164.

Dedication

This is dedicated to my grandfather Dr. Dietrich "Dieter" Wapler who was an infinite source of support – practically and inspirationally.

Contents

List of Figures **xviii**

1 Introduction **1**

1.1 Motivation 1

1.1.1 Quasi-chronological History of String Theory 1

1.1.2 AdS/CFT 6

1.1.3 Some hard problems in condensed matter physics 10

1.2 This thesis 12

1.2.1 Context 12

1.2.2 Outline 13

2 Bare Defects **15**

2.1 Defect Branes 15

2.1.1 D5-branes 17

2.1.2 D7 probes 21

2.2 Correlators 23

2.2.1 Spectral functions 24

2.2.1.1 Transverse correlator 27

2.2.1.2 Longitudinal correlator 29

2.2.1.3 Diffusion constant on the defect 30

2.2.1.4 Low Frequency Limit and Permittivity 32
2.2.2 Temperature and f dependence 33
2.2.2.1 Effective temperature 34
2.2.2.2 Resonances on the defect 37
2.3 Quasinormal modes and quasiparticles 40
2.3.1 Finding the Ansatz 42
2.3.2 Quasiparticles from the collisionless regime 44
2.3.3 Poles in the hydrodynamic regime 49
2.4 Electromagnetic duality and perturbative corrections 52
2.5 Topological Hall Effect 59

3 Dressed Defects **61**
3.1 Turning on the Condensed Matter Background 61
3.1.1 $D3$ = (N=4 SYM) background 61
3.1.2 Introducing the defect 62
3.1.3 AdS/CMT Dictionary (Supersymmetric Case) 63
3.1.4 Non-supersymmetric $D3-D7$ intersection 65
3.2 Computing the Conductivity 67
3.2.1 Electromagnetic duality 68
3.2.2 Explicit Computations 70
3.3 Weak-Coupling Condensed Matter Physics 72
3.3.1 Metals 72
3.3.2 Semiconductors 74
3.3.3 Resonances 75
3.4 Analytic results 76
3.4.1 Isotropic perturbations with small frequencies 76
3.4.1.1 DC Limit 76
3.4.1.2 Small frequencies 79

3.4.2 Large Temperatures: Diffusion limit . . . 88
3.4.3 $T \to 0$ limit . . . 91
3.4.3.1 Exponentially suppressed regime, $\tilde{q}^2 \gg 1 \gg \tilde{\omega}^2$, at small backgrounds, $|\tilde{q}| \gg |\tilde{\rho}|, |\tilde{B}|$ . . . 92
3.4.3.2 Exponentially suppressed regime at large backgrounds, $\tilde{q}^2 \gg |\tilde{\rho}|, |\tilde{B}| \gg |\tilde{q}| \gg 1$ . . . 97
3.4.3.3 Dominantly large backgrounds $\tilde{\rho}, \tilde{B} \gg \tilde{q}^2 \gg 1$ . . . 99
3.5 Numerical Results . . . 100
3.5.1 Spectral Curves . . . 100
3.5.2 Small frequency regime . . . 109
3.5.3 Landau Levels and Plasmons . . . 118

4 Discussion and Conclusion **132**
4.1 Conformal effects . . . 132
4.2 Condensed matter effects . . . 135
4.3 Closing remarks . . . 139

APPENDICES **140**

A Probe brane horizon **141**

B Corrections to D5-brane action **143**

C Hyperbolic tangent potential **147**
C.1 Finding the spectral curves . . . 147
C.2 Exact pole structure . . . 150

D Components of the metric **152**

E Thermodynamics of the defect **154**

E.1 Free Energy and Thermodynamic Variable 154

E.2 Derived quantities 157

E.2.1 Massless case 160

E.2.2 Numerical results 164

Bibliography **172**

List of Figures

1.1 Left: A generic quantum critical phase transition and quantum critical phase. Right: A generic surface phase diagram. 11

2.1 The brane profile χ for $f = 10$ above the horizon in terms of u and below the horizon in terms of r/r_0. The angle of the "tangent curve" in the plot represents the physical angle of the brane w.r.t. u or r, respectively; obtained from the unit norm vectors. The temperature scaling of the $T = 0$ profile corresponding to $\chi = -f\,u$ is fiducial. 19

2.2 The normalized transverse conductivity Re $\tilde{\sigma}_{yy}(\tilde{\omega})/\varepsilon_0$ at $\tilde{q} \in \{1, 2, 3, 4\}$ for various values of the flux f. The low temperature approximation (2.2.51) is shown as the dotted line for each $\tilde{q}$. 28

2.3 The normalized longitudinal conductivity Re $\tilde{\sigma}_{xx}(\tilde{\omega})/\varepsilon_0$ at $\tilde{q} \in \{1, 2, 3, 4\}$ for various values of the flux f. The low temperature approximation (2.2.61) is shown as the dotted line for each $\tilde{q}$. 30

2.4 The integral $I(f)$: The solid line is the exact result as given in eq. (2.2.64). The upper dashed (lower dotted) line corresponds to the first term (first two terms) in the large f expansion in eq. (2.2.70). 31

2.5 $\frac{-\text{Im } \tilde{C}_{tt}(\tilde{\omega})}{\varepsilon_0 \tilde{q}^2}$ for $f \in \{0, 4\}$ and $\tilde{q} \in \{0.1, 0.2\}$. The solid lines correspond the approximate result (2.2.73) with only the diffusion pole appearing in the hydrodynamic limit. 33

2.6 On the left, we plot the normalized transverse conductivity Re $\tilde{\sigma}_{yy}(\omega)/\varepsilon_0$ for $q = 1$ and $f = 2$ at various temperatures, in terms of the frequency ω. On the right: Re $\tilde{\sigma}_{yy}(\omega)/\varepsilon_0$ for $q = 1$ and $T = 2$ for various values of f. In both plots, the $T \to 0$ limit (2.2.51) is shown with the narrow black curve. . . . 34

2.7 Ratio of the "effective temperature" derived from the temperature and $\tilde{q}$ dependence at $\tilde{q} \gg 1 \gg \tilde{\omega}$ to the blackhole temperature as a function of the flux f. We show the exact expression derived from the $\tilde{q} \to \infty$ limit and the numerical estimate at finite $\tilde{q}$. 37

2.8 The effective Schrödinger potential $V(\rho) = \tilde{q}^2 h$ for the gauge field on the brane. We set $\tilde{q} = 1$ in the plot. 39

2.9 Comparing the conductivity obtained from the numerics, from the approximation (2.2.89), from the approximation using a tanh potential (C.1.7) and from the sum of residues obtained from its poles (C.2.16). Here we focus on the oscillatory behavior by plotting $\Delta\tilde{\sigma}_{yy} \equiv \text{Re}\left(\tilde{\sigma}_{yy}(\tilde{\omega}) - \varepsilon_0\sqrt{1-\tilde{q}^2/\tilde{\omega}^2}\right)$, *i.e.,* we subtract off the low temperature limit (2.2.51). Left: $f \in \{0, 4\}$ and $\tilde{q} = 2$. Right: $\tilde{q} \in \{2, 4\}$ and $f = 4$. 41

2.10 $\frac{\tilde{\omega}}{\tilde{\nu}}\tilde{\sigma}_{yy}(\tilde{\nu})$ for $\tilde{q} \in \{\pi/4, \pi\}$ and $f \in \{0, 4\}$. This form of the spectral function is very similar for different values of $\tilde{q}$. 42

2.11 Left: Comparing the exact location of the poles of the transverse correlator to the fit, using the approximate tanh-potential of appendix C, at values $f \in \{0, 4, 25\}$ and $\tilde{q} = 1$. Right: Comparing the poles of the transverse correlator with the ones of the longitudinal correlator at $f \in \{0, 4, 25\}$ and $\tilde{q} \in \{1, 4\}$. The lines are only shown to guide the eye as to which poles correspond to the same values of $f, \tilde{q}$. 46

2.12 Top left: The energy gap between resonances $\tilde{\nu}_0$ presented as $\pi/\tilde{\nu}_0$. The asymptotic $\sqrt{f}$ behavior is fit is several ways. Top right: The difference between the previous fits and the numerical results for $\pi/\tilde{\nu}_0$. The data in the top two plots is averaged over $\tilde{q} \in \pi/2, \pi, 2\pi$. Bottom left: The "mass to width" ratio $\tilde{\gamma}_0/\tilde{\nu}_0$ for the sequence of poles for several values of $\tilde{q}$. Bottom right: The f-dependence of the overall shift of the poles $\delta\tilde{\gamma}$. The points are the average numerical data and the narrow lines indicate the 1σ uncertainties, which includes both random and systematic errors. 48

2.13 Average over quantities appropriately scaled with $T_{eff}(f)/T$ for $f \in \{9, 16, 25, 36\}$: Top left: (In)dependence of $\tilde{\nu}_0$ on $\tilde{q}$. Top right: $\tilde{\gamma}_0/\tilde{\nu}_0$. Bottom: The complex shift $\delta\tilde{\nu}$ and $\delta\tilde{\gamma}$. 50

2.14 Left: The location of the poles on the imaginary axis below $\boldsymbol{q}_c$, rescaled by the diffusion constant. The dashed line is what one expects for the diffusion pole. Right: The critical values q_c at which the purely dissipative poles disappear, multiplied with several length scales. 51

2.15 The modification of $\varepsilon_0 \equiv \tilde{\sigma}(\tilde{\omega} \to \infty)$ as a function of f from the $1/\sqrt{\lambda}$ corrections. 55

2.16 Left: The finite-λ correction to the conductivity $\delta\tilde{\sigma}(\tilde{\omega})$ for various values of f. Right: $\tilde{\sigma}(\tilde{\omega}=0) - \tilde{\sigma}(\tilde{\omega}\to\infty)$, the change in conductivity from $\tilde{\omega}=0$ to $\tilde{\omega}\to\infty$ at finite λ. 56

2.17 Left: The extrema of $\frac{1}{\varepsilon_0\xi}\delta\tilde{\sigma}_{yy}$ for $\tilde{q} \in \{0, \pi/4, \pi/2, \pi, 2\pi\}$ and "large" $f \in \{4, 9, 16\}$. We see that all the curves are approximately bound by some universal envelope function, that decays exponentially in $\tilde{\omega}$. Right: $\frac{1}{\varepsilon_0\xi}\delta\tilde{\sigma}_{yy}$ for $\tilde{q} \in \{\pi/4, \pi/2, \pi\}$ and $f \in \{1/4, 1\}$. For $f = 1/4$ and sufficiently large $\tilde{q}$, the conductivity is not bounded by the universal envelope (shown in thin dots). 57

2.18 Left: $\sqrt{\lambda}\delta\sigma_{yy}$ in the rest-frame frequency $\tilde{\nu}$ for $\tilde{q} \in \{\pi/2, \pi\}$ and $f = 4$, scaled to 1. The dotted lines show $\sigma_{yy} - \sqrt{1-\tilde{\omega}^2/\tilde{q}^2}$, also scaled to 1. Right: $f = 16$ 57

2.19 Left: $\log \delta\tilde{\sigma}_{yy}(\tilde{\omega}=0)/\xi$ (modulo a constant shift) and $\frac{\tilde{q}}{T_{eff}(f)}$ for $\tilde{q} = \pi/2$. The accuracy of the last two points are very sensitive to possible errors in $\delta\varepsilon_0$. Right: $\log \delta\tilde{\sigma}_{yy}(\tilde{\omega}=0)$ and $\frac{\tilde{q}}{T_{eff}(f)}$ for $f = 4$. $\log \delta\tilde{\sigma}_{yy}(\tilde{\omega}=0)/\tilde{q}^2$ is shown to demonstrate the slow convergence due to polynomial factors of $\tilde{q}$. 58

3.1 The quadratic factor in the small-frequency expansion of the conductivity $\frac{\partial_{\tilde{\omega}}^2\sigma}{2\sigma}$ as a function of the magnetic field for various values of the density. Left: $\tilde{f} = 0$. Right: $f = 2$. 83

3.2 The quadratic factor in the small-frequency expansion of the conductivity $\frac{\partial_{\tilde{\omega}}^2\sigma}{2\sigma}$ as a function of the magnetic field for various values of f. Left: $\tilde{\rho} = 0$. Right: $\tilde{\rho} = 2$. 83

3.3 The ratio of the quadratic factors in the small-frequency expansion of the diagonal and Hall conductivities. Left: $\frac{\partial_{\tilde{\omega}}^2\sigma^{\parallel}\ \sigma^{\perp}}{\sigma^{\parallel}\ \partial_{\tilde{\omega}}^2\sigma^{\perp}}$ at $\tilde{B} = 10^{-5}$ as a function of $\tilde{\rho}$ for various values of f. Right: $\frac{\partial_{\tilde{\omega}}^2\sigma^{\perp}\ \sigma^{\parallel}}{\sigma^{\perp}\ \partial_{\tilde{\omega}}^2\sigma^{\parallel}}$ at large magnetic fields as a function of $\tilde{B}$ for $\tilde{\rho} = 10$ and various values of f. The density $\tilde{\rho}$ changes only the behavior at small magnetic fields and leaves the large-$\tilde{B}$ tail unchanged. . . 85

3.4 The quadratic factor in the small-frequency expansion of the conductivity $\frac{\partial_{\tilde{\omega}}^2\sigma}{2\sigma}$ as a function of the density for various values of f. 85

3.5 The quadratic factor in the small-frequency expansion of the conductivity $\frac{\partial^2_{\tilde{\omega}}\sigma}{2\sigma}$ as a function of f. Top left: The coefficient of the diagonal conductivity for various values of the density and the magnetic field, right: For various values of the magnetic field at $\tilde{\rho} = 1$. Bottom left: The coefficient of the diagonal conductivity for various values of the density at $\tilde{B} \in \{2, 4\}$, right: The coefficient of the Hall conductivity for various values of the density at $\tilde{B} \in \{0.5, 4\}$. 86

3.6 The quadratic factor in the small-frequency expansion of the conductivity $\frac{\partial^2_{\tilde{\omega}}\sigma}{2\sigma}$ as a function of $\tilde{m}$. Top left: The coefficient of the diagonal conductivity for various values of the density, right: For various values of f. Bottom left: The coefficient of the diagonal conductivity for various values of the $\tilde{B}$ at $f = 0.25$, right: The coefficient of the Hall conductivity for various values of the magnetic field at $\tilde{\rho}2$ 87

3.7 The diffusion constant $\pi T\, D$ as a function of the magnetic field and density for different values of f (left) and as a function of f and the density for different values of the magnetic field (right) 89

3.8 The relative permittivity ε_r as a function of the magnetic field and density for different values of f (left) and as a function of f and the density for different values of the magnetic field (right) 91

3.9 The "effective temperature" T_{eff}/T. Left: As a function of f and $\sqrt{\tilde{\rho}^2 + \tilde{B}^2}$. Right: As a function of $\tilde{m}$ for various values of $\tilde{\rho}$ and $\tilde{B}$ 94

3.10 Left: The check to the deviation from the $T \to 0$ limit as described in the text. Right: The numerical estimate $\frac{T}{T_{eff}} \sim -\pi\partial_{\tilde{q}} \ln\left(\frac{\tilde{\sigma}_{yy}}{\tilde{q}}\right)$ compared to the analytical result 99

3.11 The real, diagonal part of the isotropic conductivity at $\tilde{q} = 0$ as a function of frequency and net baryon density (top) or magnetic field (bottom) for $f = 0$ (left) and $f = 2$ (right). 101

3.12 The real, diagonal part of the isotropic conductivity at $\tilde{q} = 0$ as a function of frequency and magnetic field for $\tilde{B} = 4$ (left) and $\tilde{\rho} = 4$ (right) 102

3.13 The real part of the conductivity σ_{yy} at varying $\tilde{q}$, $f = 2$ and $\tilde{\rho} = 4$ (top) or $\tilde{B} = 4$ (bottom) as a function of $\tilde{\omega}$ (left) and rescaled as $\frac{\tilde{\sigma}_{yy}}{\varepsilon_0\sqrt{1-\tilde{q}^2/\tilde{\omega}^2}}$ as a function of the "rest-frame" frequency $\sqrt{\tilde{\omega}^2 - \tilde{q}^2}$ (right). 103

3.14 $\frac{\text{Re }\tilde{\sigma}_{yy}}{\varepsilon_0\sqrt{1-\tilde{q}^2/\tilde{\omega}^2}}$ at $\tilde{q}=\pi/2$ and $f=4$ as a function of the "rest-frame" frequency $\sqrt{\tilde{\omega}^2-\tilde{q}^2}$. Left: As a function of the magnetic field. Right: As a function of the density. 104

3.15 The real part of the isotropic conductivity at $\tilde{q}=0$, $\tilde{B}=4$ and $f=2$ as a function of frequency and density (top) and at $\tilde{\rho}=4$ as a function of the magnetic field (bottom). Left: diagonal part of the conductivity tensor. Right: Hall conductivity. 105

3.16 The real part of the isotropic conductivity at $\tilde{q}=0$, $\tilde{B}=4$ and $\tilde{\rho}=4$ as a function of frequency and f. Left: diagonal part of the conductivity tensor. Right: Hall conductivity. 106

3.17 The real, diagonal part of the isotropic conductivity at $\tilde{q}=0$ as a function of frequency and quark mass for $f=0$, $\tilde{m}\in[0,1.18]$ (left) and $f=0$, $\tilde{m}\in[0,8]$ (right). 107

3.18 Top: The real part of the normalized conductivity $\frac{\sigma_{yy}}{\sqrt{1-q^2/\omega^2}}$ at $\tilde{q}=\pi/2$ as a function of "rest-frame" frequency $\sqrt{\tilde{\omega}^2-\tilde{q}^2}$ and quark mass at $\tilde{q}=\pi/2$ for $f=0$, $\tilde{m}\in[0,1.18]$ (left) and $f=2$, $\tilde{m}\in[0,8]$ (right). Bottom: σ_{yy} for $f=2$, $\tilde{m}\in[0,8]$. 108

3.19 The real, diagonal part of the isotropic conductivity at $\tilde{q}=0$ as a function of frequency and quark mass at $f=2$ for $\tilde{B}=4$ (left) and $\tilde{\rho}=4$ (right) . . 109

3.20 The real, diagonal (left) and Hall (right) part of the isotropic conductivity at $\tilde{q}=0$ and $f=2$. Top: As a function of $\tilde{m}$ at $\tilde{B}=4$, $\tilde{\rho}=4$. Bottom: As a function of $\tilde{\rho}$ at $\tilde{B}=4$ and $\tilde{m}=8$. 110

3.21 $\sigma_{yy}=\sigma_{yy}$ and σ_{xy} at $\tilde{q}=0$, $\tilde{m}=32$, $\tilde{\rho}=32$ and $\tilde{B}=24$. 111

3.22 Left: Imaginary frequency of the diffusion pole and the first higher pole as a function of $\tilde{q}$ for different values of $\tilde{\rho}$. The frequency and wavenumber are scaled with D, such that the diffusion equation is $D\omega=-i(Dq)^2$. The dot indicates the point where there is the branch cut, and the mode frequency of the poles gain a real part to become quasi-particles. Right: The critical wavenumber as a function of $\tilde{\rho}$, compared to various length scales of the problem: the effective temperature, diffusion constant and the electric permittivity. 112

3.23 The location of the second pole on the imaginary axis as a function of the net baryon density for various values of f. For comparison, we show the inverse correlation time τ^{-1} computed from the conductivity for $f = 0$ only. The other curves for the relaxation time will be in worse agreement at small frequencies. 113

3.24 Left: The location of the second relaxation pole as a function of the net baryon density for various values of f. Right: The logarithm of the residue of the second relaxation pole. 114

3.25 The location of the relaxation poles as a function of the magnetic field for various values of f. 115

3.26 The location of the relaxation poles as a function of the magnetic field for different wavenumbers. 115

3.27 The location of the poles on the imaginary axis as a function of the wavenumber for different values of the magnetic fields. The frequency and wavenumber are scaled with the diffusion constant, as the diffusion behavior can be written as $iD\omega = (D\,q)^2$. 116

3.28 The imaginary frequencies of the relaxation poles as a function of the quark mass. Left: For various values of f. Right: For various values of $\tilde{q}$ 117

3.29 The location of the poles on the imaginary axis as a function of the wavenumber for different values of the quark mass. The frequency and wavenumber are scaled with the diffusion constant. For comparison, the critical mass for the embedding is $\tilde{m} \sim 1.196$. 118

3.30 The location of the poles $\omega_n = \nu_n - i\gamma_n$ in the complex frequency plane from the different estimates as described in the text. For orientation purposes, the lines connect the poles of different order in the same background. Left: Finite $\tilde{\rho} = 2$, Right: Finite $\tilde{B} = 4$ 119

3.31 The real part $\tilde{\nu}_n$ of the location of the poles in the complex frequency plane as a function of the level number. The lines are linear fits. Left: Various values for $\tilde{B}$ at $f = 2$. Right: Varying $\tilde{\rho}$ at $f = 4$ 120

3.32 The real part $\tilde{\nu}_n$ of the location of the poles in the complex frequency plane as a function of the level number at finite quark mass. Left: Varying $\tilde{m}$ at $\tilde{B} = 4$ and $f = 4$. Right: Different values of $\tilde{\rho}$ at $\tilde{m} = 8$ and $f = 2$. 121

3.33 The imaginary parameter in the location of the poles, $\tilde{\omega}_n = \tilde{\nu}_n - i\tilde{\gamma}_n$. Left: Varying values of $\tilde{\rho}$ at $f = 4$. Right: Varying mass $\tilde{m}$ at $f = 4$ and $\tilde{B} = 4$. 122

3.34 The overall shift in the poles $\delta\tilde{\nu}$ as a function of $\tilde{B}$ or $\tilde{\rho}$ for various values of f. 122

3.35 The separation $\tilde{\nu}_0$ in the spectrum of "plasmons" and "Landau levels" as a function of $\tilde{B}$ or $\tilde{\rho}$ for various values of f. The plot on a right only shows the highest f curves. 123

3.36 $\tilde{\nu}_0$ presented as $\tilde{\nu}^2$ as a function of the square of the magnetization or chemical potential $\tilde{M}^2$ or $\tilde{\mu}^2$ for various values of f. The plot on a right only shows the highest f curves. 124

3.37 The ratio $\frac{\tilde{\nu}_0 T}{T_{eff}}$ as a function of $\tilde{B}$ or $\tilde{\rho}$ for various values of f. 124

3.38 The "inverse lifetime to mass ratio" $\frac{\tilde{\gamma}_0}{\tilde{\nu}_0}$ for the magnetic and density resonances as a function of $\tilde{B}$ or $\tilde{\rho}$ for various values of f. 125

3.39 $\tilde{\nu}_0$ for various values of the quark mass parameter $\tilde{m}$ at $f = 4$. Left: As a function of the magnetic field. Right: $\tilde{\nu}_0^2$ as a function of the magnetization $\tilde{M}^2$. 126

3.40 The difference in $\tilde{\nu}_0$ between the case of the magnetic field and density at $f = 4$ for various values of the quark mass as a function of $\tilde{\rho} = \tilde{B}$. 126

3.41 The scale T_{eff}/T at $f = 1$ and various values of the quark mass as a function of the net baryon density and magnetic field. 127

3.42 Left: $\frac{T_{eff}}{T}$ as a function of the mass and the net baryon density for various (small) values of f. We choose the lower bound of the range $2 \leq \tilde{\rho} \leq 16$ to avoid the phase transition at the critical mass and numerical problems near it. Right: $\frac{T_{eff}}{T}$ as a function of the mass and the magnetic field for various values of f. 127

3.43 The "inverse lifetime to mass ratio" $\frac{\tilde{\gamma}_0}{\tilde{\nu}_0}$ for the magnetic resonances as a function of $\tilde{B}$ for $f = 4$ and various values of $\tilde{m}$. 128

3.44 The splitting of the poles due to the Hall effect at various values of $\tilde{\rho}$, $\tilde{B}$ and f. The black symbols indicate the sequence of poles in the absence of the Hall effect for some choice of f and $\tilde{B}$ or $\tilde{\rho}$. With decreasing gray shade, we turn on the $\tilde{\rho}$ or $\tilde{B}$, respectively, causing the original pole to split in two poles. 129

3.45 Left: The splitting of the energy of the quasiparticle poles due to the Hall effect, $\tilde{\nu}_\Delta$. Right: The shift in $\tilde{\nu}_0$ from turning on the second parameter, written as $\delta\tilde{\nu}_0(\tilde{B}) := \sqrt{\tilde{\nu}_0^2 - \tilde{\nu}_0(\tilde{B}=0)^2} \propto \tilde{B}$ (and $\tilde{\rho} \leftrightarrow \tilde{B}$). 130

3.46 Coefficient giving an estimate of the contribution to the resonances as described in the text. 131

C.1 The exact potential V (solid grey) and the tanh approximation V_{app} (black dotted), for $f \in \{0, 4, 25\}$ with $\tilde{q} = 1$. We also indicate a number of interesting values of ρ with narrow vertical lines: $\rho(u_{half})$, solid black; $\rho(u_{min})$, solid grey; $\rho = \frac{\pi T}{2T_{eff}}$, dashed black; and $\rho = \pi D T$, grey dashed. 148

E.1 The free energy density of the as a function of $\sqrt{f^2 + \tilde{\rho}^2 + \tilde{\nu}^2}$ (denoted for simplicity as "f". 161

E.2 The chemical potential as a function of $\tilde{\rho}$ and $\sqrt{\tilde{B}^2 + f^2}$. Note that, due to electromagnetic duality, this is the same as the magnetization as a function of $\tilde{B}$ and $\sqrt{\tilde{\rho}^2 + f^2}$, upon an appropriate scaling with a dimensionful constant. 161

E.3 The contribution of the defect to the entropy as a function of $\sqrt{\tilde{\rho}^2 + \tilde{B}^2}$ and f. 162

E.4 The contribution of the defect to the specific heat as a function of $\sqrt{\tilde{\rho}^2 + \tilde{B}^2}$ and f. 163

E.5 The magnetic susceptibility of the defect as a function of $\tilde{B}$ and $\sqrt{\tilde{\rho}^2 + f^2}$. This is the same as the density of states as a function of $\tilde{\rho}$ and $\sqrt{\tilde{B}^2 + f^2}$. 164

E.6 Value of the condensate as a function of the dimensionless mass, $\tilde{m}$ and magnetic field, $\tilde{B}$ at fixed temperature. Top left: Vanishing density and magnetic field. The light and dark gray lines identify the transition between **B** and **C** and **M**, respectively. Top right: Density $\tilde{\rho} = 0.5$. The dark gray line is now the transition between **B** and **C**, or **B** and **B1** and the black line between **C** and **B1**. The light gray line is the transition between **M** and **M1**. Bottom left: $f = 0.25$. More details are explained in the bottom right. 166

E.7 Value of the condensate as a function of the dimensionless mass and density, at fixed temperature. Left: $\tilde{B} = 0$, right $\tilde{B} = 4$. 167

E.8 Condensate as a function of the dimensionless mass and f, at fixed temperature. Left: $\tilde{B} = 0$, right $\tilde{B} = 4$. 168

E.9 The dimensionless entropy $\bar{S} = \frac{S}{8M_q^2 N_c}$ as a function of $\bar{T} = \sqrt{\lambda}\frac{T}{2^{3/2}M_q}$ and $\bar{B} = \lambda\frac{B}{8\pi^2 M_q^2}$ for $f = 0 = \bar{\rho}$ (top left) and $f = 1/2$, $\bar{\rho} = 0$ (top right) or as a function of $\bar{T}$ and $\bar{\rho}$ (bottom left) or f (bottom right). 169

E.10 The magnetization $\bar{M}$ as a function of the temperature-mass ratio $\bar{T}$ and the magnetic field $\bar{B}$ at $\bar{\rho} = 0 = f$ (left) and $f = 0$ (right). 170

E.11 The chemical potential $\bar{\mu}$ as a function of the temperature-mass ratio $\bar{T}$ and the density $\bar{\rho}$ at $\bar{B} = 0 = f$ (left) and as a function of $\bar{B}$ at $\bar{\rho} = 1/2$ (right). 170

Chapter 1

Introduction

1.1 Motivation

1.1.1 Quasi-chronological History of String Theory

String theory can be described in terms of various dual descriptions, depending on the limit from which we "probe" the theory. From a point of view of constructively trying to refute the theory, at least based on its theoretical consistency, it can be described as a Hydra – each time we try to decapitate it, i.e., each time it seems to run into an inconsistency, two new heads grow back, and furthermore, one head is immortal. From a sociological point of view, however, it is best described as a plant belonging to the family of the Poaceae, in particular the subgroup of the Bambusodae, which grow their many culms from a vast underground network of roots at a high speed in a short period and display huge mass flowerings spaced over a timescale of decades.

It was conceived in the early 1970s as a phenomenological model to explain the cross-sections observed in hadron scattering experiments, as it could successfully explain the "Regge trajectory" behavior [1]. In one form, it is based on the action of a string at tension T, that is essentially given by the volume of a string embedded in a d-dimensional spacetime with embedding coordinates X^μ in terms of the induced metric on the string "world-volume" $G_{ab} = \partial_a X^\mu \partial_b X_\mu$,

$$S_{NG} \;=\; -T \int d^2\sigma \sqrt{-\det G}\;, \tag{1.1.1}$$

referred to as the Nambu-Goto action. As this turns out to be hard to quantize, one can alternatively try to use the 2-dimensional sigma model action ("Polyakov action", invented by Brink, Deser and Howe [2])

$$S_P \;=\; -\frac{T}{2}\int d^2\sigma\sqrt{-\det h}h^{ab}\partial_a X^\mu \partial_b X_\mu \;, \tag{1.1.2}$$

which is obviously invariant under the choice of the "auxiliary" metric h on the string. It is equivalent on the classical level as it gives the same equations of motion; and it was quantized by Polyakov in [3]. The string tension is usually expressed in terms of the Regge slope α' or the string length l_s as $T = \frac{1}{2\pi\alpha'} = \frac{1}{2\pi l_s^2}$.

However, the brief period of flowering died off and activity slowed down when it turned out that string theory was in contrast with experiment and it was finally terminated by the discovery of quarks, QCD and asymptotic freedom [4]. The latter could successfully and accurately explain the observations, and later became a corner-stone of the immensely successful standard model of particle physics.

It was re-incarnated shortly after, when it was re-considered as a theory of quantum gravity because of its massless spin-2 states [5]. However, it was discovered that the theory possesses a 2d-conformal anomaly, unless one assumes the critical dimensionality of spacetime, $d = 26$ [6]. Then, it turns out that the spectrum of the theory contains a tachyon of mass-squared $m^2 = -1/\alpha'$. Furthermore, the spectrum was lacking fermions, which are a necessary constituent of a grand unified theory.

The latter shortcoming was fixed first by Ramond, and Neveu and Schwarz by adding to the d scalars X^μ of the worldsheet theory d fermions ψ^μ – the so-called RNS formalism [7]. In 1981, it was alternatively demonstrated in the Green-Schwarz, or "superspace", formalism that one can add fermions by extending the d-dimensional spacetime to include also Grassmann-odd coordinates [9]. This made the theory much more attractive. It turns out that the critical dimension, at which it becomes anomaly-free is then d=10 [10]. Furthermore, it was discovered by Gliozzi, Scherk and Olive that the theory can be restricted to a spacetime-supersymmetric sector using the so-called GSO projection, that defines a "G-parity" and projects out G-positive or G-negative states [8]. This had the important result of projecting out the tachyon, making the theory well-behaved and consistent. In some sense, this is one of the "miracles of supersymmetry" in the same spirit as the fact that the supersymmetric extension of the standard model ensures the cancellation of radiative corrections to the Higgs mass.

Eventually, it turns out that there are 5 different consistent string theories in 10 dimensions: Type II string theory contains oriented closed strings. The two type II theories,

type IIA and type IIB, differ only in the choice of the GSO projection. The consequence of this is that they share the same so-called NS-NS sector that contains at the massless level a scalar ϕ, the symmetric tensor G and a 2-form gauge potential B. They differ, however, in the so-called R-R sector that contains in the case of type IIA a 1- and a 3-form gauge potential $C^{(1)}$ and $C^{(3)}$, and in the case of type IIB string theory a scalar, 2- and a 4-form $C^{(0)}$, $C^{(2)}$ and $C^{(4)}$. Here and below, it is understood that there is further the appropriate set of superpartners. Type I string theory contains both unoriented open and closed strings. Its massless spectrum, as in type II string theory, consists of the dilaton, graviton and three-form, and additionally of the gauge field (1-form) from the open string sector. Furthermore, there are two kinds of "heterotic" string theories. Heterotic sting theories are unoriented string theories that contain the left-moving sector of the 26 dimensional bosonic string theory, and the right-moving sector of the 10 dimensional super string theory. At the massless level they display $E_8 \times E_8$ symmetry or $SO(32)$ symmetry and are called $E_8 \times E_8$ heterotic string theory or $SO(32)$ heterotic string theory, accordingly. Heterotic string theories are of great interest to string-phenomenology, but not relevant for this thesis. In addition, one also considers the low-energy limit of 11 dimensional supergravity to belong to this set of theories.

It turns out that, mysteriously, all 6 theories are linked by a set of dualities: S-duality – a strong-weak coupling duality and T-duality. If we suppose that one of the dimensions has the topology of a circle with radius R, T-duality exchanges $R \leftrightarrow l_s^2/R$. If a string in such a background had n "winding" modes and m "Kaluza-Klein" [12] (essentially periodic harmonic) modes, this duality will further exchange $m \leftrightarrow n$. Furthermore, these theories are related by taking orbifolds and orientifolds – spacetime parity operations.

Also, it was shown that the low-energy limit of the theories is 10-dimensional supergravity, at the example of type IIB string theory, the bosonic part is:

$$\begin{aligned} S_{SUGRA} \;=\; & \frac{2\pi}{(2\pi l_s)^8}\int dx^{10}\sqrt{-G}\left(e^{-2\phi}\left(R+4(\nabla\phi)^2-\frac{1}{2}|H^{(3)}|^2\right)\right. \\ & \left.-\frac{1}{2}|F^{(1)}|^2\;-\;\frac{1}{2}|\tilde{F}^{(3)}|^2\;-\;\frac{1}{4}|\tilde{F}^{(3)}|^2\right)\;-\;\frac{\pi}{(2\pi l_s)^8)}\int C^{(4)}\wedge H^{(3)}\wedge F^{(3)}\;, \end{aligned} \tag{1.1.3}$$

where $H^{(3)} = dB^{(2)}$, $F^{(n+1)} = dC^{(n)}$, $\tilde{F}^{(3)} = F^{(3)} - C^{(0)}H^{(3)}$ and $\tilde{F}^{(5)} = F^{(5)} - 1/2\, C^{(2)} \wedge H^{(3)} + 1/2\, B^{(2)} \wedge F^{(3)}$. The vacuum expectation value of e^{ϕ} is commonly referred to as the string coupling g_s. For more information , the reader is referred e.g. to [11].

At this stage, however, the theory is not even remotely close to describing observations of nature. This is because we are living in 3+1 macroscopic dimensions, and also our spectrum of fundamental particles is not the one naively obtained from string theory. This problem was later addressed in two ways.

One way was to compactify the spacetime by assuming that the spacetime is a product manifold of the type $\mathbb{R}^{(d,1)} \times \Sigma^{9-d}$, where the Σ-manifold is assumed to be compact with a small radius, such that the corresponding Kaluza-Klein excitations in the compact directions have high energies. Then, the symmetry group of that compact manifold is observed as a symmetry group of the fundamental particles from the view of the $d+1$ dimensional spacetime. Certainly, the concept of having the particle theory encoded in the geometry of spacetime, and probed by strings sounds appealing.

However, it turned out that such compactifications are generically unstable as one can naively visualize by considering a winding mode of a string trying to minimize the radius of a compact direction. This shortcoming was solved through "moduli stabilization" in so-called flux compactifications shortly after the turn of the millennium by adding a magnetic flux to the compact dimension (e.g. in [13, 14]). These models were not only able to stabilize moduli and generate a particle spectrum, but also to break supersymmetry and induce a small positive cosmological constant for the flat directions [15].

Soon it was discovered though, that such flux compactifications give rise to a large number of different consistent string theory backgrounds ("vacua") [16] and that the inverse problem of obtaining the vacuum "construction" from "observable" parameters is an NP-hard problem [17]. This raised worries that the theory might not be predictive. On the other hand, it was noted, however, that similar "landscapes" are not uncommon in physics. Furthermore, this "landscape of string theory" gave rise to statistical studies of string theory vacua (see e.g. [18]), to models of cosmological selection mechanisms and eternal inflation [19]. From another point of view, those results moved string theory from being a candidate for a unique theory of nature, depending only on the string coupling towards being a mathematical framework, that allows the construction of a large set of different consistent theories – just like quantum field theory.

Another way how the above-mentioned problem can be addressed is through D-branes, that arise naturally as follows. The string spectrum contains two kinds of strings: Open strings which have boundary conditions at their end points and closed strings, that have periodic boundary conditions. For the open strings, there are two kinds of boundary conditions that we can give to each scalar in the sigma model, i.e. to each spacetime dimension: Dirichlet boundary conditions, which we fix the value of the scalar i.e. the position of the string endpoint (i.e. such that its time derivative to zero), and Ramond-Ramond boundary conditions, which correspond to freely moving endpoints and require the derivative of the scaler along the string length to vanish. It was discovered in 1995 by Polchinski [20] that it turns out that assigning hypersurfaces in spacetime to Dirichlet boundary conditions of strings, i.e. attaching strings to them, causes these Hypersurfaces gain dynamics: They become physical objects, called "D-branes". They can be described

by the Born-Infeld action [21] in terms of the induced metric G and the gauge field strength F

$$S_{BI} \;=\; -T_{Dp}\int_{Dp}\sqrt{-\det(G_{\mu\nu}+2\pi l_s^2 F_{\mu\nu})}\;,\quad T_{Dp}=\frac{1}{g_s(2\pi l_s)^p\, l_s}\;. \tag{1.1.4}$$

In the case of superstring theory, the action still takes the same form, however spacetime supersymmetry can be incorporated by an appropriate definition of F and G, in which case the action is referred to as the Dirac-Born-Infeld action[1]. This form of the action is natural, because in the absence of a gauge field, the action is just the volume of the brane that can be written neatly as $\int d\mathcal{V}$ times the brane tension. Furthermore, it was discovered that in a supergravity background, there is the so-called Wess-Zumino term

$$S_{WZ} \;=\; T_p\int_{Dp}\left(\sum_n C^{(n)}e^{2\pi l_s^2 F}\right) \tag{1.1.5}$$

through which D-Branes interact directly with the n-form gauge fields of supergravity. It is understood that only the terms that do appropriately pull back to the brane volume are considered. D-Branes turned out to be very interesting objects. For example the gauge field on the D-Branes is sourced by the endpoints of strings ending on the brane. Reviving the concept of assigning quantum numbers, so-called Chan-Paton factors, to the end points of strings unveiled an interesting structure of symmetry groups associated to configurations of branes. String end-points of oriented strings can now be interpreted as quark-antiquark pairs. Since the endpoints are charged under the corresponding $U(1)$'s, making them degenerate, i.e. considering n coincident branes, enhances the gauge group to a $U(n)$ symmetry. Furthermore, considering the massless spectrum of strings living at the intersection of branes in an intersecting brane configurations make it possible to associate products of symmetry groups to such configurations. This allowed the use of branes not only to reduce the dimensionality of spacetime to 3+1 dimensions in "braneworld scenarios" but also to address the hierarchy problem [22] and to attempt to reproduce the standard model gauge group (see e.g. [23]). The factor of $\frac{1}{g_s}$ in the brane tension compared to the string tension implies that at weak coupling, D-branes are very heavy objects. It also turns out that Dp-branes, i.e. p+1 dimensional D-branes are sources for p+2-form flux of supergravity with one "unit" p-form charge. Consequentially, even-p branes can only be present in type IIA supergravity and odd-p branes in type IIB supergravity. These properties make them also very interesting in a gravitational context. For example, a stack of N D-branes may form a black p-brane solution, a black hole solution that looks roughly similar to a Myers-Perry black hole with a p-dimensional horizon – more precisely with the

[1]In common abusive notation also the BI action is referred to as DBI action.

solution

$$\begin{aligned} ds^2 &= Z^{-1/2}\left(-Kdt^2 + d\vec{x}_p^2\right) + Z^{1/2}\left(K^{-1}dr^2 + r^2 d\Omega_{8-p}^2\right) \\ C^{(p+1)} &= g_s^{-1}(Z^{-1}-1)dx^0 \wedge \ldots \wedge dx^p \ , \quad e^{2\phi} = g_s^2 Z^{\frac{3-p}{2}} \\ Z &= 1 + \alpha_p \left(\frac{r_p}{r}\right)^{7-p} \ , \quad K = 1 - \left(\frac{r_H}{r}\right)^{7-p} \end{aligned} \tag{1.1.6}$$

where $\alpha_p = \sqrt{1 + \frac{r_H^{14-2p}}{4r_p^{14-2p}}} - \frac{r_H^{7-p}}{2r_p^{7-p}}$ and r_p is parametrically $r_p^{7-p} \sim g_s N l_s^2$ (see e.g. [24, 25, 26]). Special cases are D3-branes for which $F^{(5)} = \star F^{(5)}$ and D7-branes whose solution has a conical deficit angle. Furthermore we get an extremal solution with $AdS_{p+2} \times S^{8-p}$ near-horizon geometry in the extremal limit $\alpha_p = 1$.

One interesting limit of D-brane solutions is the so-called decoupling limit $l_s \to 0$. This essentially corresponds in the black brane solution to dropping the "1" in Z and gives us an AdS black hole. From looking at the DBI action, we also see that this corresponds to decoupling the gravitational modes from the field theory modes, hence the name. In this limit, the solution is only stable at black hole temperatures above the Hawking-Page phase transition [27]. In contrast to Schwarzschild black holes the temperature of these solutions is proportional to r_H/L_{AdS}^2, rather than proportional to $1/r_H$.

D-branes are furthermore used for aspects in cosmology [28] or to construct "black objects"; for example for comparing the black hole entropy to the microscopic entropy obtained from the degeneracy of states first done in [29]. Hence, D-branes are an important part of most of recent attempts to put string theory in the context of physics[2].

1.1.2 AdS/CFT

D-branes also turned out to be necessary for the discovery and implementation of the gauge-gravity duality in string theory. The Holographic principle, i.e. the concept that the information for a d-dimensional theory of quantum gravity is specified on a d-1 dimensional hypersurface was was first suggested by 't Hooft in [31] and was followed-up by Susskind [32], which, however, received initially limited interest. That was changed when Maldacena conjectured the first implementation of a gauge-gravity duality in string theory [33]. His conjecture claims that type IIB string theory in an $AdS_5 \times S^5$ background with N_c units of 5-form flux be dual to a supersymmetric $\mathcal{N} = 4$ $SU(N_c)$ Yang-Mills theory, i.e. a supersymmetric $SU(N_c)$ gauge theory with 4 supercharges defined on the boundary of the

[2]Physics is considered here to be a scientific theory by Karl Popper's definition [30].

AdS spacetime, in the case of Poincaré coordinates $\partial\, AdS_5 = \mathbb{R}^{(3,1)}$. In principle, in its strongest form, the duality is supposed to hold at all values of g_s and l_s.

On the one hand, this can be motivated by the fact that the isometries of the AdS_5, $SO(4,2)$, and the S^5, $SO(6)$, give precisely the conformal group and the R-symmetry group of the field theory, respectively. The fact that the AdS isometries yield the conformal symmetry of the gauge theory led to the generalized concept of the AdS/CFT correspondence, associating d-dimensional conformal field theories of various types with string theory configurations in a spacetime that has an AdS_{d+1} factor. For a comprehensive review of such generalizations and most other aspects see [34]. On the other hand, one can see motivation in the fact that this background is the asymptotic solution in the decoupling limit of N_c coincident D3 branes, and the field theory induced by open strings ending on the branes is an $SU(N_c)$. This allows a very physical interpretation in which one considers strings extending into the spacetime from infinity to probe the spacetime. More precisely, the correspondence relates the operators $\mathcal{O}$ of the SYM to the boundary values ϕ_0 of the fields ϕ in the string theory by equating the partition function of the CFT to the partition function of the string theory, evaluated under a set of boundary conditions:

$$Z_{CFT} = \left\langle e^{\int_{\partial AdS} \phi_0 \mathcal{O}} \right\rangle = Z_{string}(\phi|_{\partial AdS} = \phi_0) \ . \tag{1.1.7}$$

Numerically, the correspondence furthermore relates the Yang-Mills coupling to the string coupling by $g_{YM}^2 = 4\pi g_s$ and the AdS length and the size of the sphere to the rank of the gauge group, $L^4_{AdS_5} = L^4_{S^5} = 4\pi g_s N_c l_s^4$. The motivation for the latter can be seen from the fact that these lengths are precisely obtained from the supergravity solution for a stack of N_c D3-branes. This becomes very interesting from the point of view of the effective coupling in the field theory. The 't Hooft coupling is given by $\lambda = g_{YM}^2 N_c$, which is in terms of gravity parameters $\lambda = \frac{L^4}{l_s^4}$, implying that at large radius of curvature, i.e. weak effective gravitational coupling, the field theory is strongly coupled.

This makes the AdS/CFT correspondence, provided it holds, an interesting computational tool in limits where conventional field theory methods fail. However, this makes it also difficult to verify, or even prove, the correspondence because in converse, the weak coupling limit in the field theory corresponds to highly curved spacetimes in string theory – and even the next-to-leading corrections to supergravity are not all known [36]. Hence, generically a check requires a non-perturbative formulation of either of the theories, and to date successful checks have concentrated on quantities that are "protected" by supersymmetry like n-point functions of chiral primary operators [37] and specific limits like the planar limit of finite λ, but still $N \to \infty$ and $g_s \to 0$ [38]. However, there is a vast amount of activity going beyond those cases e.g. using the Bethe Ansatz [39].

At large N_c, the partition function on the gravity side can be approximately expressed in terms of the supergravity action S_{sugra}, obviously evaluated with the appropriate boundary conditions, as $Z_{string} \sim e^{-S_{sugra}}$. This provides for the straightforward computation of field theory correlators [35] and also for the association of background properties or parameters in the field theory with parameters in the gravity theory. Subsequently, this method was further developed and extended to various different contexts. For example, it was extended from the decoupling limit of D3-branes to general Dp-branes where obviously the field theory is modified compared to the D3/$\mathcal{N} = 4$ SYM case [40].

The common intuition is that the radial direction of the AdS spacetime corresponds to the energy in the field theory, as can be seen from the fact that a conformal transformation in the field theory corresponds to an isomorphism in the radial coordinate in the AdS spacetime. Placing the asymptotic boundary at some finite radius corresponds then to integrating out the degrees of freedom at high energies. Similarly a finite temperature can be introduced by introducing a black hole horizon at some radius r_H, i.e. considering a stack of black D-branes. The temperature of the thermal field theory is then just given by the temperature of the dual stack of D3 branes, in the case of D3 branes $T = \frac{r_H}{\pi L^2_{AdS}}$.

For practical applications in an experimental context, one of the limitations of the above was the fact that the fields on the field theory side transform in the adjoint representation of the $U(N_c)$. To introduce matter in the fundamental representation and make the duality more relevant for the only fundamental strongly coupled field theory in nature, QCD, the approach of using probe branes was introduced. This was first done by introducing a small number of N_f "probe" D7-branes into the background, covering all of the AdS directions [41, 42]. Fields on the probe brane are then dual to operators in the fundamental representation of the $SU(N_c)$, and the $U(N_f)$ symmetry of the stack of probe branes corresponds to the flavor symmetry. This model is a good example of how one can guess the dual field theory from the massless level of the string spectrum in the gravity setup, as the massless level of the open string spectrum at the intersection in this case contains a hypermultiplet that transforms under the fundamental representation of the $SU(N_c)$. If one considers the so-called "quenched limit" of $N_f \ll N_c$, this setup is further simplified by the fact that the backreaction of the probe branes on the D3 background can be ignored at leading order. Obviously this setup is still significantly different from the standard model QCD, but studying the physical properties of both this model and the T-dual D4-D6 setup have received great interest [43, 44]. Particular activity has been related to the thermodynamics and the phase structure [45] and the "meson spectrum" [46].

From an experimental point of view, certainly the hydrodynamics have been most interesting due to the similarity to recent heavy ion collision experiments at RHIC [47] (and in the future also at the LHC) that study properties of the quark-gluon plasma - the

phase of matter at high temperatures and high densities in which quarks and gluons are in a superfluid phase, that is supposed to have existed a few tens of micro seconds after the big bang. Despite the very different details of the theory, some generic properties about this phase of matter may be predicted by AdS/CFT. The most celebrated result may have been the universal ratio of the shear viscosity to the entropy density of $\eta/s = 1/(4\pi)$, that applies to a large class of theories. In fact, including higher order terms on the gravity side suggests that this is a minimum bound [48], and experiments suggest that this bound is closely saturated in QCD [47].

Another very recent area in which the AdS/CFT correspondence has received great interest for its applications is condensed matter physics. In that context, initial interest has been on the transport properties of $2+1$ dimensional field theories, obtained from a dual M2-brane setup with $AdS_4 \times S^6$ spacetime [49], which found a very interesting result for the isotropic conductivity that turned out to be frequency independent. Subsequent research for example obtained the DC Hall conductivity from a dyonic blackhole setup [50], studied the Nernst effect [51] and other issues [52, 53]. Most interest has received the construction of gravitational setups whose field theory duals show the phase transition of a superconductor. These constructions were initially based on black holes with "scalar hair" and $SU(2)$ backgrounds outside string theory, but later setups were also constructed within string theory [54]. It is interesting to see how closely they reproduce effects observed in experimental condensed matter physics, as it was discovered for example that also the holographic constructions possess a critical magnetic field and the magnetic field is quantized in vortices [55]. Another recent branch has been the construction of gravitational setups, whose dual field theories are non-relativistic and have the conformal symmetry reduced to Schrödinger symmetry [56]. There is hope that this may yield the construction of a wide range of gravitational duals to field theories in condensed matter physics, which are in most cases non-relativistic.

The hope that AdS/CFT may prove useful in condensed matter physics is on the one hand supported by the fact that it not only can potentially provide insight and observable properties for some strongly coupled theories that may be similar to those in condensed matter physics, but also that it provides those results in a very uniform and general fashion in just one calculation, rather than deriving different approximate solutions in different limits as it is the case with current ordinary field theory methods [57, 58]. On the other hand, condensed matter physics provides an interesting playground for AdS/CFT, because there is a large number of 2+1 dimensional systems that display conformal behavior, i.e. there are potentially many different strongly coupled CFTs of relevance to experiment as we line out in the next subsection and there is a vast number of 3+1 dimensional AdS vacua in string theory that may be used to construct gravitational duals [57, 58]. In contrast to

this, there is only one QCD.

Obviously, there are many other equally fascinating applications of the AdS/CFT correspondence, such as studies of extremal black holes via the AdS_2/CFT^1 correspondence [59] or entropy counting for 3 dimensional black holes [60].

1.1.3 Some hard problems in condensed matter physics

Of particular interest for applications of AdS/CFT has become the so-called quantum critical phase of condensed matter systems. Most commonly, a phase transition is understood to be happening at finite temperature, when the temperature moves from a regime favoring one state of a system towards a regime favoring another state. There are however also phase transitions at zero temperature, which occur if one tunes a generalized "coupling" constant J, e.g. the pressure or the background magnetic field of a system, so-called "quantum phase transitions". These quantum phase transitions occur whenever there is a level crossing of the ground state of the Hamiltonian with the lowest excited state. Most commonly however, level crossings will be "avoided" in finite size systems. For large system sizes though, there is a limiting case in which the ground state and first excited state become infinitely close in energy at one point in phase space, which does also become a quantum phase transition. Examples are phase transitions in antiferromagnets and some superconductor-insulator transitions.

The system becomes scale invariant as the coupling is tuned to the quantum critical point, just like the diverging correlation length as one approaches the critical temperature of a second order phase transition. Hence, it has conformal symmetry and can be described by a conformal field theory. While it was known for a long time that at finite temperature, the quantum critical phase transition does not always continue into a single phase transition between the finite-temperature extensions of the two phases and may show some crossover phase, this area in phase space received not much interest until recently. It turns out that the phase at the quantum critical point extends into the finite temperature regime, where there is a "quantum critical phase" in which the only length scale is given by the temperature. This is shown in fig. 1.1, where we show a generic quantum phase transition between some ordered and some unordered phase.

While scale invariance is a key feature of phase transitions in condensed matter physics, also at finite temperature, this case is special, as there is a whole region of finite volume in phase space that can be described by a conformal field theory. As an example, the conductivity in the quantum critical phase is thought to be controlled by a universal function Σ that depends on the ratio ω/T and some dimensional temperature scaling,

$\sigma(\omega) = Q^2(T/c)^{d-2}\Sigma(\omega/T)$ for some microscopically determined velocity c. Obtaining Σ however is a difficult task and can only be done in certain limits. For instance, for large frequencies, one expects $\sigma \sim \omega^{d-2}$ [58].

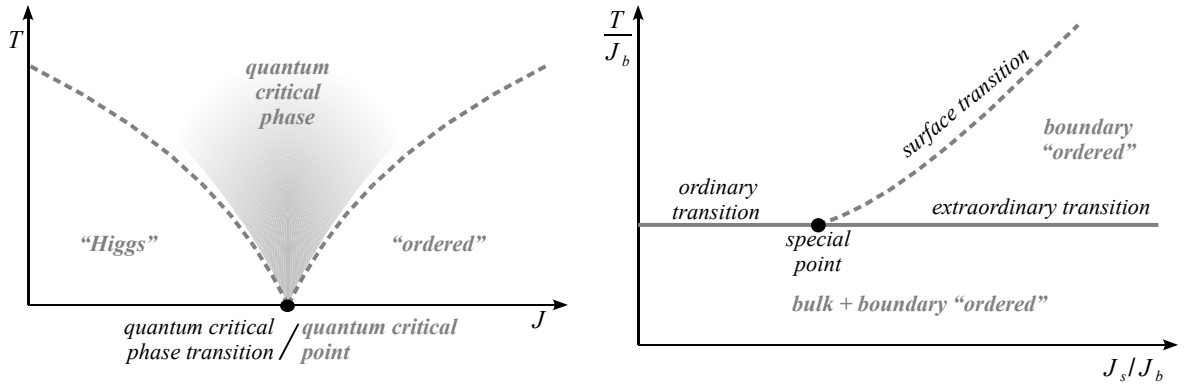

Figure 1.1: Left: A generic quantum critical phase transition and quantum critical phase. Right: A generic surface phase diagram.

Defect field theories are basically field theories in which matter that is confined to some hypersurface interacts via a field theory in the bulk. While there is some review literature in a soft condensed matter context related to aspects like the statistical mechanics of crystal defects in the context of melting behaviors, defects in polymers or flux tubes in superconductors (for a review see [61]), there seems to be not much review literature related to the defects and their aspects that we are interested in. Hence, a motivated guess may be that they have many properties in common with surfaces, which have been studied extensively.

To illustrate their properties, we can look at a generic surface phase diagram in fig. 1.1, of some system described by a bulk coupling J_b and a surface coupling, J_s – for a review on the subject see [62]. There, we see that over most of the parameter range, the surface and the bulk are in the same phase, and display a simultaneous "ordinary" phase transition. As we tune the surface coupling beyond a "special point", which is some critical multiple of the bulk coupling, the phase transitions on the surface and in the bulk separate into a surface phase transition and an "extraordinary" phase transition in which there is a phase transition only in the bulk. It is obvious from the ratio J_s/J_b in this regime that the ordered phase on the surface extends to higher temperatures than the ordered phase in the bulk. However it is quite interesting that this splitting of phase transitions typically occurs as J_s becomes greater than J_b and hence there is no "mirror symmetric" version of this plot.

1.2 This thesis

1.2.1 Context

As outlined above, most research in AdS/CFT applied to condensed matter physics studies 2+1 dimensional systems, in particular purely 2+1 dimensional systems. Since our world however is 3+1 dimensional, all 2+1 dimensional systems are strictly speaking defects. In some cases this fact may be less relevant and in other cases more relevant.

Hence, in this thesis, we are studying the physics of a 2+1 dimensional defect of charged matter ("quarks") interacting in a 3+1 dimensional $\mathcal{N} = 4$ $SU(N_c)$ SYM background, based on the transport properties of this matter along the defect. In that sense we will be put sometimes in the perspective of an experimentalist, trying to interpret our results. To identify the characteristics that are due to having a defect rather than just a plain 2+1 dimensional field theory, a major theme in this research is the inclusion of a parameter that is related to a difference in the level of the gauge group $N_c \to \delta N_c$ between both sides of the defect.

Also, we will try to link the properties obtained in different regimes rather than studying only one particular limit or one particular effect. In this spirit, we will study all frequency and wavenumber scales, from the hydrodynamic limit (the "collision-dominated" regime at small frequencies and small wavenumbers) up to the quasiparticle limit (the "collisionless" regime at large frequencies) – and we will demonstrate in several cases how a length scale obtained in one regime, direction or context will govern some properties also in another regime. Furthermore, we will be interested how effects from ordinary weakly coupled free electron gas type physics that we are familiar with will manifest themselves in this strongly coupled system, as we turn on various condensed matter parameters, i.e. the net baryon number density, background magnetic field and "quark" mass. Certainly, since we are working at finite temperatures, there will aways be a finite total "quark" density, and the net baryon number density in some sense corresponds to the difference of the number of "quarks" and "anti-quarks". While those quantities may move us away from the quantum critical point in the defect field theory, the bulk theory will still remain $\mathcal{N} = 4$ SYM. In terms of the phase diagram of surface phase transitions, this would move us along the direction of surface coupling towards the extraordinary phase transition.

One interest is furthermore to explore what happens to the result of the constant conductivity due to electromagnetic duality in [49] in this defect setup, at finite background quantities and in the presence of higher order corrections in the gravity side i.e. finite coupling in the field theory side.

Our defect CFT is realized by inserting N_f probe D5- or D7-branes into the background of a black stack of D3-branes. In either construction, the difference δN_c in the level of the gauge group of the 3+1 SYM will be introduced by an additional flux on the probe brane in the compact sphere. The defect CFT constructed with the D5-branes is certainly well known [41, 63, 64]. Certain aspects of the D7-brane construction have also been studied previously [65, 66] but we should note that the internal flux introduced here is essential to remove an instability that would otherwise appear in this construction. The finite magnetic field and net density are introduced using the well-known duals of a magnetic field and an electric field, respectively, in the world-volume of the probe brane. The finite quark mass will be obtained by a deformation of the embedding in the compact sphere in the same way in which it was done in the duals for 3+1 dimensional QCD-like systems [45, 67, 68, 44]. To obtain the transport properties, we will use linear response theory to study the conductivity on the defect at finite frequency, temperature and wave-number, *i.e.,* the conductivity of an anisotropic current.

1.2.2 Outline

The outline of this Thesis is as follows: In chapter 2, we study the properties of the defect in the absence of any of the background quantities, only considering a finite difference in the level of the gauge groups. In section 2.1, we review the holographic framework, in particular the embedding of the probe D-branes in the $AdS_5 \times S^5$ background. In section 2.2, we obtain the basic results for the spectral functions, starting with a review of the methodology and then the computation of the transverse and longitudinal conductivities in section 2.2.1. Here we also calculate the diffusion constant for charge transport in subsection 2.2.1.3 and comment on the agreement with the diffusion-dominated conductivity in the hydrodynamic regime, *i.e.,* in the regime at small frequency and wave-number $\omega, q \ll T$. This is followed by a discussion of the collisionless, ($q \gtrsim T$), regime using analytical approximations in section 2.2.2, for both the insulating case (at small frequencies) and the optical regime (at large frequencies). Using those results, we study the spectrum of quasinormal modes in section 2.3. In section 2.4, we examine the effect of stringy corrections to the gauge theory on the probe branes, which describes the behavior of the dual currents on the defect. In particular, electromagnetic duality is lost when these α'-corrections are included, which has interesting implications for the conductivity at strong but finite 't Hooft coupling. Finally, we consider the computation of a topological Hall conductivity in section 2.5. Some details of our analysis of this chapter are relegated to appendices: In Appendix A, we demonstrate the regularity of the probe brane at the horizon. Appendix B presents some details of the analysis including certain α' corrections in the D5-brane worldvolume action. In appendix

C, we do an analytical study of a slightly simplified model of the defect, which gives further qualitative insight, and aids the numerical computation of the quasinormal modes.

In chapter 3, we consider the effects of finite background parameters, the (net) baryon number density, background magnetic field and finite quark mass. In section 3.1.2, we describe how to introduce the background quantities in the defect system and describe several problems that arise in the D3-D7 setup - which motivate us not to pursue the massive D7 case. We then show in section 3.2, how we generalize the methods of section 2.2.1 in this case, and also demonstrate the effects of electromagnetic duality at finite density and magnetic field. In section 3.3, we then review some basic properties of weakly coupled systems in order to introduce the terminology and remind the reader of some intuition. In section 3.4, we derive analytic results in various limits, first in the isotropic DC limit $\omega \to 0$ and in the small frequency expansion beyond the DC limit. Then, we consider the small temperature limit small frequencies $q \gg 1 \gg \omega$ in various regimes of the density and magnetic field and finally we obtain the diffusion constant and "electric" permittivity and consider the hydrodynamic regime (ω, $q \ll 1$). The numerically-obtained full spectral curves are presented in section 3.5, where we also later present and discuss the purely dissipative poles that we obtain numerically and study the quasiparticle poles in the correlator that we obtain numerically both directly and from the spectral curves. We present the explicit form of the induced metric on the brane in appendix D, and in appendix E, we discuss the contribution of the defect to the thermodynamics and its phase structure.

Previously published material

The research presented in chapter 2 and in the related appendices has been published in : R. C. Myers and M. C. Wapler, "Transport Properties of Holographic Defects," JHEP **0812**, 115 (2008) [arXiv:0811.0480 [hep-th]].

The research presented in chapter 3 and appendix E will soon be posted on the arXiv and subsequently submitted to scientific journals.

Chapter 2

Bare Defects

2.1 Defect Branes

The AdS/CFT correspondence is most studied and best understood as the duality between type IIb string theory on $AdS_5 \times S^5$ and $\mathcal{N} = 4$ super-Yang-Mills theory with $U(N_c)$ gauge group. In this context, all fields in the SYM theory transform in the adjoint representation of the gauge group. One approach to introducing matter fields transforming in the fundamental representation is to insert probe D7-branes into the supergravity background [42]. However, this approach can also be used to construct a defect field theory, where the fundamental fields are only supported on a subspace within the four-dimensional space-time of the gauge theory. In particular, we will consider constructing a $(2+1)$-dimensional defect by inserting N_f Dp-branes, with three dimensions parallel to the SYM directions and $p-3$ directions wrapped on the S^5. In the following, we work with both probe D5- and D7-branes. If we consider the supergravity background as the throat geometry of N_c D3-branes, our defect constructions are described by the following array:

		0	1	2	3	4	5	6	7	8	9
background :	$D3$	×	×	×	×						
probe :	$D5$	×	×	×		×	×	×			
	$D7$	×	×	×		×	×	×	×	×	

(2.1.1)

The D5-brane construction is supersymmetric and the dual field theory is now the SYM gauge theory coupled to N_f fundamental hypermultiplets, which are confined to a (2+1)-dimensional defect. Note that the supersymmetry has been reduced from $\mathcal{N} = 4$ to

$\mathcal{N}=2$ by the introduction of the defect. In the D7-brane case, we have lost supersymmetry altogether and the defect supports $N_{\rm f}$ flavours of fermions, again in the fundamental representation [65]. One should worry that the lack of supersymmetry in the latter case will manifest itself with the appearance of instabilities. However, we will explicitly show below in section 2.1.2 that this problem can be avoided. In the limit $N_{\rm f} \ll N_{\rm c}$, the D5- and D7-branes may be treated as probes in the supergravity background, *i.e.,* we may ignore the gravitational back-reaction of the branes.

As we commented above, a similar holographic framework has been used extensively to study the properties of the $\mathcal{N}=2$ gauge theory constructed with parallel D7- and D3-branes, *i.e.,* the fundamental fields propagate in the full four-dimensional spacetime – *e.g.,* see [44, 43, 45]. If a mass $M_{\rm q}$ is introduced for the hypermultiplets, it was found that the scale $M_{\rm fun} \sim M_{\rm q}/\sqrt{\lambda}$ plays a special role in this theory. First, the "mesons", bound states of a fundamental and an anti-fundamental field, are deeply bound with their spectrum of masses characterized by $M_{\rm fun}$ [46]. Next at a temperature $T \sim M_{\rm fun}$, the system undergoes a phase transition characterized by the dissociation of the mesonic bound states [45]. The analogous results can be verified for the defect theories considered here. That is, the meson spectrum is characterized by the same mass scale $M_{\rm fun}$ [70, 71] and these states are completely dissociated in a phase transition at $T \sim M_{\rm fun}$ as we show in appendix E. However, these results are tangential for this chapter, as we will only consider the conformal regime with $M_{\rm q}=0$ and concentrate instead on exploring the defect-specific nature of the system.

Common to both of our constructions is the supergravity background dual to $\mathcal{N}=4$ SYM at finite temperature. This background is a planar black hole in AdS_5, corresponding to the decoupling limit of $N_{\rm c}$ black D3-branes [72]:

$$ds^2 = \frac{r^2}{L^2}\left(-h(r)dt^2 + dx^2 + dy^2 + dz^2\right) + \frac{L^2}{r^2}\left(\frac{dr^2}{h(r)} + r^2 d\Omega_5^2\right), \qquad C^{(4)}_{txyz} = -\frac{r^4}{L^4} \tag{2.1.2}$$

where $h(r) = 1 - r_0^4/r^4$. The gauge theory directions correspond the coordinates $\{t, x, y, z\}$. The radius of curvature L is defined in terms of the string coupling constant $g_{\rm s}$ and the string length scale $\ell_{\rm s}$ as $L^4 = 4\pi\, g_{\rm s} N_{\rm c}\, \ell_{\rm s}^4$. The holographic dictionary relates the Yang-Mills and string coupling constants as $g^2_{\rm YM} = 4\pi g_{\rm s}$ and so we may write $L^4 = \lambda\, \ell_{\rm s}^4$ where $\lambda = g^2_{\rm YM} N_{\rm c}$ is the 't Hooft coupling. As usual, we work in the supergravity approximation, ignoring the effects of string loops or higher derivative terms suppressed by powers of $\ell_{\rm s}$ (except in section 2.4 and appendix B). Hence, we are working in the limit where both $N_{\rm c}$, $\lambda \to \infty$. The background (2.1.2) contains an event horizon at $r = r_0$. The temperature of the SYM theory is then equivalent to the Hawking temperature:

$$T = \frac{r_0}{\pi L^2}\,. \tag{2.1.3}$$

2.1.1 D5-branes

Introducing D5-branes as in (2.1.1) was the original application of probe branes for the holographic construction of a defect CFT – *e.g.,* see [41, 63]. The worldvolume action which will determine the embedding of the probe D5-branes has the usual Dirac-Born-Infeld (DBI) and Wess-Zumino (WZ) terms:

$$I_5 = -N_{\rm f}\, T_5 \int d^6\sigma \sqrt{-det\left(P[G] + 2\pi\ell_{\rm s}^2 F\right)} + N_{\rm f}\, T_5 \int C^{(4)} \wedge 2\pi\ell_{\rm s}^2 F\,. \tag{2.1.4}$$

Implicitly we have assumed that the $N_{\rm f}$ D5-branes are all coincident. Hence, in principle, their worldvolume supports a $U(N_{\rm f})$ gauge theory, however, implicitly above and in the following, we only consider the gauge field in the diagonal $U(1)$ of this $U(N_{\rm f})$. We choose coordinates on the five-sphere in (2.1.2) such that

$$d\Omega_5^2 = d\psi^2 + \cos^2\psi\left(d\theta^2 + \sin^2\theta\, d\phi\right) + \sin^2\psi\, d\Omega_2^2\,. \tag{2.1.5}$$

The D5-branes wrap the two-sphere parameterized by $\{\theta, \phi\}$ above, fill three of the gauge theory directions $\{t, x, y\}$ and extend in the radial direction r. We also introduce a flux of the worldvolume gauge field on the two-sphere:

$$F_{\theta\phi} = \frac{q}{2\, N_{\rm f}}\, \sin\theta\,. \tag{2.1.6}$$

One may verify that this flux corresponds to dissolving q D3-branes into the worldvolume of the $N_{\rm f}$ D5-branes along the $\{t, x, y, r\}$ directions, since the branes with flux sources $C^{(4)}$ through the WZ term in (2.1.4).

Now in general, the D5-brane embedding would be specified by giving its profile in both the angular direction $\psi(r)$ and the D3-brane direction $z(r)$. These embeddings all have translational symmetry in the $\{t, x, y\}$-space, as well as invariance under $SO(3)$ rotations on the internal two-sphere. In the following, we consider only the embeddings with $\psi = 0$, *i.e.,* where the D5-brane wraps a maximal two-sphere in the internal space. One can easily verify this choice corresponds to a solution of the worldvolume embedding equations. This choice also corresponds to setting the mass of the fundamental fields to zero, *i.e.,* $M_{\rm q} = 0$, and so as we will describe below, this choice also ensures that the dual field theory with the defect remains conformal.

Hence in our analysis, we must determine the profile $z(r)$. The induced metric on the D5-branes is now described by

$$ds^2 = \frac{r^2}{L^2}\left(-h(r)dt^2 + dx^2 + dy^2\right) + \left(\frac{L^2}{r^2 h(r)} + \frac{r^2}{L^2}\partial_r z^2\right) dr^2 + L^2\left(d\theta^2 + \sin^2\theta\, d\phi\right)\,. \tag{2.1.7}$$

We can integrate over the two-sphere directions to produce a factor of

$$\oint_{S^2} d^2\sigma \sqrt{det_{S^2}\left(P[G] + 2\pi\ell_{\rm s}^2 F\right)} = 4\pi \left(N_{\rm f}^2 L^4 + \pi^2 \ell_{\rm s}^4 q^2\right)^{1/2} = 4\pi N_{\rm f} L^2 \sqrt{1+f^2} \qquad (2.1.8)$$

where

$$f \equiv \frac{\pi \ell_{\rm s}^2}{L^2}\,\frac{q}{N_{\rm f}} = \frac{\pi}{\sqrt{\lambda}}\frac{q}{N_{\rm f}} \qquad (2.1.9)$$

in the DBI part of the action (2.1.4). The full D5-brane action then becomes

$$I_5 = -4\pi N_{\rm f} T_5 \sqrt{1+f^2} \int d^3x\, dr\, r^2 \left(1 + \frac{r^4}{L^4} h(r) \partial_r z^2\right)^{\frac{1}{2}} - 4\pi N_{\rm f} T_5 \frac{f}{L^2} \int d^3x\, dr\, r^4\, \partial_r z\,. \qquad (2.1.10)$$

To simplify the analysis, we introduce the following coordinates:

$$u = \frac{r_0}{r}\,, \qquad\qquad \chi = \frac{r_0}{L^2} z\,. \qquad (2.1.11)$$

With this new notation, $h(u) = 1 - u^4$ and so the horizon is now at $u = 1$ while the asymptotic region is reached when $u \to 0$. The worldvolume action can now be written as:

$$I_5 = -4\pi r_0^3 N_{\rm f} T_5 \int d^3x\, \frac{du}{u^4} \left[\sqrt{1+f^2}\left(1 + h(u)\chi'^2\right)^{\frac{1}{2}} + f\,\chi'\right], \qquad (2.1.12)$$

where $\chi' \equiv \partial_u \chi$. This expression is independent of χ, such that the variation with respect to χ' yields a constant of motion:

$$\frac{1}{u^4}\left[\sqrt{1+f^2}\frac{h(u)\chi'}{\left(1+h(u)\chi'^2\right)^{1/2}} + f\right] = C\,. \qquad (2.1.13)$$

To avoid singular behavior at the horizon, we need to fix the integration constant to be $C = f$. In this case, (2.1.13) yields

$$\chi' = -\frac{f}{\sqrt{1+f^2 u^4}}\,. \qquad (2.1.14)$$

Given this expression, the profile $\chi(u)$ can be expressed in terms of an incomplete elliptic integral. However, in the following, it will sufficient to have a closed form expression for χ'. We illustrate a typical profile in figure 2.1.

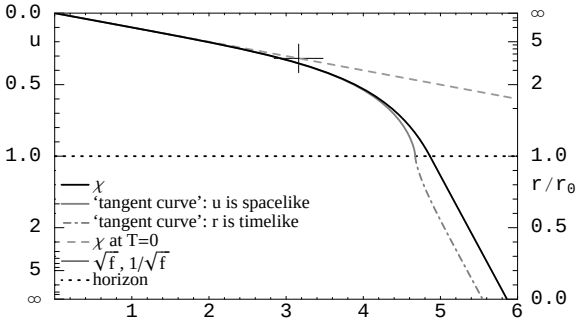

Figure 2.1: The brane profile χ for $f = 10$ above the horizon in terms of u and below the horizon in terms of r/r_0. The angle of the "tangent curve" in the plot represents the physical angle of the brane w.r.t. u or r, respectively; obtained from the unit norm vectors. The temperature scaling of the $T = 0$ profile corresponding to $\chi = -f\,u$ is fiducial.

In terms of our original coordinates, we have

$$\frac{\partial z}{\partial r} = \frac{L^2\, f}{\sqrt{r^4 + f^2\, r_0^4}}\,. \tag{2.1.15}$$

Here we may consider the supersymmetric limit with $r_0 = 0$, in which case (2.1.15) simplifies to $z = -L^2 f/r$. In this case, one can confirm that the induced metric (2.1.7) corresponds to $\mathrm{AdS}_4 \times S^2$ with an AdS radius of curvature of $L_{\mathrm{AdS}_4} = L\,\sqrt{1+f^2}$ [41]. Hence the system inherits SO(2,3) symmetry from the AdS_4 geometry, which reflects the fact that the dual field theory remains conformal in the presence of the defect. This conformal invariance can also be shown directly by an analysis of the field theory [73]. Subsequently, the construction of the fully back-reacted geometries corresponding to the D5-branes embedded in $AdS_5 \times S^5$ demonstrate that the preservation of the SO(2,3) symmetry is a fully nonperturbative result [64].

One may note that with the supersymmetric profile, $z = -L^2 f/r$, there are an additional $q = \sqrt{\lambda}\, N_{\mathrm{f}}\, f/\pi$ D3-branes stretching from $z = 0$ to $-\infty$, assuming $f > 0$. Hence if one were to include back-reaction, the asymptotic five-form flux would be shifted from $N_{\mathrm{c}} \to N_{\mathrm{c}} + q$ units on this side of the space. The same will apply at a finite temperature. Even though the brane falls through the horizon at a finite distance in this case, continuity at the horizon dictates that the background will carry $N_{\mathrm{c}} + q$ units of flux out to $z = -\infty$. In either case, the natural interpretation is that the dual CFT has a $U(N_{\mathrm{c}}+q)$ gauge group in the region $z < 0$, while the gauge group remains $U(N_{\mathrm{c}})$ for $z > 0$.

It is interesting to pursue the interpretation of the above brane configuration in the dual CFT further. A detailed AdS/CFT dictionary has been developed for this defect system [63, 73]. In particular, one finds that the defect lagrangian contains potential source terms for the adjoint scalars in the SYM theory [63, 74]. The D5-brane carrying flux f corresponds to producing a noncommutative configuration of adjoint scalars in a

$U(q)$ subgroup of the $U(N_c + q)$ in the $z < 0$ region [70]. In fact, in this supersymmetric configuration, the profile of the D5-branes can be precisely matched to the scalar profile using noncommutative geometry [75]: $r^2 = (2\pi\ell_s^2)^2 \frac{1}{N_f}\mathrm{Tr}(\Phi^2)$ where $\frac{1}{N_f}\mathrm{Tr}(\Phi^2) = \frac{q^2}{4N_f^2}\frac{1}{z^2}$.

As the D5-brane wraps a maximal two-sphere inside the S^5, one might worry about the stability of this configuration. Indeed the worldvolume field, corresponding to fluctuations in the angle ψ, is found to be a tachyon with [41]

$$m_\psi^2 = -\frac{2}{L^2(1+f^2)} = -\frac{2}{L^2_{\mathrm{AdS}_4}} > -\frac{9}{4L^2_{\mathrm{AdS}_4}}\,. \tag{2.1.16}$$

However, the last inequality indicates that the ψ-mode satisfies the Breitenlohner-Freedman bound [76] in the asymptotically AdS_4 geometry induced on the D5-brane worldvolume. Hence this field does not in fact produce an instability.

Another concern may arise in considering the intersection of the D5-branes with the event horizon in (2.1.2). There we note that

$$\chi'|_{u=1} = -\frac{f}{\sqrt{1+f^2}} \tag{2.1.17}$$

or in terms of original coordinates

$$\left.\frac{\partial z}{\partial r}\right|_{r=r_0} = \frac{L^2\, f}{r_0^2\sqrt{1+f^2}}\,. \tag{2.1.18}$$

Since the D5-brane enters the event horizon at an angle, one might worry that the induced geometry is singular [68]. However, one can verify that this intuition is incorrect and that in fact, the D5-brane geometry remains smooth as it crosses the horizon. Hence the induced metric (2.1.7) describes a smooth 'black hole' geometry on the D5-brane worldvolume. A related question is: what is the surface gravity or the temperature of the induced horizon? It is a simple exercise to show that the relevant temperature matches that of the bulk geometry, *i.e.,* that given in (2.1.3). Of course, this reflects the fact that the defect and bulk fields will be in thermal equilibrium, as expected.

We address one other potential concern related to the internal flux (2.1.6). Throughout the paper, we will be considering finite values of f, typically of $O(1)$. Hence according to (2.1.9), we are introducing $q \sim O(\sqrt{\lambda})$ D3-branes and so one might worry about whether it is reasonable to consider the probe brane limit, *i.e.,* to ignore the gravitational back-reaction of the branes. Of course, this is not a problem since the overall tension of the D5-branes is not significantly modified by the flux, as can be seen from (2.1.10). The

essential point is that the D3-branes are distributed on the D5-branes over the internal two-sphere which has an area of order $L^2 \sim \sqrt{\lambda}$ and so the density of D3-branes remains small, *i.e.,* the density is $O(f)$.

2.1.2 D7 probes

The case of D7 probe branes is similar to the previous section with D5-branes. The main difference lies in the internal part of the geometry. In particular, the D7-branes wrap a(n equatorial) four-sphere in the internal S^5. As before, we consider D3-branes dissolved into the probe branes. In the present case, the D7-branes source the three-brane charge through in the appropriate term in the WZ action: $\frac{1}{2}(2\pi\ell_{\rm s}^2)^2 T_7 \int C^{(4)} \wedge F \wedge F$. Hence, considering a stack of $N_{\rm f}$ coincident D7-branes with a $U(N_{\rm f})$ gauge symmetry, we introduce a nonvanishing second Chern class on the internal four-sphere: $q_7 = \frac{1}{8\pi^2} \oint_{S^4} TrF \wedge F$.

The D7-branes are fixed to wrap a maximal four-sphere while the embedding in the AdS_5 is described by $z = z(r)$. The induced metric on the D7-branes becomes

$$ds^2 = \frac{r^2}{L^2}\left(-h(r)dt^2 + dx^2 + dy^2\right) + \left(\frac{L^2}{r^2 h(r)} + \frac{r^2}{L^2} z'^2\right) dr^2 + L^2 d\Omega_4^2 \,. \tag{2.1.19}$$

Since the present configuration contains a nontrivial nonabelian gauge field, the worldvolume action requires a nonabelian extension of the DBI action [77]

$$I_7 = -T_7 \int d^8\sigma \, {\rm STr}\sqrt{-det\left(P[G] + 2\pi\ell_{\rm s}^2 F\right)} + \frac{1}{2} T_7 (2\pi\ell_{\rm s}^2)^2 \int {\rm Tr}\left(C^{(4)} \wedge F \wedge F\right) \,. \tag{2.1.20}$$

This action uses the proposal of a maximally symmetric gauge trace, denoted by 'STr' [78]. To be precise, the trace includes a symmetric average over all orderings of F_{ab} – and implicitly any appearances of the nonabelian scalars as well [79] but the latter will not be relevant in the present analysis. This prescription correctly agrees with the string action to fourth order in the field strength [78] but is known to miss certain commutator terms which begin to appear at sixth order [80]. However, the contribution of such terms is typically suppressed by factors of $1/N_{\rm f}$ and so they can be safely neglected for sufficiently large $N_{\rm f}$ [75, 81].

As before, we integrate over the internal space in the DBI action. Here the internal S^4 carries an nonabelian gauge field giving the instanton number q_7. This configuration was

extensively studied in [81] and hence using their results, we find

$$\begin{aligned}\oint_{S^4} d^4\Omega \quad & \mathrm{STr} \quad \sqrt{det_{S^4}\left(P[G]+2\pi\ell_{\rm s}^2 F\right)} \\ &= \oint_{S^4} d^4\Omega\,\sqrt{g_{S^4}}\,\sqrt{L^8+\frac{1}{2}L^4(2\pi\ell_{\rm s}^2)^2F_{ab}F^{ab}+\frac{1}{64}(2\pi\ell_{\rm s}^2)^4(\epsilon_{abcd}F^{ab}F^{cd})^2} \\ &= \frac{8\pi^2}{3}\left(N_{\rm f}\,L^4+6\pi^2\ell_{\rm s}^4|q_7|\right)\,. \end{aligned} \tag{2.1.21}$$

In the latter, we use (anti-)self-duality for the instanton configuration: $F_{ab}=(-)\frac{1}{2}\epsilon_{abcd}F^{cd}$ for $q_7>0$ ($q_7<0$). Implicitly, we are also assuming that the instanton number is uniform on the four-sphere, which limits $q_7\leq N_{\rm f}(N_{\rm f}^2-1)/6$ [81]. Substituting (2.1.21) and the embedding (2.1.19) into (2.1.20), the action for the background configuration becomes

$$I_7=-\frac{8\pi^2N_{\rm f}}{3}L^4(1+|Q|)T_7\int d^3\sigma dr\frac{r^2}{L^2}\sqrt{1+\frac{r^4}{L^4}h(r)}\;-\;\frac{8\pi^2N_{\rm f}}{3}L^4Q\,T_7\int d^3\sigma dr\frac{r^4}{L^4}z'\,, \tag{2.1.22}$$

where we defined for convenience $Q=6\pi^2\frac{\ell_{\rm s}^4}{L^4}\frac{q_7}{N_{\rm f}}=\frac{6\pi^2}{\lambda}\frac{q_7}{N_{\rm f}}$. Now, the computations analogous to those in section 2.1.1 yield an identical embedding $\chi(u)$ as in (2.1.14) but the constant f is replaced by

$$f_7\equiv\frac{Q}{\sqrt{1+2|Q|}}\,. \tag{2.1.23}$$

The microscopic interpretation of the D7-brane configuration in the dual CFT is not as clear in the present case. However, as before, the gauge group in the region $z<0$ will be enhanced to $U(N_{\rm c}+q_7)$ assuming $q_7>0$. There should be source terms on the defect which excite a noncommutative configuration of the adjoint scalars in the transverse space. The latter can be interpreted in terms of noncommutative geometry as giving the profile of the D7-branes, at least to leading order in $1/N_{\rm f}$ [81].

An important difference between the present case and that in the previous section with D5-branes is that in the mass of the tachyonic mode ψ corresponding to the S^4 part of the D7-branes "slipping off" the maximal S^4 in the internal space. A simple calculation reveals that

$$m_\psi^2\;=\;-\frac{4}{L^2(|Q|+1)}\;=\;-\frac{4}{L^2_{\rm AdS_4}}\,\frac{|Q|+1}{2|Q|+1}\,. \tag{2.1.24}$$

Recall that the BF bound requires $m^2>-\frac{9}{4L^2_{AdS_4}}$ [76] and hence is only satisfied for $|Q|>\frac{7}{2}$. Hence one can trust the results in the following sections for the D7-branes only

for $f_7^2 > 49/32$ and we might think of the internal flux on the S^4 as creating some pressure that stabilizes the size of the S^4. However, we should caution the reader that what we have shown is that the most obvious instability is removed for sufficiently large Q. While suggestive, this does not prove the D7-brane configuration is absolutely stable.

Beyond this crucial difference, the analysis of these two systems (*i.e.,* defects constructed with D5- or D7-branes) is completely the same. Hence in the following, we focus on the first case of D5-branes and only comment on differences in coefficients that may arise for D7-branes where appropriate.

2.2 Correlators

In this section, we obtain examine various correlators of the currents dual to the world-volume gauge field A_μ. First we review the basic form of the correlators below, following [49]. Then we numerically compute the spectral functions in 2.2.1 and then examine the dependence of the correlators on the temperature and the flux f in 2.2.2.

In the following, we use holographic techniques to calculate the retarded Green's function for a conserved current $J_\mu(x)$ on the defect. The defect degrees of freedom form a (2+1)-dimensional CFT which restricts the form of the correlators:

$$C_{\mu\nu}(x-y) = -i\,\theta(x^0-y^0)\,\langle\,[J_\mu(x), J_\nu(y)]\,\rangle\ , \tag{2.2.25}$$

where translation invariance is assumed. The correlator can be Fourier transformed to $C_{\mu\nu}(p)$ with $p^\mu = (\omega, \vec{k})$.[1] Now current conservation and rotational invariance (full Lorentz invariance is lost with $T > 0$) restrict the form of the Fourier transform of this correlator to be [49]

$$C_{\mu\nu}(p) = P^T_{\mu\nu}\,\Pi^T(p) + P^L_{\mu\nu}\,\Pi^L(p)\,. \tag{2.2.26}$$

where the transverse and longitudinal projectors can be written as

$$\begin{aligned} P^T_{ij} &= \delta_{ij} - \frac{k_i\,k_j}{k^2}\,, \qquad P^T_{0\mu} = 0\,, \\ P^L_{\mu\nu} &= \eta_{\mu\nu} - \frac{p_\mu\,p_\nu}{p^2} - P^T_{\mu\nu}\,. \end{aligned} \tag{2.2.27}$$

If we take into account that the conformal dimension of the current $J_\mu(x)$ is 2, the components $\Pi^{T,L}$ in (2.2.26) take the form:

$$\Pi^{T,L}(p) = \sqrt{p^2}\,K^{T,L}(\omega/T, \vec{k}/T)\,. \tag{2.2.28}$$

[1] We work with the mostly positive signature so that $\eta_{\mu\nu} = \mathrm{diag}(-1,+1,+1)$.

In the limit of $T = 0$, we have $\Pi^T(p) = \Pi^L(p) = \Pi(p)$ and recover the Lorentz invariant correlator

$$C_{\mu\nu}(p) = \left(\eta_{\mu\nu} - \frac{p_\mu\, p_\nu}{p^2}\right)\, \Pi(p)\,. \tag{2.2.29}$$

In order to produce physical observables, and to interpret our results from a condensed matter point of view, we will calculate the conductivity from the Kubo formula

$$\sigma_{ij} \;=\; \frac{i}{\omega} C_{ij}\;. \tag{2.2.30}$$

2.2.1 Spectral functions

In this section, we compute spectral functions for excitations of fundamental fields on the defect by studying fluctuations of the worldvolume fields on the D5-brane probes. In particular, we focus on correlators of the the worldvolume vector A_μ, which is dual to the conserved current J^μ corresponding to the diagonal $U(1)$ of the global flavour symmetry on the defect. The worldvolume gauge field gives rise to several types of modes, one of which is a vector with respect to the Lorentz group in the (2+1)-dimensional defect. These modes are characterized as having only $A_{0,1,2}$ nonzero while the components on the internal two-sphere are vanishing [71]. Further the radial component A_r can consistently be set to zero because we only study modes which are constant on the internal space [71].

While the full action for the gauge fields on the D5-branes receives contributions from both the Dirac-Born-Infeld (DBI) action plus a Wess-Zumino term, since our gauge field fluctuations have vanishing radial and S^2 components, only the DBI portion of the action is relevant in determining their dynamics. Since we only study linearized fluctuations about the background, the gauge field action is only needed to quadratic order, which is simply

$$I_{gauge} \;=\; -4\pi L^2\,\sqrt{1+f^2}N_{\rm f}\,T_5 \int d^3\sigma\, dr \sqrt{-g}\,\frac{(2\pi\ell_{\rm s}^2)^2}{4}\,F^2 \;=\; -\frac{1}{4g_4^2}\int d^3\sigma\, dr\sqrt{-g}\,F^2\,. \tag{2.2.31}$$

Here we have integrated over the internal S^2 as in (2.1.8) and use $g_{\mu\nu}$ to denote the induced metric (2.1.7) in the AdS_5 directions. Above, we also defined the effective gauge coupling for the four-dimensional Maxwell field:

$$\frac{1}{g_4^2} \equiv 16\pi^3\ell_{\rm s}^4 L^2\,\sqrt{1+f^2}N_{\rm f}\,T_5 = \sqrt{1+f^2}\frac{2}{\pi}\,\frac{N_{\rm f}\,N_{\rm c}}{\sqrt{\lambda}}\,. \tag{2.2.32}$$

For the D7 case, this becomes

$$\frac{1}{g_4^2} \equiv \frac{32\pi^4 N_{\rm f}}{3}\ell_{\rm s}^4 L^4(1+|Q|)T_7 = (1+|Q|)\frac{N_{\rm f}\,N_{\rm c}}{3\pi^2}\,. \tag{2.2.33}$$

Note that the gauge field action (2.2.31) corresponds to the standard Maxwell action in a four-dimensional curved spacetime. Hence, these gauge fluctuations will exhibit electromagnetic duality, which was shown to play and interesting role in the physics of the conformal field theory in [49]. We will explore this point further in section 2.4. Of course, Maxwell's equations follow as

$$\partial_a \left(\sqrt{-g}\, F^{ab}\right) = 0. \tag{2.2.34}$$

Using these equations of motion, the Maxwell action (2.2.31) becomes a total derivative and following the standard prescription, we obtain the desired correlator from the resulting boundary term. To proceed, let us first give the explicit metric on the brane,

$$ds^2 = \frac{L^2}{u^2}\left[\frac{r_0^2}{L^4}\big(-h(u)dt^2 + dx^2 + dy^2\big) + \frac{du^2}{h(u)}\left(1 + h(u)\chi'^2\right)\right], \tag{2.2.35}$$

in terms of the dimensionless radial coordinate u, as given in (2.1.11). Then the action (2.2.31) becomes

$$\begin{aligned} I_{gauge} &= -\frac{1}{2g_4^2}\int d^3\sigma\, du\, \partial_a\left[\sqrt{-g}\, A_b\, F^{ab}\right] \;=\; -\frac{1}{2g_4^2}\int d^3\sigma\, \left[\sqrt{-g}g^{aa}g^{uu}A_a\partial_u A_a\right]_{u\to 0}^{u\to 1} \\ &= -\frac{1}{2g_4^2}\frac{r_0}{L^2}\int d^3\sigma\, \left[\frac{1}{(1+h(u)\chi'^2)^{1/2}}\left(h(u)A_x\partial_u A_x + h(u)A_y\partial_u A_y - A_t\partial_u A_t\right)\right]_{u\to 0}^{u\to 1}. \end{aligned} \tag{2.2.36}$$

The usual AdS/CFT prescription tells us that we will only need the contribution at the asymptotic boundary $u \to 0$ [82]. Following [83], we take the Fourier transform of the gauge field,

$$A_\mu(\sigma) = \int \frac{d^3k}{(2\pi)^3} e^{ik\cdot\sigma} A_\mu(k,u)\,, \tag{2.2.37}$$

to write the boundary action as

$$\begin{aligned} I_{gauge} &= -\frac{1}{2g_4^2 1}\frac{1}{(2\pi)^3}\int d^3k\, \left[\sqrt{-g}g^{\mu\mu}g^{uu}A_\mu(u,-k)\partial_u A_\mu(u,k)\right]_{u\to 0}^{u\to 1} \\ &= -\frac{r_0}{2g_4^2L^2}\frac{1}{(2\pi)^3}\int d^3k\, \big[(1+h(u)\chi'^2)^{-1/2}\left(h(u)A_x(u,-k)\partial_u A_x(u,k)\right. \\ &\qquad \left. + h(u)A_y(u,-k)\partial_u A_y(u,k) - A_t(u,-k)\partial_u A_t(u,k)\right)\big]_{u\to 0}^{u\to 1} \end{aligned} \tag{2.2.38}$$

with a single sum of μ being implicit in the first line.

Looking at the asymptotic behavior of the fields, we write

$$A_\mu(k,u) = A_{\mu 0}(k)\frac{A_\mu(k,u)}{A_\mu(k,u_0)}\,, \tag{2.2.39}$$

where u_0 is a UV regulator and it is understood that eventually the limit $u_0 \to 0$ will be taken. We can then derive the flux factor for, say, A_y by taking variations with respect to A_{y0} [82]:

$$\mathcal{F}_{yy} = -\frac{\varepsilon_0}{2}\left[\frac{h(u)}{(1+h(u)\chi'^2)^{1/2}}\frac{A_y(u,-k)\partial_u A_y(u,k)}{A_y(u_0,-k)A_y(u_0,k)}\right], \tag{2.2.40}$$

where $\varepsilon_0 = \frac{r_0}{g_4^2 L^2} = \frac{\pi T}{g_4^2}$ — we will show later how ε_0 relates to the charge permittivity. The flux (2.2.40) should be conserved, *i.e.,* be independent of the radius u. The usual AdS/CFT prescription tells us to evaluate it at the asymptotic boundary, while applying infalling boundary conditions at the horizon ($u = 1$), to find the retarded Green's function (2.2.25) for the current J_μ in the defect CFT [82]:

$$\begin{aligned} C_{yy} = -2\mathcal{F}_{yy} &= \varepsilon_0\left[\frac{h(u)}{(1+h(u)\chi'^2)^{1/2}}\frac{A_y(u,-k)\partial_u A_y(u,k)}{A_y(u_0,-k)A_y(u_0,k)}\right]_{u,u_0\to 0} \\ &= \frac{\varepsilon_0}{\sqrt{1+f^2}}\left[\frac{\partial_u A_y(u,k)}{A_y(u,k)}\right]_{u\to 0}. \end{aligned} \tag{2.2.41}$$

The other correlators $C_{\mu\nu}$ follow in general by rewriting (2.2.39) as $A_\mu(k,u) = A_{\nu 0}(k)M^\nu{}_\mu(u,k)$ [49] and making the variation $\frac{\delta^2}{\delta A_{\mu 0}\,\delta A_{\nu 0}}$. In our case the t,t and x,x correlators are given by (2.2.41) with the indices appropriately replaced:

$$C_{xx} = \frac{\varepsilon_0}{\sqrt{1+f^2}}\left[\frac{\partial_u A_x(u,k)}{A_x(u,k)}\right]_{u\to 0} \text{ and } C_{tt} = -\frac{\varepsilon_0}{\sqrt{1+f^2}}\left[\frac{\partial_u A_t(u,k)}{A_t(u,k)}\right]_{u\to 0}. \tag{2.2.42}$$

In order to evaluate the spectral function, we must solve the equations of motion (2.2.34). It is convenient to introduce dimensionless coordinates by rescaling the defect coordinates as

$$\tilde{t} = \frac{r_0}{L^2}t\,, \qquad \tilde{x} = \frac{r_0}{L^2}x\,, \qquad \tilde{y} = \frac{r_0}{L^2}y\,. \tag{2.2.43}$$

Without loss of generality, we also assume the fluctuations only carry momentum in the $\tilde{x}$ direction, *i.e.,* $\tilde{k}^\mu = (\tilde{\omega}, \tilde{q}, 0)$ — note that, *e.g.,* $\tilde{\omega} = L^2/r_0\ \omega = \omega/\pi T$. We note that given the Fourier transform (2.2.37), the vector potentials vary as $e^{i\tilde{k}_\mu \tilde{x}^\mu}$ in the gauge theory directions.

Now the explicit equations of motion simplify to

$$b = u: \qquad 0 = \tilde{\omega} A'_{\tilde{t}} + \tilde{q}\, h\, A'_{\tilde{x}}\,, \tag{2.2.44}$$

$$b = \tilde{t}: \qquad 0 = A''_{\tilde{t}} - \frac{H'}{2H} A'_{\tilde{t}} - \frac{H}{h}\left(\tilde{q}^2 A_{\tilde{t}} + \tilde{\omega}\tilde{q} A_{\tilde{x}}\right)\,, \tag{2.2.45}$$

$$b = \tilde{x}: \qquad 0 = A''_{\tilde{x}} + \left(\frac{h'}{h} - \frac{H'}{2H}\right) A'_{\tilde{x}} + \frac{H}{h^2}\left(\tilde{\omega}^2 A_{\tilde{x}} + \tilde{\omega}\tilde{q} A_{\tilde{t}}\right)\,, \tag{2.2.46}$$

$$b = \tilde{y}: \qquad 0 = A''_{\tilde{y}} + \left(\frac{h'}{h} - \frac{H'}{2H}\right) A'_{\tilde{y}} + \frac{H}{h^2}(\tilde{\omega}^2 - h\,\tilde{q}^2) A_{\tilde{y}}\,, \tag{2.2.47}$$

where 'prime' denotes ∂_u and

$$H(u) \equiv 1 + h(u)\chi'^2\,. \tag{2.2.48}$$

Before proceeding further, we make the following convenient definition for the conductivities

$$\tilde{\sigma}_{ij} \equiv \frac{i}{\tilde{\omega}} C_{ij} = \pi T \sigma_{ij}\,. \tag{2.2.49}$$

Comparing to (2.2.30), here we are simply dividing by the dimensionless frequency $\tilde{\omega}$, rather than ω.

2.2.1.1 Transverse correlator

Let us look carefully at the $\tilde{y}$ equation (2.2.47). We see firstly, that in the limit $u \to 0$, it reduces to

$$0 = A''_{\tilde{y}} + (1+f^2)(\tilde{\omega}^2 - \tilde{q}^2) A_{\tilde{y}}\,. \tag{2.2.50}$$

The solution of interest is then $A_{\tilde{y}} = A_{\tilde{y}0}\, e^{-i\sqrt{(1+f^2)(\tilde{\omega}^2-\tilde{q}^2)}u}$, where the sign in the exponential is chosen so that the solution corresponds to an infalling wave. Given this solution, if one now calculates the correlator with (2.2.41) and applies (2.2.30), the resulting conductivity is

$$\tilde{\sigma}_{yy} = \varepsilon_0 \sqrt{1 - \tilde{q}^2/\tilde{\omega}^2}\,. \tag{2.2.51}$$

The cut in the conductivity at $\tilde{\omega} = \tilde{q}$ may be surprising and we return to this point in section 2.3.2. We will refer to this simple result as the low temperature approximation, reasoning as follows: The result applies for large dimensionless "frequencies", *i.e.*, $|(1+f^2)(\tilde{\omega}^2-\tilde{q}^2)|^{1/2} \gg 1$ to be precise. However, recalling that *e.g.*, $\tilde{\omega} = \omega/\pi T$, if we fix the dimensionful quantities $\{\omega, q\}$, then eq. (2.2.51) should apply in the limit of very low temperatures.

To solve for the full spectral functions, we must proceed with numerical calculations. First, we impose infalling boundary conditions at the horizon — recall that the time-dependence of the potentials is $e^{-i\tilde{\omega}\tilde{t}}$. If we expand about $1-u \to 0^+$, we find an appropriate description of the field to be

$$A_{\tilde{y}} \simeq (1-u^4)^{i\tilde{\omega}/4}\left(1+\beta(1-u)+\cdots\right) \tag{2.2.52}$$

where

$$\beta = \frac{i}{4}\tilde{\omega}\frac{3+5f^2}{1+f^2} + \frac{\tilde{q}^2}{\tilde{\omega}^2+4}\left(1-i\frac{\tilde{\omega}}{2}\right) . \tag{2.2.53}$$

In order to implement the infalling boundary condition and to ensure numerical stability, we choose the Ansatz

$$A_{\tilde{y}} = (1-u^4)^{i\tilde{\omega}/4}e^{-\beta u}\mathcal{F}(u) , \tag{2.2.54}$$

and solve for $\mathcal{F}(u)$, which is nonsingular at the horizon, with $\partial_u\mathcal{F}(u)=0$ at $u=1$. As the second boundary condition, we fix the asymptotic normalization: $A_{\tilde{y}}|_{u=1}=1$.

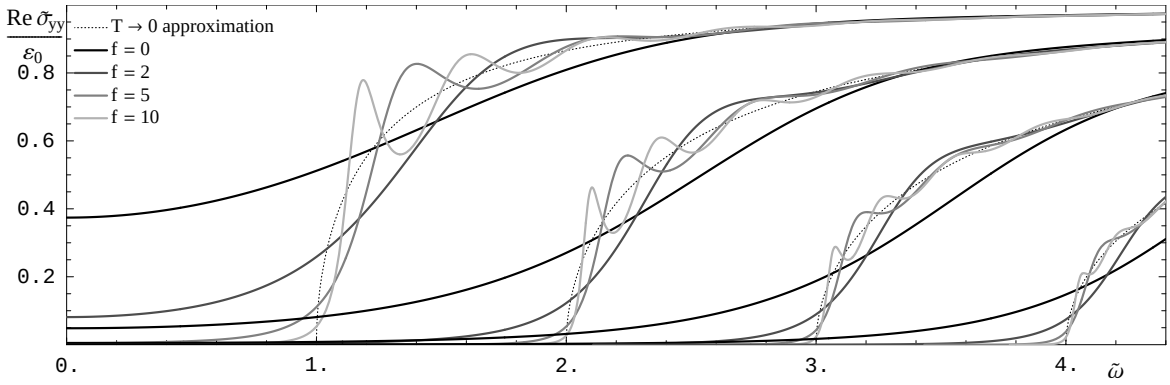

Figure 2.2: The normalized transverse conductivity Re $\tilde{\sigma}_{yy}(\tilde{\omega})/\varepsilon_0$ at $\tilde{q} \in \{1,2,3,4\}$ for various values of the flux f. The low temperature approximation (2.2.51) is shown as the dotted line for each $\tilde{q}$.

Figure 2.2 shows Re $\tilde{\sigma}_{yy}(\tilde{\omega})/\varepsilon_0$ for various values of $\tilde{q}$ and f^2. We see that at $f=0$ the spectral functions are similar to those in [49]. However, as f increases, they approach the low temperature limit (2.2.51) more closely, and show some oscillatory behavior at $\tilde{\omega} > \tilde{q}$. We will discuss aspects of this behavior in section 2.2.2.

2.2.1.2 Longitudinal correlator

Now, let us consider the tt equation (2.2.45). It is easy to see that (2.2.44-2.2.46) are not independent, and we cannot produce a second order equation involving $A_{\tilde{t}}$ only. However, we can produce one for $A'_{\tilde{t}}$:

$$0 \;=\; A'''_{\tilde{t}} - \Big(\frac{h}{H}\big(\frac{H}{h}\big)' + \frac{H'}{2H}\Big)A''_{\tilde{t}} + \Big(\frac{h}{H}\frac{H'}{2H}\big(\frac{H}{h}\big)' - \big(\frac{H'}{2H}\big)'\Big)A'_{\tilde{t}} + \frac{H}{h^2}\big(\tilde{\omega}^2 - \tilde{q}^2 h\big)A'_{\tilde{t}}\,, \quad (2.2.55)$$

which simplifies to

$$0 = \left(\frac{A'_{\tilde{t}}}{\sqrt{H}}\right)'' + \left(\frac{h'}{h} - \frac{H'}{2H}\right)\left(\frac{A'_{\tilde{t}}}{\sqrt{H}}\right)' + \frac{H}{h^2}(\tilde{\omega}^2 - h\,\tilde{q}^2)\frac{A'_{\tilde{t}}}{\sqrt{H}}\ , \quad (2.2.56)$$

and hence is the same as (2.2.47) for $A_{\tilde{y}}$ replaced by $A'_{\tilde{t}}/\sqrt{H}$. Let us set $A'_{\tilde{t}} = c\sqrt{H}\,A_{\tilde{y}}$ with some constant c to be determined. Now, to find $\partial_u A_{\tilde{t}}(u,k)/A_{\tilde{t}}(u,k)$ at $u=0$, we employ (2.2.45) and $A''_{\tilde{t}} = c\sqrt{H}\big(A'_{\tilde{y}} + \frac{H'}{2H}A_{\tilde{y}}\big)$ as in [49]. It follows then from $h'|_{u=0} = 0 = H'|_{u=0}$ that

$$c = \frac{\sqrt{1+f^2}}{A'_{\tilde{y}}|_{u=0}}\left(\tilde{q}^2 A_{\tilde{t}0} + \tilde{\omega}\tilde{q}A_{\tilde{x}0}\right)\ . \quad (2.2.57)$$

Hence, we can read off $\left[\frac{\partial_u A_{\tilde{t}}(u,k)}{A_{\tilde{t}}(u,k)}\right]_{u\to 0}$ and $\left[\frac{\partial_u A_{\tilde{t}}(u,k)}{A_{\tilde{x}}(u,k)}\right]_{u\to 0}$ from

$$A'_{\tilde{t}} = \frac{\sqrt{1+f^2}\sqrt{H}A_{\tilde{y}}}{A'_{\tilde{y}}|_{u=0}}\left(\tilde{q}^2 A_{\tilde{t}0} + \tilde{\omega}\tilde{q}A_{\tilde{x}0}\right)\ . \quad (2.2.58)$$

Finally as in [49], we find

$$C_{tt} = -\varepsilon_0^2\,\tilde{q}^2/C_{yy} \qquad \text{and} \qquad C_{xx} = -\varepsilon_0^2\,\tilde{\omega}^2/C_{yy}\,. \quad (2.2.59)$$

Applying (2.2.49), these results yield interesting relations for the corresponding conductivities. In particular, (2.2.59) yields

$$\tilde{\sigma}_{xx} = \varepsilon_0^2/\tilde{\sigma}_{yy}\ . \quad (2.2.60)$$

We can also consider a low temperature limit as above. However, this is most easily derived by combining (2.2.51) and (2.2.60) to find

$$\tilde{\sigma}_{xx} = \frac{\varepsilon_0}{\sqrt{1-\tilde{q}^2/\tilde{\omega}^2}}\,. \quad (2.2.61)$$

Again, we will return to discuss the cut appearing in the conductivity at $\tilde{\omega} = \tilde{q}$ in section 2.3.2; and the conductivity can only be found in general from numerical calculations. Some typical results for (the real part of) $\tilde{\sigma}_{xx}$ are shown in figure 2.3. We note that again that as the flux f increases, our results approach the low temperature approximation (2.2.61), together with some "oscillatory" behavior similar to that found in the transverse case. In contrast to the results in the previous section, the conductivity here diverges as $\tilde{\omega} \to \tilde{q}$, as can be anticipated from (2.2.61).

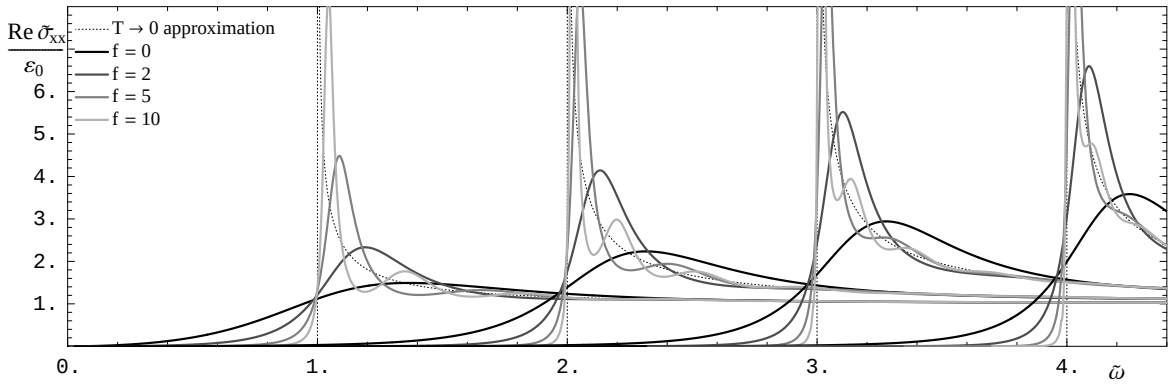

Figure 2.3: The normalized longitudinal conductivity Re $\tilde{\sigma}_{xx}(\tilde{\omega})/\varepsilon_0$ at $\tilde{q} \in \{1, 2, 3, 4\}$ for various values of the flux f. The low temperature approximation (2.2.61) is shown as the dotted line for each $\tilde{q}$.

2.2.1.3 Diffusion constant on the defect

The worldvolume gauge field corresponds to a conserved current on the defect in the dual CFT. In the hydrodynamic regime, one then expects to see the diffusion of the conserved charge according to Fick's law:

$$\partial_t j^0 = D \, \vec{\nabla}^2 j^0 \, . \tag{2.2.62}$$

This expectation can be confirmed in a holographic context [101, 102, 103] and, in fact, the computation of the diffusion constant D can be performed in a number of different ways. In the following, we use the membrane paradigm approach.

The computation of the diffusion constant via the membrane paradigm was discussed in [101] where explicit formulae for various transport coefficients in terms of metric components for a wide class of backgrounds were derived. There, the authors considered perturbations of a black brane background and a formula for the diffusion constant (eq. (2.27)

in [101]) resulted from a derivation of Fick's law. An analogous computation can be performed for the D5-branes' vector field for black hole embeddings considered here, with the result

$$\begin{aligned} D &= \frac{\sqrt{-g}}{\sqrt{h}} \frac{1}{g_{xx}\sqrt{-g_{tt}g_{\rho\rho}}}\bigg|_{\rho=1} \int d\rho \left(-g_{tt}\, g_{\rho\rho}\, \frac{\sqrt{g_{\rm int}}}{\sqrt{-g}}\right) \\ &= \frac{(1+f^2)^{1/2}}{\pi T}\int_0^1 \frac{du}{\sqrt{1+f^2u^4}} \equiv \frac{(1+f^2)^{1/2}}{\pi T}\, I(f)\,. \end{aligned} \tag{2.2.63}$$

In the first expression above, the metric g is the induced metric on the D5-branes (2.1.7) and $g_{\rm int}$ is the determinant of the metric on the internal two-sphere (with unit radius). The integral can be evaluated analytically yielding a hypergeometric function:

$$I(f) \,=\, {}_2F_1(\frac{1}{4},\frac{1}{2};\frac{5}{4};-f^2) \tag{2.2.64}$$

Figure 2.4 shows a plot of $I(f)$.

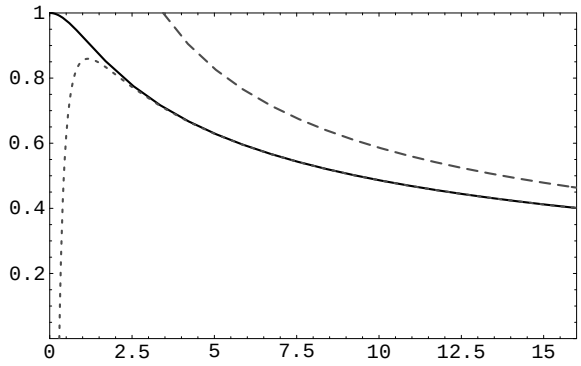

Figure 2.4: The integral $I(f)$: The solid line is the exact result as given in eq. (2.2.64). The upper dashed (lower dotted) line corresponds to the first term (first two terms) in the large f expansion in eq. (2.2.70).

This same integral in eq. (2.2.63) reappears at various points in our analysis and so it is useful to gain some better intuition for this expression. First, let us rewrite the integral as

$$I(f) \,=\, f^{-1/2}\int_0^{f^{1/2}} \frac{ds}{\sqrt{1+s^4}}\ . \tag{2.2.65}$$

Now, we find that we can expand the integrand around $s=0$ as

$$\frac{1}{\sqrt{1+s^4}} \,\sim\, 1 \,-\, \frac{1}{2}s^4 \,+\, \frac{3}{8}s^8 \,+\, \ldots \tag{2.2.66}$$

and around $s = \infty$

$$\frac{1}{\sqrt{1+s^4}} \sim \frac{1}{s^2}\big(1 - \frac{1}{2}s^{-4} + \frac{3}{8}s^{-8} + \dots\big)\,. \tag{2.2.67}$$

At $s = 1$, the convergence of both sequences goes as $\frac{1}{n!}$ and a more precise approximation is

$$\frac{1}{\sqrt{1+s^4}} \sim \frac{1}{\sqrt{2}}(1 - (s-1) + \dots)\,. \tag{2.2.68}$$

Combining (2.2.65) with these expansions, we can find the integral in various approximations

$$f \ll 1: \quad I(f) \sim 1 - \frac{1}{10}f^2 + \frac{3}{72}f^4 + \dots \tag{2.2.69}$$

$$f \gg 1: \quad I(f) \sim c_\infty f^{-1/2} - f^{-1} + \frac{1}{10}f^{-3} - \frac{3}{72}f^{-5} + \dots \tag{2.2.70}$$

$$f \sim 1: \quad I(f) \sim f^{-1/2}\Big(c_1 + \frac{1}{\sqrt{2}}\big((f^{1/2}-1) - \frac{1}{2}(f^{1/2}-1)^2 + \dots\big)\Big) \tag{2.2.71}$$

where $c_1 = \int_0^1 \frac{ds}{\sqrt{1+s^4}} = 2\pi^{-1/2}\Gamma^2\big(\frac{5}{4}\big)$ and $c_\infty = \int_0^\infty \frac{ds}{\sqrt{1+s^4}} = 2c_1 \simeq 1.854$. Further, we note that the expansion about $s = 0$ is just the expansion of the hypergeometric function as a hypergeometric series.

Hence, at small and very large f, we have for the diffusion constant

$$D\,T \to \begin{cases} \frac{1}{\pi} & \text{with } f \to 0\,, \\ \frac{c_\infty}{\pi}\sqrt{f} & \text{with } f \to \infty\,. \end{cases} \tag{2.2.72}$$

We note that the $f = 0$ result is different from but close to the value found for M2-brane hydrodynamics [104]: $D\,T = 3/4\pi$. Also note that in the limit of large f, the diffusion constant grows as $\sqrt{f}$.

2.2.1.4 Low Frequency Limit and Permittivity

We can find the permittivity ε from the hydrodynamic limit $T \gg \omega, q$ [84],

$$-\,\mathrm{Im}\; C_{tt} = \frac{\varepsilon D\,\omega q^2}{\omega^2 + (Dq^2)^2} = \frac{\varepsilon\,\pi DT\,\tilde{\omega}\tilde{q}^2}{\tilde{\omega}^2 + (\pi\,DT\,\tilde{q}^2)^2}\,. \tag{2.2.73}$$

In this regime, the spectral function is dominated by the diffusion pole $\tilde{\omega} = -i\pi\,DT\,\tilde{q}^2$, as dictated by Fick's law (2.2.62). The diffusion constant is $D = \frac{\sqrt{1+f^2}}{\pi T} I(f)$, as we calculate

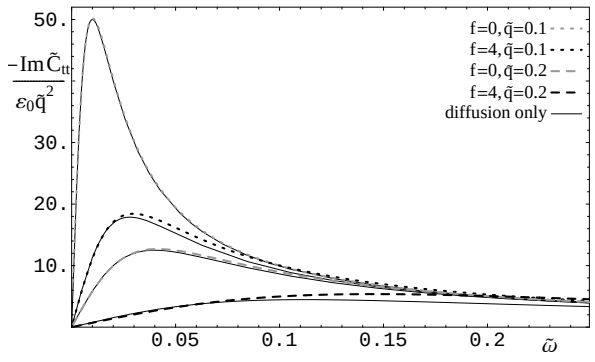

Figure 2.5: $\frac{-\mathrm{Im}\ \tilde{C}_{tt}(\tilde{\omega})}{\varepsilon_0 \tilde{q}^2}$ for $f \in \{0, 4\}$ and $\tilde{q} \in \{0.1, 0.2\}$. The solid lines correspond the approximate result (2.2.73) with only the diffusion pole appearing in the hydrodynamic limit.

in section 2.2.1.3, where we also define the function $I(f)$. Comparing to our numerical results for the spectral functions as shown in figure 2.5 for various values of f and $\tilde{q} \ll 1$, we find $\varepsilon = \frac{\varepsilon_0}{I(f)}$. We can verify the latter from the definition of the permittivity [85, 86]

$$\varepsilon = \lim_{\tilde{\omega}, \tilde{q} \to 0} C_{tt}\,, \tag{2.2.74}$$

which is in perfect agreement with the numerical result.

2.2.2 Temperature and f dependence

In the previous sections, we found an interesting dependence of the conductivity on the temperature and the flux f. These properties characterize the nature of the defect, as shown more in detail in figure 2.6. There we see that at low T or large f, there is a conduction threshold at $\omega = q$. We can interpret this as the energy required to excite a collective excitation of the conducting mode. In the regime $\omega < q$, the conductivity appears exponentially suppressed as one might expect with a chemical potential q. That is, this exponential suppression in the low-temperature "DC limit" might be interpreted as the Boltzmann tail of some thermal distribution function. Examining this behavior in more detail in the next section suggests the introduction of an effective temperature, which seems to play an interesting role in the subsequent analysis. Examining the conductivity at low T or large f also reveals "oscillations" in the spectral curves. The frequency of this oscillations has a non-trivial dependence on f and seems to depend inversely on the temperature, as one might expect from the general scaling properties. Their amplitude is roughly independent of f, but depends on some positive power of the temperature and decreases with increasing $\frac{\tilde{\omega}}{\tilde{q}}$. In the following, we will also extract some quantitative approximation to this pattern.

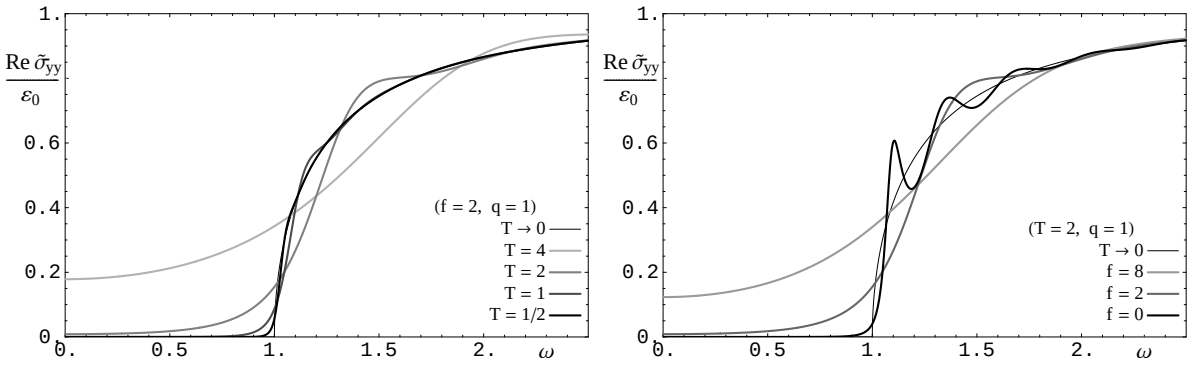

Figure 2.6: On the left, we plot the normalized transverse conductivity Re $\tilde{\sigma}_{yy}(\omega)/\varepsilon_0$ for $q = 1$ and $f = 2$ at various temperatures, in terms of the frequency ω. On the right: Re $\tilde{\sigma}_{yy}(\omega)/\varepsilon_0$ for $q = 1$ and $T = 2$ for various values of f. In both plots, the $T \to 0$ limit (2.2.51) is shown with the narrow black curve.

First, we study these two effects analytically as a perturbation around the zero temperature limit. Next, we will show how they arise from poles in the spectral functions that can be interpreted in the field theory as the quasiparticle states of the resonances on the defect and arise on the gravity side through the quasinormal modes of the vector field. Finally, we will demonstrate the latter by reconstructing the location of the poles in the complex frequency plane from the data on the real axis and also by analytically solving a toy model that is very similar to our present problem.

2.2.2.1 Effective temperature

First let us study the temperature dependence of the DC limit. This can be easily done by finding an approximate solution in the $q \gg T$ limit. For simplicity, we will also take $\omega \ll T$. We will concentrate on the transverse correlators, but we will see that the conductivity is obtained from a small perturbation around a large background, such that by (2.2.59), a similar behavior applies to the longitudinal correlator in the limit that we will consider. Before proceeding, it is useful to recall here that $h(u) \equiv 1 - u^4$ while $H(u)$ is given by (2.2.48), so that asymptotically as $u \to 0$, $H \to \sqrt{1+f^2}$ while near the horizon where $u \to 1$, $H \to 1$.

Let us first re-express (2.2.47) in terms of the Ansatz $A_{\tilde{y}} = A_{\tilde{y}0}\, e^{\int^u \zeta}$, such that $C_{yy} =$

$\frac{\varepsilon_0}{\sqrt{1+f^2}} \lim_{u\to 0}\zeta$:

$$\zeta' + \zeta^2 \,+\, \left(\frac{h'}{h} - \frac{H'}{2H}\right)\zeta + \frac{H}{h}\left(\frac{\tilde{\omega}^2}{h} - \tilde{q}^2\right) \,=\, 0\ . \tag{2.2.75}$$

We see that for large $\tilde{q}$ (*i.e.*, $q \gg T$), this equation is dominated by the second and last terms, such that an approximate solution is $\zeta = \pm\zeta_0$, $\zeta_0 \equiv \tilde{q}\sqrt{\frac{H}{h}}$. Implicitly, here we have chosen the branch corresponding to $A_{\tilde{y}}$ decaying near the horizon. Further, as we will see below, this also corresponds to an infalling boundary condition at the horizon. The terms that we ignored are then of the order $\tilde{q}h^{-3/2}$, such that the approximation is valid in the region $1-u \gg \tilde{q}^{-2}$. The subleading terms in ζ are of the order $\tilde{q}^0 u^3 h^{-1}$.

Next, we study the linearized equation for a small perturbation $\zeta \to \zeta_0 + \epsilon$:

$$\epsilon' \,+\, \epsilon\left(\frac{h'}{h} - \frac{H'}{2H} - 2\zeta_0\right) \,+\, \frac{\tilde{\omega}^2 H}{h^2} - \zeta_0' + \left(\frac{h'}{h} - \frac{H'}{2H}\right)\zeta_0 \,\equiv\, \epsilon' \,-\, \epsilon\alpha(u) \,-\, \beta(u) \tag{2.2.76}$$

with the general solution

$$\epsilon \,=\, e^{\int_0^u d\bar{u}\,\alpha(\bar{u})}\left(\epsilon_0 \,+\, \int_0^u d\acute{u}\, e^{-\int_0^{\acute{u}} d\bar{u}\,\alpha(\bar{u})}\beta(\acute{u})\right)\ . \tag{2.2.77}$$

In the limit that we considered for ζ_0 this reduces simply to $\epsilon \,=\, \epsilon_0 e^{2\int_0^u d\bar{u}\,\zeta_0}$ because of the exponential suppression in the last term in (2.2.77). As one would have physically expected, this perturbation grows as one approaches the horizon, and decays away near infinity. The subleading terms from the part of $\alpha(u)$ that we ignored in the integral in the exponent is again of order $\tilde{q}^0 u^3 h^{-1}$.

To find ϵ_0, fix the ω dependence and further constrain the subleading terms, we proceed by considering an approximate solution in the region $h = 1-u^4 \ll 1$, which has overlap with $h \gg \tilde{q}^{-2}$. The equation we need to solve is now

$$4\partial_h\zeta \,-\, \zeta^2 \,+\, \frac{4}{h}\zeta \,+\, \frac{\tilde{q}^2}{h} - \frac{\tilde{\omega}^2}{h^2} \,=\, 0\,, \tag{2.2.78}$$

which has a general analytic but not very illuminating solution in terms of Bessel functions, allowing for a combination of infalling and outgoing waves at the horizon $u=1$. Choosing an infalling boundary condition leaves us with

$$\zeta \,=\, -\frac{\tilde{q}^2 h\,{}_0F_1\big(2+i\frac{\tilde{\omega}}{2};\tilde{q}^2\frac{h}{16}\big) \,-\, 16i\frac{\tilde{\omega}}{2}\big(2+i\frac{\tilde{\omega}}{2}\big){}_0F_1(2+i\frac{\tilde{\omega}}{2};\tilde{q}^2\frac{h}{16})}{8h\big(2+i\frac{\tilde{\omega}}{2}\big){}_0F_1\big(1+i\frac{\tilde{\omega}}{2};\tilde{q}^2\frac{h}{16}\big)}\ , \tag{2.2.79}$$

where ${}_0F_1(a;x)$ is the confluent hypergeometric limit function [90]. To match with the $h \ll 1$ regime of the asymptotic solution, we begin by expanding to first order in $\tilde{\omega}$ and then do an expansion around $\tilde{q}^2 h \gg 1$, which gives us

$$\zeta \sim -\frac{\tilde{q}}{\sqrt{h}} + \frac{1}{h} + \cdots - i\tilde{\omega}\tilde{q}\frac{16\pi}{\sqrt{h}} e^{-\tilde{q}\sqrt{h}} + \cdots . \tag{2.2.80}$$

Hence the full solution for $h \gg \tilde{q}^{-2}$ is:

$$\zeta = -\tilde{q}\sqrt{\frac{H}{h}} + \frac{1}{h} + A(u,\tilde{q},f) - i\tilde{\omega}\tilde{q}\frac{16\pi}{\sqrt{h}} e^{-2\tilde{q}\int_u^1 \sqrt{\frac{H}{h}}} \big(1 + B(u,\tilde{q},f)\big) , \tag{2.2.81}$$

where $A(u,\tilde{q},f)$ is some function that behaves away from the horizon as $\leq \mathcal{O}(u^3,\tilde{q}^0)$ and $B(u,\tilde{q},f)$ behaves as $\leq \mathcal{O}(u^0,\tilde{q}^0)$. Near the horizon, *i.e.,* for $h \ll \tilde{q}^{-2}$, the solution behaves as $\zeta \sim -i\frac{\tilde{\omega}}{h} - \frac{2-i\tilde{\omega}}{8+2\tilde{\omega}^2} + \cdots$. As a consistency check in the region $1 \gg h \gg \tilde{q}^{-2}$, it is easy to verify that the (small) imaginary and (dominating) real parts do indeed satisfy (2.2.77) when taking into account the next-to-leading terms.

From (2.2.81), we find that the leading term in the conductivity is

$$\sigma_{yy} \sim 16\pi\varepsilon_0\tilde{q}\, e^{-2\tilde{q}\int_u^1 \sqrt{\frac{H}{h}}} . \tag{2.2.82}$$

Inspired by a Boltzmann factor, and by the zero-temperature conduction threshold $\omega_0 = q$, we can interprete the exponential factor as $\exp[-q/T_{eff}]$ where

$$T_{eff} = \frac{\pi}{2} T \left(\int_0^1 du \sqrt{\frac{H(u)}{h(u)}} \right)^{-1} . \tag{2.2.83}$$

We note that the integral is finite since the integrand converges as $h^{1/2}$ at $u \to 1$. There are two limits in which we can evaluate this integral analytically: $f = 0$ and $f \gg 1$. In these limits one finds

$$f = 0 : \qquad T_{eff} = T\frac{\sqrt{\pi}}{2}\frac{\Gamma\left(\frac{3}{4}\right)}{\Gamma\left(\frac{5}{4}\right)} \sim 1.198\, T \tag{2.2.84}$$

$$f \gg 1 : \qquad T_{eff} \simeq \frac{\Gamma(3/4)^2}{\sqrt{\pi}}\frac{T}{\sqrt{f}}\left(1 + \left(\frac{4\Gamma(3/4)^2}{\pi^{3/2}} - \frac{1}{\sqrt{2}}\right)\frac{1}{\sqrt{f}}\right) \tag{2.2.85}$$

$$\sim 0.847\,\frac{T}{\sqrt{f}}\left(1 + 0.372/\sqrt{f}\right) .$$

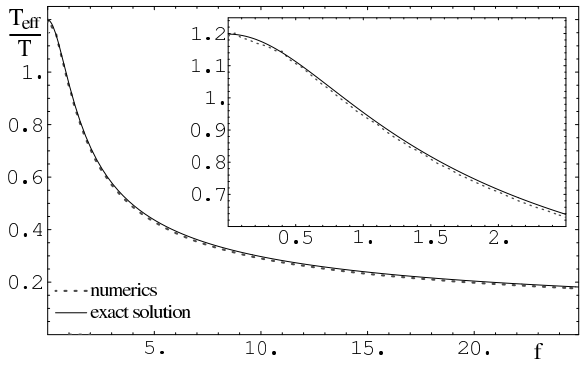

Figure 2.7: Ratio of the "effective temperature" derived from the temperature and $\tilde{q}$ dependence at $\tilde{q} \gg 1 \gg \tilde{\omega}$ to the blackhole temperature as a function of the flux f. We show the exact expression derived from the $\tilde{q} \to \infty$ limit and the numerical estimate at finite $\tilde{q}$.

Comparing these results with the numerics, we find good convergence in a consistent manner of both the profile of $A_y(u)$ and the effective temperature with increasing $\tilde{q}$. Since the approximation that gave us the integrand in (2.2.83) is valid up to roughly $h \gtrsim \tilde{q}^{-2}$, we expect that T_{eff}/T measured at finite $\tilde{q}$ has a relative accuracy of roughly $\tilde{q}^{-1}$. A simple way to estimate the effective temperature from the conductivity is to compute $\partial_{\tilde{q}} \log \frac{\tilde{\sigma}_{yy}}{\tilde{q}} \sim \frac{\pi}{T_{eff}}$ at large values of $\tilde{q}$. The factor of $\tilde{q}^{-1}$ that we have included here ensures that the convergence to the actual value of T_{eff} is faster than logarithmic in $\tilde{q}$. In figure 2.7, we show the comparison to the numerical estimate computed at $q/T_{eff} \sim 47$, that is the best numerically stable estimate, and demonstrate how the estimates converge to the exact results.

As illustrated in figure 2.7, our new effective temperature does not match the actual temperature of the system, except for $f \simeq 0.85$. At this point, we emphasize that, as discussed in section 2.1, the degrees of freedom on the defect are in equilibrium with the thermal bath of adjoint fields with temperature T. Of course, T_{eff} is still a scale that seems to play an interesting role in the defect conformal field theory, as we will see in the following. Again, the reason that we assign this scale the appellation of "effective temperature" is that it appears to play the role of a temperature when the conductivity (2.2.82) is interpreted as a Boltzmann distribution. It would be interesting if one could also give a physical interpretation to the pre-factor $16\pi\tilde{q}$ in front of the exponential in (2.2.82).

2.2.2.2 Resonances on the defect

Next, we study the oscillatory behavior of the spectral functions at $\tilde{\omega} > \tilde{q}$, using two different methods. Our results for the transverse correlator C_{yy} obviously can also be translated to give us the longitudinal correlators C_{xx}, C_{tt} using (2.2.59). Hence we will only discuss the former case.

We begin with the WKB-like expansion that gave (2.2.76), which was the starting point for the effective temperature above. Now however, we do not have the scale $h \sim \tilde{q}^2$ where we can match the near-horizon approximation to the asymptotic approximation. Furthermore, the dominant solution for ϵ is now oscillatory since $\zeta \sim \zeta_0 = i\frac{\sqrt{H}}{h}\omega\sqrt{1-h\frac{\tilde{q}^2}{\tilde{\omega}^2}}$, rather than exhibiting the exponential decay found above. The latter also reduces the validity of the approximation that led to (2.2.76) and further we have to worry about the logarithmically diverging integral $\int \zeta_0 \propto \ln h$ as $u \to 1$. So let us take the solution (2.2.77), but now with

$$\zeta_0 = i\frac{\sqrt{H}}{h}\omega\sqrt{1-h\frac{\tilde{q}^2}{\tilde{\omega}^2}}\,, \quad \alpha = 2\zeta_0 - \left(\ln\frac{h}{\sqrt{H}}\right)' \,, \quad \beta = \zeta_0' + \left(\ln\frac{h}{\sqrt{H}}\right)'\zeta_0 \tag{2.2.86}$$

and match this in the limit $u \to 1$ to the appropriate expansion of (2.2.79):

$$\zeta \;\sim\; -\frac{i\tilde{\omega}}{h} \;+\; \frac{i\tilde{q}^2}{2\tilde{\omega}-4i} \;+\mathcal{O}(h) \;=\; -\zeta_0 \;+\; \frac{\tilde{q}^2}{\tilde{\omega}^2+2i\tilde{\omega}} \;+\; \mathcal{O}(h)\,. \tag{2.2.87}$$

Now, we see that the divergent oscillations from the $e^{\int\alpha}$ terms in (2.2.77) must cancel, and the approximation $\epsilon \ll \zeta_0$ should be valid near the horizon. Taking the limit $\lim_{u\to 1}\epsilon = \frac{\tilde{q}^2}{\tilde{\omega}^2+2i\tilde{\omega}} \equiv \epsilon_H$ of (2.2.77), and solving for ϵ_0 gives us then

$$\begin{aligned}
\epsilon\big|_{u=0} \;=\; \epsilon_0 \;&=\; \epsilon_H e^{-\int_0^1 du\alpha(u)} \;+\; \int_0^1 du\epsilon_H e^{-\int_0^u d\tilde{u}\alpha(\tilde{u})}\beta(u) \\
&=\; \epsilon_H \;-\; \int_0^1 du\, h\sqrt{\frac{1+f^2}{H}}e^{-2\int_0^u d\tilde{u}\zeta_0}\left(\epsilon_H\alpha - \frac{1}{2}\zeta_0\frac{h'\tilde{q}^2/\tilde{\omega}^2}{1-h\tilde{q}^2/\tilde{\omega}^2}\right)
\end{aligned} \tag{2.2.88}$$

It turns out that the $\mathcal{O}(h^{-1})$ divergent terms in $\epsilon_H\alpha+\beta$ in (2.2.88) do indeed cancel, such that the integral converges with the integrand $\propto h^2 h^{i\tilde{\omega}/2}$ as $u \to 1$. Unfortunately, we were not able to evaluate this integral analytically, even in the limits where various quantities involved getting large or small. We show this approximate result (2.2.88) compared to the full numerical result in figure 2.9.

Because of the rapid convergence as $u \to 1$, we see however that most of the contribution to the integral comes from regions where $h \sim 1$, in particular for large f. Hence as a very crude approximation, we can set $h = 1$ and hence $\beta = 0$, which allows us to compute the integral analytically:

$$\epsilon_0 \;\sim\; \epsilon_H\sqrt{1+f^2}e^{-2i\tilde{\omega}\sqrt{1+f^2}I(f)\sqrt{1-\tilde{q}^2/\tilde{\omega}^2}}\,. \tag{2.2.89}$$

While we do not expect this latter expression to give us the correct phase and amplitude information, we still anticipate that this result gives a good approximation for the frequency of the oscillations, $2\sqrt{1+f^2}I(f)\sqrt{1-\tilde{q}^2/\tilde{\omega}^2}$.

There is an alternative way of seeing more physically from the bulk point of view, how the finite temperature effects arise by casting the equation of motion for A_y (2.2.47) in the form of the Schrödinger equation, as suggested in [91]:

$$\left(-\partial_\rho^2 + h\,\tilde{q}^2\right) A_y \,=\, \tilde{\omega}^2 A_y \qquad \text{where} \;\; \rho \,=\, \int_0^u d\tilde{u}\frac{\sqrt{H}}{h}\;. \tag{2.2.90}$$

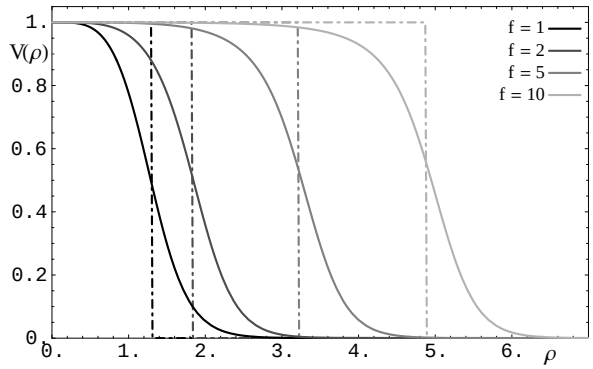

Figure 2.8: The effective Schrödinger potential $V(\rho) = \tilde{q}^2 h$ for the gauge field on the brane. We set $\tilde{q} = 1$ in the plot.

In terms of this new radial coordinate, the horizon gets mapped to $\rho \to \infty$, and we see that ρ is rapidly varying only for $u \lesssim f^{-1/2}$ and for $h \ll 1$. This suggests that for large f we can approximately split the problem in two regions: An asymptotic one where $h \sim 1$ and $\rho \sim \rho_\infty(u) = \int_0^u d\tilde{u}\sqrt{H}$ and the near-horizon region, where $h \ll 1$ and $\rho \sim \rho_H(u) = \rho_0 - \frac{1}{4}\ln(h)$ for some ρ_0. Going even further in our approximation, we assume a square potential $V = \tilde{q}^2$ for $\rho < \rho_\infty(1) = \sqrt{1+f^2}I(f)$ and $V = 0$ for $\rho > \rho_\infty(1)$, which is displayed in figure 2.8, where we see that this approximation is indeed justified. At this point, we might also observe that the effective Schrödinger potential appearing here is very similar in structure to that found for supergravity modes [92] and for mesonic modes, as discussed in [93].

With the square potential, it is trivial to find the solution for infalling boundary conditions at the horizon:

$$A_y \,\sim\, \begin{cases} A_0\, 2\sqrt{1-\tilde{q}^2/\tilde{\omega}^2}\, e^{-i\tilde{\omega}(\rho-\sqrt{1+f^2}I(f))} & : \;\; \rho < \sqrt{1+f^2}I(f) \\ A_0\Big(\big(1+\sqrt{1-\tilde{q}^2/\tilde{\omega}^2}\big)e^{-i\tilde{\omega}\sqrt{1-\tilde{q}^2/\tilde{\omega}^2}(\rho-\sqrt{1+f^2}I(f))} & \\ \quad -\big(1-\sqrt{1-\tilde{q}^2/\tilde{\omega}^2}\big)e^{i\tilde{\omega}\sqrt{1-\tilde{q}^2/\tilde{\omega}^2}(\rho-\sqrt{1+f^2}I(f))}\Big) & : \;\; \rho > \sqrt{1+f^2}I(f) \end{cases} .$$

Keeping in mind the change of coordinates, this gives us in terms of the Ansatz that we used for the perturbative treatment

$$\zeta|_{u=0} \;=\; -i\tilde{\omega}\sqrt{1+f^2} \times \begin{cases} \frac{1-\tilde{q}^2/\tilde{\omega}^2}{1-\frac{\tilde{q}^2}{\tilde{\omega}^2}\cos^2\left(\tilde{\omega}\sqrt{1+f^2}I(f)\sqrt{1-\tilde{q}^2/\tilde{\omega}^2}\right)} & : \;\; \tilde{\omega} > \tilde{q} \\ \frac{1-\tilde{q}^2/\tilde{\omega}^2}{\cosh^2\left(\tilde{\omega}\sqrt{1+f^2}I(f)\sqrt{\tilde{q}^2/\tilde{\omega}^2-1}\right)-\tilde{q}^2/\tilde{\omega}^2} & : \;\; \tilde{\omega} < \tilde{q} \end{cases} \quad .$$

The solution for $\tilde{\omega} > \tilde{q}$ has the same location of the maxima as (2.2.89), up to a small shift because of the overall slope of the curve, but it is missing an exponential suppression factor (for increasing frequencies) in the amplitude because we approximated the smooth potential by a discontinuous one. For $\tilde{\omega} \ll \tilde{q}$, we also find the exponential suppression that leads to the effective temperature computed at $\tilde{\omega} \to 0$, (2.2.81). Hence, we can clearly see how both effects arise from a resonant mode on the width of the defect, and from tunnelling through the defect region, respectively. In appendix C, we approximate the potential by a hyperbolic tangent, for which we can find an analytic solution, and find that is very closely reproduces the exact result with a significant deviation only at frequencies $|1-\tilde{q}^2/\tilde{\omega}^2| \ll 1$ where the spectral function is most sensitive to the details of the potential.

We show a comparison of the conductivity obtained from the different approximations in figure 2.9. As expected, the perturbative approximation in (2.2.88) gives a very close approximation for small perturbations around the $T \to 0$ result, $\left|\frac{C_{yy}-\lim_{T\to 0} C_{yy}}{\lim_{T\to 0} C_{yy}}\right| \ll 1$, but deviates significantly wherever the finite temperature effects become important. The analytical result (C.1.7) from the approximate tanh potential (C.1.3) however, provides a good fit for small $\tilde{q}$ and all values of $\tilde{\omega}$. For larger $\tilde{q} \gtrsim \pi$ and $\tilde{\omega} > \tilde{q}$, there is a significant phase shift proportional to the separation of the resonances but their amplitudes, separation and the tailoff for $\tilde{\omega} < \tilde{q}$ fit very closely. This is because the phase ϕ is sensitive to absolute changes in the integral of the potential, $\delta\phi \propto \int \delta V \propto \tilde{q}^2$, such that already small deviations in $V/\tilde{q}^2$ may have a big effect.

2.3 Quasinormal modes and quasiparticles

In general, the thermal correlators will have poles in the lower half of the complex frequency plane — *e.g.,* see discussion in [91] or [93]. The positions of these poles characterize the energy and lifetime of various excitations in the system. When one of these poles is close to the real axis, the spectral function will show a distinct peak and the corresponding excitation can be interpreted as a quasiparticle. That is, the excitation satisfies Landau's criterion for a quasiparticle that the lifetime is much greater than the inverse energy. As

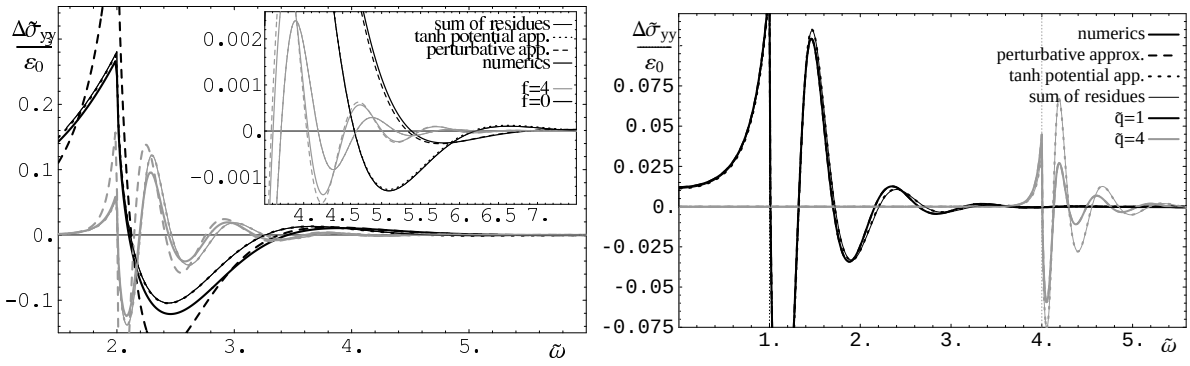

Figure 2.9: Comparing the conductivity obtained from the numerics, from the approximation (2.2.89), from the approximation using a tanh potential (C.1.7) and from the sum of residues obtained from its poles (C.2.16). Here we focus on the oscillatory behavior by plotting $\Delta\tilde{\sigma}_{yy} \equiv \text{Re}\,\left(\tilde{\sigma}_{yy}(\tilde{\omega}) - \varepsilon_0\sqrt{1-\tilde{q}^2/\tilde{\omega}^2}\right)$, *i.e.,* we subtract off the low temperature limit (2.2.51). Left: $f \in \{0, 4\}$ and $\tilde{q} = 2$. Right: $\tilde{q} \in \{2, 4\}$ and $f = 4$.

illustrated in figures 2.2 and 2.3, which essentially plot the spectral function, the defect theory is developing metastable quasiparticles in the large f regime. Hence it is of interest to examine the pole structure of the correlators and the spectrum of quasiparticles in the defect conformal field theory. This gives us not only more information on the defect field theory, but also allows us to speculate more on the nature of the defect.

In principle, we could always find the poles in the thermal correlators by simply numerically computing them over the entire complex frequency plane. Of course, such a brute force approach would present an enormously challenging problem at a technical level. However, since the correlators should be meromorphic, we can alternatively try to extract this information by fitting along the real axis, the spectral function derived from an approximate analytical solution of poles and positive powers – an approach similar in spirit to that followed in [93]. To do so, we use the complex "rest frame" frequency $\tilde{\nu} = \sqrt{\tilde{\omega}^2 - \tilde{q}^2}$ which maps $[0, \tilde{q}] \to [i\tilde{q}, 0]$ and $[\tilde{q}, \infty[\to [0, \infty[$. The motivation to do so is the fact that the resonance pattern is most suitably characterized by $\frac{\tilde{\omega}}{\tilde{\nu}}\tilde{\sigma}_{yy} - 1$ as a function of $\tilde{\nu}$, as shown in figure 2.10. There we see that even at finite temperature this quantity varies only slowly with varying $\tilde{q}$. Certainly, in the low temperature limit, we expect Lorentz invariance to be restored and then correlators will naturally depend on the combination $\tilde{\omega}^2 - \tilde{q}^2$, as is implicit in (2.2.51) and (2.2.61).

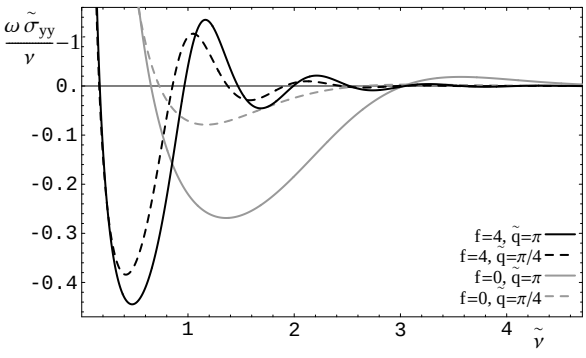

Figure 2.10: $\frac{\tilde{\omega}}{\tilde{\nu}}\tilde{\sigma}_{yy}(\tilde{\nu})$ for $\tilde{q} \in \{\pi/4, \pi\}$ and $f \in \{0, 4\}$. This form of the spectral function is very similar for different values of $\tilde{q}$.

2.3.1 Finding the Ansatz

The strategy that we will take to find the poles is to take a suitable Ansatz for the location of the n^{th} pole in the complex frequency plane, $\tilde{\nu}_n = \pm\tilde{\nu}_0(n) - i\tilde{\gamma}_0(n)$, and for the corresponding residue, and allow for the parameters to vary slowly. If the Ansatz is good enough, and the parameters vary slowly enough, then we can fit the conductivity resulting from a sequence with constant parameters $(\tilde{\nu}_0, \tilde{\gamma}_0)$ to the numerical result using only the data in the region around the n^{th} "resonance". This data can be parametrized by the amplitude of the resonance around the background and by the gap between the resonances. The resulting parameters $(\tilde{\nu}_0(n), \tilde{\gamma}_0(n))$ then give the location of the pole $\tilde{\nu}_n$, and it's residue.

A suitable guess for the full Ansatz is

$$C_{yy} \;=\; -\varepsilon_0 \sum_{n\geq 1} \frac{1}{\pi}\left(\frac{n(\tilde{\nu}_0 + i\tilde{\gamma}_0)^2}{\tilde{\nu} + n(\tilde{\nu}_0 + i\tilde{\gamma}_0)} - (\tilde{\nu}_0 + i\tilde{\gamma}_0) \;+\; \frac{n(\tilde{\nu}_0 - i\tilde{\gamma}_0)^2}{\tilde{\nu} - n(\tilde{\nu}_0 - i\tilde{\gamma}_0)} + (\tilde{\nu}_0 - i\tilde{\gamma}_0)\right)\;, \tag{2.3.91}$$

where the constant terms were introduced to cancel the otherwise divergent behavior of the series, since the pole terms do not decay for large n. The condition that allows us to locally treat the sum as an infinite series with constant $\{\tilde{\nu}_0, \tilde{\gamma}_0\}$ is now $\partial_n \log\{\tilde{\nu}_0(n), \tilde{\gamma}_0(n)\} \ll 1$ and $\partial_n \log\{\tilde{\nu}_0(n), \tilde{\gamma}_0(n)\} \ll \frac{\tilde{\nu}_0^2}{n^2\tilde{\gamma}_0^2}$. Rewriting (2.3.91) in a more suggestive form, we find for $\tilde{\nu} \in \mathbb{R}$, *i.e.*, $\tilde{\omega} > \tilde{q}$

$$\text{Im}\; C_{yy} \;=\; \varepsilon_0\,\text{Im}\;\tilde{\nu}\cot\left(\pi\frac{\tilde{\nu}}{\tilde{\nu}_0 + i\tilde{\gamma}_0}\right) \;=\; \varepsilon_0\,\text{Im}\;\tilde{\nu}\frac{\sin\frac{2\pi\tilde{\nu}\tilde{\nu}_0}{\tilde{\nu}_0^2+\tilde{\gamma}_0^2} \;-\; i\sinh\frac{2\pi\tilde{\nu}\tilde{\gamma}_0}{\tilde{\nu}_0^2+\tilde{\gamma}_0^2}}{\cosh\frac{2\pi\tilde{\nu}\tilde{\gamma}_0}{\tilde{\nu}_0^2+\tilde{\gamma}_0^2} \;-\; \cos\frac{2\pi\tilde{\nu}\tilde{\nu}_0}{\tilde{\nu}_0^2+\tilde{\gamma}_0^2}}\;, \tag{2.3.92}$$

such that we get the conductivity

$$\tilde{\sigma}_{yy} \;=\; \varepsilon_0 \,\frac{\tilde{\nu}}{\tilde{\omega}} \frac{\sinh \frac{2\pi\tilde{\nu}\tilde{\gamma}_0}{\tilde{\nu}_0^2+\tilde{\gamma}_0^2}}{\cosh \frac{2\pi\tilde{\nu}\tilde{\gamma}_0}{\tilde{\nu}_0^2+\tilde{\gamma}_0^2} \;-\; \cos \frac{2\pi\tilde{\nu}\tilde{\nu}_0}{\tilde{\nu}_0^2+\tilde{\gamma}_0^2}} \,, \tag{2.3.93}$$

which turns out to be finite at $\tilde{\nu} \to 0$. These exponentially suppressed resonances are characteristically what we expect and we can, in principle, fit the parameters $\tilde{\nu}_0$ and $\tilde{\gamma}_0$ to the resonance pattern.

To be more precise however, we need to go back to the original "physical" frequency $\tilde{\omega}$. Keeping the location of the poles and the residue fixed, the sum becomes now

$$\begin{aligned} C_{yy} = \varepsilon_0 \,\frac{\tilde{\omega}}{\pi} \log\left(\frac{\tilde{\nu}_0 - i\tilde{\gamma}_0}{\tilde{\nu}_0 + i\tilde{\gamma}_0}\right) \;+ \qquad\qquad (2.3.94)\\ \varepsilon_0 \sum_{n\geq 1} \frac{1}{\pi} \left(\frac{n(\tilde{\nu}_0 - i\tilde{\gamma}_0)}{\left(\tilde{q}^2 + n^2(-\tilde{\nu}_0 + i\tilde{\gamma}_0)^2\right)^{1/2}} \left(\frac{n(\tilde{\nu}_0 - i\tilde{\gamma}_0)^2}{\tilde{\omega} - \left(\tilde{q}^2 + n^2(\tilde{\nu}_0 - i\tilde{\gamma}_0)^2\right)^{1/2}} + \frac{n(\tilde{\nu}_0 - i\tilde{\gamma}_0)^2}{\left(\tilde{q}^2 + n^2(\tilde{\nu}_0 - i\tilde{\gamma}_0)^2\right)^{1/2}} \right) \right.\\ \left. - \frac{n(\tilde{\nu}_0 + i\tilde{\gamma}_0)}{\left(\tilde{q}^2 + n^2(\tilde{\nu}_0 + i\tilde{\gamma}_0)^2\right)^{1/2}} \left(\frac{n(\tilde{\nu}_0 + i\tilde{\gamma}_0)^2}{\tilde{\omega} + \left(\tilde{q}^2 + n^2(\tilde{\nu}_0 + i\tilde{\gamma}_0)^2\right)^{1/2}} - \frac{n(\tilde{\nu}_0 + i\tilde{\gamma}_0)^2}{\left(\tilde{q}^2 + n^2(\tilde{\nu}_0 + i\tilde{\gamma}_0)^2\right)^{1/2}} \right) \right), \end{aligned}$$

where the term $\frac{\tilde{\omega}}{\pi} \log \frac{\tilde{\nu}_0 - i\tilde{\gamma}_0}{\tilde{\nu}_0 + i\tilde{\gamma}_0}$ cancels the unphysical negative DC conductivity in the $\tilde{q} \gg \tilde{\nu}_0, \tilde{\gamma}_0$ limit that would arise otherwise. Note there is still a logarithmic divergence in the real part, that we are not interested in. This sequence does not sum to any known analytic expression, but the integral approximation can be computed straightforwardly analytically, such that in order to eventually study the sequence numerically, we will only sum the first few hundred poles and add a small "background" contribution from the rest of the poles using the integral.

Following the same considerations, we also find an Ansatz for the longitudinal correlator,

$$\begin{aligned} C_{xx} \;=\; \varepsilon_0 \sum_{n\geq 1} \frac{1}{(n-\frac{1}{2})\pi} \left(\frac{(n-\frac{1}{2})(\tilde{\nu}_0 - i\tilde{\gamma}_0)}{\left(\tilde{q}^2 + \left(n-\frac{1}{2}\right)^2(\tilde{\nu}_0 - i\tilde{\gamma}_0)^2\right)^{1/2}} \; \frac{1}{\tilde{\omega} - \left(\tilde{q}^2 + \left(n-\frac{1}{2}\right)^2(\tilde{\nu}_0 - i\tilde{\gamma}_0)^2\right)^{1/2}} \right.\\ \left. - \frac{(n-\frac{1}{2})(\tilde{\nu}_0 + i\tilde{\gamma}_0)}{\left(\tilde{q}^2 + \left(n-\frac{1}{2}\right)^2(\tilde{\nu}_0 + i\tilde{\gamma}_0)^2\right)^{1/2}} \; \frac{1}{\tilde{\omega} + \left(\tilde{q}^2 + \left(n-\frac{1}{2}\right)^2(\tilde{\nu}_0 + i\tilde{\gamma}_0)^2\right)^{1/2}} \right) , \end{aligned} \tag{2.3.95}$$

which converges and needs no regularization or terms with positive powers of $\tilde{\omega}$. In terms of $\tilde{\nu}$, the poles are located at $(n-1/2)(\pm\tilde{\nu}_0 - i\tilde{\gamma}_0)$, with residues $\frac{1}{n-1/2}$, as we expect by (2.2.59) from the ansatz for C_{yy}.

In order to finally obtain the location of the poles and their residue, we split the spectral function at the minima into segments around each maximum and simply fit them to our Ansatz giving us a set of parameters that we attribute to the local properties of the sequence at the most nearby pole, as described in the beginning of the section. We obtain both $\tilde{\nu}_0$ and $\tilde{\gamma}_0$ and an overall factor $(1+\epsilon_{\mathscr{R}})$ (or $(1+\epsilon_{\mathscr{R}})^\star$ on the negative branch) for the residues. The latter is needed because the resonance pattern is exponentially suppressed already for reasonably small $\tilde{\nu} \gtrsim \pi$, such that the background of the fitted sequence needs to be adjusted to in precise agreement with the background of the data, in order to extract the relevant information which is contained in the resonances. As it turns out that $|\epsilon_{\mathscr{R}}| \ll 1$, we will not comment about its value for the rest of the paper, because it is irrelevant for both the quantitative and the qualitative discussions. In principle, one can introduce more parameters, such as an overall shift in the frequency, but this would not improve the results, since in practice, it simply introduces extra degeneracy in parametrizing the fit.

2.3.2 Quasiparticles from the collisionless regime

Given the Ansatz for the transverse and longitudinal correlators above, we will now discuss the results for determining the positions of the poles. The results are only displayed for Re $\tilde{\nu} > 0$ but as shown in (2.3.91), there is a corresponding set of poles with Re $\tilde{\nu} < 0$. In this section, we focus on the collisionless or short-wavelength regime with $\tilde{\omega} \gg 1$ and $\tilde{q} \gtrsim 1$.

As a first test, we compare the fitted location of the poles to their exact location for the tanh potential in appendix C.2. We expect that this gives us a good estimate for the quality of the fit for the actual spectral functions. Some typical results are shown in the first plot of figure 2.11. We find that for $f = 0$, the fit is very poor, with the $\tilde{q} = \pi/4$ result being worse than the $\tilde{q} = \pi$ case, and there is a small deviation for $f = 4$ at large $\tilde{\omega}$, again with a slightly better fit for larger $\tilde{q}$. Apart from that, *i.e.,* for large f or large $\tilde{q}$ and small $\tilde{\omega}$, the fit is very good. This is just what we would have expected from our conditions for the validity of the Ansatz as smaller $\tilde{q}$ imply more rapidly varying $\tilde{\nu}_0, \tilde{\gamma}_0$ at least for the first few poles and both small f and $\tilde{q}$ and large $\tilde{\omega}$ move the poles further away from the real axis. Furthermore, for large $\tilde{\omega}$, the amplitude of the resonance pattern becomes quickly suppressed and so it is subject to systematic deviations and noise.

Now, let us look at the qualitative behavior. We see that, as anticipated with the Ansatz, the poles lie roughly equally spaced on a straight line, *i.e.,* they are resonances in a region of fixed width with fixed "mass" to inverse lifetime ratio. With increasing f, both the separation of the poles and the slope of the line of poles decreases, *i.e.,* the poles are

moving closer to the real axis. Of course, these changes are reflected by the appearance of distinct peaks in the previous plots of conductivity at large f. This behavior is roughly independent of $\tilde{q}$, and there is an overall shift depending on $\tilde{q}$, that is larger for smaller values of f. One might expect both the decreasing energy gap and the increasing mass to width ratio since the length scale due to the width of the defect increases and the shape of the step in the potential is approximately fixed. The deviation of the poles from a straight line is stronger for large $\tilde{q}$ and reflects the fact that the shallow potential at small $\tilde{q}$ is fully probed at small $\tilde{\nu}$, whereas at large $\tilde{q}$, the resonances at small $\tilde{\nu}$ are only sensitive to the details of the top of the potential, and only probe the steeper regions at higher n. This effect is obviously more visible at large f because of the closer spacing of the resonances. We also see that the poles of the transverse correlator lie roughly half-way between the poles of the longitudinal correlator, as anticipated in (2.2.59). Comparing the various approximations to the location of the poles of the actual spectral function, we see the behavior that we saw in figure 2.9 encoded in a different way. Here, we see the shift of the poles of the tanh potential that is more significant for larger $\tilde{q}$.

As an aside, let us briefly return to the cuts that appeared in the the transverse and longitudinal conductivities, in (2.2.51) and (2.2.61), with the limit $T \to 0$. Given the present analysis, it is natural to conclude that this cut arises through an accumulation of poles near $\tilde{\omega} \sim \tilde{q}$. Assuming the locations of the poles in the $\tilde{\nu}$ plane, $\tilde{\nu}_n$, to be roughly independent of $\tilde{q}$, we find that for $\tilde{q} \gg 1$ we get $\tilde{\omega}_n = \sqrt{\tilde{\nu}_n^2 + \tilde{q}^2} \sim \tilde{q} + \tilde{\nu}_n^2/\tilde{q}$. This then leads to an infinite number of poles accumulating near $\tilde{\omega} = \tilde{q}$ as $T \to 0$ and resulting in a cut.

While the Ansatz (2.3.91) fixes the poles along a straight line with a fixed spacing, *i.e.,* $\tilde{\nu} = n(\tilde{\nu}_0 - i\tilde{\gamma}_0)$ in the Re $\tilde{\nu} > 0$ region, we fit the parameters locally to each peak of the spectral function and so the fitted poles deviate slightly from this simple Ansatz. Keeping in mind the limitations, let us try to extract some quantitative information on these deviations. In particular, at large n, the poles approach a straight line of the form $\tilde{\nu}_n = \delta\tilde{\nu} + i\delta\gamma + n(\tilde{\nu}_0 + i\tilde{\gamma}_0)$ ($\tilde{\nu}_n = \delta\tilde{\nu} + i\delta\gamma + (n-1/2)(\tilde{\nu}_0 + i\tilde{\gamma}_0)$ in the longitudinal case). To extract this information, we use different techniques in different regimes, which we outline to forewarn the reader about the validity of the results. For large f, where we have at least the first 5 well-fitted poles, we ignore the first 0-3 poles, leaving us at least 5 poles, such that we can fit the asymptotic lines plus a decaying exponential to Re $\tilde{\nu}_n$ and Im $\tilde{\nu}_n$ and still get information about the accuracy. For some cases, the exponential fit fails, and we resort to fitting a straight line and estimate the accuracy from the second derivative in the location of the poles.

The assumption of an exponential deviation from a straight line may seem somewhat arbitrary, but it turns out to be the right choice, as it is the only natural candidate whose

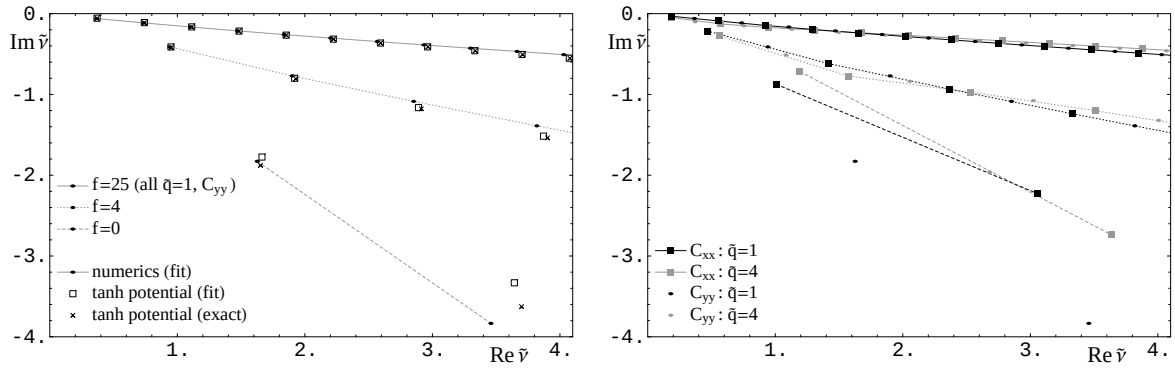

Figure 2.11: Left: Comparing the exact location of the poles of the transverse correlator to the fit, using the approximate tanh-potential of appendix C, at values $f \in \{0, 4, 25\}$ and $\tilde{q} = 1$. Right: Comparing the poles of the transverse correlator with the ones of the longitudinal correlator at $f \in \{0, 4, 25\}$ and $\tilde{q} \in \{1, 4\}$. The lines are only shown to guide the eye as to which poles correspond to the same values of $f, \tilde{q}$.

results are independent within errors from the particular choice of the number of poles used for the regression. The location of the poles from the tanh potential, for example, contains by this criterion an $\mathcal{O}(\ln n)$ term as expected from (C.2.10).

In the borderline case, where there are 4 poles, we extract the uncertainties by fitting the last 3 poles to the asymptotic line with the deviation estimated by the fit with 4 points. For 3 poles only, we still get a rough estimate for the asymptotic limit (from the last 2 points) and for the accuracy by including the first point. For $f = 0$, we always find only the first two poles, so we can give only an order of magnitude guess for the rest of the sequence. Finally, we estimate the uncertainties from the errors in the fit of the sequence of poles and from the deviation of the estimated location of poles to their exact location in the case of the tanh potential. We use the latter also to add a shift to try to correct for systematic errors in the fit of the Ansatz (2.3.94, 2.3.95) to the numerical data. We are somewhat sloppy with the uncertainties in the sense that we do not distinguish between random and systematic errors. So we assume that the accuracy of the fits is limited by systematic uncertainties in the convergence towards the asymptotic straight line, which may result in a slight overestimating of uncertainties in the averaged data that we present below. As expected, the results from the transverse and longitudinal poles are identical within the errors and so we average over them.

Let us now examine some of the results of our fitting in figure 2.12. In the first two plots, we show results for the energy gap between the quasinormal modes, $\tilde{\nu}_0$. In particular

for large f, we see that the asymptotic behavior of $\pi/\tilde{\nu}_0$ matches a simple straight-line fit: $\pi/\tilde{\nu}_0 = c_1\sqrt{f} + c_0$ with $c_1 \simeq 1.821$ and $c_0 \simeq -0.539$. In the first plot, this behavior seems to match well with the asymptotic behavior of $\pi T/(2T_{eff})$ and $\pi D(f)T$. Note, however, that the second plot shows that upon closer examination, the deviation between $\pi/\tilde{\nu}_0$ and the curves set by these scales in the large f regime seems to be beyond the errors expected for our numerical fit to $\tilde{\nu}_0$. Note that large f behavior in (2.2.85) gives $\pi T/(2T_{eff}) \simeq 1.854\sqrt{f} - 0.690$, while (2.2.72) yields $\pi DT \simeq 1.854\sqrt{f} - 1$. The asymptotic behaviors for these quantities have precisely the same slope and the difference is in the constant term (and the subleading $1/\sqrt{f}$ terms), as can be seen in figure 2.12. This slope is only a fair match for that found in our straight-line fit. We expect that this is because of subleading $1/\sqrt{f}$ terms and that we would see better convergence at larger values of f. In any event, it seems then that $\tilde{\nu}_0$ is closely related to other characteristic scales in the defect theory. Note that here since $\tilde{\nu}_0$ appears to be independent of $\tilde{q}$ within the errors (see figure 2.13), the data in figure 2.12 is averaged over $\tilde{q} \in \pi/2, \pi, 2\pi$.

We also show the overall shift $\delta\tilde{\gamma}$ and the ratio $\tilde{\gamma}_0/\tilde{\nu}_0$ separately in figure 2.12 for the cases $\tilde{q} \in \pi/2, \pi, 2\pi$. In each case, these parameters show a $1/\sqrt{f}$ falloff for large f. In particular, this means that the width $\tilde{\gamma}_0$ is falling as $1/f$ and so we see the origin of the quasiparticle peaks in the spectral curves. In each plot, we also show $\pi T/(2T_{eff})$ for each case and see there is good agreement within the estimated errors of the numerical results. This is just what we expect, since the detailed shape of the step in the effective Schrödinger potential and hence the ratio between the two modes in the asymptotic region of the potential, is to a good approximation independent of f. The slowly varying part of this ratio gives rise to the finite shift and the exponential suppression factor gives rise to $\tilde{\gamma}_0/\tilde{\nu}_0$, which are in the limit of large $\tilde{\omega}$ proportional to the inverse of the width of the asymptotic region of the potential. This can be more easily seen from the expressions in appendix C.2. From the boundary point of view, it comes at no surprise that the overall shift of the poles is proportional to the overall energy scale, and that the quasiparticle excitations become more stable with increasing f, which is proportional to the width of the potential step. One could make a similar plot of $\delta\tilde{\nu}$ but we do not show the results here. While on the whole the trends appear similar to those for $\delta\tilde{\gamma}$, the values are typically smaller by a factor of roughly 2 while the relative errors are larger by a similar factor. Hence at least for the smaller values of $\tilde{q}$, the results are consistent with zero shift.

Now let us turn to the $\tilde{q}$ dependence of the quasinormal modes. Because of the good agreement of the f dependence with T_{eff}/T, we improve the accuracy of our results by taking a (weighted) average over the suitably scaled values of the characteristic quantities for $f \in \{9, 16, 25, 36\}$. In figure 2.13, we show the $\tilde{q}$ dependence of the same quantities as in figure 2.12. First, we see that $\tilde{\nu}_0$, which is supposed to depend only on the width of

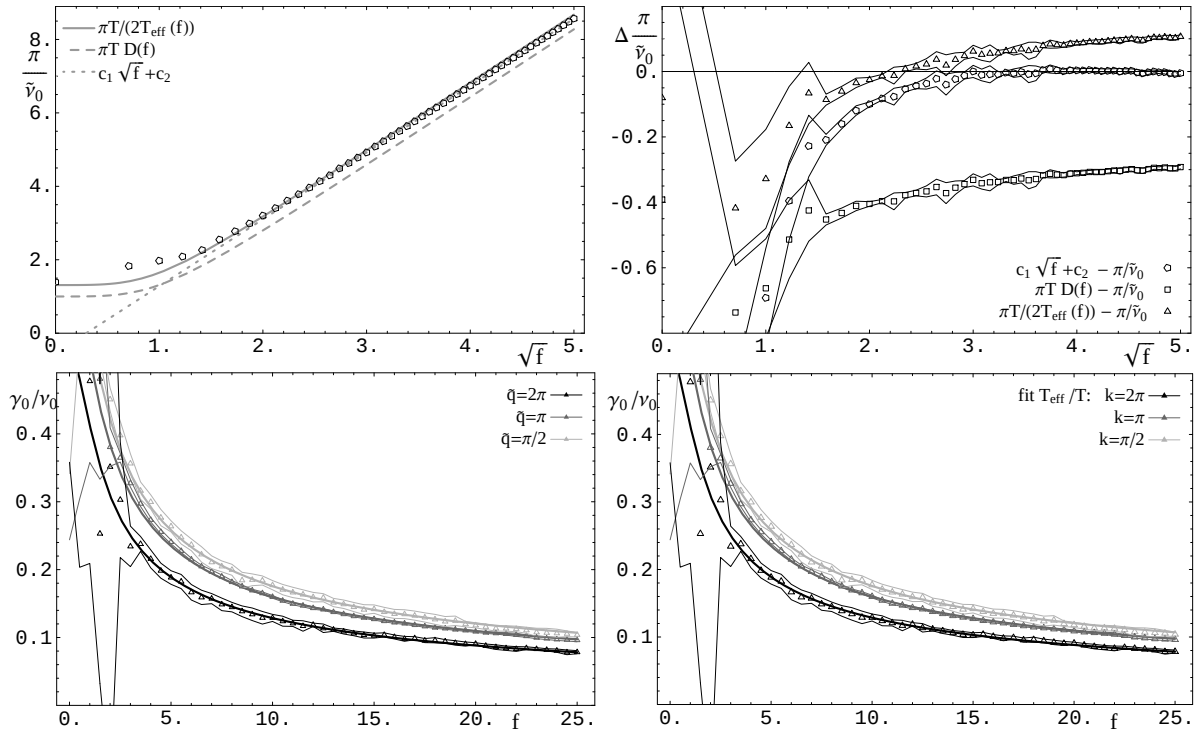

Figure 2.12: Top left: The energy gap between resonances $\tilde{\nu}_0$ presented as $\pi/\tilde{\nu}_0$. The asymptotic $\sqrt{f}$ behavior is fit is several ways. Top right: The difference between the previous fits and the numerical results for $\pi/\tilde{\nu}_0$. The data in the top two plots is averaged over $\tilde{q} \in \pi/2, \pi, 2\pi$. Bottom left: The "mass to width" ratio $\tilde{\gamma}_0/\tilde{\nu}_0$ for the sequence of poles for several values of $\tilde{q}$. Bottom right: The f-dependence of the overall shift of the poles $\delta\tilde{\gamma}$. The points are the average numerical data and the narrow lines indicate the 1σ uncertainties, which includes both random and systematic errors.

the potential, is within the uncertainties independent of $\tilde{q}$. Any change in $\tilde{q}$ however scales only the height of the potential step.

From the results in appendix C.2, we would expect that varying $\tilde{q}$ changes only the overall shift of the poles, but we know already that the full result has fundamentally different characteristics coming from the shape of the potential step because of the absence of a significant $\mathcal{O}(\ln n)$ term. In general, however, $\tilde{\nu}_0$ should not change significantly, since we consider here only $f \geq 9$, so the potential is already so wide that small details of probing the potential step should not change the the quasinormal modes too much. Both the shift, and the deviation from the linear Ansatz conspire to give us both the right "low temperature background" with approximately symmetric oscillations around it as in figure 2.10. From the fact that this behavior resembles that in the resulting conductivity from (2.3.92), one should assume that there are small shifts and deviations for small $\tilde{q}$. One also expects the shift to grow not faster than $\propto \ln \tilde{q}$, provided that the ratio of the two modes in the asymptotic region depends at most on some power of the height of the step in the potential.

In figure 2.13, we find roughly this behavior of the shift, with small $\delta\tilde{\nu}, \tilde{\gamma}$ at small $\tilde{q}$ and an indication of some converging or slowly growing behavior at large $\tilde{q}$. We also find a small drop in $\tilde{\gamma}_0/\tilde{\nu}_0$ with some converging behavior at large $\tilde{q}$. In principle, we could try to use this information to try to reverse engineer the calculations in appendix C.2, *i.e.,* to reconstruct the ratio of the incoming and outgoing modes. For example, the absence of a significant $\mathcal{O}(\ln n)$ term tells us that there is no significant $\tilde{\nu}$ dependence, the approximately constant (in f) ratio $\delta\tilde{\nu}/\delta\tilde{\gamma}$ shows us that the ratio of the modes has a complex phase (and also its value) but there is nothing really interesting to learn from this. A somewhat interesting point though is that the change in $\tilde{\gamma}_0/\tilde{\nu}_0$ tells us that at small $\tilde{q}$, the potential "appears smoother" than at large $\tilde{q}$.

2.3.3 Poles in the hydrodynamic regime

In this section, we focus on the hydrodynamic regime where $\tilde{\omega}, \tilde{q} \ll 1$. In this regime, the diffusion pole (2.2.73) dominates the structure of the correlators. One might wonder, why we have not included the diffusion pole into the sum for C_{yy}, as in (2.3.91). As we will show below, this is because the diffusion pole disappears at a critical value of the wave-number, $\tilde{q}_c$, which is below the values of $\tilde{q}$ that we have considered to this point. Below $\tilde{q}_c$ there are two poles on the imaginary axis in the $\tilde{\omega}$ plane, one of them being the diffusion pole, and the other one at larger absolute imaginary values of $\tilde{\omega}$, which decreases slowly as $\tilde{q}$ grows, as shown in figure 2.14. While the diffusion pole is in perfect agreement with what

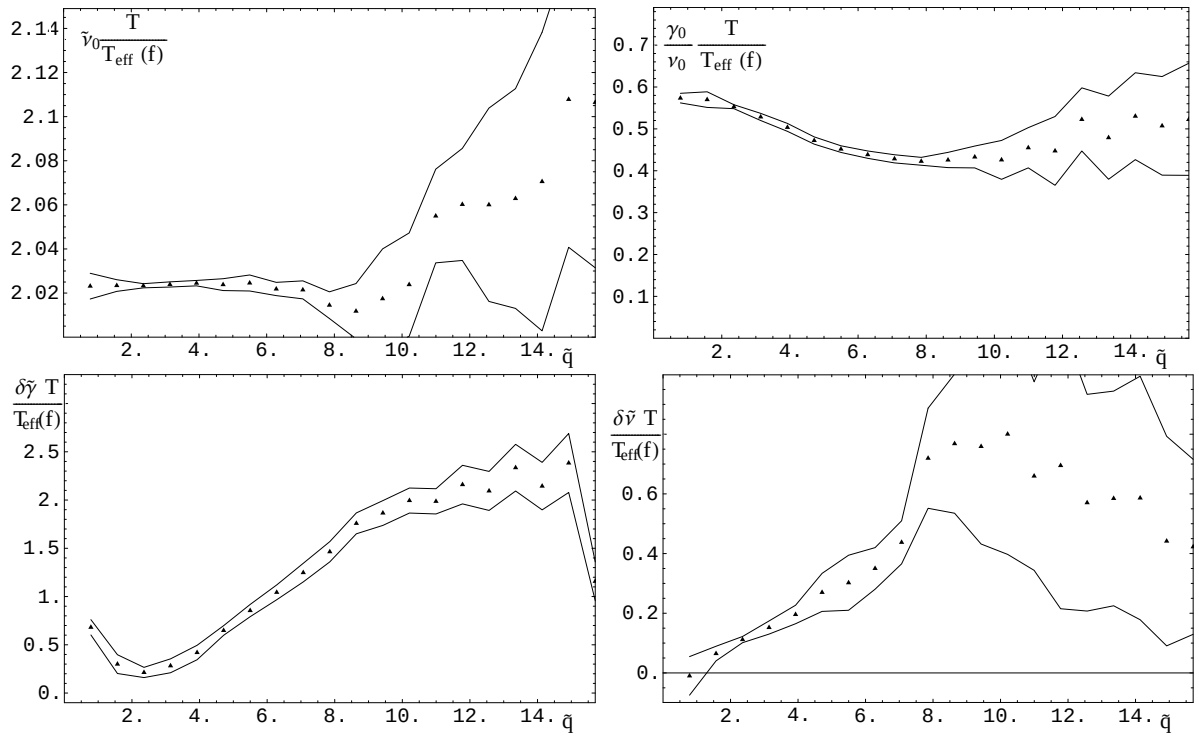

Figure 2.13: Average over quantities appropriately scaled with $T_{eff}(f)/T$ for $f \in \{9, 16, 25, 36\}$: Top left: (In)dependence of $\tilde{\nu}_0$ on $\tilde{q}$. Top right: $\tilde{\gamma}_0/\tilde{\nu}_0$. Bottom: The complex shift $\delta\tilde{\nu}$ and $\delta\tilde{\gamma}$.

we expected, the second pole, corresponding to rapid (*i.e.,* on thermal scales) decay of long-range modes, is somewhat puzzling. In particular, it has a non-trivial f dependence at small values of $\tilde{q}$. It seems that for large f, the lifetime of those modes is not anymore proportional to the length scale of the defect, but increases less rapidly.

At $\tilde{q}_c$, there is a branch cut, and the poles move away from the imaginary axis out into the complex plane to turn into the first quasiparticle poles, *i.e.,* the $n = 1$ poles in (2.3.91). Hence at this point, the transport changes from the collision dominated phase to the collisionless phase. This is a good example of the interplay between various length scales. We can interpret this on the one hand as the height of the effective potential being smaller or larger than the inverse length scale of the defect (and hence the effective temperature) and on the other hand as separating between between modes smaller and larger than the size of the defect. From a hydrodynamic viewpoint, however this branch cut gives us approximately the mean free path, which is in strongly coupled systems proportional to, and of the same order as, the temperature scale, and we see an approximate scaling of $\tilde{q}_c$ with the effective temperature.

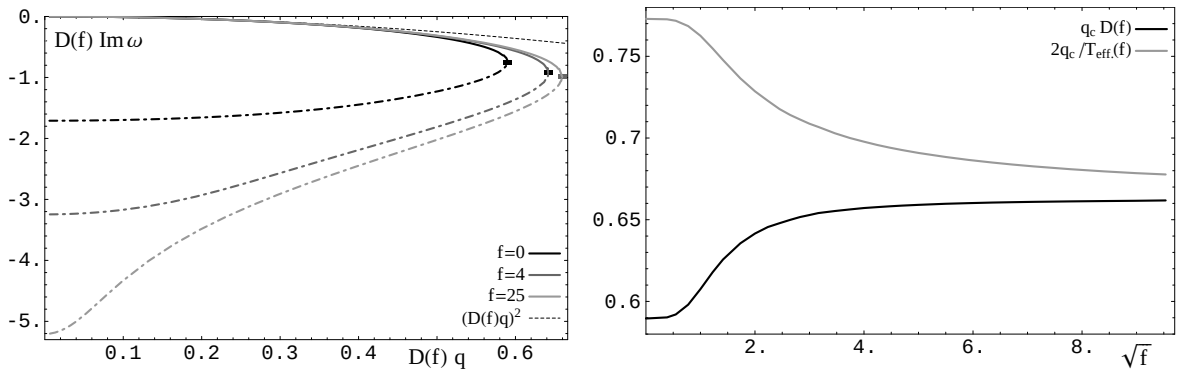

Figure 2.14: Left: The location of the poles on the imaginary axis below $\boldsymbol{q}_c$, rescaled by the diffusion constant. The dashed line is what one expects for the diffusion pole. Right: The critical values q_c at which the purely dissipative poles disappear, multiplied with several length scales.

On the right in figure 2.14, we compare $\tilde{q}_c$ with the various length scales in the problem, as we did before for the spacing of the quasiparticle masses in figure 2.12. Since we are in the completely opposite regime in terms of length scales of the perturbations, it is no surprise that there is significant disagreement between the scaling of $\tilde{q}_c$ and $\tilde{\nu}_0$, but the disagreement is surprisingly small. In addition to the opposite limit of the size of the perturbations, the data in figure 2.12 contains only frequencies, which one can interpret as being related

directly to the width of the defect, whereas here we consider the f-dependence of relevant values of $\tilde{q}$, which measure scales along the defect. Overall, it seems that in the limit of large f, $\tilde{q}_c \simeq 2/(3\,D)$ or $\tilde{q}_c \simeq 4T_{eff}/3$. The relative factor between these two expressions is not surprising given that, in the previous section, we noted that $D = 2/T_{eff}$ as $f \to \infty$. Further, given our previous expressions for D and T_{eff}, we note that $\tilde{q}_c \propto T/\sqrt{f}$ for large f, *i.e.,* $\tilde{q}_c$ decreases as f grows. Then as the plot shows, up to an overall numerical factor, most features of the f-dependence of $\tilde{q}_c$ can be related to either of these other physical scales.

In principle, the decreasing residue of the poles with increasing n allows us to track the location of the first few poles of the longitudinal correlator even further, directly by fitting a sequence of Lorentzians, but we will not bother about such a detailed discussion of the hydrodynamic regime in this paper. It is interesting to see however, how the small-$\tilde{q}$ limit of the shift $\delta\tilde{\nu} + i\delta\tilde{\gamma}$ shown in figure 2.13 qualitatively agrees with a shift towards the bifurcation point.

It is interesting to note that this pairing of the diffusion pole with a fast dissipative mode was also recently found in the quasinormal mode spectrum of black holes in AdS_4 [94]. However, an infinite number of pairs of poles were identified there, appearing along the imaginary axis. In that case, the critical wave-number at which the higher pairs meet at smaller and move off into the complex plane decreases for pairs higher up along the imaginary axis. We looked for similar higher dissipative modes in the present framework but it seems that the diffusion mode and its partner are the only modes appearing on the imaginary frequency axis.

2.4 Electromagnetic duality and perturbative corrections

At the outset of our analysis, we set $M_{\rm q} = 0$ which maintains conformal invariance in the defect system. In the brane construction, this means the internal geometry is fixed and the low energy effective action on the effective four-dimensional brane reduces to Maxwell theory (2.2.31) with a fixed coupling (independent of the radius).[2] Hence resulting equations of motion are invariant under electromagnetic duality, which has interesting implications for the transport coefficients, as emphasized in [49].

[2]In the D5-brane embeddings for $M_{\rm q} \neq 0$, the size of the internal S^2 varies and so the effective coupling of the Maxwell theory (2.2.31) depends on the radius. As explained in [49], the gauge field equations are no longer duality invariant and as a result the correlators discussed here are independent.

Given the Maxwell action (2.2.31), the gauge field equations can be expressed as

$$\nabla^\mu F_{\mu\nu} = 0\,, \qquad \nabla^\mu \widetilde{F}_{\mu\nu} = 0 \qquad \text{with } \widetilde{F}_{\mu\nu} = \frac{1}{2}\,\varepsilon_{\mu\nu\rho\sigma} F^{\rho\sigma}\ . \tag{2.4.96}$$

Hence we have electromagnetic duality with $F_{\mu\nu}$ and $\widetilde{F}_{\mu\nu}$ satisfying the same equations of motion. Implicitly, we used this duality in deriving the relation between the transverse and longitudinal correlators (2.2.59), *i.e.,* the key step was demonstrating the $A_{\tilde{t}}$ and $A_{\tilde{y}}$ equations, (2.2.45) and (2.2.47), could be put in the same form. As in [49], this result (2.2.59) subsequently restricts the transport coefficients to satisfy

$$\Pi^T(\tilde{\omega},\tilde{q})\,\Pi^L(\tilde{\omega},\tilde{q}) = -\varepsilon_0^2(\tilde{\omega}^2 - \tilde{q}^2)\ . \tag{2.4.97}$$

Since with $\tilde{q} = 0$, we have $\Pi^T(\tilde{\omega},0) = \Pi^L(\tilde{\omega},0)$, it follows that:

$$\tilde{\sigma}(\tilde{\omega}) = i\frac{\Pi(\tilde{\omega},0)}{\tilde{\omega}} = \varepsilon_0 = \pi\, D\, T\, \varepsilon \quad \text{or} \quad \sigma(\omega) = D\,\varepsilon\,. \tag{2.4.98}$$

That is, $\sigma(\omega)$ is independent of frequency and temperature. One can show that this remarkable result is consistent with the Einstein relation,[3] as noted already in [49]. This is also remarkable from the point of view that at $\tilde{q} = 0$, the conductivity at all frequencies obeys the diffusion behavior, which is not what one would generically expect.

However, as for any low energy action in string theory, we must expect that there are higher derivative interactions correcting the Maxwell action (2.2.31). In fact, the action (2.1.4) implicitly captures an infinite set of these stringy corrections, as would be illustrated if we expanded the DBI term in powers of F. This expansion would also demonstrate that these higher order terms are suppressed by factors of $\alpha' = \ell_{\rm s}^2$. In terms of the dual CFT, the contributions of these α' interactions will provide corrections to the leading supergravity results for a finite 't Hooft coupling. However, none of the higher order terms coming from the DBI action will modify the two-point correlators in the planar limit, *i.e.,* in the large $N_{\rm c}$ limit, because these interactions all involve higher powers of the field strength. One must keep in mind though that, as already alluded to in section 2.1.2, the DBI action does not capture all of the higher dimension stringy interactions. The full low-energy action includes additional terms involving derivatives of the gauge field strength [95, 96], as well as higher derivative couplings to the bulk fields, *e.g.,* curvature terms [97, 98]. In principle, any such interaction, which is quadratic in F, has the potential to make finite λ corrections to the correlators which we have studied above.

[3] See e.g. [85], section 7.4 for a suitable discussion of the Einstein relation.

In appendix B, we identified a particular higher derivative term which makes a quadratic correction (B.0.2) to the four-dimensional low energy action. This term makes the leading correction to the correlators, at least when the internal flux is nonvanishing. Including this term, the vector equations of motion become

$$\nabla^\mu F_{\mu\nu} = \xi\, L^2\, \nabla^\mu \Box F_{\mu\nu}\,, \qquad \nabla^\mu \widetilde{F}_{\mu\nu} = 0 \qquad \text{with } \xi = \frac{\zeta(3)}{2\pi\sqrt{\lambda}} \frac{f^2}{\sqrt{1+f^2}}\ . \tag{2.4.99}$$

We can recognize the higher derivative term as a string correction by recalling that $L^2/\sqrt{\lambda} = \ell_{\rm s}^2$. Clearly these equations are no longer invariant under the replacement: $F_{\mu\nu} \to \widetilde{F}_{\mu\nu}$. One could attempt an α'-corrected electromagnetic duality by defining $\widetilde{X}_{\mu\nu} = (1 - \xi\, L^2 \Box)\, F_{\mu\nu}$. Formally treating ξ as a small expansion parameter, one can rewrite (2.4.99) as

$$\nabla^\mu X_{\mu\nu} = -\xi\, L^2\, \nabla^\mu \Box X_{\mu\nu}\,, \qquad \nabla^\mu \widetilde{X}_{\mu\nu} = 0\ . \tag{2.4.100}$$

Hence an exchange $F_{\mu\nu} \to X_{\mu\nu}$ does not quite leave the equations of motion invariant either, *i.e.,* the sign of the ξ term changes between (2.4.99) and (2.4.100). This then confirms the initial intuition that the α'-corrected low energy theory describing the four-dimensional dynamics of the vector field is no longer invariant under electromagnetic duality. Hence we can longer expect (2.4.97) and (2.4.98) to apply when finite λ corrections are taken into account for the defect CFT.

In the following, we examine in more detail the effect of this leading finite λ correction. For simplicity,[4] we focus on the modifications to the transverse conductivity $\tilde{\sigma}_{yy}$. Here we simply present the results of our numerical calculations. The preliminary analysis determining the analytic form of the transverse correlator is given in appendix B. There are two distinct contributions to the modification of the correlator. First, since the bulk action contains an additional term, there are new surface terms (B.0.8) which must be evaluated in the holographic calculation. Remarkably, as described in the appendix, the net effect of this contribution is to shift the permittivity

$$\varepsilon_0 \to \varepsilon_0 \left(1 - \frac{1}{\sqrt{\lambda}} \frac{f^2\, \zeta(3)}{\pi (1+f^2)^{3/2}}\right) = \varepsilon_0 \left(1 - \frac{2\,\xi}{1+f^2}\right)\ . \tag{2.4.101}$$

The second modification of the correlator arises because the bulk equations of motion have been corrected, as in (2.4.99). Hence the solutions for the vector are modified and this change of the solution alone leads to changes in the correlator coming from the leading

[4]Similar considerations apply to the longitudinal conductivity but the calculations are somewhat more involved.

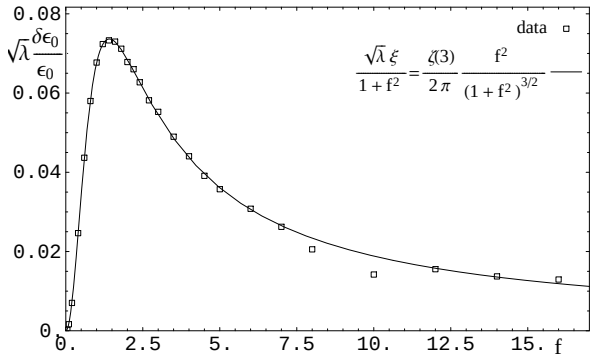

Figure 2.15: The modification of $\varepsilon_0 \equiv \tilde{\sigma}(\tilde{\omega}\to\infty)$ as a function of f from the $1/\sqrt{\lambda}$ corrections.

supergravity expression (2.2.41). Now, we have some ambiguity in how we might define ε_0 in the theory with finite-λ corrections. Recall that this quantity originally appeared in (2.2.40) but above was simply related to the conductivity (2.4.98) found in the infinite λ limit. Hence a convenient choice, which we adopt at finite λ, is: $\varepsilon_0 \equiv \tilde{\sigma}(\tilde{\omega}\to\infty)$. Then our numerical results indicate that this second finite-λ correction also shifts ε_0 precisely as in (2.4.101) except for a factor of $-3/2$. The total shift is shown in figure 2.15 and the result seems to match precisely $-1/2$ times the shift given in (2.4.101).

Given that the invariance under electromagnetic duality is lost at finite λ, the frequency independence of the conductivity $\tilde{\sigma}(\tilde{\omega}) = \tilde{\sigma}_{yy}(\tilde{\omega}, \tilde{q}=0)$ found in (2.4.98) is also lost as shown in figure 2.16. Note that here we are plotting the change arising from the inclusion of the finite λ corrections, *i.e.,* $\delta\tilde{\sigma}(\tilde{\omega}) = \tilde{\sigma}(\tilde{\omega}) - \varepsilon_0$ where our subtraction includes the finite-λ correction to ε_0, as described above. Note that in the figure, the factor $1/\xi \propto \frac{\sqrt{1+f^2}}{f^2}$ is included to cancel the f dependence coming from the factor in front of the higher order term in (B.0.4). While the resulting conductivity shows an oscillatory behavior, we note that the DC conductivity, *i.e.,* at $\tilde{\omega}=0$, is generally smaller than at high frequencies, *i.e.,* for $\tilde{\omega}\to\infty$. The net difference is plotted in figure 2.16, as a function of f. As shown, the numerical results are very well fit with a simple analytic form proportional to $f^2/(1+f^2)$. Note that the first few points in this plot (including where the difference becomes positive) are not reliable, because of the high sensitivity to errors in $\delta\varepsilon_0$, which was only computed approximately in a numerical calculation.

One of the interesting features that figure 2.16 seems to exhibit is that the oscillations of $\tilde{\sigma}(\tilde{\omega})/(\xi\varepsilon_0)$ for various values of f are all contained within some universal envelope, that is decaying with $\tilde{\omega}$. In fact, this same envelope also applies for the conductivity at finite values of $\tilde{q}$, as illustrated in figure 2.17. In this figure, we are showing $\delta\tilde{\sigma}_{yy}/(\varepsilon_0\xi)$ for $f \in \{1,4,9,16\}$ and $\tilde{q} \in \{0, \pi/4, \pi/2, \pi, 2\pi\}$, where $\delta\tilde{\sigma}_{yy} \equiv \tilde{\sigma}_{yy}(\tilde{\omega},\tilde{q}) - \tilde{\sigma}_{yy}(\tilde{\omega}\to\infty,\tilde{q})$. Again, the factor $1/\xi$ is included in the figure to cancel the f dependence explicitly appearing in

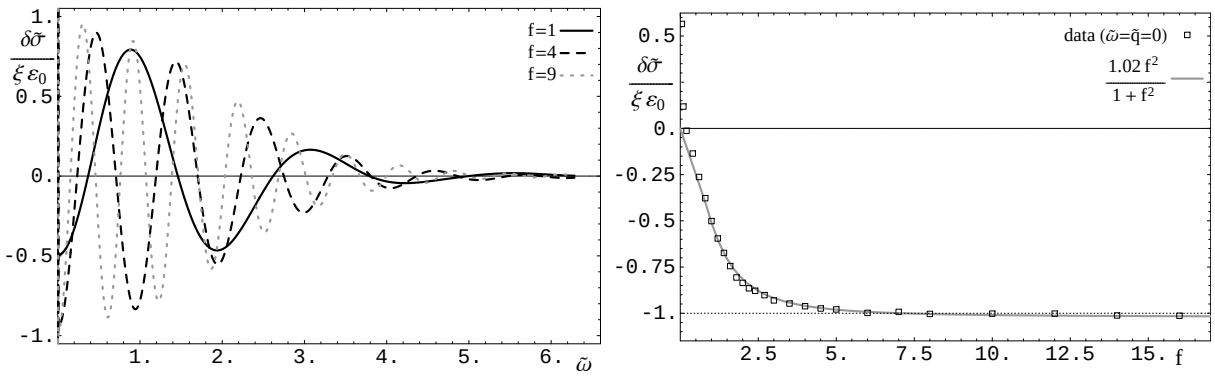

Figure 2.16: Left: The finite-λ correction to the conductivity $\delta\tilde{\sigma}(\tilde{\omega})$ for various values of f. Right: $\tilde{\sigma}(\tilde{\omega}=0)-\tilde{\sigma}(\tilde{\omega}\to\infty)$, the change in conductivity from $\tilde{\omega}=0$ to $\tilde{\omega}\to\infty$ at finite λ.

the higher order term in (B.0.4). In particular, we see here that the envelope appears to be independent of $\tilde{q}$. However, as shown in figure 2.17, for sufficiently small f ($f=1/4$ in the figure), there exists a critical value of $\tilde{q}$, above which the conductivity is no longer bounded by this universal envelope. Note that for the same values of f, the curves below the critical value of $\tilde{q}$ are still bounded by the envelope. However, note that both $\xi, \varepsilon_0 \propto f$ for large f and so the amplitude of oscillations in $\tilde{\sigma}(\tilde{\omega})$ alone is actually growing with f.

At finite $\tilde{q}$, the leading order result (for infinite λ and N_c) for $\tilde{\sigma}_{yy}$ also exhibited similar damped oscillations which were confined within a certain envelope, as discussed in 2.2.2.2. Comparing this previous envelope with that for $\delta\tilde{\sigma}_{yy}$ (for large $f \gtrsim 2$), we see that the previous one does not depend only on $\tilde{\omega}$, in contrast to the behavior found above. The exponential decay of the amplitude at large $\tilde{\omega}$ is also slower than here than with the envelope for the leading infinite-λ result. This would imply that the finite-λ corrections become more and more significant at large $\tilde{\omega}$, while they become less significant with increasing $\tilde{q}$.

The "frequency" of the oscillations is approximately the same for the leading term and the finite-λ correction. Figure 2.18 shows this in more detail by plotting $\frac{\sqrt{\lambda}}{\varepsilon_0}\delta\tilde{\sigma}_{yy}$ in terms of $\sqrt{\tilde{\omega}^2-\tilde{q}^2}$ and also for comparison the oscillations of the infinite-λ or "zero'th order" result.

We find that there is a phase shift of between $\pi/2$ and π in the oscillations, implying that they will shift towards larger $\tilde{\omega}$ and decrease in amplitude. We can also see that there is some tendency for a smaller phase shift (i.e. less/no decrease in amplitude, less shift) as f and $\tilde{\omega}$ increase. In terms of the location of the poles, this implies a shift towards larger

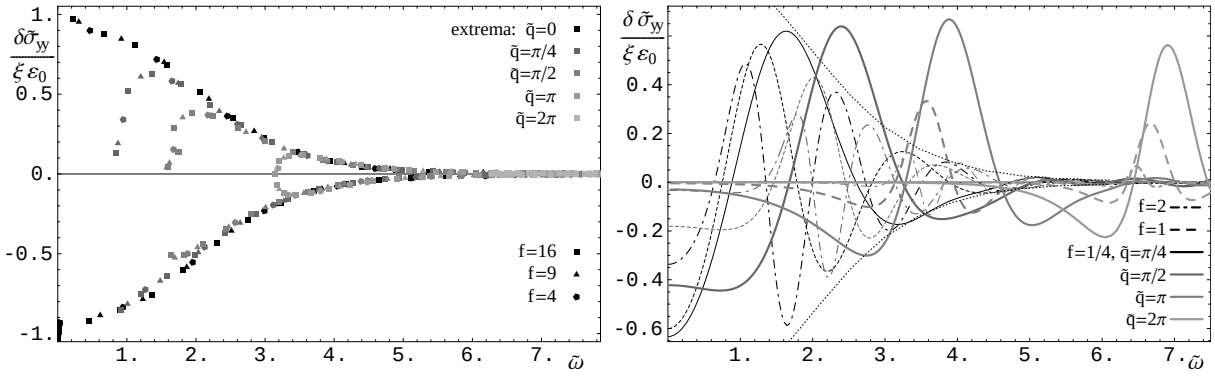

Figure 2.17: Left: The extrema of $\frac{1}{\varepsilon_0 \xi}\delta\tilde{\sigma}_{yy}$ for $\tilde{q} \in \{0, \pi/4, \pi/2, \pi, 2\pi\}$ and "large" $f \in \{4, 9, 16\}$. We see that all the curves are approximately bound by some universal envelope function, that decays exponentially in $\tilde{\omega}$. Right: $\frac{1}{\varepsilon_0 \xi}\delta\tilde{\sigma}_{yy}$ for $\tilde{q} \in \{\pi/4, \pi/2, \pi\}$ and $f \in \{1/4, 1\}$. For $f = 1/4$ and sufficiently large $\tilde{q}$, the conductivity is not bounded by the universal envelope (shown in thin dots).

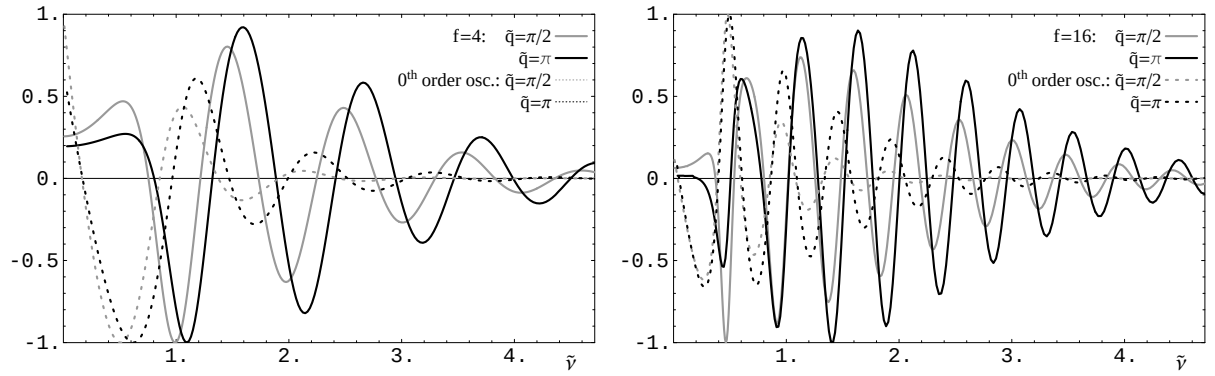

Figure 2.18: Left:$\sqrt{\lambda}\delta\sigma_{yy}$ in the rest-frame frequency $\tilde{\nu}$ for $\tilde{q} \in \{\pi/2, \pi\}$ and $f = 4$, scaled to 1. The dotted lines show $\sigma_{yy} - \sqrt{1 - \tilde{\omega}^2/\tilde{q}^2}$, also scaled to 1. Right: $f = 16$

real and imaginary frequencies and an increased spacing between the quasinormal modes, again more significant for large f, small $\tilde{q}$ and large $\tilde{\omega}$. Another point to view this is that there is a finite-λ behavior, that becomes important for the higher resonances. In principle one could quantify this more precisely by doing a perturbative treatment of the methods used in section 2.3, but we will not discuss this here. The shift ε_0 can be absorbed into the residue. In terms of the potential, this implies that the potential becomes narrower, especially at small f and small $\tilde{q}$ (or large T), which simply means that the length scale that we attributed to the strong coupling decreases and disappears. The $\tilde{\omega}$ dependence also implies that the potential becomes smoother at finite coupling.

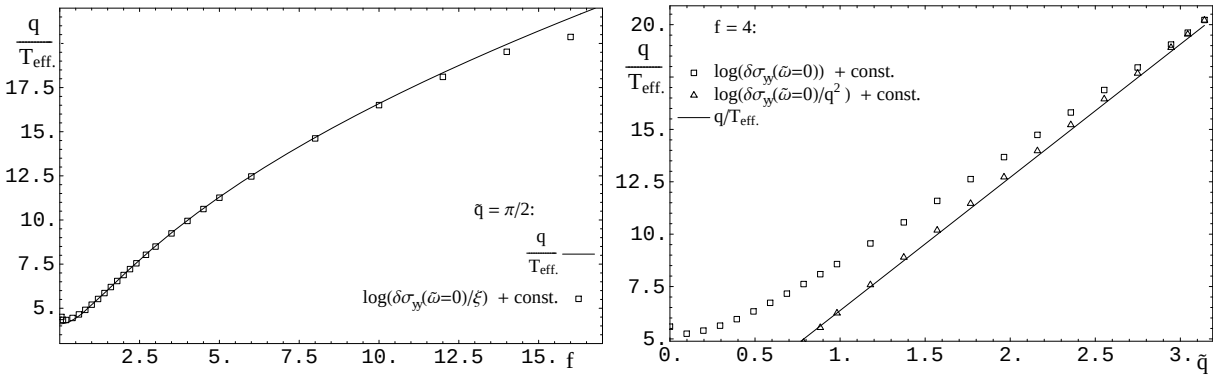

Figure 2.19: Left: $\log \delta\tilde{\sigma}_{yy}(\tilde{\omega}=0)/\xi$ (modulo a constant shift) and $\frac{\tilde{q}}{T_{eff}(f)}$ for $\tilde{q}=\pi/2$. The accuracy of the last two points are very sensitive to possible errors in $\delta\varepsilon_0$. Right: $\log \delta\tilde{\sigma}_{yy}(\tilde{\omega}=0)$ and $\frac{\tilde{q}}{T_{eff}(f)}$ for $f=4$. $\log \delta\tilde{\sigma}_{yy}(\tilde{\omega}=0)/\tilde{q}^2$ is shown to demonstrate the slow convergence due to polynomial factors of $\tilde{q}$.

For $\tilde{\omega}-\tilde{q}<0$, the finite-$\lambda$ correction becomes quickly negative and exponentially suppressed with increasing f and $\tilde{q}$, roughly as described by the "effective temperature", such that the exponential suppression does not get broken but is possibly modified. We show the shift $\frac{\delta\tilde{\sigma}_{yy}(\tilde{\omega}=0)}{\varepsilon_0\xi}$ as a function of f for $\tilde{q}=0$ and a function of $\tilde{q}$ for $f=1$ in figure 2.19. Recall that figure 2.16 shows the same results for $\tilde{q}=0$.

The form of $\delta\tilde{\sigma}_{yy}$ for $f \lesssim 2$ is more similar to the resonances associated with the infinite-λ result for $\tilde{\sigma}_{yy}$, as the amplitude seems to decay exponentially with $\tilde{\nu}$ and depends only polynomially on $\tilde{q}$, as we show in figure 2.17. Just as for the large f, the decay is slower than the one in the 0^{th} order term. This demonstrates that the effects of finite λ are more significant for small f, where the length scales are still dominated by the $f=0$ length scale, that we can attribute to the strong coupling. Further it shows that the length scale due to the "width" of the defect has a tendency to persist.

2.5 Topological Hall Effect

The conductivity in section 2.2 is diagonal reflecting the parity invariance of the defect theory. Recently AdS/CFT techniques were applied to study Hall conductivity in the three-dimensional conformal field theories dual to an AdS_4 background [50, 69]. The construction in [50] involved breaking the parity invariance by introducing a background magnetic field, and this is along the lines that we will do in chapter 3. However, it turns out that there is an alternative way a Hall effect may arise – in an entirely "conformal" manner. In [69], parity invariance is broken by the introduction of an auxiliary gauge field with a nonzero θ-term. This construction is closely related to the following where we produce an off-diagonal conductivity by the addition of a topological θ-term to the four-dimensional SYM action [99]. A related model of the quantum Hall effect based on a probe brane construction appears in [66].

To introduce an xy component to the conductivity, we begin by considering the Chern-Simons part of the D5-brane action. In particular, the latter includes the following term:

$$\Delta I = \frac{(2\pi\ell_s^2)^3}{3!} N_{\rm f}\, T_5 \int C^{[0]}\, F\wedge F\wedge F \tag{2.5.102}$$

where $C^{[0]}$ is the RR scalar. Now the background (2.1.2) remains a consistent solution of the type IIB supergravity equations if we set this scalar to some arbitrary constant, *i.e.,* $C^{[0]} = a$. Of course, this choice corresponds to adding a topological θ-term to the action of the dual SYM theory [99]. Now if we recall the magnetic flux (2.1.6) on the internal S^2, the above contribution (2.5.102) reduces to the following four-dimensional action

$$\Delta I = (2\pi)^4 \ell_s^6\, T_5\, 2\pi\, a\, q \int F\wedge F\,, \tag{2.5.103}$$

where q is the magnetic flux quantum number (2.1.6), indicating the number of D3-branes dissolved into the D5-brane. Thus upon integrating out the S^2 part of the probe brane geometry, this term (2.5.102) has become a topological *theta*-term for the four-dimensional worldvolume gauge fields. Since it is a topological term, it does not modify the equations of motion (2.2.44–2.2.47) for the gauge field. However, it does produce an additional boundary term,

$$\Delta I = 2(2\pi)^4 \ell_s^6\, T_5\, a\, q \int d^3\sigma\, \left[A_y\left(\partial_t A_x - \partial_x A_t\right)\right]_{u\to 0^+}\,, \tag{2.5.104}$$

which will modify the correlators. Note that we have simplified the above expression by assuming that in the cases of interest (as in previous sections) the gauge fields are

independent of y. Introducing the Fourier transform (2.2.37), this boundary term becomes

$$\Delta I = -i4\pi\ell_s^6\, T_5\, a\, q \int d^3k\, \left[A_y(-k,u)\,(\omega\, A_x(k,u) + k_x\, A_t(k,u))\right]_{u\to 0^+}\,. \tag{2.5.105}$$

Now following the same steps as in section 2.2.1, we arrive at the following off-diagonal contributions to the retarded Green's function:

$$C_{xy} = i8\pi(2\pi\ell_s^2)^3 T_5\, a\, q\, \omega\,, \qquad C_{ty} = -i8\pi(2\pi\ell_s^2)^3 T_5\, a\, q\, k_x\,. \tag{2.5.106}$$

Note that in the $T = 0$ limit, we expect this contribution to the Green's function can be assembled in the Lorentz invariant expression:

$$\Delta C_{\mu\nu} = i\,\alpha\,\varepsilon_{\mu\nu\rho}\,k^\rho\,, \tag{2.5.107}$$

where α is the dimensionless constant:

$$\alpha = 8\pi(2\pi\ell_s^2)^3 T_5\, a\, q = \frac{2\,a\,q}{\pi g_{\rm s}} = \frac{8\,a\,q}{g_{\rm YM}^2}\,. \tag{2.5.108}$$

The corresponding analysis in the D7 framework gives

$$\alpha_7 = 16\pi^2(2\pi\ell_s^2)^4 T_7\, a\, q_7 = \frac{2a\,q_7}{\pi g_{\rm s}} = \frac{8\,a\,q_7}{g_{\rm YM}^2}\,. \tag{2.5.109}$$

While in principle, this form (2.5.107) need not be preserved at finite temperature, our results (2.5.106) calculated at finite T indicates that in fact the form is preserved. Of course, this independence of the temperature is undoubtedly related to the topological nature of the θ-term which is responsible for this off-diagonal contribution. It is amusing to note that since q (and q_7) is an integer, (2.5.108) and (2.5.109) take just the form of the integer quantum Hall effect, *i.e.*, $\sigma_{xy} = \frac{n\,e^2}{2\pi}$ with $n \in \mathbb{Z}$. By this analogy, we would associate $e^2 = 4a/g_{\rm s}$.

Chapter 3

Dressed Defects

3.1 Turning on the Condensed Matter Background

3.1.1 $D3$ = (N=4 SYM) background

Let us remind ourselves of the super Yang-Mills background outlined in section 2.1. We start off with the well-known $AdS_5 \times S^5$ background of N_c D3 branes corresponding to an $N = 4$ SYM theory on the boundary [33, 35, 34]. We work in the limit of $N_c \to \infty$, at Yang-Mills coupling $g^2_{YM} = 2\pi g_s \to 0$ in the field theory, such that we consider the large t'Hoft coupling limit $\lambda = g^2_{YM} N_c \to \infty$ and we can use the supergravity limit as $L^4 = 4\pi g_s N_c l_s^4 \to \infty$. At finite temperature $T = \frac{r_0}{\pi L^2}$, the background metric is written as

$$ds^2 \;=\; \frac{r^2}{L^2}\left(-h(r)dt^2 + d\vec{x}_3^2\right) + \frac{L^2}{r^2}\left(\frac{dr^2}{h(r)} + r^2 d\Omega_5^2\right)\;, \qquad C^{(4)}_{0123} = -\frac{r^4}{L^4}\;, \tag{3.1.1}$$

which we used in section 2.1 to obtain the brane embedding $z(u)$. Considering only $T > 0$ allows us to go to dimensionless coordinates $u = \frac{r_0}{r},\ \tilde{t} = \frac{r_0 t}{L^2},\ \tilde{\vec{x}} = \vec{x}\frac{r_0}{L^2}$:

$$ds^2 \;=\; \frac{L^2}{u^2}\left(-(1-u^4)d\tilde{t}^2 + d\tilde{\vec{x}}_3^2 + \frac{du^2}{1-u^4} + u^2 d\Omega_5^2\right). \tag{3.1.2}$$

3.1.2 Introducing the defect

In the supergravity limit, the D5 brane action of the $U(1)$ subgroup of the $SU(N_f)$ is just the DBI action plus a Chern-Simons term

$$S = -T_5 N_f \int_{D5} \sqrt{-det(P[G] + 2\pi l_s^2 F)} + T_5 N_f \int_{D5} C^{(4)} \wedge 2\pi l_s^2 F \ , \tag{3.1.3}$$

where the factors of N_f arise from taking the trace over the flavor degrees of freedom, arising from the stack of N_f coincident branes. To simplify things further, we work in the quenched approximation $N_f \ll N_c$, such that we can ignore the backreaction of the probe branes.

Preserving translational invariance in the flat directions and rotational invariance on the sphere, together with the choice of the embedding (2.1.1) dictates the induced metric on the D5 brane to be of the form

$$\begin{aligned} ds^2 &= \frac{L^2}{u^2}\left(-(1-u^4)d\tilde{t}^2 + d\vec{\tilde{x}}_2^2 + \left(1 + (1-u^4)\left(z'(u)^2 + u^2\frac{\Psi'(u)^2}{1-\Psi(u)^2}\right)\right)\frac{du^2}{1-u^4}\right. \\ &\qquad \left. + u^2(1-\Psi(u)^2)d\Omega_2^2\right) \ . \end{aligned} \tag{3.1.4}$$

In chapter 2, we chose the trivial solution $F = 0$ for the $U(1)$ background in the flat directions and for the S^2 radius $\Psi = 0$. Even though Ψ has a tachyonic mode, corresponding to shrinking to zero size, it's mass lies above the Breitenlohner-Friedmann bound $m_\Psi = \frac{-2}{L^2_{AdS_4}} > \frac{-9}{L^2_{4AdS_4}}$ [76], such that it does not cause an instability. The discussion of the setup was limited to the case of vanishing "quark" mass for the matter on the defect, vanishing net density of matter and antimatter on the defect (net baryon number density) and vanishing external magnetic field applied to the defect, but a flux $F = \frac{q}{N_f} d\Omega_2$ on the compact sphere was turned on. This corresponds on the gravity side to having an extra set of q D3 branes pulling on the D5 from one side of the defect and on the field theory side to having an extra number of colors, $\delta N_c = q$ on that side of the defect. Both from the embedding geometry $z(u)$, and from the resulting quasiparticle spectrum in the field theory, it was argued that this flux also introduced a finite width, Δz, of the defect. The embedding was found to be

$$z(u)' = \frac{-f}{\sqrt{1+f^2u^4}} \ , \tag{3.1.5}$$

which has in principle some analytical solution. Here, as everywhere in this thesis, we use the notation $(\cdot)' := \partial_u(\cdot)$.

3.1.3 AdS/CMT Dictionary (Supersymmetric Case)

Now the situation is slightly more non-trivial, as we wish to introduce finite values for the mass, baryon density and magnetic field. Using the AdS/CFT dictionary in [34] in analogy with the $3+1$ dimensional system, e.g. [67, 110, 50], we find the gravity dual of the baryon density

$$\rho_0 \;=\; -2\pi^2 \frac{\delta S}{\delta F_{tr}} = 2\pi^2 (\pi T)^2 \varepsilon_0 \lim_{u\to 0} A'(u) =: -2\pi^2 (\pi T)^2 \lim_{u\to 0} E(u) \tag{3.1.6}$$

and magnetic field B to be related to a non-trivial $U(1)$ background on the brane:

$$F|_{u\to 0} \;=\; -E(u) dt \wedge dr + B dx \wedge dy \;=:\; F_E + F_B. \tag{3.1.7}$$

We can also define the (asymmetric) background metric

$$G = g + F \ . \tag{3.1.8}$$

By analogy with the $3+1$ dimensional $D3-D7$ system, we can repeat the arguments in [45, 67, 68, 44], and associate a non-trivial embedding $\Psi(u)$ with a finite quark mass M_q and dual condensate C. This condensate has on the one hand an interpretation as a chemical potential for M_q and on the other hand is considered in QCD contexts considered as the order parameter of chiral symmetry breaking.

We can parametrize the S^5 as $d\Omega_5^2 = d\psi^2 + \cos^2\psi \, d\Omega_2^2 + \sin^2\psi \, d\Omega_2^2$ and put the D5 on the first S^2, such that $\sin\psi =: \Psi$ gives us a suitable scalar describing the size of the sphere. In the parametrization (3.1.7) the DBI-CS action becomes then

$$\begin{aligned} S &= 4\pi L^2 T_5 \int d\sigma^4 \left(\sqrt{-\det G} \sqrt{(1-\Psi^2)^2 + f^2} + f u^4 \partial_u z \right) \\ &= 4\pi L^2 T_5 \int d\sigma^4 \left(\sqrt{-\det G} \sqrt{1+F_E^2} \sqrt{1+F_{\tilde{B}}^2} \sqrt{(1-\Psi^2)^2 + f^2} + f u^4 \partial_u z \right), \end{aligned} \tag{3.1.9}$$

and one trivially finds the background solution

$$\begin{aligned} B &= const. \\ E(u) &= \frac{\tilde{\rho} \sqrt{1+f^2} \sqrt{1-\Psi^2(u) + u^2 h(u) \Psi'(u)^2}}{\sqrt{1-\Psi(u)^2} \sqrt{1 + \big(f^2 + (\tilde{\rho}^2 + \tilde{B}^2)(1+f^2)\big) u^4 + (1+\tilde{B}^2 u^4) \Psi(u)^2 (\Psi(u)^2 - 2)}} \\ \partial_u z &= \frac{-f \sqrt{1-\Psi^2(u) + u^2 h(u) \Psi'(u)^2}}{\sqrt{1-\Psi(u)^2} \sqrt{1 + \big(f^2 + (\tilde{\rho}^2 + \tilde{B}^2)(1+f^2)\big) u^4 + (1+\tilde{B}^2 u^4) \Psi(u)^2 (\Psi(u)^2 - 2)}} \end{aligned} \tag{3.1.10}$$

for all the physically relevant fields, except for $\Psi(u)$, because that one enters the action both directly and with one derivative. As a reminder, our notation is $h(u) = 1 - u^4$. For convenience, we defined the dimensionless parameters $\tilde{\rho} := \frac{\rho_0}{2\pi^2(\pi T)^2\varepsilon_0}$ and $\tilde{B} = \frac{B}{(\pi T)^2}$. We see that the width of the defect from the brane picture, $z_{max} := \lim_{u->1} z(u)$, decreases as we increase B and ρ_0 as they appear only in the denominator. This may appear somewhat counter-intuitive from a weakly coupled point of view, but it is what we should expect, as the system is strongly coupled, or the correlation length diverges, and hence the "contractive force" scales with the total number of particles.

The equation of motion for $\Psi(u)$ becomes

$$\frac{2(1+\tilde{B}^2u^4)(1-\Psi^2)^3 + u^2(1-u^4)\big(1-(f^2+(\tilde{\rho}^2+\tilde{B}^2)(1+f^2))u^4+(1+\tilde{B}^2u^4)\Psi^2(\Psi^2-2)\big)\Psi'^2}{u^4(1-\Psi^2)\sqrt{(1-\Psi^2)\big(1-\Psi^2+(u^2-u^6)\Psi'^2\big)\big(1+(f^2+(\tilde{\rho}^2+\tilde{B}^2)(1+f^2))u^4+(1+\tilde{B}^2u^4)\Psi^2(\Psi^2-2)\big)}}$$
$$= \partial_u\left(\Psi'\frac{1-u^4}{u^2}\sqrt{\frac{1+(f^2+(\tilde{\rho}^2+\tilde{B}^2)(1+f^2))u^4+(1+\tilde{B}^2u^4)\Psi^2(\Psi^2-2)}{(1-\Psi^2)(1-\Psi^2+(u^2-u^6)\Psi'^2)}}\right) \tag{3.1.11}$$

which has no analytical solution, except for some limiting cases. For $u \to 0$, it is easy to see that the solution becomes

$$\Psi \sim \tilde{m}\,u + \tilde{c}\,u^2\,, \tag{3.1.12}$$

where $\tilde{m}$ and $\tilde{c}$ are dimensionless free parameters that are determined by the boundary conditions. Now, we see that the argument of the T-dual case of the D3-D7 system with $3+1$ intersecting directions [45, 67, 68, 44] also applies to our case, and the quark mass M_q and condensate C are given by

$$M_q = \frac{r_0\,\tilde{m}}{2^{3/2}\pi l_s^2} = \sqrt{\lambda}\frac{T}{2^{3/2}}\tilde{m} \quad \text{and} \quad C = \sqrt{2}4\pi^2\tilde{c}\,r_0^2N_f l_s^2T_5 = \frac{1}{4\pi}\tilde{c}T^2N_fN_c\,. \tag{3.1.13}$$

This can be straightforwardly obtained from the results in [45], but also in our case we see that this relates to the length of a string spanning on the sphere from the D3 branes to the D5 branes. In appendix E, eq. (E.1.7), we do indeed verify that C is the dual chemical potential to the mass. In order to find the solution for the full geometry for a given mass however, we need consider the equation near the horizon, where (3.1.11) reduces to first order,

$$\Psi'|_{u\to1} = \frac{1}{2}\frac{(1+\tilde{B}^2)\Psi_0(1-\Psi_0^2)^2}{(1-\Psi_0^2)^2+f^2+\tilde{\rho}^2+\tilde{B}^2\big(1+(1-\Psi_0^2)^2\big)}\,, \tag{3.1.14}$$

effectively relating $\tilde{m}$ and $\tilde{c}$. The only remaining boundary condition at the horizon is then $\Psi_{u\to1} = \Psi_0$. Because this boundary condition is dictated to us by the equation of

motion, which becomes first order at this point, and hence is determined by the other boundary condition $\Psi|_{u=0} = 0$, we use $\tilde{m}$ instead as a boundary condition, but we have to find recursively Ψ_0 for a given value of $\tilde{m}$. This is because implicitly, on-shell, $\tilde{c}$ is a function of $\tilde{m}$ and starting to integrate at $u = 0$ with some random combination of $\tilde{c}$ and $\tilde{m}$ means the equations of motion cannot be on-shell as we approach the horizon.

At vanishing density ρ_0 and vanishing compact flux f, we find again that the black hole embedding which gives us free quarks limits $M_q < M_{crit}$. At M_{crit}, we have the $2+1$ analogue of the phase transition that was found for the $3+1$ system in [45, 44]. It turns out that the critical mass decreases as we turn on the magnetic field in the $2+1$ field theory. This is discussed in detail in appendix E. This phase transition disappears (at least in our case where we consider only the $U(1)$ background) as we turn on either a finite baryon density ρ_0, or as we choose the compact magnetic flux f to be non-zero. Essentially, this happens because the charge can only be supported by the blackhole embedding and the action becomes singular when $\Psi(u) = 0$ at finite flux just as in the $3+1$ dimensional case in [45].

Some of our studies of the effects of finite masses will have be done at finite ρ_0 or f, to allow for sufficiently large masses. In the limit of very large masses (i.e. $\Psi \to 1_-$ near the horizon), one can see that over $u \in]0, 1]$, the equation of motion for Ψ is also solved by $\Psi \sim 1$ – to see this in eq. (3.1.11), one needs to take $\Psi' \to 0$ first. This demonstrates how a new length scale arises for large masses, $\tilde{m} \gg 1$ as the profile splits approximately into two parts - one with $u > u_m \sim \frac{1}{\tilde{m}}$ and $\Psi \sim 1$ for some value u_m and one given approximately by the asymptotic solution (3.1.12). Around u_m, Ψ'' diverges. It would be interesting to see whether this limit has any relation to the recent discussion of non-relativistic AdS/CFT [56].

A more thorough discussion of the thermodynamics and the phase structure can be found in appendix E.

3.1.4 Non-supersymmetric $D3 - D7$ intersection

The non-supersymmetric case is very similar to the D5 case as it differs in the massless case only by the geometry and field configuration in the S^5 factor. Now we parametrize the S^5 in the bulk space as $d\Omega_5^2 = d\psi^2 + \cos^2\psi\, d\Omega_4^2$, such that we have the induced metric

$$\begin{aligned} ds^2 &= \frac{L^2}{u^2}\left(-(1-u^4)d\tilde{t}^2 + d\vec{\tilde{x}}_2^2 + \left(1 + (1-u^4)\left(z'(u)^2 + u^2\frac{\Psi'(u)^2}{1-\Psi(u)^2}\right)\right)\frac{du^2}{1-u^4}\right. \\ &\qquad \left. + u^2(1-\Psi(u)^2)d\Omega_4^2\right) \ . \end{aligned} \tag{3.1.15}$$

and we set up an instanton on the S^4 instead of the magnetic charge on the S^2. The coupling to the five-form flux comes now via the Chern-Simons term

$$\frac{(2\pi l_s^2)^2}{2} T_7 N_f \int_{D7} C^{(4)} \wedge F \wedge F \ . \tag{3.1.16}$$

This CS term however also causes the $D7$ setup to differ from the $D5$ setup in the massive case, as can be seen most easily by integrating this term by parts to give us (modulo a total derivative)

$$\frac{(2\pi l_s^2)^2}{2} T_7 N_f \int_{D7} F^{(5)} \wedge A \wedge F \ \rightarrow \ 8 T_7 N_f \frac{\pi^5 l_s^4}{L^4} \int_0^1 du \frac{\Psi'}{\sqrt{1-\Psi^2}} \int_{\mathbb{R}^{(2,1)}} A \wedge F \ . \tag{3.1.17}$$

The term on the right hand side with the factor Ψ' arises from the fact that the deformed embedding of the S^4 inside the S^5 causes the dual F^5 on the sphere to pull back to the brane worldvolume. Integrating out the S^4 of the worldvolume gives us then the right hand side, which is just a Chern-Simons term with radius-dependent coupling. This was used in [69] to obtain a Hall effect. This term will obviously modify the two-point functions, and will be interesting to consider in further work, but there are some problems with the massive D7 case that we will outline below, so we will here only consider the massless $D7$ defect.

The instanton solution was found in [75, 81] and outlined in section 2.1.2 and yields

$$\frac{1}{8\pi^2} \oint_{S^4} TrF \wedge F \ =: \ q_7 \ \in \ \mathbb{Z} \tag{3.1.18}$$

and the S^4 factor

$$\oint_{S^4} d^4\Omega \ = \ \frac{8\pi^2}{3} \left(N_{\rm f} L^4 (1-\Psi^2) + 6\pi^2 \ell_{\rm s}^4 |q_7| \right) \ , \tag{3.1.19}$$

such that the Ansatz (3.1.7) puts the action into the form

$$S \ = \ \frac{8\pi^2}{3} N_f \, L^4 T_7 \int d\sigma^4 \left(\sqrt{\det G} ((1-\Psi^2) + |Q|) + Q u^4 \partial_u z \right) \tag{3.1.20}$$

where we remind ourselves of the definition $Q = 6\pi^2 \frac{\ell_{\rm s}^4}{L^4} \frac{q_7}{N_{\rm f}} = \frac{6\pi^2}{\lambda} \frac{q_7}{N_{\rm f}}$. In the general case ($\Psi \neq 0$), this action gives different solutions than (3.1.10), however in the case $\Psi = 0$ the solutions are given precisely by (3.1.10), provided we replace the flux parameter with $f_7 \equiv \frac{Q}{\sqrt{1+2|Q|}}$.

In section 2.1.2 it was found that the mass of the tachyonic mode of the S^4 radius of the D7 probe brane satisfies the BF bound only for $f^2 > 49/32$, and a quick calculation shows that this also happens to apply in this background – independent of $\tilde{\rho}$ and $\tilde{B}$. This, we will see, is reflected in the asymptotic behavior of $\Psi(u)$. We will not bother the reader with the lengthy form of the equations of motion for Ψ, however, we note that the asymptotic solution takes the form

$$\Psi(u) \sim u^{\alpha_\pm} \quad , \quad \alpha_\pm = \frac{3}{2} \pm \sqrt{\frac{4Q^2 - 7 - 12Q}{2 + 4Q}} \tag{3.1.21}$$

which implies that above the BF bound, the solution will be a power law, and below the BF bound it will be oscillatory – indicating the instability. Above the BF bound, we could, in principle, identify those two modes with a "mass-like" operator (and a "condensate" operator) of non-integer conformal dimension, motivated by the fact that this is related to the separation of the D3 and D7 branes in the sphere. Possibly one could interpret this behavior with a "running" mass. However, there is a very significant problem that may be more worrying than the instability at vanishing mass: A solution of N_7 D7 branes causes an asymptotic deficit angle of $\frac{N_f}{12}$ from backreaction (see e.g. [26]). At the necessary finite f_7, and hence q_7 of order λ, we need at stack of D7 branes as determined by the limit $\frac{N_f(N_f^2-1)}{6} \geq q_7$ for spherically symmetric solution from [81]. In order to still have the same kind of field theory with the same symmetries, we require $N_f \gg 12$, which implies that the solution cannot connect to an asymptotic space-time. Note that this was exactly the S^4 factor which broke supersymmetry, and this factor would be highly modified for solutions with q_7 below this bound. Below the BF bound the oscillatory asymptotic solution is non-physical in our setup and furthermore the corresponding operator would have complex conformal dimension. It seems that there are some non-standard ways to interpret the $f_7 = 0$ case in the context of the quantum Hall effect [66], but we will not pursue the $\Psi \neq 0$ case in the rest of this thesis. It is a noteworthy curiosity, that in the absence of the pullback of the CS term to the flat directions, the resulting spectral functions are identical to the D5 case under an appropriate identification of the mass-like operators.

3.2 Computing the Conductivity

As in chapter 2, we will compute the conductivity using linear response theory, i.e. applying the Kubo formula

$$\pi^{-1} T \tilde{\sigma}_{ij} = \sigma_{ij} = \frac{i}{\omega} C_{ij} \quad \text{or for convenience} \quad \tilde{\sigma}_{ij} := \pi T \sigma_{ij} = \frac{i}{\tilde{\omega}} C_{ij} \quad , \tag{3.2.22}$$

that gives the conductivity for currents resulting from small perturbations in terms of the retarded Green's function, which is given in terms of the correlator as

$$C_{ij}(x-y) = -i\,\theta(x^0-y^0)\,\langle\,[J_i(x),J_j(y)]\,\rangle\ . \tag{3.2.23}$$

We define for later convenience $\tilde{\sigma} = \frac{\sigma}{\pi T}$. Since the baryon number current J_i is dual to the gauge field of the $U(1)$ subgroup of the $U(N_f)$, A_i, the correlator is given by the variation of the on-shell action

$$C_{ij} = \frac{\delta^2 S}{\delta A^\star_{i,0}\delta A_{j,0}}, \tag{3.2.24}$$

where A_0 is the boundary value of the gauge field at the asymptotic boundary $u=0$. The action for the gauge field becomes to second order

$$S = -\frac{1}{4g_4^2}\int d^4x \frac{\sqrt{(1-\Psi^2)^2+f^2}}{\sqrt{1+f^2}}\sqrt{-\det\,G}\left(F_{\alpha\beta}G^{\alpha\gamma}F_{\gamma\delta}G^{\delta\alpha} - \frac{1}{2}F_{\alpha\beta}G^{\alpha\beta}F_{\gamma\delta}G^{\gamma\delta}\right)\ , \tag{3.2.25}$$

where G is the asymmetric combined metric (3.1.8), and g_4^2 is defined as

$$\frac{1}{g_4^2} \;=\; 4\pi(2\pi l_s^2)^2L^2\sqrt{1+f^2}T_5 \;=\; \sqrt{1+f^2}\frac{2}{\pi}\frac{N_c}{\sqrt{2\lambda}}\ . \tag{3.2.26}$$

In some sense, there is now a radius dependent coupling $\frac{\sqrt{(1-\Psi^2)^2+f^2}}{\sqrt{1+f^2}}$, that always goes to unity asymptotically or obviously everywhere in the massless case. Surprisingly, the gauge field background dies off sufficiently fast asymptotically, such that as $u\to 0$, the action just becomes the Maxwell action with coupling g_4 and in a suitable gauge $A_u = 0$ the correlator is still given by the asymptotic mode function

$$C^{ij} = \frac{\varepsilon_0}{\sqrt{1+f^2}}\,\frac{\delta\left(\partial_u A_j\right)}{\delta A_i}\bigg|_{u\to 0}\ , \tag{3.2.27}$$

where ε_0 is defined as $\varepsilon_0 = \frac{\pi T}{g_4^2}$.

3.2.1 Electromagnetic duality

In this background, we see that the effective action for the gauge field is not invariant under electromagnetic duality $F\to\star F$. Hence, the relation $C_{xx} = -\frac{\varepsilon_0^2\omega^2}{C_{yy}}$ that was found in [49] does not apply in this case. Since the DBI action at constant coupling, i.e. in

the massless case, however still obeys this duality, one would expect that it survives in some form under the exchange of the magnetic and electric charges on the probe brane, i.e. under the exchange of the density and magnetic field in the field theory side. To quantify this further, let us look at the transformations under $F \to \star F$ of the Fourier-transformed gauge field in the gauge $A_u = 0$ that led to (3.2.27), obviously at $M_q = 0$. The relevant components are at asymptotic infinity:

$$(\star F)_{tx}|_{u=0} \;=\; -\sqrt{1+f^2}F_{uy}|_{u=0} \quad \text{and} \quad (\star F)_{ty}|_{u=0} \;=\; \sqrt{1+f^2}F_{ux}|_{u=0}\;, \tag{3.2.28}$$

such that the variation w.r.t. the gauge field becomes in terms of the transformed gauge field, denoted in abusive notation as $\star A$:

$$\left.\frac{\partial}{\partial A_x}\right|_{u=0} = -\frac{\sqrt{1+f^2}}{i\tilde{\omega}}\left(\frac{\partial A'_y}{\partial A_x}\frac{\partial}{\partial(\star A)_x} - \frac{\partial A'_x}{\partial A_x}\frac{\partial}{\partial(\star A)_y}\right)_{u=0} = \frac{\partial}{\varepsilon_0}\left(\tilde{\sigma}_{xy}\frac{\partial}{\partial(\star A)_x} - \tilde{\sigma}_{xx}\frac{1}{\partial(\star A)_y}\right)_{u=0} \tag{3.2.29}$$

$$\left.\frac{\partial}{\partial A_y}\right|_{u=0} = -\frac{\sqrt{1+f^2}}{i\tilde{\omega}}\left(\frac{\partial A'_y}{\partial A_y}\frac{\partial}{\partial(\star A)_x} - \frac{\partial A'_x}{\partial A_y}\frac{\partial}{\partial(\star A)_y}\right)_{u=0} = \frac{\partial}{\varepsilon_0}\left(\tilde{\sigma}_{yy}\frac{1}{\partial(\star A)_x} + \tilde{\sigma}_{xy}\frac{\partial}{\partial(\star A)_y}\right)_{u=0} \tag{3.2.30}$$

Rewriting the conductivity obtained from (3.2.24) then in terms of the transformed fields gives us

$$\tilde{\sigma}_{xx} \;=\; \frac{1}{\varepsilon_0^2}\left(\tilde{\sigma}_{xy}\tilde{\sigma}_{xy}[\star\tilde{\sigma}]_{xx} + \tilde{\sigma}_{xx}\tilde{\sigma}_{xx}[\star\tilde{\sigma}]_{yy}\right) \tag{3.2.31}$$

$$\tilde{\sigma}_{yy} \;=\; \frac{1}{\varepsilon_0^2}\left(\tilde{\sigma}_{yy}\tilde{\sigma}_{yy}[\star\tilde{\sigma}]_{xx} + \tilde{\sigma}_{xy}\tilde{\sigma}_{xy}[\star\tilde{\sigma}]_{yy}\right) \tag{3.2.32}$$

$$\tilde{\sigma}_{xy} \;=\; \frac{1}{\varepsilon_0^2}\left(\tilde{\sigma}_{xy}\tilde{\sigma}_{yy}[\star\tilde{\sigma}]_{xx} + \tilde{\sigma}_{xx}\tilde{\sigma}_{xy}[\star\tilde{\sigma}]_{yy} + (\tilde{\sigma}_{xy}\tilde{\sigma}_{xy} - \tilde{\sigma}_{xx}\tilde{\sigma}_{yy})[\star\tilde{\sigma}]_{xy}\right) \tag{3.2.33}$$

where we used (3.2.27) and $S[F] = S[\star F]$, and defined $[\star\sigma]_{\mu\nu} = \frac{\delta^2 S[\star F]}{\delta[\star A]_{i,0}\delta[\star A]_{j,0}}$. Since $F \leftrightarrow \star F$ exchanges the electric and magnetic charges on the probe brane defined at infinity – i.e. exchanges density and magnetic field in the field theory side – $\star\sigma$ is just the conductivity and the exchange of $\tilde{\rho}$ and $\tilde{B}$. Finally, we can solve for $\star\sigma$ and obtain

$$\sigma[\tilde{B},\tilde{\rho}]_{ab} \;=\; \left(\star\sigma[\tilde{\rho},\tilde{B}]\right)_{ab} \;=\; \frac{1}{\varepsilon_0^2}\left(\left(\tilde{\sigma}[\tilde{\rho},\tilde{B}]\right)^{-1}\right)_{cd}\varepsilon_a^c\varepsilon_b^d \tag{3.2.34}$$

where $a, b \in \{x, y\}$.

This result is remarkable, since it relates the transport properties under the exchange of two quantities that are completely distinct in nature from the condensed matter point

of view. Furthermore, it applies to a whole class of strongly coupled $2+1$ dimensional systems, whose gravity dual obeys the electromagnetic duality. Hence, such a relation is a generic prediction from AdS/CFT for a quantum critical 2-dimensional system. For theories not obeying (3.2.27), there may be potentially additional terms in (3.2.34). It seems that this is an implication of the "particle-vortex duality" found in [100, 99].

This duality holds always in the massless case to numeric accuracy. Hence it is not possible to visually "compare" the result in a plot.

3.2.2 Explicit Computations

To proceed further let us start by writing out the equations of motion explicitly:

$$\begin{aligned} A_y : 0 &= (\sqrt{-G}G^{yy}G^{uu}A'_y)' \; + \; \sqrt{-G}G^{yy}(G^{xx}\partial_x^2 + G^{tt}\partial_t^2)A_y \\ &\quad + \; \left(\sqrt{-G}G^{tu}G^{xy}\right)'(\partial_x A_t - \partial_t A_x) \end{aligned} \tag{3.2.35}$$

$$A_u : 0 = G^{tt}\partial_t A'_t \; + \; G^{xx}\partial_x A'_x \tag{3.2.36}$$

$$A_t : 0 = (\sqrt{-G}G^{tt}G^{uu}A'_t)' + \sqrt{-G}G^{tt}G^{xx}\left(\partial_x^2 A_t - \partial_t\partial_x A_x\right) - \left(\sqrt{-G}G^{tu}G^{xy}\right)'\partial_x A_y \tag{3.2.37}$$

$$A_x : 0 = (\sqrt{-G}G^{xx}G^{uu}A'_x)' + \sqrt{-G}G^{tt}G^{xx}\left(\partial_t^2 A_x - \partial_t\partial_x A_t\right) + \left(\sqrt{-G}G^{tu}G^{xy}\right)'\partial_t A_y \tag{3.2.38}$$

For convenience of the reader, we stick here to the concise notation in terms of G and summarize the exact form of the components G in appendix D. Also, in this expression, and for the rest of this thesis, we absorbed the radius-dependent coupling into the determinant of the metric, in somewhat abusive notation:

$$\frac{\sqrt{(1-\Psi^2)^2+f^2}}{\sqrt{1+f^2}}\sqrt{-\det G} \; \to \; \sqrt{-G} \; . \tag{3.2.39}$$

Finally, we also remind ourselves that $G^{yy} = G^{xx}$, so while keeping them distinctively for didactic reasons in most places, in some places they will be interchanged to simplify expressions.

As in section 2.2.1.2, it can be easily verified by using the equation for A_u, that the equations for A_t and A_x are degenerate. Hence, we will again as in 2.2.1.2 eliminate A_t from the equation for A_x and produce an equation for A'_x, by multiplying (3.2.37) with

$\sqrt{-G}G^{yy}G^{uu}$ and differentiating with respect to u. This gives us:

$$\begin{aligned} 0 &= \left(\sqrt{-G}G^{yy}G^{uu}A_y'\right)' + \left(\sqrt{-G}G^{yy}G^{xx}\partial_x^2 + \sqrt{-G}G^{yy}G^{tt}\partial_t^2\right)A_y \\ &\quad + \frac{\left(\left(\sqrt{-G}G^{tu}G^{xy}\right)'\right)^2}{\sqrt{-G}G^{tt}G^{xx}}A_y + \frac{\left(\sqrt{-G}G^{tu}G^{xy}\right)'}{\sqrt{-G}G^{tt}G^{xx}}\mathcal{A}_x' \end{aligned} \tag{3.2.40}$$

$$\begin{aligned} 0 &= \left(\sqrt{-G}G^{yy}G^{uu}\mathcal{A}_x'\right)' + \left(\sqrt{-G}G^{yy}G^{xx}\partial_x^2 + \sqrt{-G}G^{yy}G^{tt}\partial_t^2\right)\mathcal{A}_x \\ &\quad - \frac{\left(-G\,G^{tt}G^{uu}G^{xx}G^{yy}\right)'}{\sqrt{-G}G^{tt}G^{xx}}\mathcal{A}_x' + (-G)\,G^{tt}G^{uu}G^{xx}G^{yy}\left(\frac{\left(\sqrt{-G}G^{tu}G^{xy}\right)'}{\sqrt{-G}G^{tt}G^{xx}}A_y\right)', \end{aligned} \tag{3.2.41}$$

where $\mathcal{A}_x = \frac{\sqrt{-G}G^{uu}G^{xx}A_x'}{i\tilde{\omega}}$. These equations separate at vanishing density or vanishing magnetic field – as they should, because we do not expect a Hall effect in this case.

Using (3.2.38), we can recover $A_x|_{u=0} = -i\frac{\mathcal{A}'_x}{\omega(1+f^2)}$, which will allow us to compute the conductivity tensor. Near the horizon, the solutions become approximately

$$A_y = (1-u)^{i\omega/4}\left(A_y^{(0)} + A_y^{(1)}(1-u)\right)\ ,\ \ \mathcal{A}_x = (1-u)^{i\omega/4}\left(\mathcal{A}_x^{(0)} + \mathcal{A}_x^{(1)}(1-u)\right)\ , \tag{3.2.42}$$

where $A_y^{(0)}$ and $\mathrm{A}_x^{(0)}$ are arbitrary constants and $A_y^{(1)}$ and $\mathrm{A}_x^{(1)}$ are determined straightforwardly in terms of ρ_0, B, Ψ_0, $A_y^{(0)}$ and $\mathcal{A}_x^{(0)}$, but somewhat lengthy and without physical insight and hence omitted here. To compute the conductivity, we could then fix the boundary conditions for $A_y \in \{1, 0\}$ and $\mathcal{A}_x \in \{1, 0\}$ at $u \to 0$ and enforce the leading behavior of (3.2.42) as a boundary condition at $u \to 1$ as done in section 2.2.1.1. This is however a numerically non-trivial boundary value problem. Hence, it is more reliable and less time-intensive to simply enforce (3.2.42) for two independent choices of $\{A_y^{(0)}, \mathrm{A}_x^{(0)}\}$, labeled $\mathfrak{a}$ and $\mathfrak{b}$, to obtain $\{A_y(\mathfrak{a}), A_y'(\mathfrak{a}), \mathrm{A}_x(\mathfrak{a}), \mathrm{A}_x'(\mathfrak{a})\}$ and $\{A_y(\mathfrak{b}), A_y'(\mathfrak{b}), \mathrm{A}_x(\mathfrak{b}), \mathrm{A}_x'(\mathfrak{b})\}$ at $u \to 1$ and then use the linearity of the problem to compute the variation in (3.2.27) exactly. Furthermore, this strategy is very suitable from a computational point of view, as it allows us to naturally the parallelize solving the equations of motion, i.e. the most time consuming step, on a dual-core processor.

Putting everything together, we finally obtain:

$$\tilde{\sigma} = \varepsilon_0 \left[\begin{array}{cc} -i\sqrt{1+f^2}\tilde{\omega}\frac{\mathcal{A}_x(\mathfrak{a})A_y(\mathfrak{b})-\mathcal{A}_x(\mathfrak{b})A_y(\mathfrak{a})}{\mathcal{A}_x'(\mathfrak{a})A_y(\mathfrak{b})-\mathcal{A}_x'(\mathfrak{b})A_y(\mathfrak{a})} & -\frac{1}{\sqrt{1+f^2}}\frac{\mathcal{A}_x(\mathfrak{b})\mathcal{A}_x'(\mathfrak{a})-\mathcal{A}_x(\mathfrak{a})\mathcal{A}_x'(\mathfrak{b})}{\mathcal{A}_x'(\mathfrak{a})A_y(\mathfrak{b})-\mathcal{A}_x'(\mathfrak{b})A_y(\mathfrak{a})} \\ -\sqrt{1+f^2}\frac{A_y(\mathfrak{b})A_y'(\mathfrak{a})-A_y(\mathfrak{a})A_y'(\mathfrak{b})}{\mathcal{A}_x'(\mathfrak{a})A_y(\mathfrak{b})-\mathcal{A}_x'(\mathfrak{b})A_y(\mathfrak{a})} & \frac{i}{\sqrt{1+f^2}\tilde{\omega}}\frac{\mathcal{A}_x'(\mathfrak{a})A_y'(\mathfrak{b})-\mathcal{A}_x'(\mathfrak{b})A_y'(\mathfrak{a})}{\mathcal{A}_x'(\mathfrak{a})A_y(\mathfrak{b})-\mathcal{A}_x'(\mathfrak{b})A_y(\mathfrak{a})} \end{array}\right]_{u\to 0}.$$

Formally, this is asymmetric, such that the (anti)symmetry of the numerical result is a check for the consistency and the accuracy of the numerical solutions for $\mathcal{A}_x$ and A_y. We

also note that in the limit of $\{\rho_0, B, \Psi\} = 0$, we just recover the equations that were found in section 2.2.1. In principle, the duality from 3.2.1 suggests that there may exist a field redefinition for A_y and $\mathcal{A}_x$, such that the asymptotic solutions for the resulting fields are exchanged under $\tilde{\rho} \leftrightarrow \tilde{B}$. However, there is no guarantee that this redefinition can be written analytically.

3.3 Weak-Coupling Condensed Matter Physics

Even though we are interested in the strong coupling regime which one expects to be quite different from the free electron gas picture, some intuition and generic properties can be learned from this very straightforward limit and it can serve as a phenomenological description. Hence, we remind the reader of the very basic model, which can be found in standard textbooks [87].

3.3.1 Metals

In the Drude model, we assume a gas of non-interacting charge carriers with finite (effective) mass m_{eff} and charge $\mathfrak{e}$, which we will write out explicitly. Eventually, it will turn out, however, that using the coefficients that do not involve m_{eff} is a suitable parametrization also in the relativistic case. To obtain the conductivity, one then considers a small electromagnetic background field, to which the charge carriers are coupled classically via the Lorentz force $m_{eff}(\partial_t \vec{p} - \tau^{-1}\vec{p}) = \mathfrak{e}\vec{E} + \mathfrak{e}\vec{v} \times \vec{B}$. As the charge carriers are massive, they have a finite net velocity $\vec{v}$, which is assumed to be neutralized on the time scale of a relaxation time τ. Classically, one has then a mean velocity $\vec{v} = \frac{\mathfrak{e}\tau}{m_{eff}}\vec{E} =: \mu\vec{E}$, where we defined the charge carrier mobility μ. The charge carrier mobility is related to the Diffusion constant by the Einstein relation

$$D \;=\; \frac{\mu T}{\mathfrak{e}} \;. \tag{3.3.43}$$

Further, for our massive case, the magnetic field can be rewritten in terms of the cyclotron frequency as $\omega_c = \frac{B\,\mathfrak{e}}{m_{eff}} = \mu B/\tau$. Now, let us consider two species of charge carriers with equal mass and relaxation time, but opposite charge $\pm\mathfrak{e}$, such that we have a total density of charge carriers $\mathfrak{n} = \mathfrak{n}_+ + \mathfrak{n}_-$ and a net charge density $\Delta\mathfrak{n} = \mathfrak{n}_+ - \mathfrak{n}_-$. This is relevant in our case, since even at vanishing net baryon number density, $\rho_0 = 0$, at finite temperature $T \gtrsim M_q$ we will always have a finite total baryon density.

To obtain the conductivity, one then assumes an oscillatory electric field $\vec{E} = \vec{E}_0 e^{-i\omega t}$ and current $\vec{j} = \vec{j}_0 e^{-i\omega t}$, but constant magnetic field $\vec{B}$ and obtains the diagonal conductivity

$$\sigma^{\parallel} = \frac{\mathfrak{e}\mathfrak{n}\mu(1-i\omega\tau)}{(1-i\omega\tau)^2+\omega_c^2\tau^2} = \frac{\mathfrak{e}\mathfrak{n}\mu}{1+\omega_c^2\tau^2}\left(1+i\omega\tau\frac{1-\omega_c^2\tau^2}{1+\omega_c^2\tau^2}-\omega^2\tau^2\frac{1-3\omega_c^2\tau^2}{(1+\omega_c^2\tau^2)^2}\right)+\mathcal{O}(\omega\tau)^3 \ . \tag{3.3.44}$$

Taking into account the positive and negative charges, the Hall conductivity becomes

$$\sigma^{\perp} = \frac{\mathfrak{e}\Delta\mathfrak{n}\mu\omega_c\tau}{(1-i\omega\tau)^2+\omega_c^2\tau^2} = \frac{\mathfrak{e}\Delta\mathfrak{n}\mu\omega_c\tau}{1+\omega_c^2\tau^2}\left(1+\frac{2i\omega\tau}{1+\omega_c^2\tau^2}-\omega^2\tau^2\frac{3-\omega_c^2\tau^2}{(1+\omega_c^2\tau^2)^2}\right)+\mathcal{O}(\omega\tau)^3 \ . \tag{3.3.45}$$

The dissipative part of the conductivity is then

$$\text{Re}\ \sigma^{\parallel} = \mathfrak{e}\mathfrak{n}\mu\frac{1+\omega^2\tau^2+\omega_c^2\tau^2}{(1+\omega_c^2\tau^2-\omega^2\tau^2)^2+4\omega_c^2\tau^2} \quad \text{and} \tag{3.3.46}$$

$$\text{Re}\ \sigma^{\perp} = \mathfrak{e}\Delta\mathfrak{n}\mu\omega_c\tau\frac{1-\omega^2\tau^2+\omega_c^2\tau^2}{(1+\omega_c^2\tau^2-\omega^2\tau^2)^2+4\omega_c^2\tau^2} \ . \tag{3.3.47}$$

The DC conductivity at $B = 0$ is commonly referred to as the Drude conductivity, and at small frequencies it is also called the Drude peak, due to the small value of τ in metals at room temperature. Similarly, the fact that the DC conductivity is suppressed at finite magnetic fields is referred to as the magnetoresistance effect.

It is also interesting to notice that at the magnetic resonance around ω_c, the Hall conductivity changes sign, and this turns into a pole at large τ, i.e. in practice at very small temperatures or in very "clean" semiconductors.

We can also observe a few generic properties of the frequency dependence. For example, at $B = 0$, $\frac{\partial_\omega^2\sigma^{\parallel}}{\sigma^{\parallel}} = \frac{2}{\tau^2}$ and, provided the relaxation time is independent of the magnetic field, the behavior at large frequencies is $\frac{\partial_\omega^2\sigma^{\parallel}}{\sigma^{\parallel}} = -\frac{6}{\omega_c^2\tau^4}$. An interesting relation is also $\frac{\partial_\omega^2\sigma^{\parallel}}{\sigma^{\parallel}}\frac{\sigma^{\perp}}{\partial_\omega^2\sigma^{\perp}} = \frac{1}{3}$ at vanishing magnetic field and 3 at large magnetic fields. Also, the magnetic field at which $\frac{\partial_\omega^2\sigma}{\sigma}$ changes sign is $\tau^2\omega_c^2 = \frac{1}{3}$ for $\sigma^{\parallel}$ and 3 for $\sigma^{\perp}$. The fact that the quadratic term changes sign implies that the Drude peak moves away from the real axis and becomes a magnetic resonance.

We already see a limitation of the free electron gas picture, because – as we will see in section 3.3.3 – the quantum mechanical treatment implies that the first magnetic resonance is at $\frac{1}{2}\omega_c$ and taking into account a finite coupling implies that there will be plasma density resonances.

3.3.2 Semiconductors

Semiconductors are somewhat less generic than the Drude model of conductivity, i.e. we must assume that we are dealing with fermions, but the discussion obviously carries over to any system of charge carriers with an excitation gap. In a semiconductor, we assume that the valence and conduction bands are separated, $E_v < E_c$, where the valence band is, as the name says, filled such that the chemical potential lies between the bands $E_v < \mu < E_c$.

At small temperatures, the dissipative conductivity will be dominated by $\mathfrak{n}$, such that we are most interested in obtaining the density of conduction "electrons" $\mathfrak{n}_c$ and valence "holes" $\mathfrak{n}_v$ assuming some density of states g_c and g_v:

$$\mathfrak{n}_c \;=\; \int_{E_c}^{\infty} dE\, g_c(E) \frac{1}{e^{(E-\mu)/T}+1} \tag{3.3.48}$$

and

$$\mathfrak{n}_v \;=\; \int_{-\infty}^{E_v} dE\, g_v(E) \left(1 - \frac{1}{e^{(E-\mu)/T}+1}\right) \;=\; \int_{-\infty}^{E_v} dE\, g_v(E) \frac{1}{e^{(\mu-E)/T}+1} \;. \tag{3.3.49}$$

Assuming that we are dealing with low temperatures $E_c - \mu \gg T$ and $\mu - E_v \gg T$, we can re-write this as

$$\mathfrak{n}_c(T) \;=\; N_c(T) e^{-(E_c-\mu)/T} \;, \quad \mathfrak{n}_v(T) \;=\; N_v(T) e^{-(\mu-E_v)/T} \tag{3.3.50}$$

where we defined the edge densities of states as

$$N_c(T) \;:=\; \int_{E_c}^{\infty} dE\, g_c(E) e^{-(E-E_c)/T} \;, \quad N_v(T) \;:=\; \int_{\infty}^{E_v} dE\, g_v(E) e^{-(E_v-E)/T} \;. \tag{3.3.51}$$

Using those definitions, we can combine the equations (3.3.50) to write down the "law of mass action"

$$\mathfrak{n}_c \mathfrak{n}_v \;=\; N_c N_v e^{-(E_c-E_v)/T} \;=\; \mathfrak{n}_i(T)^2 \tag{3.3.52}$$

which determines the charge carrier density of an intrinsic (undoped) semiconductor, $\mathfrak{n}_i = \mathfrak{n}_v = \mathfrak{n}_c$. This small charge carrier density implies (together with the purity of the crystal) that τ may diverge at small temperatures, as it is usually (in a metal or metallic phase with high charge carrier density) dominated by the charge carriers and their thermal motion (independent of the purity). Hence semiconductors may show, for example, a finite Hall conductivity even if the material is effectively an insulator.

The chemical potential can then be obtained from the edge densities of state

$$\mu \;=\; \frac{E_v + E_c}{2} \;+\; \frac{1}{2} T \ln \frac{N_v}{N_c} \;. \tag{3.3.53}$$

One can see that in practice in an intrinsic semiconductor at $E_c - E_v \gg T$, the edge density of states has only a very small influence on the chemical potential, and hence on the conduction threshold and the suppression of the conductivity.

3.3.3 Resonances

In the "optical" regime at larger frequencies, we are interested in quasiparticle resonances, in particular in Landau levels and plasmons. In the case of massive charged particles, the derivation of Landau levels is straightforward. Assuming coordinates $\{t, x, y, z\}$ with the magnetic field in the z direction, the gauge potential can be written as $A = B\, x\, dy$. Substituting this into the Schrödinger equation gives rise to a quantum harmonic oscillator with a frequency $\omega_c = \frac{\mathfrak{e}B}{m}$, with the solution

$$E_n \;=\; E^{(z)}_{kin.} \;+\; \omega_c (n - \frac{1}{2}) \;, \quad n \in \mathbb{Z}^+ \;. \tag{3.3.54}$$

Obviously, our charge carries are constrained to the $z = 0$ plane, so $E^{(z)}_{kin.} = 0$. Using the same naive strategy for a scalar in the Klein-Gordon equation, we find that

$$E_n^2 \;=\; p_z^2 \;+\; m^2 \;+\; \omega_M^2 (2n - 1) \;, \quad \omega_M^2 \;=\; \mathfrak{e}B \;, \tag{3.3.55}$$

putting the Landau levels in the massless case at $E_n = \pm \omega_M \sqrt{2n - 1}$. In either case, one can apply a simple argument by assuming a finite sample size to derive the density of states (per unit area) of

$$\frac{N_{Lan.}}{A} \;=\; \mathfrak{e}\, B \;. \tag{3.3.56}$$

In a similar fashion, Landau levels can also be obtained from the Dirac equation (see [89] and references therein): For massless chiral fermions e.g in graphene, the result is [89]

$$E_n \;=\; \pm \omega_M |v_F| \sqrt{|n|} \;, \quad n \in \mathbb{Z} \tag{3.3.57}$$

where v_F is the Fermi speed ($v_f = 1$ for a "real" relativistic system) and for a system of chiral fermions with finite effective mass, as in multi-layered graphene, [89]

$$E_n \;=\; \pm \omega_c \sqrt{|n|(|n| + 1)} \;, \quad n \in \mathbb{Z} \;. \tag{3.3.58}$$

The zero-energy, field-independent Landau level is unique to chiral fermions, which makes them very easy to identify [89].

The other quasi-particles that we are interested in are plasmons. These are collective excitations resulting from density perturbations of the (electron) gas. They can be derived in several ways. Classically it can be derived simply from the continuity equation $\nabla\cdot\vec{j} = \partial_t\rho$ and from Gauss' law $\nabla\cdot\vec{E} = 4\pi\rho$. Using $\sigma^{\parallel}\vec{E} = \vec{j}$, we can arrive with an equation for ω, $4\pi\mathfrak{n}\mu\tau^{-1} = \omega(\omega + i\tau^{-1})$. Another classical derivation is to assume a neutral gas of positive and negative charges in which the charges are displaced in, say the x direction, leaving two strips of density $\pm\Delta\mathfrak{n}$ with a width d that obeys the classical equation of motion $\partial_t^2 d = -\frac{4\pi\mathfrak{e}^2|\Delta\mathfrak{n}|}{m}$. Finally, a proper derivation is based on computing the Green's function in a gas of weakly interacting fermions (of equal charge in magnitude and sign) with the Coulomb potential. A very instructive derivation can be found in [88] and yields

$$\omega_p \;=\; \frac{8\pi}{3}\frac{k_F^3}{m} \;=\; \frac{4\pi\mathfrak{e}^2\mathfrak{n}}{m}\;. \tag{3.3.59}$$

where k_F is the momentum corresponding to the Fermi energy. The Green's function is at small momenta $|q| \ll |\omega|$

$$D \;=\; \frac{4\pi}{q^2}\frac{1}{1-\frac{\omega_p^2}{(\omega+i\tau^{-1})^2}}\;. \tag{3.3.60}$$

The derivation follows with only small changes also in the massless case, where we find $\omega_p = k_F^2\, 8\pi/3$. Plasmons are usually (i.e. in weakly coupled systems) observed through optical scattering, where one can observe spectra from multiple plasmon excitations. Studying plasmons and surface plasmons in various materials an using them for photonic devices seems to be a very active field of research.

3.4 Analytic results

3.4.1 Isotropic perturbations with small frequencies

3.4.1.1 DC Limit

One limit of obvious interest is the isotropic DC limit (i.e. $\tilde{\omega}, \tilde{q} \ll \{1, f^{-1}, b^{-1}, \tilde{\rho}^{-1}\}$). To analyze this case, we define a new radial coordinate s, $\frac{\partial s}{\partial u} = \left(\sqrt{-G}G^{yy}G^{uu}\right)^{-1}$ and study

the original equations of motion. Now, they just read

$$\begin{aligned}
A_y: \quad 0 = \;& \partial_s^2 A_y \;+\; \sqrt{-G}G^{yy}G^{uu}(\sqrt{-G}G^{yy}G^{xx}\partial_x^2 + \sqrt{-G}G^{yy}G^{tt}\partial_t^2)A_y \\
& + \;\sqrt{-G}G^{yy}G^{uu}\left(\sqrt{-G}G^{tu}G^{xy}\right)'(\partial_x A_t - \partial_t A_x) && (3.4.61)\\
A_u: \quad 0 = \;& G^{tt}\partial_t\partial_s A_t \;+\; G^x\partial_x\partial_s A_x && (3.4.62)\\
A_t: \quad 0 = \;& \frac{G^{tt}}{G^{yy}}\partial_s^2 A_t \;+\sqrt{-G}G^{yy}G^{uu}\left(\frac{G^{tt}}{G^{yy}}\right)'\partial_s A_t \;+\; (-G)G^{yy}G^{uu}G^{tt}G^{xx}\left(\partial_x^2 A_t - \partial_t\partial_x A_x\right) \\
& - \;\sqrt{-G}G^{yy}G^{uu}\left(\sqrt{-G}G^{tu}G^{xy}\right)'\partial_x A_y && (3.4.63)\\
A_x: \quad 0 = \;& \partial_s^2 A_x \;+\; (-G)G^{yy}G^{uu}G^{tt}G^{xx}\left(\partial_t^2 A_x - \partial_t\partial_x A_t\right) \\
& + \;\sqrt{-G}G^{yy}G^{uu}\left(\sqrt{-G}G^{tu}G^{xy}\right)'\partial_t A_y\;. && (3.4.64)
\end{aligned}$$

First, we consider the equations in the limit $u \to 1$. In this limit, we have $\frac{\partial s}{\partial u} = \frac{1+\tilde{B}^2+F^2}{\sqrt{(1+f^2)\tilde{B}^2\left(f^2+(1-\Psi_0^2)^2\right)+(1+f^2)^2\left(f^2+\tilde{\rho}^2+(1-\Psi_0^2)^2\right)}}\frac{1}{(1-u^4)} + \mathcal{O}(1) =: \frac{4c_s}{(1-u^4)} + \mathcal{O}(1)$, such that $s \sim -c_s\ln(1-u^4)$ or $(1-u^4) \sim e^{-\frac{s}{c_s}}$. Note that in this coordinate, the horizon is located at $s \to \infty$ and asymptotic infinity is at $s = 0$. Now, the equations of motions reduce to

$$\begin{aligned}
0 \;&=\; \partial_s^2 A_{y,x} + (1+f^2)\frac{\tilde{B}^2\left(f^2+(1-\Psi_0^2)^2\right)+(1+f^2)(\tilde{\rho}^2+f^2+(1-\Psi_0^2)^2)}{(1+\tilde{B}^2+f^2)^2}\partial_t^2 A_{y,x} && (3.4.65)\\
0 \;&=\; \partial_s A_t \;\;,\quad 0 \;=\; \partial_s^2 A_t\;, && (3.4.66)
\end{aligned}$$

up to order $e^{-\frac{s}{c_s}}$. This has the solution

$$\begin{aligned}
A_t \;&=\; A_t^0 \quad,\quad A_{x,y} = A_{x,y}^0 e^{i\nu s} \;\;; && (3.4.67)\\
\nu \;&=\; \tilde{\omega}\sqrt{1+f^2}\frac{\sqrt{\tilde{B}^2\left(f^2+(1-\Psi_0^2)^2\right)+(1+f^2)(\tilde{\rho}^2+f^2+(1-\Psi_0^2)^2)}}{1+\tilde{B}^2+f^2}\;.
\end{aligned}$$

Then, we consider the region of $s \in [0, \mathcal{O}(1)\times c_s]$. To obtain the diagonal and Hall conductivities, we set e.g. $A_x = 0$ and $A_t = 0$ at $s = 0$, and study the linear dependence of $\partial_s A_y$ and $\partial_s A_x$ on A_y. Combining the equations (3.4.61) to (3.4.64), we find that $\partial_s^2 A_y \lesssim \mathcal{O}\left((\tilde{\omega}^2+\tilde{q}^2)(1+f^2+\tilde{B}^2+\tilde{\rho}^2)\right)A_y$, such that the change in $\partial_s A_y$ over this region is $\delta(\partial_s A_y) \lesssim \mathcal{O}\left((\tilde{\omega}^2+\tilde{q}^2)c_s(1+f^2+\tilde{B}^2+\tilde{\rho}^2)\right)A_y$. Hence, we have to leading order

$$\partial_s A_y \;=\; i\nu A_y\;, \qquad (3.4.68)$$

which gives us the isotropic DC diagonal conductivity and also allows us to obtain the Hall conductivity.

Looking at A_x, we find that to leading order in $\tilde{\omega}, \tilde{q}$, we have

$$\begin{aligned} 0 &= \partial_u \partial_s A_x + i\tilde{\omega} A_y \partial_u \left(\sqrt{-G} G^{tu} G^{xy}\right) \quad \text{or} \\ 0 &= \partial_s^2 A_x + i\tilde{\omega} A_y \sqrt{-G} G^{uu} G^{yy} \partial_u \left(\sqrt{-G} G^{tu} G^{xy}\right) \ , \end{aligned} \tag{3.4.69}$$

and hence A_x^0 is a consistent solution near the horizon at large s. In the asymptotic region at small s and in the limit of $\tilde{\omega} \ll 1$ the first integral of u can be done analytically, such that we obtain

$$\partial_s A_x \ = \ -i\tilde{\omega} A_y^0 \left[\sqrt{-G} G^{tu} G^{xy}\right]_{u=1}^{u=u} \tag{3.4.70}$$

since we should have by consistency $\partial_s A_x \to 0$ as $s \to 0$. Hence $A_x|_{u=0} \sim A_y \times \mathcal{O}(\tilde{\omega}) \ll A_y|_{u=0}$

Finally, we note that $\frac{\partial s}{\partial u} = 1$ as $u \to 0$, such that we can write down the DC conductivity tensor

$$\tilde{\sigma}^{DC} = \varepsilon_0 \begin{bmatrix} \frac{\sqrt{\tilde{B}^2\left(f^2+(1-\Psi_0^2)^2\right)+(1+f^2)(\tilde{\rho}^2+f^2+(1-\Psi_0^2)^2)}}{1+\tilde{B}^2+f^2} & \frac{\tilde{B}\tilde{\rho}}{1+\tilde{B}^2+f^2} \\ -\frac{\tilde{B}\tilde{\rho}}{1+\tilde{B}^2+f^2} & \frac{\sqrt{\tilde{B}^2\left(f^2+(1-\Psi_0^2)^2\right)+(1+f^2)(\tilde{\rho}^2+f^2+(1-\Psi_0^2)^2)}}{1+\tilde{B}^2+f^2} \end{bmatrix} .$$

It is straightforward to verify that at $\Psi_0 = 0$, i.e. $M_q = 0$, this expression obeys the duality under exchange of $\tilde{\sigma} \leftrightarrow \frac{1}{\varepsilon_0}\tilde{\sigma}^{-1}$, $x \leftrightarrow y$, $\tilde{\rho} \leftrightarrow \tilde{B}$. Obviously, to obtain the full dependence at finite mass, we have to invert $M_q(f, \tilde{\rho}, \tilde{B}, \Psi_0)$, in order to obtain Ψ_0 as a function of $\{M_q, f, \tilde{\rho}, \tilde{B}\}$ – but this is not possible in closed-form. At small masses $\tilde{m} \ll 1$ and small f, $\tilde{\rho}$ and $\tilde{B}$, however, one can use $\tilde{m} \sim \Psi_0$, and at large quark mass $\tilde{m} \gg 1$ at finite $\tilde{\rho}$ and f, we have $\Psi_0 \sim 1$ and the result becomes independent of the quark mass.

If we compare this result with the Drude conductivity (3.3.44), we find that this is qualitatively what one would expect. We can identify $\frac{\tilde{B}}{\sqrt{1+f^2}} = \omega_c \tau$, $\mu\, \Delta\mathfrak{n} = \frac{\varepsilon_0}{\pi T}\tilde{\rho}$ and $\mu\mathfrak{n} = \frac{\varepsilon_0}{\pi T}\frac{\sqrt{\tilde{B}^2\left(f^2+(1-\Psi_0^2)^2\right)+(1+f^2)(\tilde{\rho}^2+f^2+(1-\Psi_0^2)^2)}}{1+f^2}$. The fact that the expression for $\mu\mathfrak{n}$ is somewhat complicated is not surprising, since it results from the density of quark-antiquark pairs in thermal equilibrium. What is somewhat surprising is the fact that at finite f, there is only very limited dependence on the quark mass M_q – because one might have thought that (at vanishing ρ_0) $\mathfrak{n}$ is strongly suppressed at large M_q – but one should not interpret too much into this result. What comes as expected though is the fact that $\mu\mathfrak{n} \propto \tilde{\rho}$ at large $\tilde{\rho}$.

3.4.1.2 Small frequencies

Next, let us try to extract the subleading terms in the conductivity at small frequencies. To do so, we perturb the equations of motion for A_y and A_x (3.4.61),(3.4.64) around the DC solution by taking $A_{x,y} \to A^0_{x,y} e^{i\nu s} + A^{(1)}_{x,y}$. The equations of motion for $A^{(1)}_{x,y}$ becomes then at $\tilde{q} = 0$

$$\begin{aligned}
\partial_s^2 A_x^{(1)} &= \delta\left(\mathcal{G}^{tu}\mathcal{G}^{uy}\right)\tilde{\omega}^2 A_x^{(0)} e^{i\nu s} + i\tilde{\omega}\mathcal{G}^{uy}\left(\mathcal{G}^{\perp}\right)' A_y e^{i\nu s}\,, && (3.4.71)\\
\partial_s^2 A_y^{(1)} &= \delta\left(\mathcal{G}^{tu}\mathcal{G}^{uy}\right)\tilde{\omega}^2 A_y^{(0)} e^{i\nu s} - i\tilde{\omega}\mathcal{G}^{uy}\left(\mathcal{G}^{\perp}\right)' A_x e^{i\nu s}\,, && (3.4.72)\\
\mathcal{G}^{uy} &:= \sqrt{-G}G^{yy}G^{uu}\,,\quad \mathcal{G}^{ty} := \sqrt{-G}G^{yy}G^{tt}\,,\quad \mathcal{G}^{\perp} := \sqrt{-G}G^{xy}G^{tu}\,,\\
\delta(\cdot) &:= (\cdot) - (\cdot)_{u\to 1}\,.
\end{aligned}$$

We also write out the symbols $\mathcal{G}$ in appendix D. For simplicity, we choose as above $s|_{u=0} = 0$, and we use u as a variable to work with. Before proceeding, we look at the correction to the conductivity:

$$\tilde{\sigma}_{yy} = -\varepsilon_0 \frac{i}{\omega}\left.\frac{\delta A_y'}{\delta A_y}\right|_{u\to 0} \sim \tilde{\sigma}^{DC}_{yy}\left(1 + \frac{1}{i\nu}\frac{\partial_s A_y^{(1)}}{A_y^{(0)}} - \frac{A_y^{(1)}}{A_y^{(0)}}\right)_{u\to 0,\ A_x^{(0)}=0}\,.$$

Primarily, we are interested in the $\mathcal{O}(\omega^2)$ corrections to the real part of the conductivity, so we need to keep track of $A^{(1)}$ up to $\mathcal{O}(\omega^2)$ and $\partial_u A^{(1)}$ up to $\mathcal{O}(\omega^3)$, which coincides with the accuracy of the first perturbation, as the natural expansion parameter is ω^2. In the case of $\rho_0 B = 0$, only the diagonal term in the equations of motion contributes, so we find to the relevant order

$$\begin{aligned}
\partial_s A_y^{(1)} &= -\tilde{\omega}^2 A_y^{(0)} \int_u^1 d\tilde{u}(1 + i\nu s(\tilde{u}))\frac{\delta\left(\mathcal{G}^{tu}\mathcal{G}^{uy}\right)}{\mathcal{G}^{uy}} && (3.4.73)\\
A_y^{(1)} &= \tilde{\omega}^2 A_y^{(0)} \int_u^1 d\hat{u}\frac{1}{\mathcal{G}^{uy}}\int_{\hat{u}}^1 d\tilde{u}\frac{\delta\left(\mathcal{G}^{tu}\mathcal{G}^{uy}\right)}{\mathcal{G}^{uy}}\,. && (3.4.74)
\end{aligned}$$

We remind ourselves that $s(u) = \int_0^u \frac{1}{\mathcal{G}^{uy}}$, such that $s(u)$ and the first integral of $\frac{\delta\left(\mathcal{G}^{tu}\mathcal{G}^{uy}\right)}{\mathcal{G}^{uy}}$ can be easily computed analytically at $M_q = 0$ and expressed in terms of hypergeometric functions. The second integrals however have to be computed numerically even in the massless case. To demonstrate convergence, we note that any combination of the form $\sqrt{-G}G^{\mu\nu}G^{\alpha\beta}$ is finite at $u \to 0$ and at $u \to 1$ we have $s \propto -\ln(1-u^4)$, $\mathcal{G}^{uy} \propto (1-u^4) \propto \delta\left(\mathcal{G}^{tu}\mathcal{G}^{uy}\right)$. The convergence of $\int du \ln(1-u^4)$ is also the reason why we could expand the exponential at sufficiently small ω.

Including the case of $B \times \rho_0 \neq 0$ is slightly more tedious. First, we compute A_x up to $\mathcal{O}(\omega^2)$ under the condition that $A_x|_{u=0} = 0$. To do so, we first need to integrate $\partial_u(\partial_s A_x)$ in (3.4.64). The condition $A_x|_{u=0} = 0$ implies then that $\partial_s A_x|_{u=1} \sim i\nu \int_{u=0}^{u=1} \partial_s A_x$, such that we can, in the limit of small $\tilde{\omega}$, use $\partial_s A_x|_{u=1} = 0$. Hence, we get:

$$\begin{aligned} A_x &= i\tilde{\omega} A_y^{(0)} \int_0^u d\tilde{u} \frac{\delta\left(\mathcal{G}^{\perp}\right)}{\mathcal{G}^{uy}} - \tilde{\omega}\nu A_y^{(0)} \int_0^u d\hat{u} \left(s(\hat{u}) \frac{\delta\left(\mathcal{G}^{\perp}\right)}{\mathcal{G}^{uy}} - \frac{1}{\mathcal{G}^{uy}} \int_0^{\hat{u}} d\tilde{u} \frac{\delta\left(\mathcal{G}^{\perp}\right)}{\mathcal{G}^{uy}} \right) \\ &\quad - \nu\tilde{\omega} A_y^{(0)} \int_0^1 du \frac{\delta\left(\mathcal{G}^{\perp}\right)}{\mathcal{G}^{uy}} \ . \end{aligned} \tag{3.4.75}$$

Here, as in the rest of this section, we performed the integration by parts in order to limit the number of consecutive integrals to two integrals. Now, we can compute the additional contribution to $A_y^{(1)}$, which can still be written in terms of double integrals, with the first one computable analytically at $M_q = 0$:

$$\begin{aligned} \delta\partial_s A_y^{(1)} &= \tilde{\omega}^2 A_y^{(0)} \left(\left[\mathcal{G}^{\perp} \int_0^{\hat{u}} d\tilde{u} \frac{\delta\left(\mathcal{G}^{\perp}\right)}{\mathcal{G}^{uy}} \right]_{\hat{u}=u}^1 - \int_u^1 d\tilde{u} \frac{\mathcal{G}^{\perp}\delta\left(\mathcal{G}^{\perp}\right)}{\mathcal{G}^{uy}} \right) \qquad (3.4.76) \\ &\quad - i\tilde{\omega}^2\nu A_y^{(0)} \left(\left[\mathcal{G}^{\perp} \int_0^{\bar{u}} d\hat{u} \left(s(\hat{u}) \left(\frac{\delta\left(\mathcal{G}^{\perp}\right)}{\mathcal{G}^{uy}} + \int_0^1 du \frac{\delta\left(\mathcal{G}^{\perp}\right)}{\mathcal{G}^{uy}} \right) - \frac{1}{\mathcal{G}^{uy}} \int_0^{\hat{u}} d\tilde{u} \frac{\delta\left(\mathcal{G}^{\perp}\right)}{\mathcal{G}^{uy}} \right) \right]_{\bar{u}=u}^1 \right. \\ &\quad \left. - \int_u^1 d\hat{u}\, \mathcal{G}^{\perp} \left(s(\hat{u}) \left(\frac{\delta\left(\mathcal{G}^{\perp}\right)}{\mathcal{G}^{uy}} + \int_0^1 du \frac{\delta\left(\mathcal{G}^{\perp}\right)}{\mathcal{G}^{uy}} \right) - \frac{1}{\mathcal{G}^{uy}} \int_0^{\hat{u}} d\tilde{u}\, \frac{\delta\left(\mathcal{G}^{\perp}\right)}{\mathcal{G}^{uy}} \right) \right) \\ \delta A_y^{(1)} &= \tilde{\omega}^2 A_y^{(0)} \int_u^1 d\bar{u} \frac{1}{\mathcal{G}^{uy}} \left(\left[\mathcal{G}^{\perp} \int_0^{\hat{u}} d\tilde{u} \frac{\delta\left(\mathcal{G}^{\perp}\right)}{\mathcal{G}^{uy}} \right]_{\hat{u}=\bar{u}}^1 - \int_{\bar{u}}^1 d\tilde{u} \frac{\mathcal{G}^{\perp}\delta\left(\mathcal{G}^{\perp}\right)}{\mathcal{G}^{uy}} \right) \ . \qquad (3.4.77) \end{aligned}$$

The integral for $\delta A_y^{(1)}$ might seem divergent to the reader, but by close inspection it is apparent that the integrand is finite as $u \to 1$. Finally, we can write the correction to the diagonal conductivity which simplifies significantly after some simple algebra: After setting $u = 0$, we can eliminate the first term in the first line and all of the second line in (3.4.76) and then it turns out that most of the terms in $A_y^{(1)}$ and $\partial_s A_y^{(1)}$ are pairwise equal,

such that we obtain

$$\begin{aligned}\tilde{\sigma}_{yy} &= \tilde{\sigma}^{DC}_{yy}\left(1-\tilde{\omega}^2\left(2\int_0^1 d\,u\,s(u)\frac{\delta\left(\mathcal{G}^{ty}\mathcal{G}^{uy}\right)}{\mathcal{G}^{uy}} - 2\int_0^1 du\,s(u)\frac{\delta(\mathcal{G}^{\perp})^2}{\mathcal{G}^{uy}}\right.\right.\\ &\left.\left. - 2\int_0^1 du\,\frac{\delta(\mathcal{G}^{\perp})}{\mathcal{G}^{uy}}\int_0^u d\tilde{u}\,\frac{\delta\left(\mathcal{G}^{\perp}\right)}{\mathcal{G}^{uy}} - \int_u^1 du\,\mathcal{G}^{\perp}\,s(u)\int_0^1 du\frac{\delta\left(\mathcal{G}^{\perp}\right)}{\mathcal{G}^{uy}}\right)\right)\\ &+ i\varepsilon_0\tilde{\omega}\left(\int_0^1 d\,u\frac{\delta\left(\mathcal{G}^{ty}\mathcal{G}^{uy}\right)}{\mathcal{G}^{uy}} + \int_0^1 d\tilde{u}\frac{\delta(\mathcal{G}^{\perp})^2}{\mathcal{G}^{uy}}\right)\,. \end{aligned} \tag{3.4.78}$$

For completeness, we can also compute the contribution to the Hall conductivity. To do so, we again consider a pertubation that keeps $A_x|_{u=0}=0$. The Hall conductivity will then be to order ω^2

$$\tilde{\sigma}_{xy} = \tilde{\sigma}^{DC}_{xy}\left(1-\left.\frac{A_y^{(1)}}{A_y^{(0)}}\right|_{u\to 0}+\left.\frac{\partial_s A_x^{(1)}}{\partial_s A_x^{(0)}}\right|_{u\to 0}\right)\,. \tag{3.4.79}$$

We already know $\frac{A_y^{(1)}}{A_y^{(0)}}$, so we only need to compute $\partial_s A_x^{(0)}$. There will be two contributions, from the diagonal and off-diagonal terms in the equation of motion for A_x. Using as zeroth order the first term

$$A_x^{(0)} = i\tilde{\omega}A_y^{(0)}\int_0^1 d\tilde{u}\frac{\delta\left(\mathcal{G}^{\perp}\right)}{\mathcal{G}^{uy}} \tag{3.4.80}$$

from (3.4.75), we find that the contributions from the diagonal term in (3.4.71) is

$$\partial_s A_x^{(1)} = i\tilde{\omega}^3 A_y^{(0)}\int_u^1 d\bar{u}\frac{\delta\left(\mathcal{G}^{ty}\mathcal{G}^{uy}\right)}{\mathcal{G}^{uy}}\int_0^{\bar{u}} d\tilde{u}\frac{\delta\left(\mathcal{G}^{\perp}\right)}{\mathcal{G}^{uy}} - \tilde{\omega}\nu A_y^{(0)}\int_0^1 d\tilde{u}\frac{\delta\left(\mathcal{G}^{\perp}\right)}{\mathcal{G}^{uy}}\,, \tag{3.4.81}$$

where the second term comes from the oscillatory behavior towards the horizon at large s.

In the off-diagonal term, let us first write the $\mathcal{O}(\omega^2)$ term

$$\delta\partial_s A_x^{(1)} = \tilde{\omega}\nu A_y^{(0)}\left(\mathcal{G}^{\perp}s(u)-\int_u^1 d\tilde{u}\frac{\mathcal{G}^{\perp}}{\mathcal{G}^{uy}}\right) \tag{3.4.82}$$

$$\delta A_x^{(1)} = \tilde{\omega}\nu A_y^{(0)}\int_0^u\frac{d\tilde{u}}{\mathcal{G}^{uy}}\left(\mathcal{G}^{\perp}s(\tilde{u})-\int_{d\tilde{u}}^1 d\bar{u}\frac{\mathcal{G}^{\perp}}{\mathcal{G}^{uy}}\right)\,, \tag{3.4.83}$$

giving rise to an $\mathcal{O}(\omega^3)$ term

$$\delta_1\partial_s A_x^{(1)} = 2i\tilde{\omega}\nu^2 A_y^{(0)}\int_0^1 du\frac{\mathcal{G}^{\perp}s(\tilde{u})}{\mathcal{G}^{uy}}\,. \tag{3.4.84}$$

Using the fact that $\mathcal{G}^{\perp}|_{u=0} = 0$, the direct $\mathcal{O}(\omega^3)$ contributions from the cross-term are read off from (3.4.73) and (3.4.77):

$$\begin{aligned}
\delta_2 \partial_s A_x^{(1)} &= i\tilde{\omega}\nu^2 A_y^{(0)} \mathcal{G}^{\perp} s(u)^2 + 2\int_u^1 d\tilde{u} \frac{\mathcal{G}^{\perp}}{s}(\tilde{u}) \mathcal{G}^{uy} \\
&\quad - i\tilde{\omega}^3 A_y^{(0)} \left(\mathcal{G}^{\perp} \int_u^1 d\tilde{u} \frac{1}{\mathcal{G}^{uy}} \int_{\tilde{u}}^1 d\bar{u} \frac{\delta(\mathcal{G}^{tx}\mathcal{G}^{uy})}{\mathcal{G}^{uy}} + \int_u^1 d\tilde{u} \frac{\mathcal{G}^{\perp}}{\mathcal{G}^{uy}} \int_{\tilde{u}}^1 d\bar{u} \frac{\delta(\mathcal{G}^{tx}\mathcal{G}^{uy})}{\mathcal{G}^{uy}} \right. \\
&\quad - \mathcal{G}^{\perp} \int_u^1 \frac{d\tilde{u}}{\mathcal{G}^{uy}} \left(\delta(\mathcal{G}^{\perp}) \int_0^{\tilde{u}} d\bar{u} \frac{\delta(\mathcal{G}^{\perp})}{\mathcal{G}^{uy}} - \int_0^{\tilde{u}} d\bar{u} \frac{\left(\delta(\mathcal{G}^{\perp})\right)^2}{\mathcal{G}^{uy}} \right) \\
&\quad \left. + \int_u^1 d\tilde{u} \frac{\mathcal{G}^{\perp}}{\mathcal{G}^{uy}} \left(\delta(\mathcal{G}^{\perp}) \int_0^{\tilde{u}} d\bar{u} \frac{\delta(\mathcal{G}^{\perp})}{\mathcal{G}^{uy}} - \int_0^{\tilde{u}} d\bar{u} \frac{\left(\delta(\mathcal{G}^{\perp})\right)^2}{\mathcal{G}^{uy}} \right) \right) \qquad (3.4.85)
\end{aligned}$$

We can note that the first term in each line vanishes if we take $u \to 0$. In this case, also the contribution from (3.4.77) and the last two "sub-terms" all combine into one term, the contributions from (3.4.84) and the first line are equal, as are the second line and the contribution from (3.4.81). Hence, we see that the result can be written as :

$$\begin{aligned}
\tilde{\sigma}_{xy} &= \varepsilon_0 \frac{\tilde{\rho}\tilde{B}}{1 + f^2 + \tilde{B}^2} + 2i\nu\varepsilon_0 \int_0^1 d\tilde{u} \frac{\delta\left(\mathcal{G}^{\perp}\right)}{\mathcal{G}^{uy}} \qquad (3.4.86) \\
&\quad + \tilde{\omega}^2 \varepsilon_0 \int_0^1 du \frac{\delta(\mathcal{G}^{tu}\mathcal{G}^{xy}) - \delta(\mathcal{G}^{\perp})}{\mathcal{G}^{uy}} \int_0^u d\tilde{u} \frac{\delta(\mathcal{G}^{\perp})}{\mathcal{G}^{uy}} - \nu^2 \varepsilon_0 \int_0^1 du\, s(u) \frac{\delta(\mathcal{G}^{\perp})}{\mathcal{G}^{uy}} \int_0^u d\tilde{u} \frac{\delta(\mathcal{G}^{\perp})}{\mathcal{G}^{uy}} \ .
\end{aligned}$$

Let us now look at the fruits of this algebra.

In figure 3.1, we show the behavior of quadratic term in relation to the magnetic field. We see that it behaves approximately as in the simple Drude conductivity picture outlined in section 3.3.1, with a few differences in the details. Essentially the second order terms for the diagonal and Hall conductivities start off at $B \to 0$ (In practice $\tilde{B} = 10^{-5}$) at some negative value that is approximately proportional to the density and represents the relaxation time τ^{-2} – where we notice the diverging relaxation time at $\rho_0 = 0 = B$ that gave rise to the constant DC conductivity of (2.4.98). At larger magnetic fields, it rises $\propto B^2$ and becomes positive and then tails off after some maximum. The coefficient for the diagonal conductivity approaches a constant at large magnetic fields and the one of the Hall conductivity tails off approximately $\propto B^{-1}$ whilst the expectation from the Drude picture at constant τ would have been $\propto B^{-2}$ – indicating at least a B-dependence of relaxation time. The most striking feature is the "node" at which the correction term becomes independent of the density. In the Drude model, this would be the value of $\omega_c\tau$ at

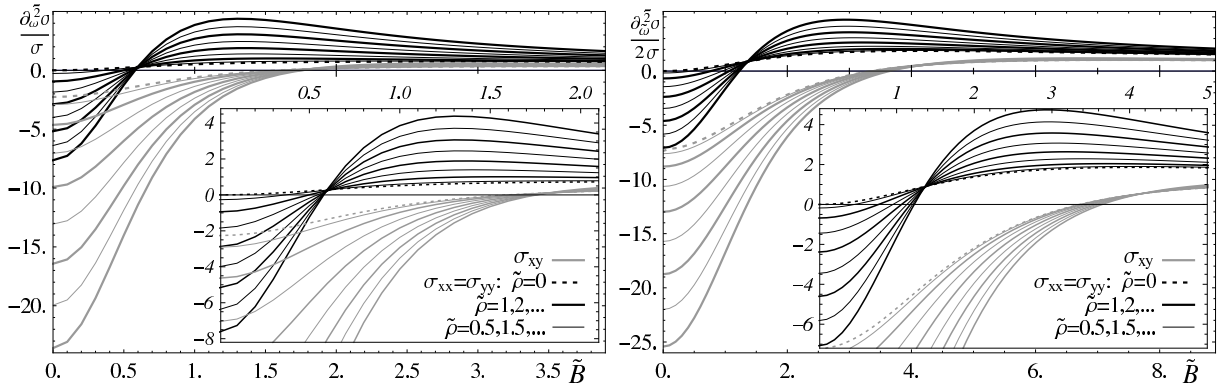

Figure 3.1: The quadratic factor in the small-frequency expansion of the conductivity $\frac{\partial_\omega^2 \sigma}{2\sigma}$ as a function of the magnetic field for various values of the density. Left: $f = 0$. Right: $f = 2$.

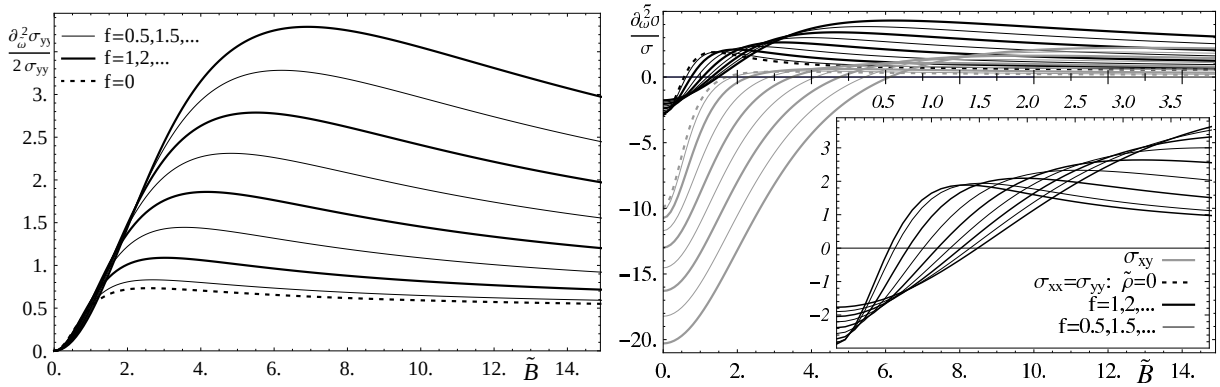

Figure 3.2: The quadratic factor in the small-frequency expansion of the conductivity $\frac{\partial_\omega^2 \sigma}{2\sigma}$ as a function of the magnetic field for various values of f. Left: $\tilde{\rho} = 0$. Right: $\tilde{\rho} = 2$.

which the quadratic term vanishes. Looking in fig. 3.2 at how f shifts those curves, we find that at small $\tilde{B}$, in the negative region in the case of finite $\tilde{\rho}$, that they are shifted towards 0 for increasing f, implying that the relaxation time increases, whereas for large values of $\tilde{B}$, they are shifted to larger values – which is simply an implication of the observation that $\omega_c\tau \sim \frac{\tilde{B}}{\sqrt{1+f^2}}$.

Going a step further, we can check the generic predictions from section 3.3.1. In fig. 3.4, we see that the ratio $\frac{\partial_\omega^2\sigma^\parallel\ \sigma^\perp}{\sigma^\parallel\ \partial_\omega^2\sigma^\perp}$ at $\tilde{B} \to 0$ approaches precisely the prediction value $\frac{1}{3}$ at large densities with a convergence rate that decreases with increasing f – even though we are in a completely different, i.e. strong coupling, regime. This also indicates that at large net densities and small f, we approach the classical Drude behavior, whereas for small densities or large f, we are in a completely different "phase". At large magnetic fields, however, this ratio does not become constant and depends significantly on f, but at least it seems that always $\frac{\partial_\omega^2\sigma^\parallel}{\sigma^\parallel} > \frac{\partial_\omega^2\sigma^\perp}{\sigma^\perp}$. Furthermore, we can look at the location of the node, $\tilde{B}_{crit}$, which indicates the $\tilde{B}$ value where $\frac{\partial_\omega^2\sigma}{2\sigma} = 0$, i.e. where the peak turns into a minimum. For the diagonal conductivity, we find that $\frac{\tilde{B}^2_{crit}}{1+f^2} \approx 0.342$ at $f = 0$ which converges to $\frac{\tilde{B}^2_{crit}}{1+f^2} \approx 0.397$ at large f. For the Hall conductivity, the value starts at 3.15, has a maximum of 3.90 around $f \sim 80$ and then converges to 3.88. The variation in the ratio of those critical $\tilde{B}^2$ values is even smaller - between 9.18 and 9.84. If we were to associate $\tau\omega_c = \frac{\tilde{B}}{\sqrt{1+f^2}}$ as suggested from the DC conductivity in section 3.4.1.1, this is reasonably close to the values from the Drude model of $\frac{1}{3}(\omega_c\tau)^2$ and $3(\omega_c\tau)^2$.

Looking in figure 3.3 at the quadratic term of σ_{xx} at $\tilde{B} = 0$, where $\frac{\partial_{\tilde{\omega}}^2\sigma}{2\sigma}$ becomes $\frac{\partial_{\tilde{\omega}}^2\sigma}{2\sigma} = -\tau^{-2}$, we find in fig. 3.3, that τ^{-2} is approximately proportional to the density, with a coefficient of $\tau^{-2} \approx 2.6\tilde{\rho}$. From another perspective, this means that the relaxation time is approximately proportional to the mean distance between "quarks", $\tau \propto \rho_0^{-1/2}$, but not the naive geometric mean free path in a system of weakly coupled particles. The proportionality coefficient is approximately $\tau \sim 2.6\pi\sqrt{\frac{2\varepsilon_0}{\rho_0}}$. The f-dependence is not surprising, as increasing f appears to increase the relaxation time, which is consistent with a decreasing effective temperature that was a recurring theme throughout chapter 2. It is interesting though that at large densities, the effect of f is only to shift the curves in fig. 3.3 and leaves the proportionality factor constant.

Looking at the coefficients as a function of f in fig. 3.5 shows our observations from a different perspective. Essentially, the effect of f is to increase the relaxation time, and to decrease $\omega_c\tau$ at fixed $\tilde{B}$. The most striking feature is the observation that we had above, that the coefficient in the Hall conductivity is proportional to f in regimes where it is

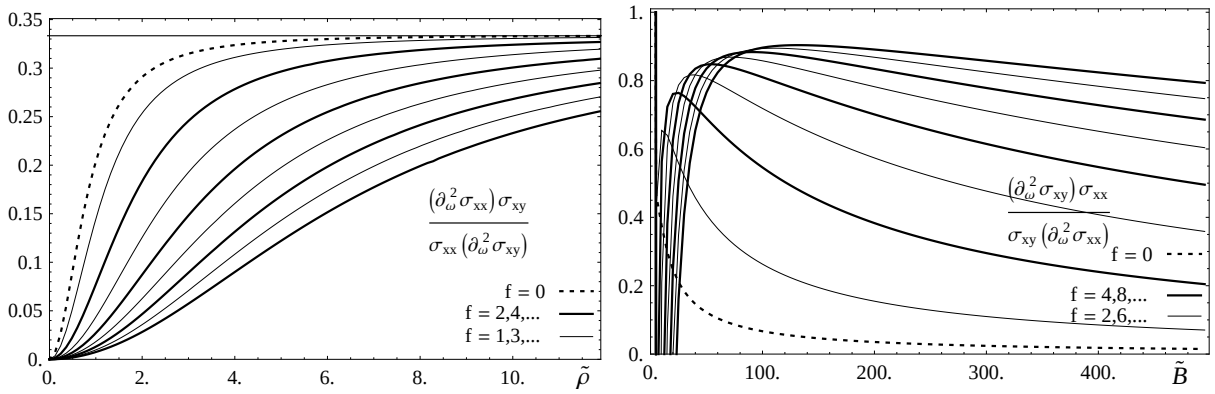

Figure 3.3: The ratio of the quadratic factors in the small-frequency expansion of the diagonal and Hall conductivities. Left: $\frac{\partial_\omega^2 \sigma^\parallel \;\sigma^\perp}{\sigma^\parallel \;\partial_\omega^2 \sigma^\perp}$ at $\tilde{B} = 10^{-5}$ as a function of $\tilde{\rho}$ for various values of f. Right: $\frac{\partial_\omega^2 \sigma^\perp \;\sigma^\parallel}{\sigma^\perp \;\partial_\omega^2 \sigma^\parallel}$ at large magnetic fields as a function of $\tilde{B}$ for $\tilde{\rho} = 10$ and various values of f. The density $\tilde{\rho}$ changes only the behavior at small magnetic fields and leaves the large-$\tilde{B}$ tail unchanged.

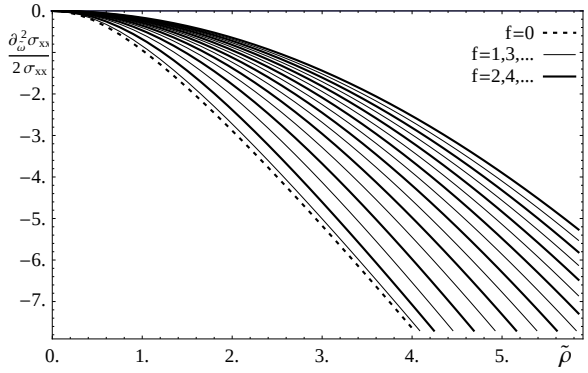

Figure 3.4: The quadratic factor in the small-frequency expansion of the conductivity $\frac{\partial_\omega^2 \sigma}{2\sigma}$ as a function of the density for various values of f.

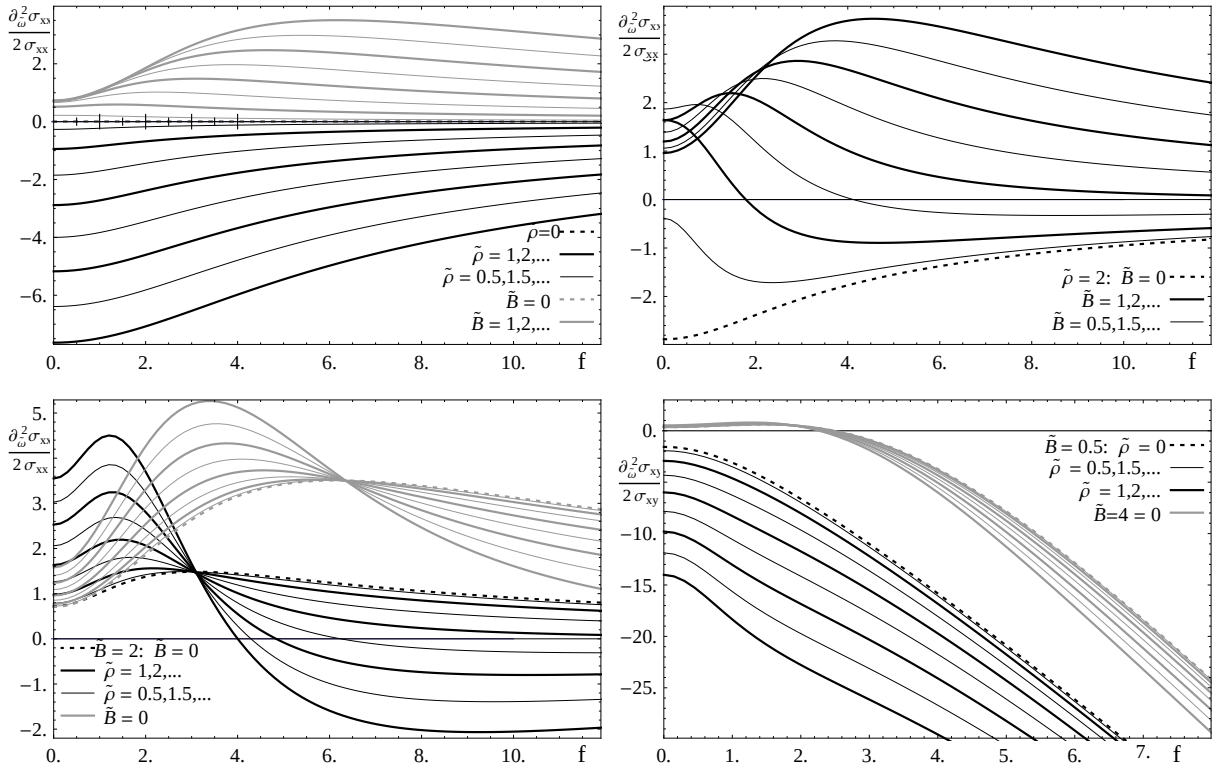

Figure 3.5: The quadratic factor in the small-frequency expansion of the conductivity $\frac{\partial^2_\omega \sigma}{2\sigma}$ as a function of f. Top left: The coefficient of the diagonal conductivity for various values of the density and the magnetic field, right: For various values of the magnetic field at $\tilde{\rho} = 1$. Bottom left: The coefficient of the diagonal conductivity for various values of the density at $\tilde{B} \in \{2, 4\}$, right: The coefficient of the Hall conductivity for various values of the density at $\tilde{B} \in \{0.5, 4\}$.

negative, i.e. the "Hall peak" becomes narrower.

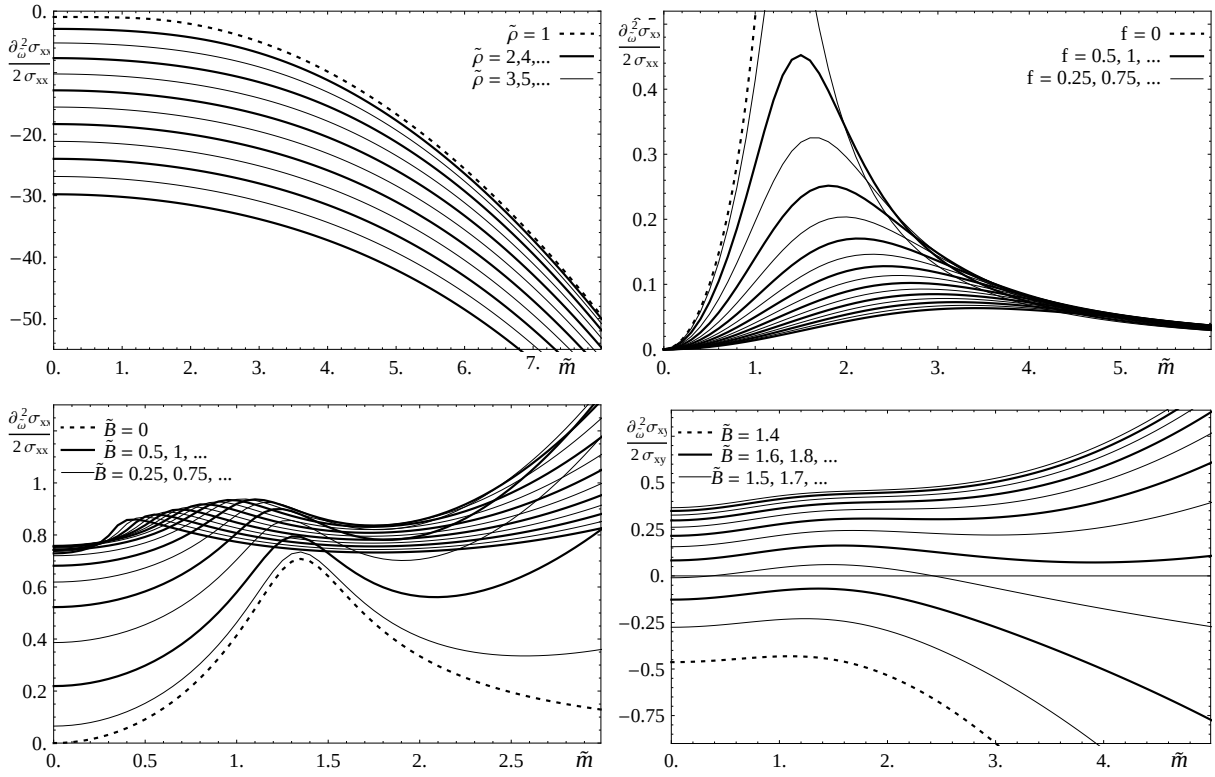

Figure 3.6: The quadratic factor in the small-frequency expansion of the conductivity $\frac{\partial_\omega^2 \sigma}{2\sigma}$ as a function of $\tilde{m}$. Top left: The coefficient of the diagonal conductivity for various values of the density, right: For various values of f. Bottom left: The coefficient of the diagonal conductivity for various values of the $\tilde{B}$ at $f = 0.25$, right: The coefficient of the Hall conductivity for various values of the magnetic field at $\tilde{\rho}2$

Finally, we can look at the mass dependence in fig. 3.6. The biggest surprise from the Drude picture view is the quadratic dependence of second the expansion coefficient on the mass. This indicates $\tau \propto \tilde{m}^{-1}$, which is somewhat counterintuitive since one would have thought that the relaxation time increases with increasing mass. If one considers the Drude peak however to be a quasiparticle resonance, this is what one does classically expect since it means that the quasi particle becomes more stable at larger quark mass due to slower thermal motion and hence reduced collision rates. At vanishing density and different values of f, the result is also in contradiction with the free particle picture, since the DC conductivity is in a minimum at finite mass. There is an interesting maximum

in the coefficient, which corresponds as $f \to 0$ to the critical quark mass of the phase transition discussed in appendix E. Hence, it occurs at the transition from the small-mass to the large-mass regime. This feature is even more apparent when plotting the coefficient against $\tilde{B}$ for a small value of $f = 0.25$, where there is a small maximum around the critical mass. Looking at the Hall conductivity, the regimes in $\tilde{B}$ in which there is a Drude peak and in which there is a magnetoresistance minimum behave approximately like the pure Drude peak and magnetoresistance effects. It is an interesting curiosity, that the transition between those regimes receives a very small mass dependence.

3.4.2 Large Temperatures: Diffusion limit

In the diffusion limit, i.e. at $\tilde{\omega} \ll \tilde{q} \ll 1$, we expect to be able to predict the transport properties from the diffusion behavior, i.e. from the diffusion constant D and the susceptibility ε because we expect the "mean free path" to be set by the temperature scale.

The diffusion constant was computed e.g. in [101] by studying the equations of motion of the gauge field in the gravity side to obtain Fick's Law,

$$\vec{j}(t,\vec{x}) \;=\; -D\,\vec{\nabla} j_0(t,\vec{x}) \;, \tag{3.4.87}$$

on the field theory side. The derivation in [101] is very instructive and can be followed also in our case in the presence of background fields. The expression for the diffusion constant is then slightly modified and yields

$$D \;=\; \frac{1}{\pi T}\left(-G\sqrt{-G^{tt}G^{uu}}G^{xx}\right)_{u\to 1}\int_0^1 \frac{d\,u}{\sqrt{-G}G^{tt}G^{uu}} \;, \tag{3.4.88}$$

where we keep in mind that in our notation $\sqrt{-G}$ contains a factor of the u dependent coupling $g_{eff}^{-2}(u) = \sqrt{f^2 + (1-\Psi(u)^2)^2}$.

At $M_q = 0$, this can be evaluated analytically and expressed in terms of hypergeometric

functions as:

$$\begin{aligned}\pi T D &= \frac{(1+f^2)\sqrt{1+f^2+\tilde{B}^2+\tilde{\rho}^2}}{1+f^2+\tilde{B}^2}\int_0^1 d\,u\,\frac{1+f^2+b^2u^4}{\left(1+f^2+(\tilde{B}^2+\tilde{\rho}^2)u^4\right)\sqrt{1+(f^2+\tilde{B}^2+\tilde{\rho}^2)u^4}} \\ &= \frac{(1+f^2)\sqrt{1+f^2+\tilde{B}^2+\tilde{\rho}^2}}{1+f^2+\tilde{B}^2}\times \\ &\left({}_2F_1\left(\frac{1}{4},\frac{1}{2};\frac{5}{4};-(f^2+\tilde{B}^2+\tilde{\rho}^2)\right) - \tilde{\rho}^2\,\frac{F_1\left(\frac{5}{4};\frac{1}{2},1;\frac{9}{4};-(f^2+\tilde{B}^2+\tilde{\rho}^2),-\frac{\tilde{\rho}^2+\tilde{B}^2}{1+f^2}\right)}{5(1+f^2)}\right),\end{aligned} \tag{3.4.89}$$

where we met the Gauss hypergeometric function ${}_2F_1$, which is asymptotically in our case $\sim \frac{\Gamma(1/4)^2}{4\sqrt{\pi}(f^2+\tilde{B}^2+\tilde{\rho}^2)^{1/4}}$, in 2.2.1.3 and F_1 is an Appell hypergeometric function that is here at $f=0$ asymptotically $\sim \frac{9\Gamma(5/4)^2}{5\sqrt{\pi}(\tilde{B}^2+\tilde{\rho}^2)^{5/4}}$. At $F\neq 0$, the decay will be with a smaller, non-rational, power. In fig. 3.7, we see that the diffusion constant is for small f approximately

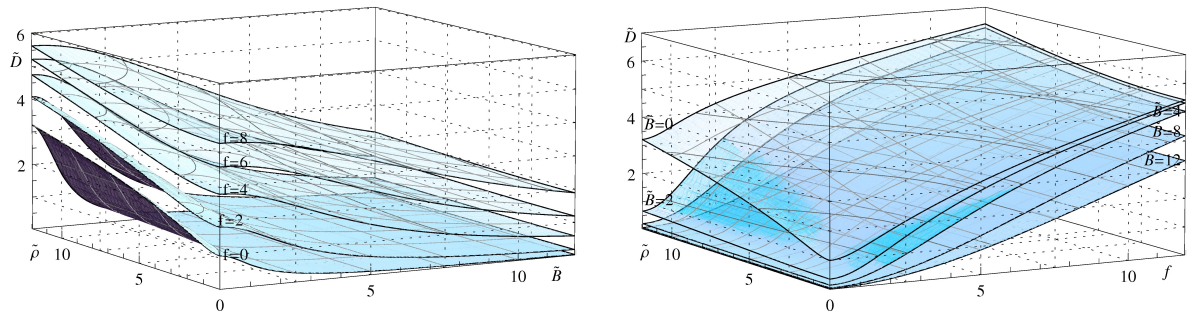

Figure 3.7: The diffusion constant $\pi T\,D$ as a function of the magnetic field and density for different values of f (left) and as a function of f and the density for different values of the magnetic field (right)

proportional to $\sqrt{\tilde{\rho}}$ whereas for large f the dependence is approximately linear. This may be due to the strong coupling because the usual classical geometric result for the diffusion constant is proportional to the mean free path – which one expects to be inversely related to the density – and the mean free path should dominated by the baryon density at large baryon density, at least in weak-coupling intuition. However if we are for example in a superfluid, this intuition does obviously not apply anymore.

At small f, the diffusion constant decays inversely proportional to the magnetic field, which represents the fact that charged particles in magnetic fields receive extra "drag" and become localized. At larger f, this decay slows down. Looking at the f-dependence, we see that the diffusion constant is approximately proportional to f, with an asymptotic slope that is independent from $\tilde{B}$. This contrasts to the dependence on $\tilde{\rho}$, which disappears at large $\tilde{B}$.

Obtaining the permittivity is similarly straightforward. By definition [85, 86]

$$\varepsilon \;=\; \lim_{\omega,q\to 0} C_{tt} \;, \tag{3.4.90}$$

where it is understood that the limit $\omega \to 0$ is to be taken first. Taking the limit $\omega, q \to 0$ of the equation of motion for A_t, (3.2.37) gives us a Poisson equation

$$\left(\sqrt{-G}G^{tt}G^{uu}A_t'(u)\right)' \;=\; 0 \;. \tag{3.4.91}$$

We note that this equation does not yield an appropriate infalling wave behavior near the horizon, but it is easy to see from the full equations for A_t and A_x that for very small but finite $\omega \ll q \ll 1$, the behavior will be appropriately resolved near the horizon. Near the horizon, A_t and A_x are strongly coupled, with $A_t \sim \frac{\omega}{q}A_x$, and A_x follows an oscillatory behavior, just like A_y in section 2.2.2. To solve for A_t, we then simply integrate (3.4.91) with $A_t = 0$ as a boundary condition at $u \to 1$, which gives us readily the permittivity

$$\varepsilon \;=\; \varepsilon_0 \left.\frac{A_t'}{A_t}\right|_{u\to 1} \;=\; \varepsilon_0 \frac{(\sqrt{-G}G^{tt}G^{uu})_{u=0}}{\int_0^1 d\,u\,\sqrt{-G}G^{tt}G^{uu}} \;=:\; \varepsilon_0\varepsilon_r \;, \tag{3.4.92}$$

where $(\sqrt{-G}G^{tt}G^{uu})_{u=0} = 1$. We can now see immediately, that the isotropic DC conductivity in section 3.4.1.1 is given by the diffusion result $\sigma_{yy} = \sigma_{xx} = \varepsilon D$ and in the DC limit there is no contribution from other modes, as expected. However, in contrast to the remarkable result in section 2.4 where the conductivity was at all frequencies determined precisely by the diffusion behavior, the diffusion behavior is now only valid at small frequencies and receives corrections as we move away from $\omega = 0$ as outlined in section 3.4.1.2. Since the integral is the same as the one for the diffusion constant, we find that for $M_q = 0$, we obtain the relative permittivity

$$\varepsilon_r^{-1} \;=\; {}_2F_1\left(\frac{1}{4},\frac{1}{2};\frac{5}{4};-(f^2+\tilde{B}^2+\tilde{\rho}^2)\right) \;-\; \tilde{\rho}^2\,\frac{F_1\left(\frac{5}{4};\frac{1}{2},1;\frac{9}{4};-(f^2+\tilde{B}^2+\tilde{\rho}^2),-\frac{\tilde{\rho}^2+\tilde{B}^2}{1+f^2}\right)}{5(1+f^2)} \;. \tag{3.4.93}$$

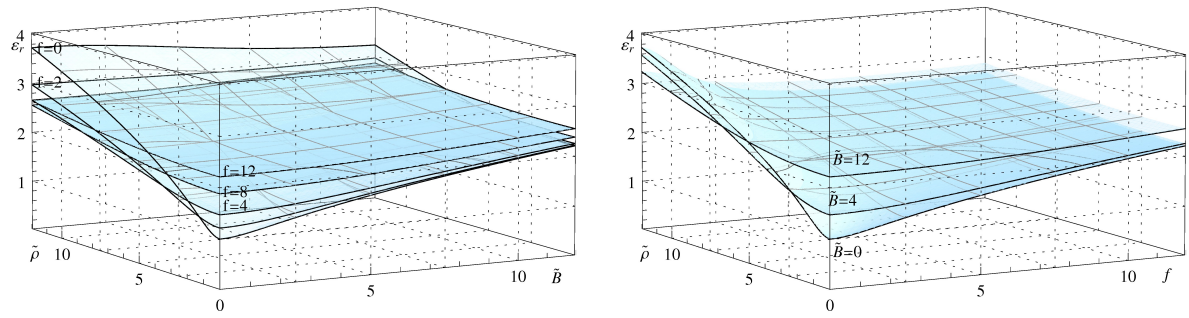

Figure 3.8: The relative permittivity ε_r as a function of the magnetic field and density for different values of f (left) and as a function of f and the density for different values of the magnetic field (right)

In figure 3.8, we see the interesting fact that at large f, the relative permittivity becomes approximately constant. While one does not generically expect any specific dependence on the magnetic field, one would expect in a simple solid state model $\varepsilon_r \propto \mathfrak{n}$ and hence $\varepsilon_r \propto \rho_0$ at large $\tilde{\rho}$, which is realized here at large f, but at small f it is proportional to $\sqrt{\rho_0}$ at large values of $\tilde{\rho}$.

If we compare the results of this section to the Drude model reviewed in section 3.3.1, we can identify from the Einstein relation (3.3.43)

$$\mu \,=\, \frac{D}{T} \quad \text{and} \quad \mathfrak{n} \,=\, \pi T^2 \varepsilon_0 \varepsilon_r \ . \tag{3.4.94}$$

3.4.3 $T \to 0$ limit

Next, let us look at the low temperature limit of $\tilde{q}, \tilde{\omega} \gg 1$. Here, we are interested in the equations near $u = 0$. The equations for A_y and $\mathcal{A}_x$ (3.2.40),(3.2.41) are identical in this limit, and become

$$A_y'' \,+\, \left(\tilde{\omega}^2 - \tilde{q}^2\right) A_y \,=\, 0 \tag{3.4.95}$$

as in the "conformal limit" in section 2.2.1, up to order $\tilde{m}^2 \frac{u^2}{\tilde{\omega}^2}$ or $(e^2, b^2)\frac{u^4}{\tilde{\omega}^2}$. The appropriate solution gives us the diagonal conductivity $\tilde{\sigma}_{yy} = \varepsilon_0 \sqrt{1 - \tilde{q}^2/\tilde{\omega}^2}$ and $\tilde{\sigma}_{xx} = \frac{\varepsilon_0}{\sqrt{1-\tilde{q}^2/\tilde{\omega}^2}}$.

3.4.3.1 Exponentially suppressed regime, $\tilde{q}^2 \gg 1 \gg \tilde{\omega}^2$, at small backgrounds, $|\tilde{q}| \gg |\tilde{\rho}|, |\tilde{B}|$

To study the low temperature limit more in detail, we start with the regime $|\tilde{\rho}|, |\tilde{B}| \ll |\tilde{q}|$ which is similar to the approximation in section 2.2.2.

It is straightforward to see that the dominating term in the solution at finite $h = 1-u^2$ will still be $A_y, \mathcal{A}_x \sim A_y^0, \mathcal{A}_x e^{\pm\tilde{q}\int\sqrt{-G^{xx}/G^{uu}}}$. Using this to estimate the contribution of the cross-terms in (3.2.40),(3.2.41), we find that they are suppressed by a factor of $\tilde{q}^{-1}$ with respect to the dominant diagonal terms. In the near-horizon regime at $\omega^2/q^2 \ll h \ll 1$, they are suppressed by a factor of $h/\tilde{q}$, and in the regime $h \ll \omega^2/q^2 \ll 1$, they are suppressed by $h^2\tilde{q}/\tilde{\omega}^2$. Hence, we can proceed as follows: First we will obtain the diagonal conductivity $\tilde{\sigma}_{yy}$ ($\tilde{\sigma}_{xx}$ follows similarly) by solving the homogeneous part, because the contribution from the cross-terms to the diagonal conductivity will be suppressed by the order of the square of the suppression of the cross-terms and can hence be safely ignored. Then we will compute the Hall conductivity from the inhomogeneous part.

Again, let us use the Ansatz $A_y = A_y^0 e^{\int^u \zeta}$, which gives us

$$\zeta^2 + \zeta' + \frac{\left(\sqrt{-G}G^{uu}G^{yy}\right)'}{\sqrt{-G}G^{uu}G^{yy}}\zeta + \frac{\left(\left(\sqrt{-G}\,G^{tu}G^{xy}\right)'\right)^2}{-G\,G^{tt}G^{uu}G^{xx}G^{yy}} + \frac{G^{xx}}{G^{uu}}\left(\frac{G^{tt}}{G^{xx}}\tilde{\omega}^2 - \tilde{q}^2\right) = 0\,, \quad (3.4.96)$$

with the approximate result at $h \gg \omega^2/q^2$ up to $\mathcal{O}(1)$, $\zeta = -\frac{\left(\sqrt{-G}G^{uu}G^{yy}\right)'}{2\sqrt{-G}G^{uu}G^{yy}} \pm \frac{\zeta_0'}{2\zeta_0} \pm \zeta_0$, $\zeta_0 := \tilde{q}\sqrt{\frac{G^{xx}}{G^{uu}}}$, where we pick the negative sign corresponding to a solution that decays towards the horizon. Next, we take $\zeta = -\zeta_0 - \frac{\left(\sqrt{-G}G^{uu}G^{yy}\right)'}{2\sqrt{-G}G^{uu}G^{yy}} - \frac{\zeta_0'}{2\zeta_0} + \epsilon$ and gather the remaining terms up to linear order in ϵ

$$\begin{aligned} 0 &= \epsilon' - \epsilon\left(\frac{\zeta_0'}{\zeta_0} + 2\zeta_0\right) + \frac{\left(\left(\sqrt{g}\,G^{tu}G^{xy}\right)'\right)^2}{-G\,G^{tt}G^{uu}G^{xx}G^{yy}} \\ &\quad + \left(\frac{\left(\sqrt{-G}G^{uu}G^{yy}\right)'}{2\sqrt{-G}G^{uu}G^{yy}} + \frac{\zeta_0'}{2\zeta_0}\right)\frac{\zeta_0'}{2\zeta_0} - \left(\frac{\left(\sqrt{-G}G^{uu}G^{yy}\right)'}{2\sqrt{-G}G^{uu}G^{yy}} + \frac{\zeta_0'}{2\zeta_0}\right)' + \frac{G^{tt}}{G^{uu}}\tilde{\omega}^2 \\ &=: \epsilon' - \epsilon\alpha(u) - \beta(u)\,. \end{aligned} \quad (3.4.97)$$

The general solution to this equation is

$$\epsilon = e^{\int_0^u d\bar{u}\alpha(\bar{u})}\left(\epsilon_0 + \int_0^u d\tilde{u} e^{-\int_0^{\tilde{u}} d\bar{u}\alpha(\bar{u})}\beta(\tilde{u})\right)\,. \quad (3.4.98)$$

The second part is a small contribution $\in \mathbb{R}$ that is at most of order $\tilde{q}^{-2}$, so we are only interested in the first part that evaluates to $\epsilon = \epsilon_0 \zeta_0 e^{2\int_0^u d\bar{u}\zeta_0(\bar{u})}$, or $\epsilon = \epsilon_H \zeta_0 e^{-2\int_u^1 d\bar{u}\zeta_0(\bar{u})}$. ϵ_H will be fixed in the region $\tilde{\omega}^2/\tilde{q}^2 \ll h \ll 1$, where there is an overlap between the asymptotic and near horizon solutions.

At $h \ll 1$, the equation becomes:

$$-4\partial_h\zeta + \zeta^2 - \frac{4}{h}\zeta + \frac{\tilde{\omega}^2}{h^2} - \frac{1}{1+\frac{\tilde{B}^2}{1+f^2}+\frac{\tilde{\rho}^2}{(1-\Psi_0^2)^2+f^2}}\frac{\tilde{q}^2}{h} = 0 \,. \tag{3.4.99}$$

Again, as in section 2.2.2, this can be solved analytically in terms of hypergeometric functions and then be expanded for $\frac{\tilde{q}^2}{1+\frac{\tilde{B}^2}{1+f^2}+\frac{\tilde{\rho}^2}{(1-\Psi_0^2)^2+f^2}}h \gg 1$, giving us in the overlap region

$$\begin{aligned}\zeta \sim & -\frac{\tilde{q}^2}{\sqrt{h}\sqrt{1+\frac{\tilde{B}^2}{1+f^2}+\frac{\tilde{\rho}^2}{(1-\Psi_0^2)^2+f^2}}} + \frac{1}{h} + \dots \\ & - \frac{\pi i\tilde{\omega}\tilde{q}}{\sqrt{h}\sqrt{1+\frac{\tilde{B}^2}{1+f^2}+\frac{\tilde{\rho}^2}{(1-\Psi_0^2)^2+f^2}}} e^{-\tilde{q}\frac{\sqrt{h}}{\sqrt{1+\frac{\tilde{B}^2}{1+f^2}+\frac{\tilde{\rho}^2}{(1-\Psi_0^2)^2+f^2}}}} + \dots \,.\end{aligned} \tag{3.4.100}$$

This solution connects nicely to the asymptotic region, even matching subleading terms in the overlap region, to give us

$$\begin{aligned}\zeta = & -\tilde{q}\sqrt{\frac{G^{yy}}{G^{uu}}} - \frac{\left(\sqrt{-G}G^{uu}G^{yy}\right)'}{2\sqrt{-G}G^{uu}G^{yy}} - \frac{\sqrt{\frac{G^{yy}}{G^{uu}}}'}{2\sqrt{\frac{G^{yy}}{G^{uu}}}} + \mathcal{O}(\tilde{q}^{-2}) \\ & - i\pi\tilde{\omega}\tilde{q}\sqrt{\frac{G^{yy}}{G^{uu}}}e^{-2\tilde{q}\int_u^1 d\bar{u},\sqrt{\frac{G^{yy}}{G^{uu}}}}\left(1+\mathcal{O}(\tilde{\omega}^2,\tilde{q}^{-2})\right) \,.\end{aligned} \tag{3.4.101}$$

Hence, the dissipative part of the diagonal conductivity reads to leading order

$$\text{Re}\ \tilde{\sigma}_{yy} = \varepsilon_0\pi\tilde{q}e^{-2\tilde{q}\int_0^1 d\,u\sqrt{\frac{G^{yy}}{G^{uu}}}} \,, \tag{3.4.102}$$

where one could again interpret the result as having an "effective temperature" scale of

$$\frac{T}{T_{eff}} = \frac{2}{\pi}\int_0^1 d\,u\,\sqrt{\frac{G^{yy}}{G^{uu}}} \,. \tag{3.4.103}$$

In the massless limit we can, as usual, find an analytic expression, which evaluates to

$$\frac{T}{T_{eff}} \;=\; \frac{2\Gamma(5/4)}{\sqrt{\pi}\Gamma(3/4)}\sqrt{1+f^2}\,{}_2F_1\left(\frac{1}{4},\frac{1}{2};\frac{3}{4};-(f^2+\tilde{\rho}^2+\tilde{B}^2)\right)\;. \tag{3.4.104}$$

If we were to describe this result qualitatively as the behavior of a semiconductor, then the edge density of states would correspond to total density of baryons and anti-baryons in thermal equilibrium, and the difference $N_c - N_v$ would correspond to the baryon density ρ_0.

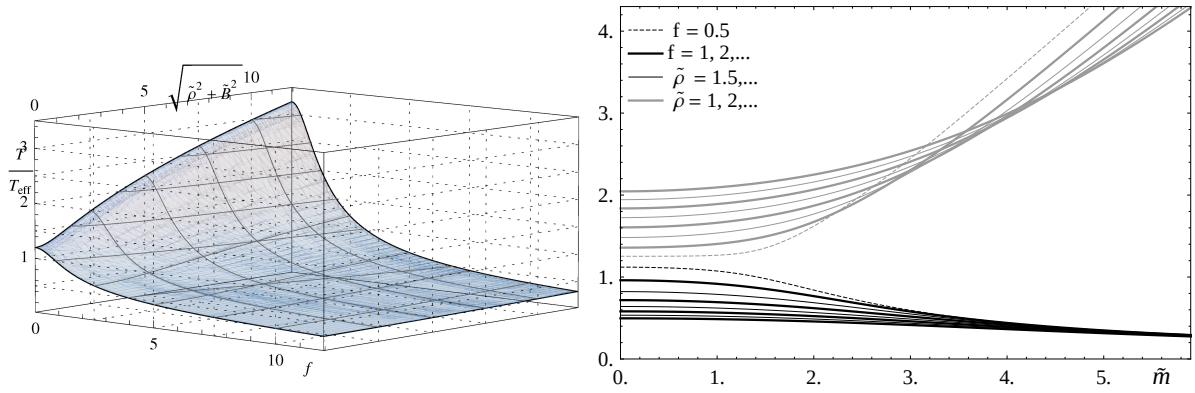

Figure 3.9: The "effective temperature" T_{eff}/T. Left: As a function of f and $\sqrt{\tilde{\rho}^2+\tilde{B}^2}$. Right: As a function of $\tilde{m}$ for various values of $\tilde{\rho}$ and $\tilde{B}$

In fig. 3.9, we show how the effective temperature depends on the parameters of the defect. In addition to the dependence on f, that we saw throughout chapter 2, turning on a magnetic field or a finite density raises now the effective temperature approximately $\propto (\tilde{B}^2+\tilde{\rho}^2)^{1/4}$. Furthermore, we find that turning on a finite mass in some sense "enhances" the effect of the density and of f but the dependence on the mass in the presence of only $\tilde{B}$ is not very significant.

Next, let us look at the off-diagonal terms. Do do so, we first need to write out the homogeneous part of the equation of motion for $\mathcal{A}_x =: \mathcal{A}_x^0 e^{\int^u \zeta_x}$:

$$\zeta_x^2 \,+\, \zeta_x' \,+ - \frac{\left(\sqrt{-G}G^{tt}G^{xx}\right)'}{\sqrt{-G}G^{tt}G^{xx}}\zeta_x \,+\, \frac{G^{xx}}{G^{uu}}\left(\frac{G^{tt}}{G^{xx}}\tilde{\omega}^2 \,-\, \tilde{q}^2\right) \;=\; 0\;, \tag{3.4.105}$$

which has the solution up to $\mathcal{O}(1)$, $\zeta_x = \frac{\left(\sqrt{-G}G^{tt}G^{xx}\right)'}{2\sqrt{-G}G^{tt}G^{xx}} \pm \frac{\zeta_0'}{2\zeta_0} \pm \zeta_0$, where we again pick the

negative sign. The dominant terms in the full homogeneous solutions are then

$$\mathcal{A}_x \;=\; \mathcal{A}_x^0 \sqrt{\frac{\sqrt{-G}G^{tt}G^{xx}}{\zeta_0}} e^{-\int_0^u \zeta_0} \quad \text{and} \quad A_y \;=\; A_y^0 \frac{1}{\sqrt{\sqrt{-G}G^{uu}G^{yy}\zeta_0}} e^{-\int_0^u \zeta_0} \;. \tag{3.4.106}$$

There are now two ways to determine the perturbative contribution coming from the cross terms. Either we again solve for the exponents ζ – which would then contain factors of A_y^0/A_x^0 - or we can directly take a pertubation for A_y. Even though the latter one may seem most natural, in particular since the system is linear, we will use the first method since it gives us the result in a very neat way. Substituting (3.4.106) into the equation of motion for A_y (3.2.40), we see that the equation for ϵ (3.4.97) receives now an additional term

$$\beta(u) \;\to\; \beta(u) \;-\; \zeta_x \left(\sqrt{-G}G^{tu}G^{xy}\right)' \sqrt{\frac{G^{uu}}{G^{tt}}} \frac{\mathcal{A}_x^0}{A_y^0} \;, \tag{3.4.107}$$

such that we obtain an extra contribution to ϵ, taking only the leading term in $\beta \propto \tilde{q}$

$$\epsilon \;=\; e^{2\int_0^u \zeta} \left(\epsilon_0 - \int_0^u d\tilde{u} \left(\zeta_x \left(\sqrt{-G}G^{tu}G^{xy}\right)' \sqrt{\frac{G^{uu}}{G^{tt}}} e^{-2\int_0^{\tilde{u}} \zeta} \right) \frac{\mathcal{A}_x^0}{A_y^0} \right) \;. \tag{3.4.108}$$

Now, if we look at the equations of motion (3.2.40),(3.2.41), we remind ourselves that in the near horizon geometry, the equations of motion for A_y and $\mathcal{A}_x$ look the same and the cross terms are suppressed by a factor of $h/\tilde{q}$ with respect to the dominant terms. Hence the coupling occurs over the range $u \in]0, 1-\varepsilon]$ for small ε and not in the near-horizon region. We keep ε to regulate the asymptotic solution in the near horizon region, in which it is not valid. To capture the mixing then correctly, we fix ϵ_H at the horizon as above, such that we find

$$\begin{aligned} \epsilon \;&\simeq\; \sqrt{\frac{G^{yy}}{G^{uu}}} e^{-2\int_u^{1-\varepsilon} \zeta_0} \left(\epsilon_H + \int_u^{1-\varepsilon} d\tilde{u} \left(\zeta_x \left(\sqrt{-G}G^{tu}G^{xy}\right)' \frac{G^{uu}}{\sqrt{-G^{tt}G^{xx}}} e^{2\int_{\tilde{u}}^{1-\varepsilon} \zeta_0} \right) \frac{\mathcal{A}_x^0}{A_y^0} \right) \\ &=:\; \epsilon_{hom.} + \epsilon_{inh.} \end{aligned} \tag{3.4.109}$$

where we absorbed a factor of $\sqrt{\frac{G^{uu}}{G^{xx}}}\Big|_{u=1-\varepsilon}$ into ϵ_H. Because of the exponential factor in the second term, the integral will be dominated around small $\tilde{u}$. The appropriate expansion gives us to leading order at $u \ll 1$

$$\begin{aligned} \epsilon_{inh.} \;&=\; -4 \frac{\tilde{\rho}\tilde{B}}{1+f^2} \tilde{q} \frac{\mathcal{A}_x^0}{A_y^0} e^{2\sqrt{1+f^2}\tilde{q}u} \int_u^1 d\tilde{u}\, u^3 e^{-2\sqrt{1+f^2}\tilde{q}\tilde{u}} \\ &=\; 4 \frac{\tilde{\rho}\tilde{B}}{1+f^2} \tilde{q} \frac{\mathcal{A}_x^0}{A_y^0} e^{2\sqrt{1+f^2}\tilde{q}u} \left[\frac{\tilde{u}^4}{16\tilde{q}^4(1+f^2)^2} \Gamma(4, 2\tilde{q}\tilde{u}) \right]_{\tilde{u}=u}^1 \end{aligned} \tag{3.4.110}$$

and in the limit $u \to 0$, we find

$$\lim_{u\to 0} \epsilon_{inh.} \;=\; -\frac{3}{2}\,\frac{\tilde{\rho}\tilde{B}}{(1+f^2)^{5/2}\;\tilde{q}^3}\,\frac{\mathcal{A}_x^0}{A_y^0} \;+\; \mathcal{O}(\tilde{m}/\tilde{q}^5) \;+\; \mathcal{O}(1/\tilde{q}^7)\;. \tag{3.4.111}$$

Finally, keeping $A_y|_{u=0} = A_y^0$ fixed, we get the leading terms (ignoring the exponentially suppressed terms)

$$\partial_u A_y \;=\; -\sqrt{1+f^2}\,\tilde{q}\,A_y^0 \;-\; \frac{3}{2}\,\frac{\tilde{\rho}\tilde{B}}{(1+f^2)^{5/2}\;\tilde{q}^3}\,\mathcal{A}_x^0 \;+\; \mathcal{O}(M_q^2/\tilde{q}^5) \;+\; \mathcal{O}(1/\tilde{q}^7)\;, \tag{3.4.112}$$

and hence we can compute the Hall conductivity

$$\tilde{\sigma}_{yx} \;=\; -\varepsilon_0\sqrt{1+f^2}\,\frac{\delta A_y'}{\delta \mathcal{A}_x'}\bigg|_{u\to 0} \;=\; -\varepsilon_0\,\frac{3}{2}\,\frac{\tilde{\rho}\tilde{B}}{(1+f^2)^{5/2}\;\tilde{q}^4} + \mathcal{O}(M_q^2/\tilde{q}^6) + \mathcal{O}(1/\tilde{q}^8)\;. \tag{3.4.113}$$

Following through the analysis attentively, one can also see that the imaginary part of the Hall conductivity is exponentially suppressed by a factor of $e^{-q/T_{eff}}$.

This result is remarkable, since the diagonal part of the dissipative conductivity is heavily suppressed with a factor $e^{-q/T_{eff}}$, while the off-diagonal part is only suppressed by a factor of T^4/q^4. This reflects the fact that at small temperatures we approach conformal symmetry in the field theory and hence the form of the conductivity in [99] that we discussed in section 2.5. Having a purely off-diagonal conductivity is not surprising as it is for example the case on the Hall plateaus in the quantum Hall effect or as we demonstrated above in intrinsic semiconductors at small temperatures.

Interestingly it occurs also in intrinsic semiconductors at low temperatures. There the absence of defects and the highly suppressed charge carrier density cause the relaxation time τ to diverge, whilst the carrier mobility remains approximately unchanged. Hence the diagonal conductivity (3.3.44) is suppressed, while the factor $\omega_c\tau$ in the Hall conductivity (3.3.45) causes the Hall conductivity to remain finite.

3.4.3.2 Exponentially suppressed regime at large backgrounds, $\tilde{q}^2 \gg |\tilde{\rho}|, |\tilde{B}| \gg |\tilde{q}| \gg 1$

This regime is slightly more non-trivial, because now ζ_0 splits into three regimes (for simplicity at $M_q = 0$):

$$u \lesssim \frac{1}{\sqrt{\tilde{B}}}, \frac{1}{\sqrt{\tilde{\rho}}} \quad : \quad \zeta_0 \sim \tilde{q}\sqrt{1+f^2}\,, \tag{3.4.114}$$

$$\frac{1}{\sqrt{\tilde{B}}}, \frac{1}{\sqrt{\tilde{\rho}}}, \sqrt{\tilde{\rho}} \lesssim u \ll 1 \quad : \quad \zeta_0 \sim \frac{q\sqrt{1+f^2}}{\sqrt{f^2+\tilde{B}^2+\tilde{\rho}^2 u^2}} \quad \text{and} \tag{3.4.115}$$

$$h \ll 1 \quad : \quad \zeta_0 \sim \frac{q\sqrt{1+f^2}}{\sqrt{f^2+\tilde{B}^2+\tilde{\rho}^2 h}}\,. \tag{3.4.116}$$

In the asymptotic region, the solution is dominated by the decaying exponential, whereas in the near horizon region, it can be written in terms of the coordinate s from section 3.4.1.1 as

$$A_y \;=\; A_y^0 e^{i\nu\, s} \;=\; A_y^0 e^{i\nu\, s \int_0^u \frac{1}{\sqrt{-\bar{G}G^{uu}G^{yy}}}}\,, \tag{3.4.117}$$

where $\nu = \tilde{\omega}\sqrt{1+f^2}\frac{\sqrt{\tilde{B}^2\left(f^2+(1-\Psi_0^2)^2\right)+(1+f^2)(\tilde{\rho}^2+f^2+(1-\Psi_0^2)^2)}}{1+\tilde{B}^2+f^2}$. If this solution were to overlap with the "tail" of the asymptotic solution, $u^4 > f^2+\tilde{\rho}^2+\tilde{B}^2$, we could match them at some $1 \gg u_H \gtrsim (f^2+\tilde{\rho}^2+\tilde{B}^2)^{1/4}$. The fact that they do not overlap, however, can be simply seen from the different u dependence of $\partial_u s = \frac{1}{\sqrt{-\bar{G}}G^{uu}G^{yy}}$ and $\zeta_0 = \tilde{q}\sqrt{\frac{G^{xx}}{G^{uu}}}$. Hence, whatever we try now, the conductivity will disagree by some finite factor. One way to pretend that they do overlap is to simply set $h = 1-u^4 \to 1$ and $u \to 1$, which corresponds to extending the $\frac{1}{\sqrt{\tilde{B}}}, \frac{1}{\sqrt{\tilde{\rho}}} \lesssim u \ll 1$ region towards the horizon and the near-horizon limit into the intermediate region. Matching the solutions under these conditions and ignoring the second part of the solution for ϵ (3.4.98) gives us

$$\epsilon \;=\; -i\tilde{\omega}\sqrt{\frac{1+f^2+\tilde{\rho}^2+\tilde{B}^2}{1+f^2}}\sqrt{\frac{G^{yy}}{G^{uu}}}e^{-2\tilde{q}\int_u^1\sqrt{\frac{G^{yy}}{G^{uu}}}} \tag{3.4.118}$$

with the corresponding conductivity

$$\tilde{\sigma}_{yy} \;=\; -i\varepsilon_0\frac{\tilde{q}}{\tilde{\omega}} + \ldots + \varepsilon_0\sqrt{\frac{1+f^2+\tilde{\rho}^2+\tilde{B}^2}{1+f^2}}e^{-2\tilde{q}\int_0^1\sqrt{\frac{G^{yy}}{G^{uu}}}} + \ldots\,. \tag{3.4.119}$$

Certainly we cannot trust any $\mathcal{O}(1)$ and polynomial factors, but the point to make here is that we should still expect the exponential suppression from the effective temperature (3.4.103). This is because the integral in the exponent is dominated by the region in which ζ_0 does indeed dominate the solution, we took care of the deep near horizon region and elsewhere there are no "large" terms in the equations of motion.

In principle one can also try to find a solution in the regime $\frac{1}{\sqrt{\tilde{B}}}, \frac{1}{\sqrt{\tilde{\rho}}} \lesssim u \lesssim 1$ and then "glue" it to the near horizon and asymptotic solutions to gain more accuracy, but there is limited insight to be learned from this and it would be much more tedious than the calculations in 3.4.3.1.

The Hall conductivity will still be dominated by the asymptotic regime since the mixing from the near horizon region is exponentially suppressed. In principle, it is then still $\tilde{\sigma}_{yx} = -\varepsilon_0 \frac{3}{2} \frac{\tilde{\rho}\tilde{B}}{(1+f^2)^{5/2}\tilde{q}^4}$, however we need to note that the integral that was computed in section 3.4.3.1 is dominated around the maximum of $u^3 e^{-2\tilde{q}\sqrt{1+f^2}u}$ at $u_{max} = \frac{3}{2\tilde{q}\sqrt{1+f^2}}$ and decays then also on the scale $\delta u = \frac{1}{2\tilde{q}\sqrt{1+f^2}}$. ζ and hence also the exponential suppression however start to change around $u_{stop} \sim (f^2+\tilde{\rho}^2+\tilde{B}^2)^{-1/4}$. To properly evaluate the integral in the approximation of 2.2.2, u_{stop} need to be significantly larger than u_{max} – otherwise the "tail" of the polynomial term in the integral will not be sufficiently suppressed and will give a finite contribution to the result, which will greatly overestimate the Hall conductivity. Certainly one can always use the full integral

$$\tilde{\sigma}_{yx} = -\varepsilon_0 \frac{\sqrt{1+f^2}}{\tilde{q}} e^{-2\int_0^1 \zeta_0} \int_0^1 d\tilde{u}\, \zeta_x \left(\sqrt{-G} G^{tu} G^{xy}\right)' \frac{G^{uu}}{\sqrt{-G^{tt}G^{xx}}} e^{2\int_{\tilde{u}}^1 \zeta_0} \tag{3.4.120}$$

but this is certainly a somewhat less insightful result and cannot be computed analytically. In figure 3.10, we demonstrate the boundaries between the different regimes. To see how far the regime of the previous section reaches, we plot $\ln(\sigma_{yy}) - \ln\left(\sigma_{yy}^{(asym.)}\right)$ against $\frac{\ln \tilde{q}}{\ln \tilde{\rho}}$. $\sigma_{yy}^{(asym.)}$ is defined taking $\ln\left(\frac{\sigma_{yy}^{(asym.)}}{\tilde{q}}\right)$ to be the linear expansion of $\ln\left(\frac{\sigma_{yy}}{\tilde{q}}\right)$ at large values of $\tilde{q}$ approximately where $\tilde{\sigma}_{yy} \sim 10^{-15}\varepsilon_0$, shortly before the numerics fail. $\frac{\ln \tilde{q}}{\ln \tilde{\rho}} = n$ corresponds to $\tilde{q} = \tilde{\rho}^n$. This is sensitive to changes in the factor in front of the suppressed conductivities at large $\tilde{q}$. To check for the overall limit of the exponentially suppressed regime, we look directly at $\sigma_{yy} - \sigma_{yy}^{(asym.)}$. It is easy to see that the boundaries at approximately $\tilde{\rho}, \tilde{B} \sim \tilde{q}$ and $\tilde{\rho}, \tilde{B} \sim \tilde{q}^2$ are verified. Using that data, we also looked at the $\mathcal{O}(1)$ factor π in front of the exponential term in the conductivity in (3.4.102). It turns out that for our values of $\frac{q}{T_{eff}} \sim 35$, the numerically estimated factor varied from ≈ 3.8 at $\tilde{\rho} = 0$ to 15 at $\tilde{\rho} = 140$, where the numerics carried us only up to $\tilde{q} \sim \tilde{\rho}$. At the latter values, we could not expect

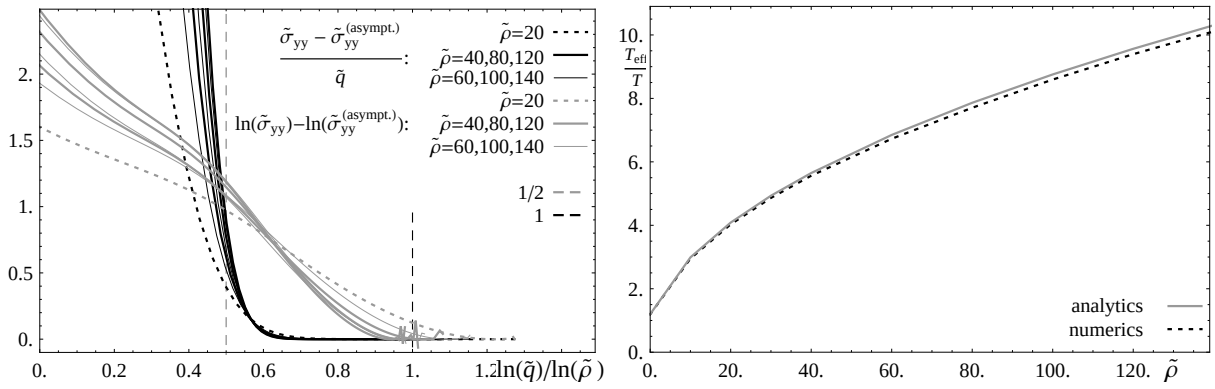

Figure 3.10: Left: The check to the deviation from the $T \to 0$ limit as described in the text. Right: The numerical estimate $\frac{T}{T_{eff}} \sim -\pi\partial_{\tilde q} \ln\left(\frac{\tilde\sigma_y y}{\tilde q}\right)$ compared to the analytical result

close agreement because we were outside the regime that we considered in section 3.4.3.1 – and the value of 3.8 seems reasonably close to π.

3.4.3.3 Dominantly large backgrounds $\tilde\rho, \tilde B \gg \tilde q^2 \gg 1$

As $\tilde\rho, \tilde B \gg \tilde q^2$, we find that $\int_0^1 \zeta_0 \sim 2\tilde q (f^2+\tilde\rho^2+\tilde B^2)^{-1/4} \ll 1$, and hence the exponential suppression factor disappears. Furthermore, as indicated above, our estimate for the Hall conductivity does not apply anymore, as it will be dominated by the region of u in which the assumption $\zeta_0 \gg 1$ does not apply anymore.

Looking at the problem in another way in terms of the coordinate s from section 3.4.1.1 for the DC conductivity with the equation for A_y (3.4.61) gives us the relevant term

$$\partial_u \partial_s A_y = \ldots + \sqrt{-G} G^{yy} G^{xx} \tilde q^2 A_y \ . \tag{3.4.121}$$

Integrating this analytically in the massless case and for for sufficiently slowly varying $\partial_s A_y \ll A_y$, i.e. $\nu \ll 1$, we find $\delta\, \partial_s A_y \int_0^1 du\, \partial_s A_y \lesssim \frac{(1+f^2)\tilde q^2}{(f^2+\tilde B^2+\tilde\rho^2)^{1/4}} \in \mathbb{R}$. A second integration gives $\frac{\delta A_y}{A_y} \lesssim \frac{(1+f^2)\tilde q^2}{\sqrt{f^2+\tilde B^2+\tilde\rho^2}}$ and for larger frequencies ν, the oscillatory behavior of A_y implies that the integral is further suppressed by a factor $1/\tilde\omega$.

Hence, for $\tilde\rho, \tilde B \gg \tilde q^2$, the real part of the conductivity is dominated by the results of the isotropic case in section 3.4.1. The inductive (imaginary) part of the conductivity obviously still receives the term $\tilde\sigma_y y \sim -i\varepsilon_0 \frac{\tilde q}{\tilde\omega}$.

3.5 Numerical Results

In this section, we study information that can be derived from computing the correlators numerically, in particular the overview of the frequency-dependent conductivity (i.e. the spectral curves), the diffusion and relaxation behavior in the hydrodynamic regime, and the spectrum of quasi-particles.

3.5.1 Spectral Curves

In this section, we present the conductivity spectrum in the presence of various background quantities.

First, let us look at the case of finite density and magnetic field alone in fig. 3.11. From the result of the electromagnetic duality in section 3.2.1, and the very generic results for the Hall conductivity in section 3.3.3, we expect to see a sequence of resonances, in which maxima and minima are exchanged between the case of finite net baryon density and magnetic field. The fact that "plasmon" (finite-density) resonances are relatively strong is not surprising since this is a strongly coupled system – and plasmons are a finite coupling effect. The small-frequency regime reflects very well the classical Drude model expectations and the small-frequency expansion from section 3.4.1 – with the Drude peak and magnetoresistance. Looking at the resonances, we find that they are approximately equally spaced at $n\omega_p$ or $(n-1/2)\omega_c$, respectively – and they decay quickly. Comparing this to what we learned in section 3.3.3 reveals interesting information about the quasi-particles that carry the current: They a) must be massive and b) do not consist of chiral fermions, in sharp contrast to graphene [89]. It is also interesting to see that we again have an exponentially decaying amplitude as in the resonance on the width of the defect that we studied in 2.3. The frequencies ω_c and ω_p are, however, not proportional to $\tilde{B}$ and, respectively, $\tilde{\rho}$ and even start off at a finite value. In terms of generic weak-coupling intuition, this would need to be explained by a non-linear magnetization behavior and non-linear chemical potential, and in terms of a changing mass of the quasi-particles that carry the current.

Looking at the f-dependence in figure 3.12, we find that on the one hand, increasing f, i.e. an increasing width z_{max} or stronger "confining potential", reduces the amplitude of the resonances at small frequencies. This is consistent with the value that we found for the DC conductivity (3.4.1.1). In contrast to this, we find that the suppression of the resonances with increasing frequencies decreases with increasing f and we can see the tower of modes, that is at small amplitudes hinted at by the $\tilde{\sigma} = \varepsilon_0$ lines in the plot. This agrees with the

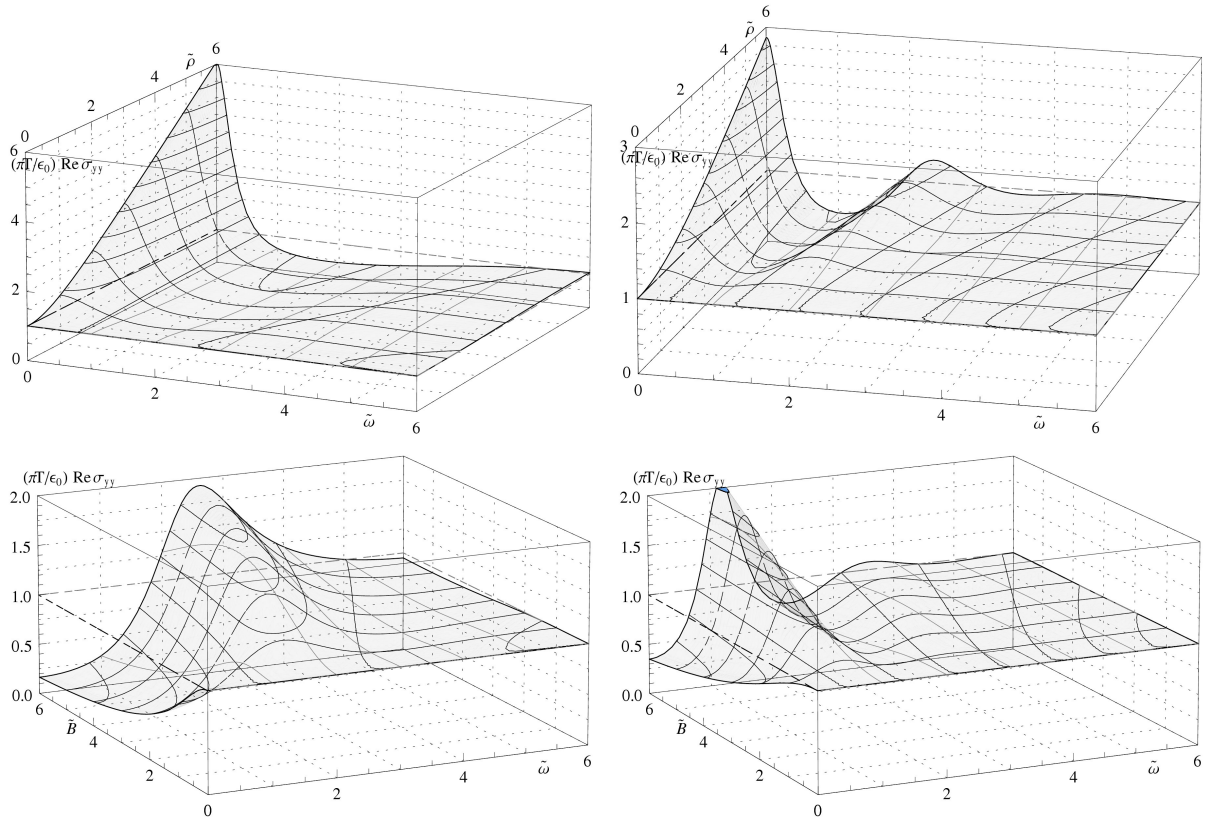

Figure 3.11: The real, diagonal part of the isotropic conductivity at $\tilde{q} = 0$ as a function of frequency and net baryon density (top) or magnetic field (bottom) for $f = 0$ (left) and $f = 2$ (right).

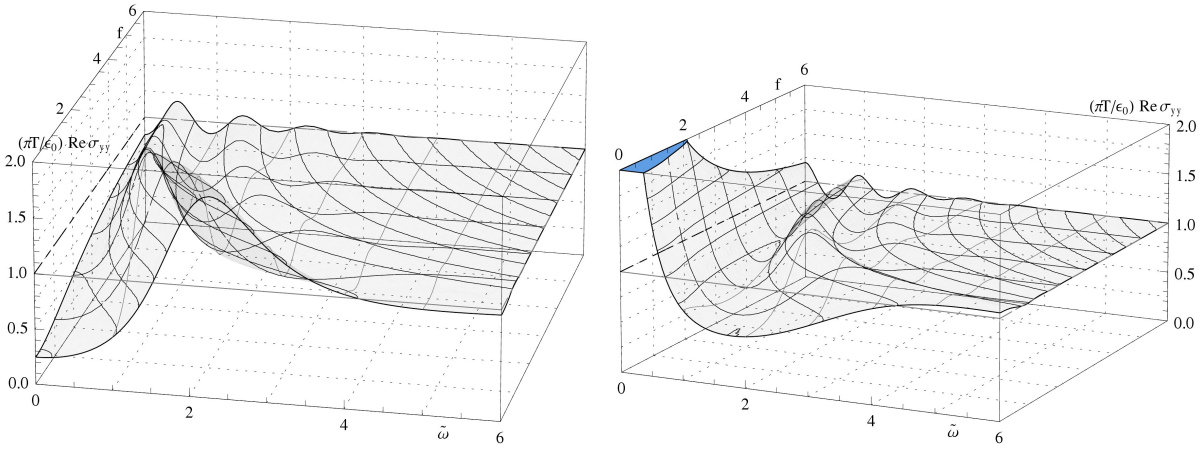

Figure 3.12: The real, diagonal part of the isotropic conductivity at $\tilde{q} = 0$ as a function of frequency and magnetic field for $\tilde{B} = 4$ (left) and $\tilde{\rho} = 4$ (right)

effective temperature (3.4.103) that decreases proportionally to $f^{-1/2}$. Secondly, we find that the parameters ω_c and ω_p decrease with increasing f, which we can again explain by a non-linear behavior of the response functions or by an f-dependent quasiparticle mass.

To see what happens when we turn on a finite wavenumber of the perturbations, we look at fig. 3.13, where we show a few of the higher resonances at $f = 4$ in order to see how they depend on the wavenumber $\tilde{q}$. Looking at the plots on the left, there seems to be only a small difference between the behavior of the Landau levels and plasmons. This difference becomes however very significant when one plots the "normalized" conductivity, $\frac{\tilde{\sigma}}{\sqrt{1-\tilde{q}^2/\tilde{\omega}^2}}$, as a function of the "rest-frame frequency" $\sqrt{\tilde{\omega}^2 - \tilde{q}^2}$ as we had done in section 2.2.2.2. Then, we see that the density resonances connect smoothly to the resonances in the optical regime (i.e. above the conduction threshold $\tilde{\omega} = \tilde{q}$) in the "semiconductor" case at $\tilde{q} \gg 1$. Certainly the statement about the continuity of the pole or "resonance" at $\sqrt{\tilde{\omega}^2 - \tilde{q}^2} = 0$ is somewhat meaningless, since this arises always due to the rescaling (at finite temperatures), but only says that the correlator is finite at $\omega = q$ and does not imply a pole in the correlator. The magnetic resonances, however, seem to be discontinuous – the $n = 0$ Landau level seems to disappear, when the $\sqrt{\tilde{\omega}^2 - \tilde{q}^2} = 0$ pole arises, and the higher resonances behave in a non-monotonic way. In order to see more in detail where this discontinuity comes from, we can look at the $\tilde{B}$ and $\tilde{\rho}$-dependence at a finite wavenumber $\tilde{q} = \pi/2$ and finite $f = 4$ in figure 3.14. There we see that we start off with the "bare defect" and its finite-width resonances, and as we turn on the net baryon density, they shift smoothly, as if we were to decrease the width of the defect. As we turn on a magnetic field,

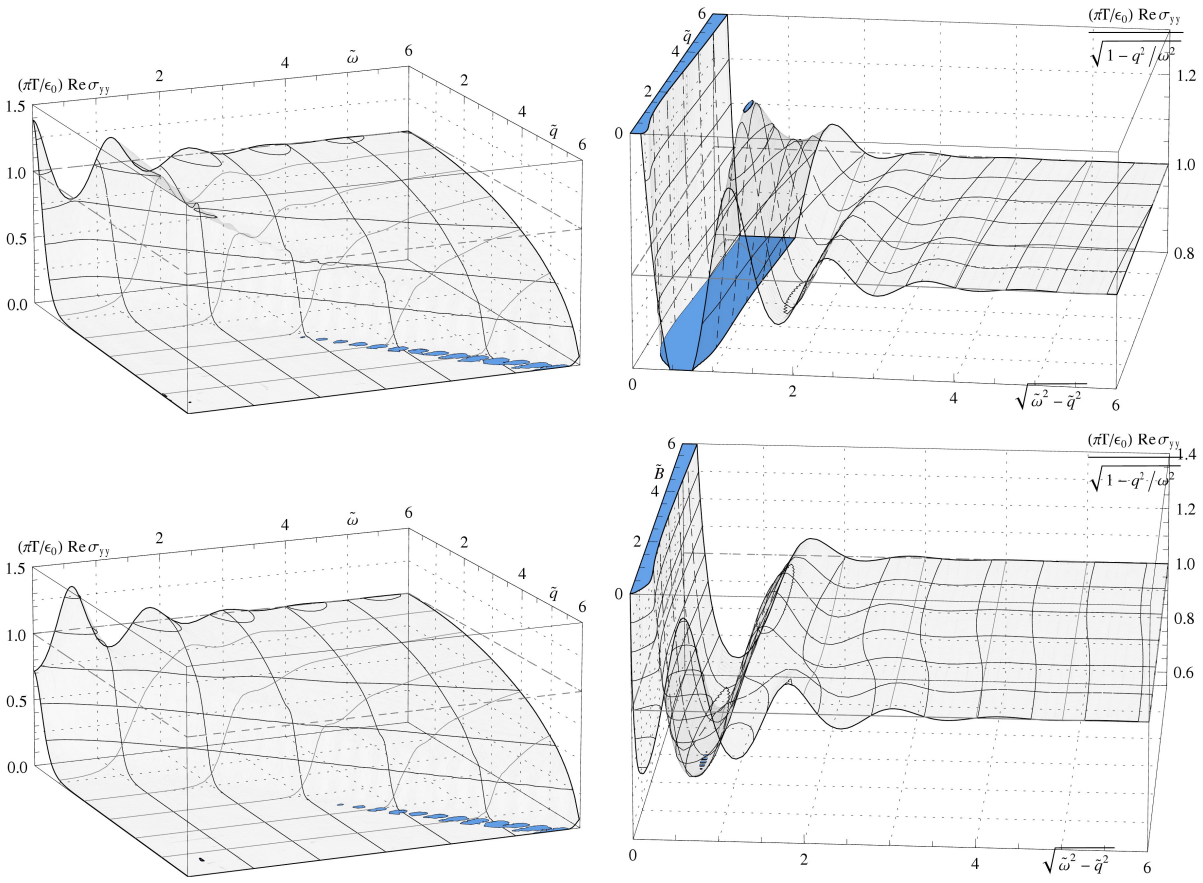

Figure 3.13: The real part of the conductivity σ_{yy} at varying $\tilde{q}$, $f = 2$ and $\tilde{\rho} = 4$ (top) or $\tilde{B} = 4$ (bottom) as a function of $\tilde{\omega}$ (left) and rescaled as $\frac{\tilde{\sigma}_{yy}}{\varepsilon_0\sqrt{1-\tilde{q}^2/\tilde{\omega}^2}}$ as a function of the "rest-frame" frequency $\sqrt{\tilde{\omega}^2-\tilde{q}^2}$ (right).

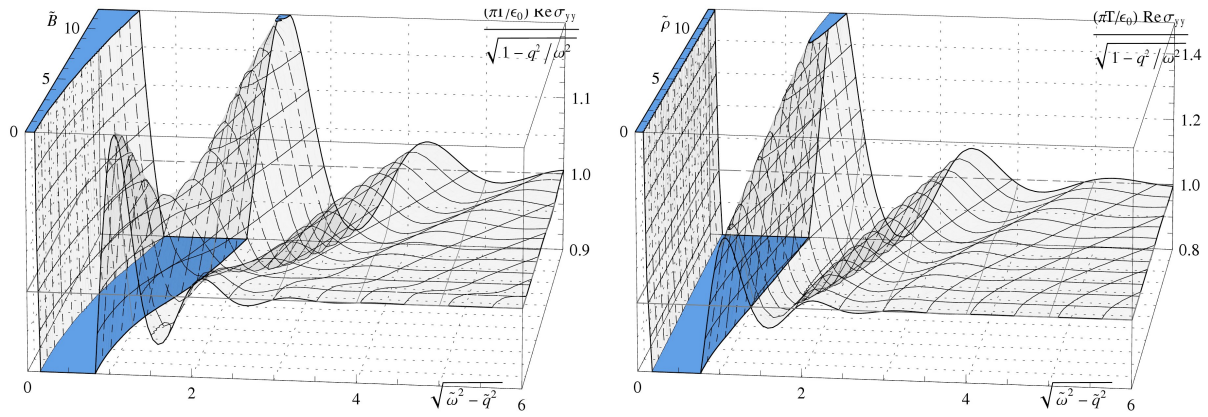

Figure 3.14: $\frac{\mathrm{Re}\ \tilde{\sigma}_{yy}}{\varepsilon_0\sqrt{1-\tilde{q}^2/\tilde{\omega}^2}}$ at $\tilde{q}=\pi/2$ and $f=4$ as a function of the "rest-frame" frequency $\sqrt{\tilde{\omega}^2-\tilde{q}^2}$. Left: As a function of the magnetic field. Right: As a function of the density.

while there is still no apparent splitting of resonances – as one might expect if new kinds of resonances are turned on, they are not monotonically connected. This implies that there are some non-monotonous changes in the residue and location of the poles. It can be easily seen from the electromagnetic duality in the plain defect, that at wavenumber $\tilde{q}=0$, there can be only one pole, which is at $\tilde{\omega}=0$, and hence, assuming continuity, the residue of the poles from the finite-width resonances must be proportional to $\tilde{q}$. On the gravity side, this corresponds to the fact that at $\tilde{q}=0$ there is only one mode function in the gauge field and the equations for A_y and $\mathcal{A}_x$ are the same, but at finite $\tilde{q}$, the equations for A_y (3.2.40) and $\mathcal{A}_x$ (3.2.41) become different. Hence we find two distinct mode functions. The same argument applies for turning on $\tilde{\rho}$ or $\tilde{B}$. This also reflects the fact that generically, the density of states of Landau levels (3.3.56) is proportional to the magnetic field.

A rough, argument in the field theory is that turning on $\tilde{q}$ corresponds to introducing an inhomogeneity in the x direction. Hence, the $U(1)$ perturbations become localized in that direction, whereas they are not localized in the y direction. Plasmons are not generically localized, so they do not change this configuration. Landau levels however are intrinsically localized quasi-particles, so they break translation invariance also in the y direction and change the pattern of the resonances less smoothly. From EM duality, we know that magnetic resonances in σ_{xx} connect smoothly to the finite-width resonances and the density resonances connect less smoothly. This is precisely because in the x direction the translation invariance of the plasmons becomes broken by finite $\tilde{q}$, whereas the Landau levels were already localized.

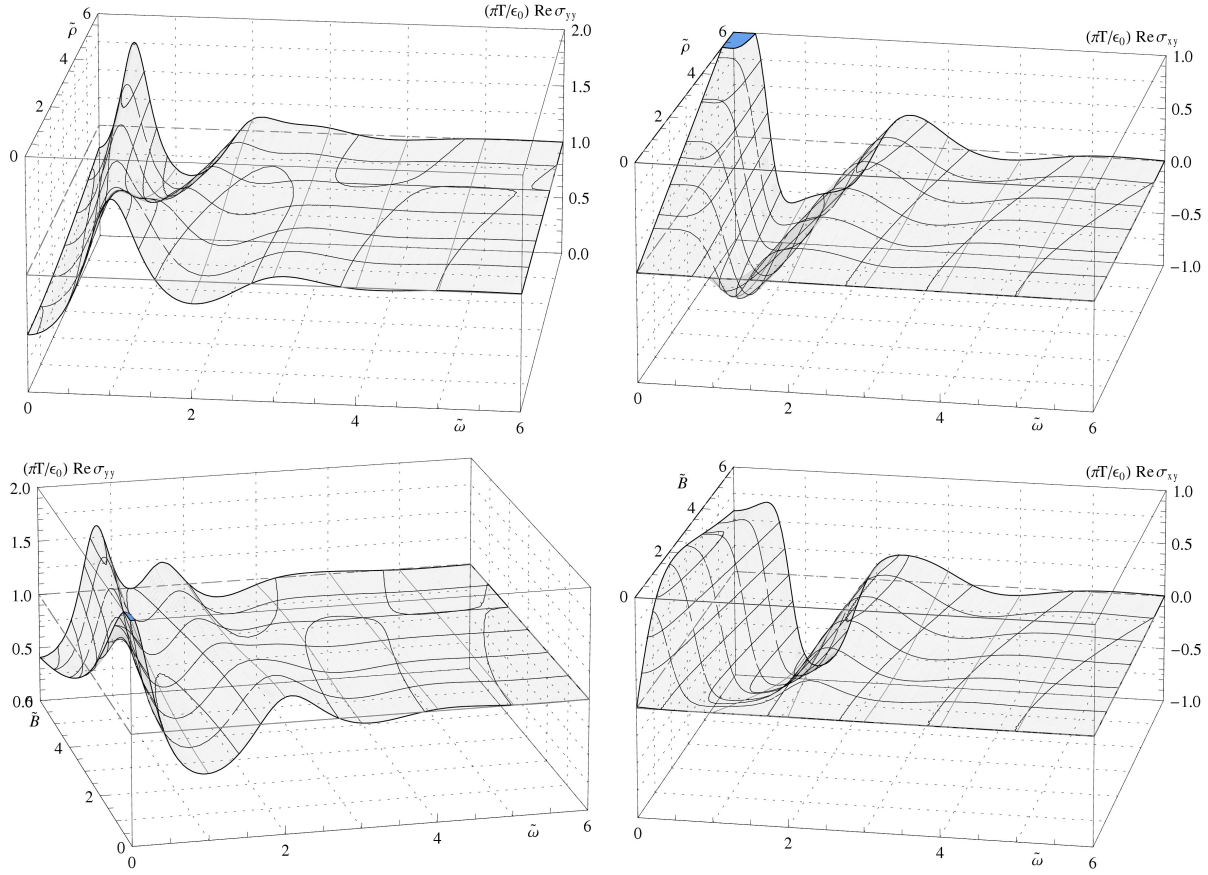

Figure 3.15: The real part of the isotropic conductivity at $\tilde{q} = 0$, $\tilde{B} = 4$ and $f = 2$ as a function of frequency and density (top) and at $\tilde{\rho} = 4$ as a function of the magnetic field (bottom). Left: diagonal part of the conductivity tensor. Right: Hall conductivity.

After studying the effects of having either $\tilde{B}$ or $\tilde{\rho}$ turned on, let us look at the case when they appear simultaneously in fig. 3.15. In the diagonal part of the conductivity tensor, we see that the magnetic- or density resonances split in two as we turn on a net density or magnetic field, respectively. It is interesting, that there is no "tower" of excitations splitting off each resonance and that the mean frequency of each "split level" changes only by a small amount. Furthermore, we find that at each resonance in the diagonal conductivity, the Hall conductivity changes sign, at least for the first two resonances. This is just the continuation of what one expects classically for the first resonance as we saw in section 3.3.1. It is also what one expects semi-classically, if the split states have either positive or negative magnetic moment, carrying a total net Hall current similar to the edge current in the Quantum Hall effect. By continuity, this implies that the plasmons (at zero magnetic field) and the Landau levels (at zero net "charge" density) have vanishing net magnetic moment and equal degeneracy (2). It is also worth noting that it is impossible to have any of the resonances cross $\omega = 0$ no matter how much one tunes the parameters, which clearly indicates that the system has no Fermi level in the classical sense. Otherwise we would see Landau levels crossing $\omega = 0$.

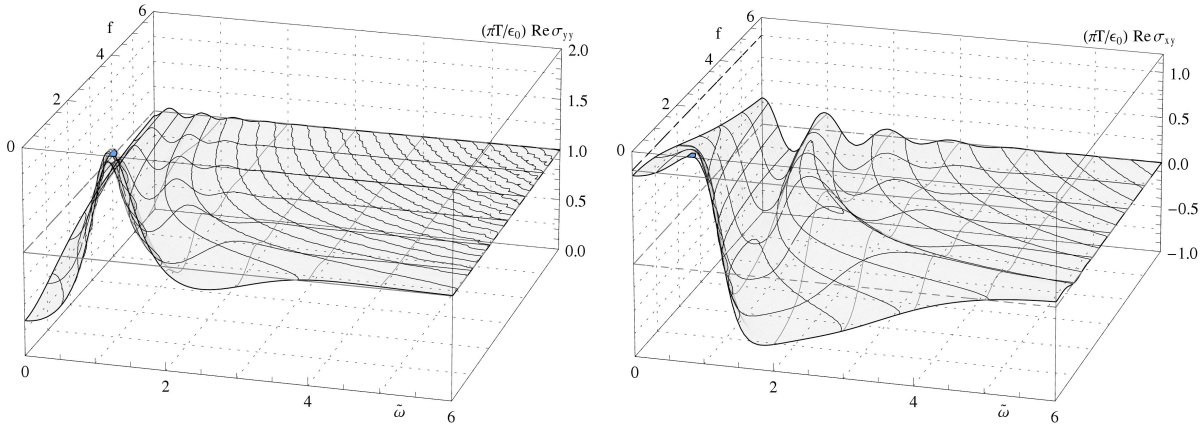

Figure 3.16: The real part of the isotropic conductivity at $\tilde{q} = 0$, $\tilde{B} = 4$ and $\tilde{\rho} = 4$ as a function of frequency and f. Left: diagonal part of the conductivity tensor. Right: Hall conductivity.

For completeness, we can look at the f-dependence of the Hall effect in figure 3.16. This confirms our observations of the relation between the resonances in the diagonal part of the conductivity and the Hall conductivity. In the regime of highly suppressed resonances this appears through their periodicity that differ by a factor of 2. We can also see that

their frequencies roughly behave as the resonance frequencies of the plasmons and Landau levels.

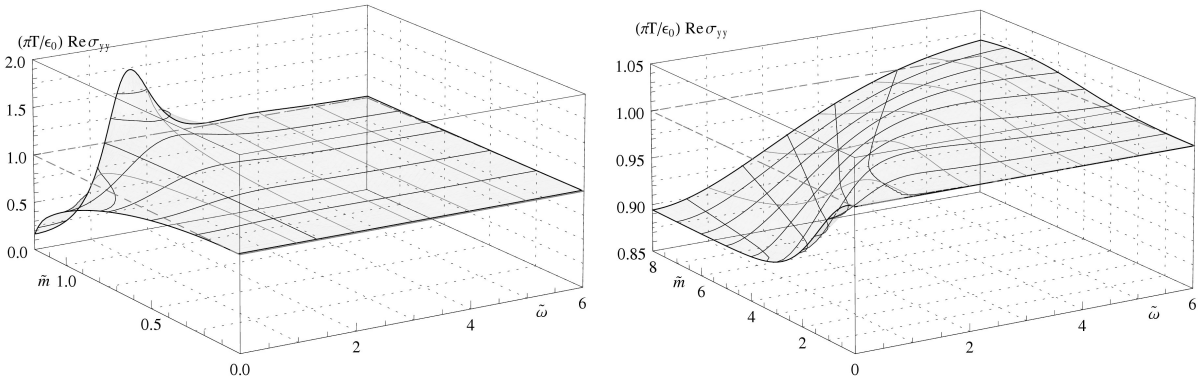

Figure 3.17: The real, diagonal part of the isotropic conductivity at $\tilde{q} = 0$ as a function of frequency and quark mass for $f = 0$, $\tilde{m} \in [0, 1.18]$ (left) and $f = 0$, $\tilde{m} \in [0, 8]$ (right).

Finally, let us look at the mass dependence. In fig. 3.17, we look at the conductivity at $\tilde{q} = \tilde{\rho} = \tilde{B} = 0$, where we actually see the DC conductivity from (3.4.1.1). At $f = 0$, we see a significant change of the conductivity with a resonance around $\tilde{\omega} \sim 1.7$ as $\tilde{m}$ approaches the critical mass of the phase transition from appendix E. This $\tilde{m}$-dependence is suppressed at finite f, and at $f = 2$, the most significant change takes place only over $\tilde{m} \sim 0 \ldots 4$ – simply because it depends roughly on $f^2 + (1 - \Psi^2)^2$ and not on the mass directly, such that the mass dependence becomes "frozen" as Ψ_0 becomes close to 1. In contrast to this indirect mass dependence, the location of the very shallow maximum seems to be roughly proportional to $\tilde{m}$. This gives some nice insight into the IR and UV dependence of the underlying physics. Processes that take place at small energies, i.e. in the IR will be dominated by gravity background near $u = 1$, and hence depend on Ψ_0 and show most of their mass dependence in the regime of $\tilde{m} \sim \mathcal{O}(1)$. Effects that depend on high energies, i.e. the UV, however depend on the background near $u = 0$ and hence depend on $\tilde{m}$ and (only to subleading order) on $\tilde{c}$. We can observe the influence of the quark mass on the finite-$\tilde{q}$ resonances in figure 3.18. There we see that the gap between the resonances is roughly proportional to $\tilde{m}^{-1}$ at large $\tilde{m}$ and the change starts $\propto \tilde{m}^2$ at small $\tilde{m}$ - as one does generically expect for a relativistic system. As naively expected, the resonances are also narrower at large $\tilde{m}$ and their amplitude increases. If we look at the overall level of the conductivity (i.e. ignore the resonances) there seems to be the correction that we found at $\tilde{q} = 0$, now as a correction to the background around which the resonances take place at small $\sqrt{\tilde{\omega}^2 - \tilde{q}^2}$. This also agrees with the picture that we see at $f = 0$. Looking at

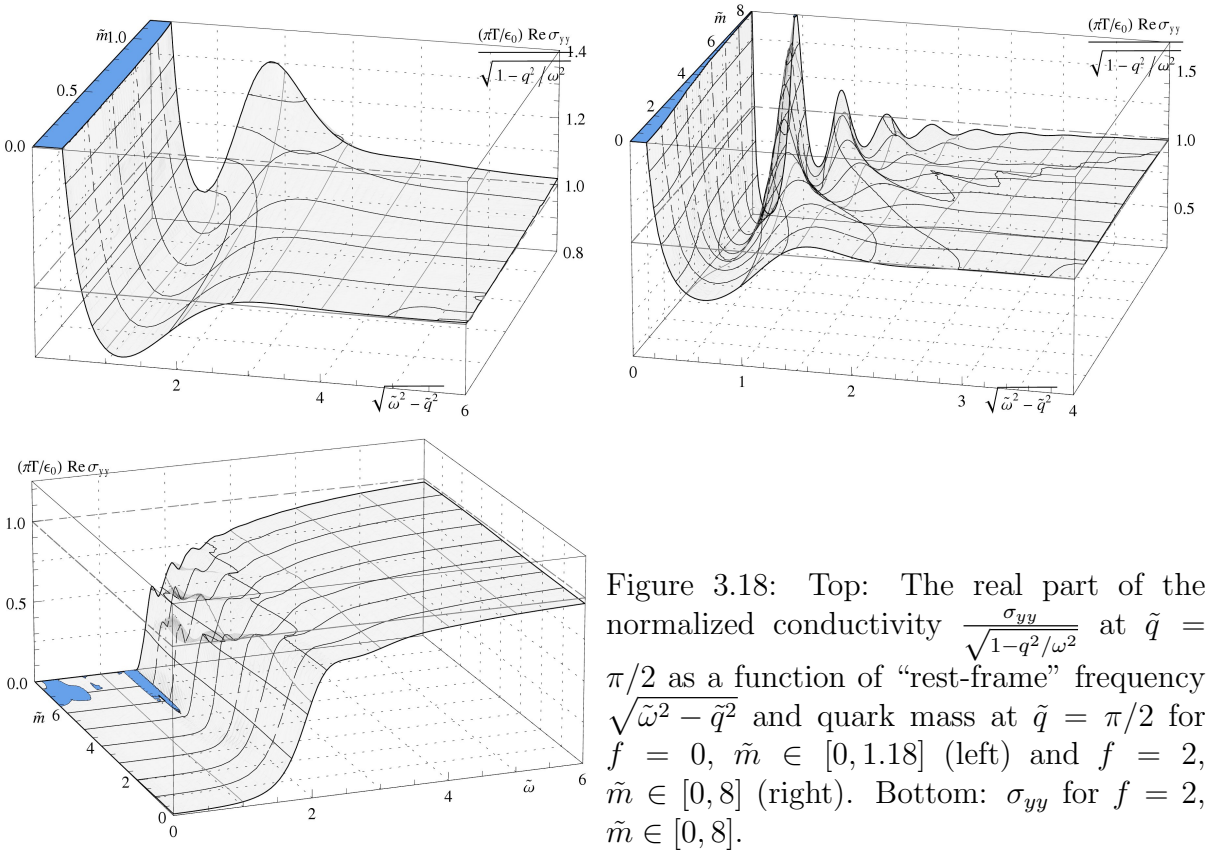

Figure 3.18: Top: The real part of the normalized conductivity $\frac{\sigma_{yy}}{\sqrt{1-q^2/\omega^2}}$ at $\tilde{q} = \pi/2$ as a function of "rest-frame" frequency $\sqrt{\tilde{\omega}^2 - \tilde{q}^2}$ and quark mass at $\tilde{q} = \pi/2$ for $f = 0$, $\tilde{m} \in [0, 1.18]$ (left) and $f = 2$, $\tilde{m} \in [0, 8]$ (right). Bottom: σ_{yy} for $f = 2$, $\tilde{m} \in [0, 8]$.

the un-scaled conductivity, at the bottom in fig. 3.18, we also see that the conductivity approaches the $t \to 0$ limit, $\tilde{\sigma}_{yy} = \varepsilon_0 \mathrm{Re}\ \sqrt{1 - \tilde{q}^2/\tilde{\omega}^2}$ as we increase the quark mass.

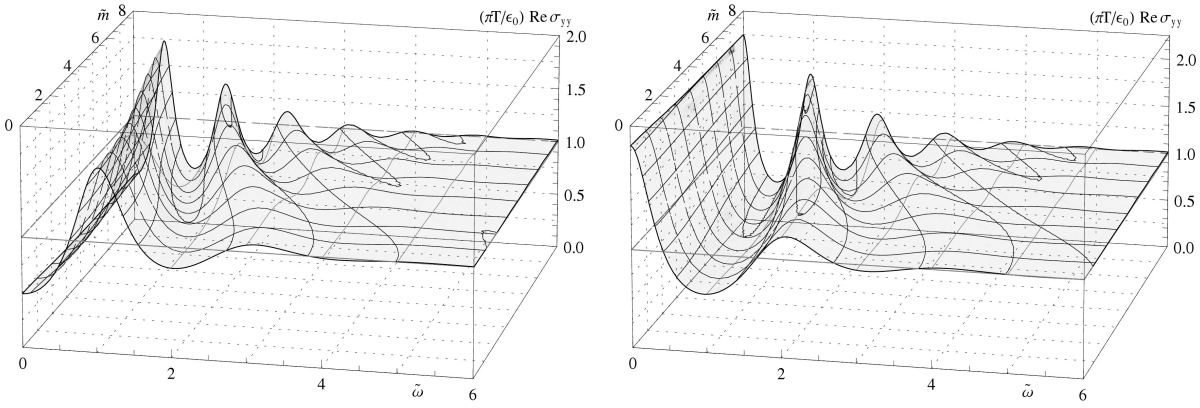

Figure 3.19: The real, diagonal part of the isotropic conductivity at $\tilde{q} = 0$ as a function of frequency and quark mass at $f = 2$ for $\tilde{B} = 4$ (left) and $\tilde{\rho} = 4$ (right)

These generic effects of turning on M_q can also be seen in the plasmons and Landau levels, and in the Hall effect, in figures 3.19 and 3.20. Again, we see that on the one hand, the resonances become more stable at large $\tilde{m}$, and that on the other hand the energy levels receive at small $\tilde{m}$ a small correction $\propto \tilde{m}^2$ and at large masses scale $\propto m^{-1}$, just like ω_c and ω_p do classically.

Finally, we can turn on a large mass (in this case $\tilde{m} = 32$) in order to study the structure of the Hall effect more rigorously. In fig. 3.21, we see that the Hall conductivity has a small overall positive (or negative if we rather look at σ_{yx} or negative $\tilde{B}\tilde{\rho}$) background, and there are poles with alternating residue, each precisely located at a maximum of the diagonal part of the conductivity. This supports exactly our suggestion above that the Hall current is carried collectively by localized states with net positive or negative magnetic moment.

3.5.2 Small frequency regime

In this section, we look at the behavior of the purely dissipative poles of the correlator C_{xx} on the imaginary axis, that dominate the conductivity at small frequencies and wavenumbers. Our particular interest is how they influence the DC conductivity and how the transition to "semiconductor-like" in the quasiparticle regime at larger wavenumbers occurs, i.e. how those poles disappear. We recall that in section 2.3.3, we found two poles

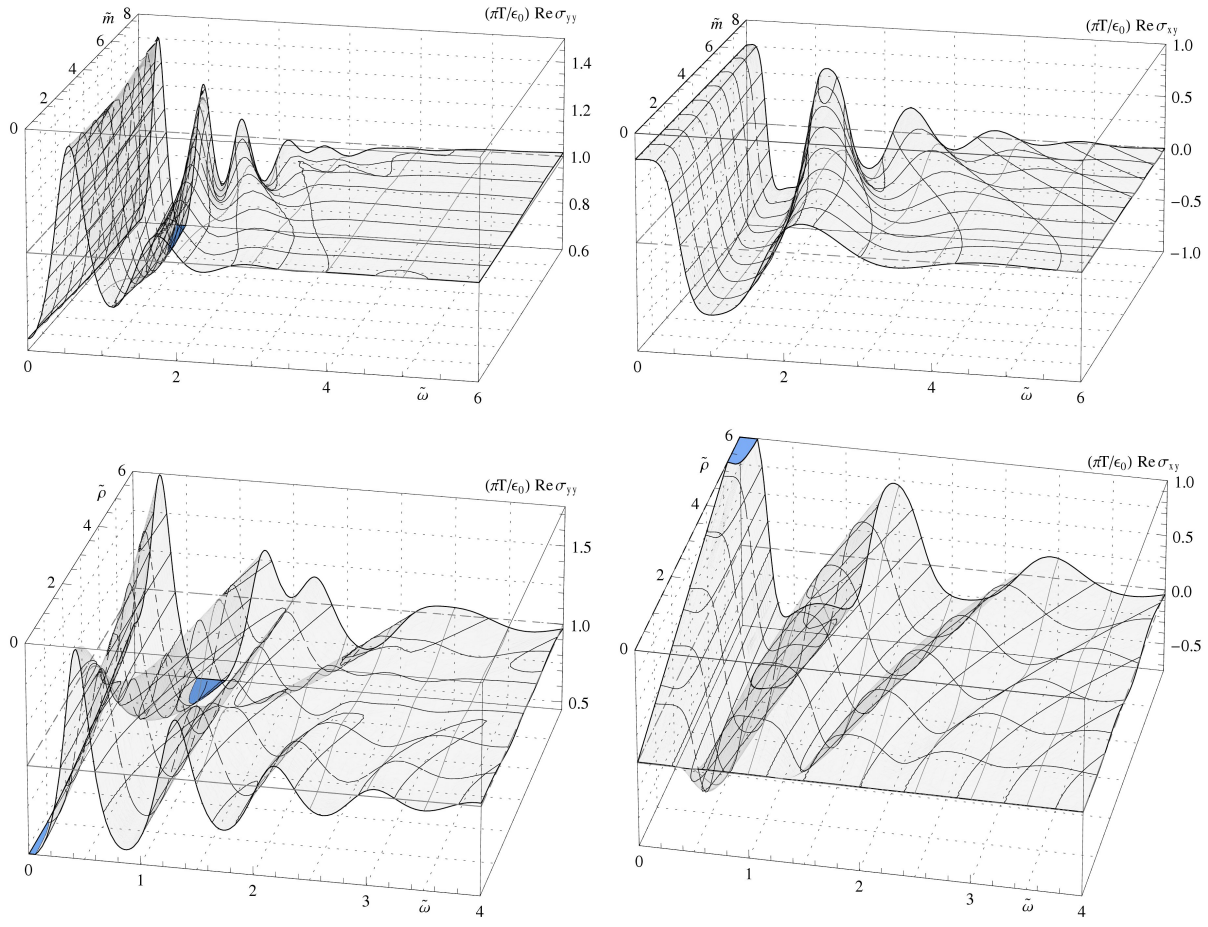

Figure 3.20: The real, diagonal (left) and Hall (right) part of the isotropic conductivity at $\tilde{q} = 0$ and $f = 2$. Top: As a function of $\tilde{m}$ at $\tilde{B} = 4$, $\tilde{\rho} = 4$. Bottom: As a function of $\tilde{\rho}$ at $\tilde{B} = 4$ and $\tilde{m} = 8$.

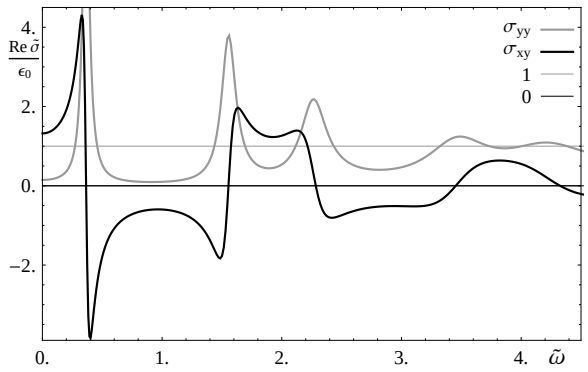

Figure 3.21: $\sigma_{yy} = \sigma_{yy}$ and σ_{xy} at $\tilde{q} = 0$, $\tilde{m} = 32$, $\tilde{\rho} = 32$ and $\tilde{B} = 24$.

– the diffusion pole and one corresponding to decay on thermal scales. Those poles were found to move along the imaginary axis as we increase the wavenumber, meet at some critical wavenumber, and for more short scale excitations turn into massive quasi-particles.

The numerical strategy behind locating the poles is reasonably straightforward. First, we divide the imaginary axis in three regions, based on an educated guess, and localize the poles in these regions in a simple recursive process at some initial wavenumber, magnetic field, quark mass and density. Then, we can identify regions around those poles that allow us to "track" them as we change the parameters, without having to scan the whole imaginary axis. One caveat though is, that it is numerically increasingly difficult to find the poles as their residue decreases, so we keep a minimum wavenumber (we will use $\tilde{q} \geq 0.02$) to always find the "middle" pole. We may also "lose track" of poles if their residue becomes too small. The other caveat is that with our rudimentary method, we need to filter the result afterwards for whether a suspected pole is a pole or just a local extremum or noise. In most cases the distinction is obvious, but in some cases we will look at the value of the residue that we estimate. Furthermore, since this process is reasonably numerically intensive, we will limit the computations to a few examples.

Compared to section 2, we apply more accurate numerics to find that there is also a third pole, corresponding to more rapidly decaying excitations. Obviously, at $\tilde{q} = \tilde{B} = \tilde{\rho} = 0$, there can only be the diffusion pole because then the electromagnetic duality together with isotropy restricts $\varepsilon_0^{-1}\tilde{\sigma} \in \{-1, 1\}$. As we tune these quantities to zero, the residue of both poles vanishes. One of them just disappears to a constant conductivity, while the other one turns into a unit step function of frequency in the conductivity.

First, let us look at the poles in the presence of a finite density. In fig. 3.22, we show the frequency of the diffusion pole and the second pole as a function of $\tilde{\rho}$, and we see that the lower pole follows, at small $\tilde{q}$, the diffusion behavior, and then, at some critical wavenumber,

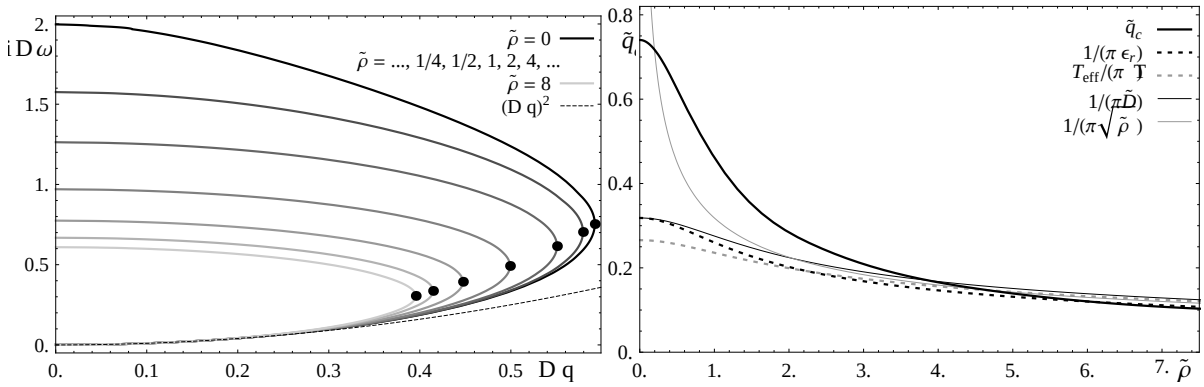

Figure 3.22: Left: Imaginary frequency of the diffusion pole and the first higher pole as a function of $\tilde{q}$ for different values of $\tilde{\rho}$. The frequency and wavenumber are scaled with D, such that the diffusion equation is $D\omega = -i(Dq)^2$. The dot indicates the point where there is the branch cut, and the mode frequency of the poles gain a real part to become quasi-particles. Right: The critical wavenumber as a function of $\tilde{\rho}$, compared to various length scales of the problem: the effective temperature, diffusion constant and the electric permittivity.

they merge and we have again the branch cut with the transition from the dissipative to quasiparticle behavior. It is interesting to note that even beyond the diffusion behavior, the curves agree reasonably closely upon the appropriate rescaling with the diffusion constant. In fig. 3.22, we also plot the critical wavenumber as a function of $\tilde{\rho}$. We see that there is no length scale in our system that fits it particularly well compared to a simple $\pi^{-1}\tilde{\rho}^{-1/2}$ approximation – even though $\frac{1}{\pi\tilde{D}}$ seems to fit best asymptotically. As in the case of the diffusion constant, we note that the critical wavenumber is proportional to $1/\sqrt{\rho}$, and $\sqrt{\rho}$ is approximately the mean separation of the quarks. So at a small net quark density, q_c is dominated by scattering off gluons and quarks from the thermal equilibrium, and at a large net quark density, it is the baryon density that sets this scale.

The imaginary frequency of the third pole is slightly increasing with increasing $\tilde{q}$, but it has a very small residue that decreases with increasing $\tilde{q}$. Hence it can only be seen at $\tilde{q} \sim \mathcal{O}(0.1)$ and we do not plot it here.

To study the nature of the second pole, we look in figure 3.23 at how the location of that pole depends on the net baryon density. We find that this too is proportional to $\tilde{\rho}^{-1/2}$ at large $\tilde{\rho}$, and approaches some finite value at small $\tilde{\rho}$. Also, the dependence on f dominates only the small-$\tilde{\rho}$ regime. In that figure, we also compare the location of this pole to the

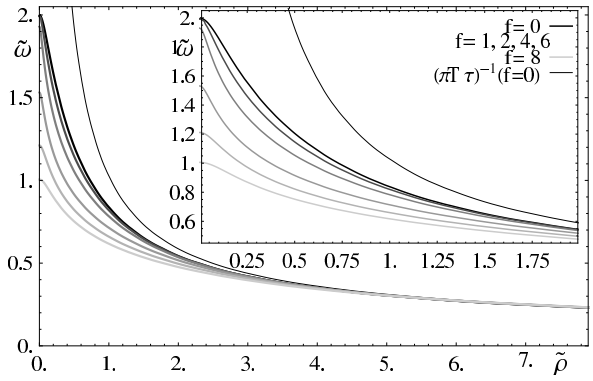

Figure 3.23: The location of the second pole on the imaginary axis as a function of the net baryon density for various values of f. For comparison, we show the inverse correlation time τ^{-1} computed from the conductivity for $f = 0$ only. The other curves for the relaxation time will be in worse agreement at small frequencies.

inverse of the relaxation time τ^{-1} that we obtain from $\frac{\partial_\omega^2 \sigma_{yy}}{\sigma_{yy}}\Big|_{B,\omega\to 0}$ as defined in section 3.3.1 and computed in 3.4.1.2. We find that for large $\tilde{\rho}$, they are in perfect agreement, whereas for small $\tilde{\rho}$, the inverse relaxation time diverges. For clarity, we show only the relaxation time for $f = 0$. The relaxation time for larger f is in worse agreement (τ^{-1} becomes larger at small $\tilde{\rho}$), however the agreement at large $\tilde{\rho}$ is equally good. This disagreement at small $\tilde{\rho}$ reflects the special conformal nature of the system at $\rho = 0$, with the constant conductivity from the electromagnetic duality in (2.4.98). This causes the relaxation time that we computed from the conductivity to vanish, while we can obviously expect that any excitation still decays on a finite timescale as dictated for example by causality. The reason why we do not see this relaxation time in the conductivity at $\tilde{q} = \tilde{\rho} = 0$ and hence why the constant conductivity does not violate causality is that the residue of this relaxation pole vanishes in the isotropic limit at vanishing density. Furthermore, we notice that this theme of exact convergence to the Drude model ((3.3.44) has precisely a pole at $\omega = -i\tau^{-1}$) at large $\tilde{\rho}$ is recurrent and was already seen in figure 3.4 in section 3.4.1.2. From naive intuition about weak coupling, one might be puzzled as to why the relaxation time scales as $\sqrt{\tilde{\rho}}$, i.e. proportional to the inverse of mean separation between the quarks whereas in a simple geometric weakly coupled model, the relaxation time is proportional to the mean free path, that is proportional to the density. Because this system is strongly coupled and there are long-range correlations, however, this intuition breaks down.

This case of very small $\tilde{q} = 0.02$, varying $\tilde{\rho}$ and f is also a good example to study what happens to the third pole. To do that, we can look at fig. 3.24, which shows the location of this higher relaxation pole and (the logarithm of) its residue as a function of $\tilde{\rho}$, at various values of f. We see that the residue decreases exponentially with increasing $\tilde{\rho}$, while the poles move to higher imaginary frequencies, until they can't be tracked anymore. To illustrate this better, the frequency in the region of $\tilde{\rho}$ in which there is no reliable residue information anymore is plotted dashed. This is because the accuracy of the location of

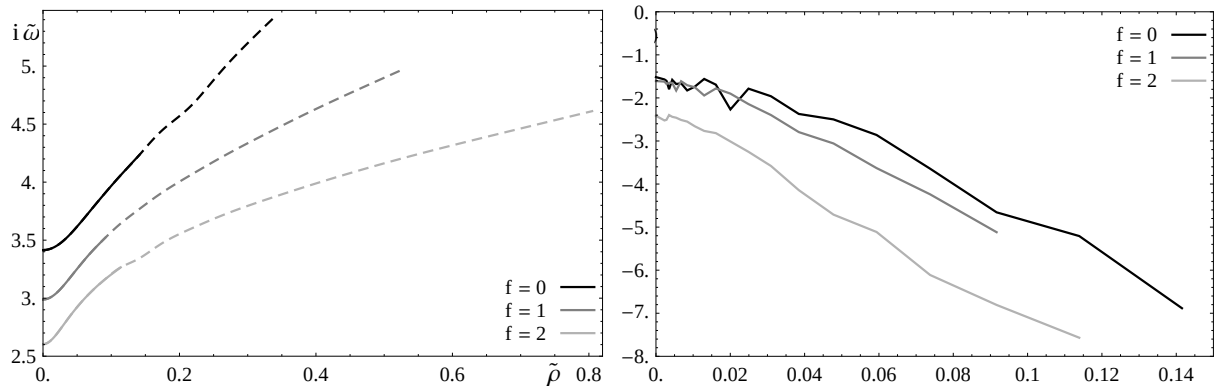

Figure 3.24: Left: The location of the second relaxation pole as a function of the net baryon density for various values of f. Right: The logarithm of the residue of the second relaxation pole.

the pole that is necessary to determine the residue with our methods is of the order of the residue. Obviously, there is no guarantee that the extremum that one finds actually is a pole if there is not good enough data to compute the residue. One could argue that we could go to much higher accuracy since the accuracy grows exponentially with the number of steps. However the number of steps needed to track the poles grows with the inverse of the residue, i.e. exponentially with increasing $\tilde{\rho}$ or $\tilde{q}$. If we look at the density dependence of this pole, we find that its imaginary frequency increases with increasing density – which is just what we expect for a naive model of weakly-coupled particles with finite cross sections σ. In particular, for small cross sections in d dimensions, $\sigma^{1/(d-1)} \ll \rho^{-1/d}$, one expects classically $\tau_{cl.}^{-1} \sim v\sigma\rho$, where v is some characteristic speed. Hence for larger densities or larger cross sections, the scaling would naively approach $\sqrt{\rho}$. This is just what we see in fig. 3.24. Hence, despite the limited accuracy and reliability in tracking these poles, we can safely associate this pole with a classical, weakly-coupled relaxation behavior.

A behavior very much in contrast to the case of turning on the finite density can be found in fig. 3.25, where we show how the relaxation poles behave at small wavenumber in the presence of a magnetic field. We see that with increasing magnetic field, the relaxation poles merge at some critical magnetic field, $\tilde{B}_c$, and then turn into the first Landau level. This contrasts to the classical Drude-model analysis, where the magnetic pole moves away from the imaginary axis as soon as the magnetic field is turned on. Essentially what is happening is that the creation of the first Landau level is inhibited below $\tilde{B}_c$ because of the strong coupling. If we assume a crude model, in which the frequencies are given by

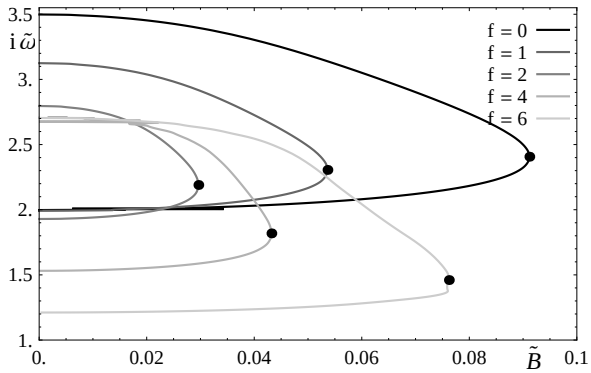

Figure 3.25: The location of the relaxation poles as a function of the magnetic field for various values of f.

$-i\frac{\tau_{cl.}^{-1}+\tau^{-1}}{2} \pm \sqrt{\tilde{\omega}_c^2 - \frac{(\tau_{cl.}^{-1}-\tau^{-1})^2}{4}}$, then we see the reason for the dependence of the curves on f. Now, remember that we found in section 3.4.1.1, that $\tilde{\omega}_c\tau \sim \frac{\tilde{B}}{\sqrt{1+f^2}}$, such that $\tilde{B}_c$ is approximately given by the ratio of the relaxation times at vanishing magnetic field, $\tilde{B}_c \sim \frac{\sqrt{1+f^2}}{2}\left(\frac{\tau_{cl.}^{-1}}{\tau^{-1}} - 1\right)_{B=0}$. This ratio depends non-monotonically on f, because apparently the location of the classical relaxation pole is not closely related to the location of the first relaxation pole. Obviously, this generic behavior is not exact, but provides a rather qualitative description.

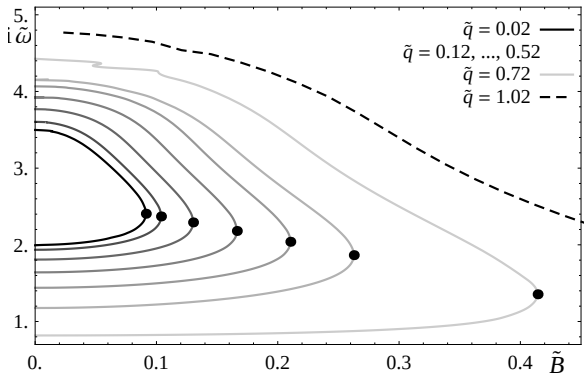

Figure 3.26: The location of the relaxation poles as a function of the magnetic field for different wavenumbers.

This magnetic dependence is consistent with the dependence of the relaxation poles on the wavenumber that we show in fig. 3.26. In fact, now it is most apparent that the behavior is reasonably well-described in terms of $\tau_{cl.}/\tau$ only. This can be seen by computing $\frac{1}{2\tilde{B}_c}\left(\frac{\tau_{cl}^{-1}}{\tau^{-1}} - 1\right)_{B=0}$. For the data in fig. 3.26, this ratio is approximately constant, ranging from 4.2 at $\tilde{q} = 0.02$ to 5.3 at $\tilde{q} = 1.2$. Certainly it is not close to 1, but we could not expect

this, as we chose our expression only as an example of how a branch cut in the solution for the location of the poles as a function of the background parameters can look like. This shows us however how suppressing the first Landau level is related to strong coupling, as the critical magnetic field is proportional in some approximation to the difference between the classical and strong-coupling inverse relaxation times.

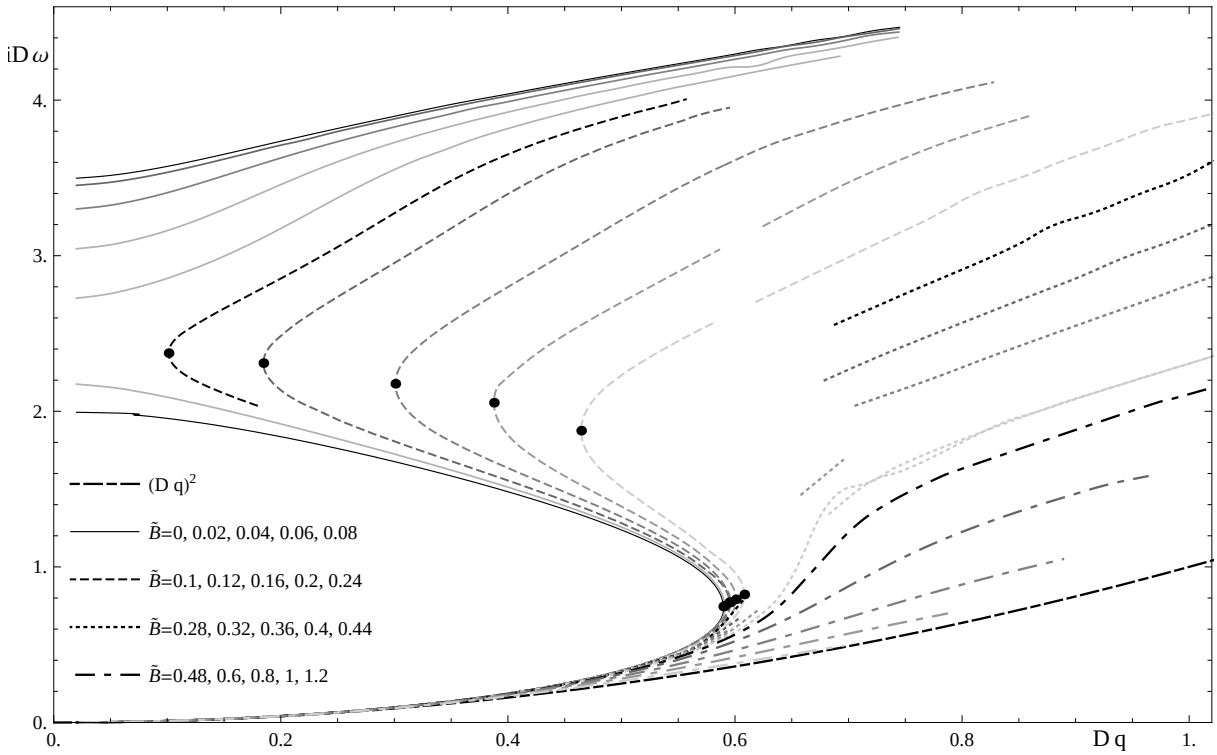

Figure 3.27: The location of the poles on the imaginary axis as a function of the wavenumber for different values of the magnetic fields. The frequency and wavenumber are scaled with the diffusion constant, as the diffusion behavior can be written as $iD\omega = (D\,q)^2$.

Finally, we can look in fig. 3.27 at the dependence of the location of all three poles on the wavenumber at varying magnetic field. At vanishing magnetic field, we start off with the system in which there is the hydrodynamic to quasiparticle transition, and there exists always the classical relaxation pole, that moves towards larger $\tau_{cl.}^{-1}$ with increasing $\tilde{q}$. Going beyond the critical magnetic field, we see that the relaxation poles re-appear at some wavenumber $q_B < q_c$ that increases with increasing magnetic field. Beyond some second critical magnetic field, at which $\tilde{q}_B = \tilde{q}_c$, there is only one imaginary pole, that

starts off at small $\tilde{q}$ as a diffusion pole and turns at large $\tilde{q}$ into the classical relaxation pole. Interestingly, at large wavenumbers, we always see only the classical relaxation pole, so the "strong" relaxation pole is an effect that arises only at small wavenumbers, i.e. long-distance perturbations, which is what one actually expects, because of the diverging correlation length. The effect that the magnetic field inhibits relaxation on large length scales is precisely what we expect because of the localizing effect of the magnetic field on charged particles. This behavior between the critical magnetic fields, in which a pair quasiparticle poles (with positive and negative real part of the frequency) turns into a pair of relaxation poles and then into a different quasiparticle pole nicely reflects the transition between the regime dominated by Landau levels and the regime dominated by resonances on the width of the defect, that we observed in the previous section. Furthermore, we see just as in section 2.3.3, that under the appropriate rescaling with the diffusion constant, the curves agree even beyond the actual behavior proportional to $\tilde{q}^2$ – indicating that $\tilde{q}_c$ is reasonably well-described by the lengthscale from the diffusion constant. The attentive reader will notice the "hole" in the plot near $\tilde{q}_c$. This arises because it is difficult to track the poles in this regime using our method of scanning the frequency for each value of $\tilde{q}$ in this case. Obviously, swapping that order should allow us to determine the location of the poles also in this regime.

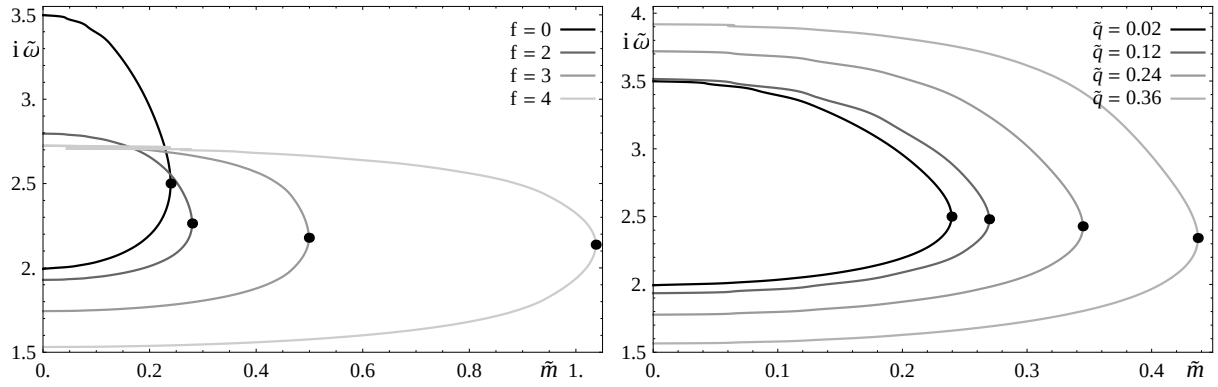

Figure 3.28: The imaginary frequencies of the relaxation poles as a function of the quark mass. Left: For various values of f. Right: For various values of $\tilde{q}$

The effect of turning on a finite quark mass is very similar to the case of the background magnetic field, as we see in fig. 3.28. The most significant difference is in the f-dependence, as the critical mass at which the relaxation frequencies receive a real part increases quickly as we increase f. This is due to the fact that the hydrodynamics is dominated by physics in the IR, i.e. at small radii and hence depends on Ψ_0 rather than the mass directly and

the quark mass as a function of Ψ_0 increases with increasing f.

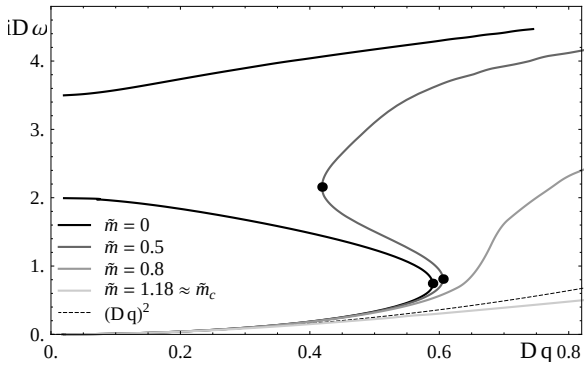

Figure 3.29: The location of the poles on the imaginary axis as a function of the wavenumber for different values of the quark mass. The frequency and wavenumber are scaled with the diffusion constant. For comparison, the critical mass for the embedding is $\tilde{m} \sim 1.196$.

Looking at the picture of the location of the poles as a function of the wavenumber in fig. 3.29, we find again that the system at small imaginary frequencies and small wavenumbers is well-described by the diffusion behavior, however not up to as high wave numbers as in the case of the background magnetic field. The critical mass above which there is always only the classical relaxation pole is just below $\tilde{m} \sim 0.75$.

3.5.3 Landau Levels and Plasmons

In this subsection, we will try to shed some light on the nature of the magnetic and density resonances that we observed in section 3.5.1, by studying the corresponding quasiparticle poles. For simplicity, we will focus on the isotropic ($\tilde{q} = 0$) case. In principle, there are again different methods of estimating the location of the poles. The least reliable method is simply fitting Lorentzians to the resonances. However it cannot give the right answer, as we expect a sequence of infinitely many poles with separation $\nu_0 - i\gamma_0$, and if we consider the n^{th} resonance and provided ν_0 and γ_0 are of the same order, we need to consider more than $\mathcal{O}(n)$ neighboring poles. The more precise method involving only the data on the real (frequency) axis is then as in section 2.3.1 based on assuming an appropriate sequence of poles, summing it (ideally analytically), and fitting the parameters locally around each maximum - assuming they vary slowly enough, such that the "backreaction" from the varying parameters is sufficiently suppressed. The third method is simply trying to fit the poles by scanning an area in the complex frequency plane using an appropriate guess obtained from the data on the real axis. Then, we can use the usual recursion to find the poles. The most time consuming step in that method is to scan the search area for the first time, since we can not assume that the poles are the only local extrema. For the former

technique, we use again the Ansatz (2.3.91) – but it turns out that methods to try to fit the resulting analytic expression (2.3.92) are unreliable in this case, mainly because of the periodicity of the expression. This Ansatz basically says that all the poles are located with equal spacing on a straight line at $\nu_n = n(\pm\nu_0 - i\gamma_0)$ (or $\nu_n = (n-1/2)(\pm\nu_0 - i\gamma_0)$ for the Landau levels), with residues $\frac{\varepsilon_0}{\pi}\frac{\nu_n}{n}$ (or $\frac{\varepsilon_0}{\pi}\frac{\nu_n}{n-1/2}$). From (2.3.93), we can then obtain the parameters for the poles from the n^{th} local maximum, σ_n, ω_n and its neighboring minima $\sigma_{n-1/2}$, $\sigma_{n+1/2}$. Assuming $\sigma_{n-1/2} = \sigma_{n+1/2} = \sigma_{min}$, the exact result is in the case of plasmons

$$\sigma_n - \sigma_{min} \;=\; -2\frac{\varepsilon_0}{\sinh\frac{2\pi\tilde{\omega}_n\tilde{\gamma}_0}{\tilde{\nu}_0^2+\tilde{\gamma}_0^2}} \quad , \quad \tilde{\omega}_n \;=\; n\frac{\tilde{\nu}_0^2+\tilde{\gamma}_0^2}{\tilde{\nu}_0} \tag{3.5.122}$$

and similar for Landau levels. This expression can be trivially inverted to obtain $\tilde{\nu}_0$ and $\tilde{\gamma}_0$. Taking into account that $\sigma_{n-1/2} \neq \sigma_{n+1/2}$, the correction when using $\sigma_{min} = \frac{1}{2}\left(\sigma_{n-1/2} + \sigma_{n+1/2}\right)$ will be of order $\frac{\pi^2\tilde{\gamma}_0^2}{\tilde{\nu}_0^2}\left(\cosh\frac{n\tilde{\gamma}_0}{\tilde{\nu}_0}\right)^{-1}$, i.e. it will only be significant for the first few poles. However this seems to be a less bothersome shortcoming to take than "misfitting" poles because of the periodicity. Note that the two terms in the error term, make sure that beyond $n = 1$ always either of them gives us a good suppression.

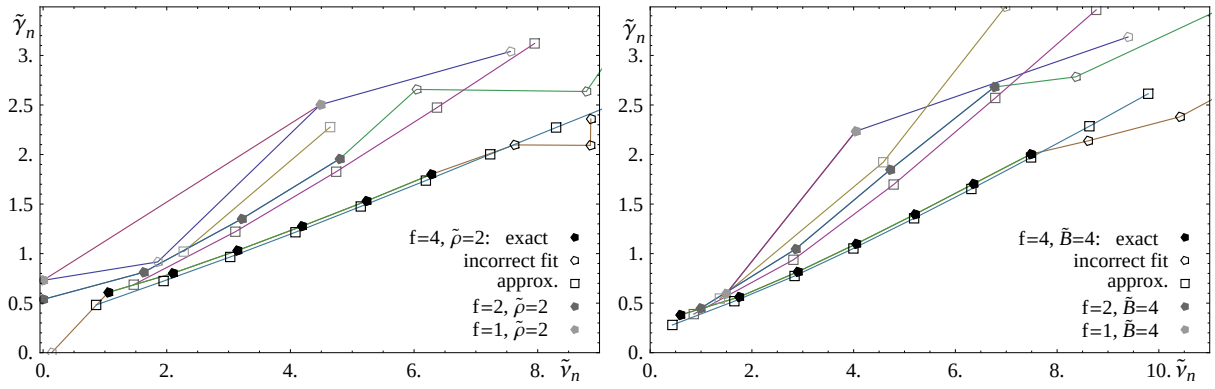

Figure 3.30: The location of the poles $\omega_n = \nu_n - i\gamma_n$ in the complex frequency plane from the different estimates as described in the text. For orientation purposes, the lines connect the poles of different order in the same background. Left: Finite $\tilde{\rho} = 2$, Right: Finite $\tilde{B} = 4$

In fig. 3.30, we compare the two methods to obtain the poles – the "exact" direct search and the "approximate" result from fitting to the Ansatz – for various values of f, $\tilde{B}$ and $\tilde{\rho}$. In the direct search, we used the maximum value of the spectral function in

the last recursion as an indicator as to whether the pole has been found, with a threshold at $\frac{\tilde{\sigma}(\tilde{\nu})}{\varepsilon_0} = 100$. In practice the value will be either much larger or much smaller than this number. In the plot, we still show the "misfitted" poles for reference. Overall, we see that the agreement of $\tilde{\nu}_0$ is very good at finite f, and the estimates from the spectral curves are much more reliable in the sense that there are no poles that are "not found" or have large displacements. In fact, even if there is some disagreement, the spacing $\tilde{\nu}_0$ between the poles is more accurate than the overall shift of the poles. While there may be larger disagreements for the first pole and at small values of f, we should note that in those cases the direct fitting also fails frequently. There is no clear trend for the dependence on $\tilde{\rho}$ and $\tilde{B}$. Typically the approximation is slightly worse for very large values and very small values, because in the former case the decay is more rapid, causing the resonances to be more asymmetric. In the latter case, we also see only the first few resonances and are not in the slowly decaying oscillatory regime – this time because of the larger spacing between resonances. We will not demonstrate this in the plots in fig. 3.30, simply because $\tilde{\gamma}_0/\tilde{\nu}_0$ is approximately constant when varying $\tilde{B}$ or $\tilde{\rho}$ at fixed f, and hence this is difficult to display in a clear fashion. The agreement in the imaginary direction is slightly worse, which is not unexpected because it depends more on the conjectured form of the residues for the Ansatz.

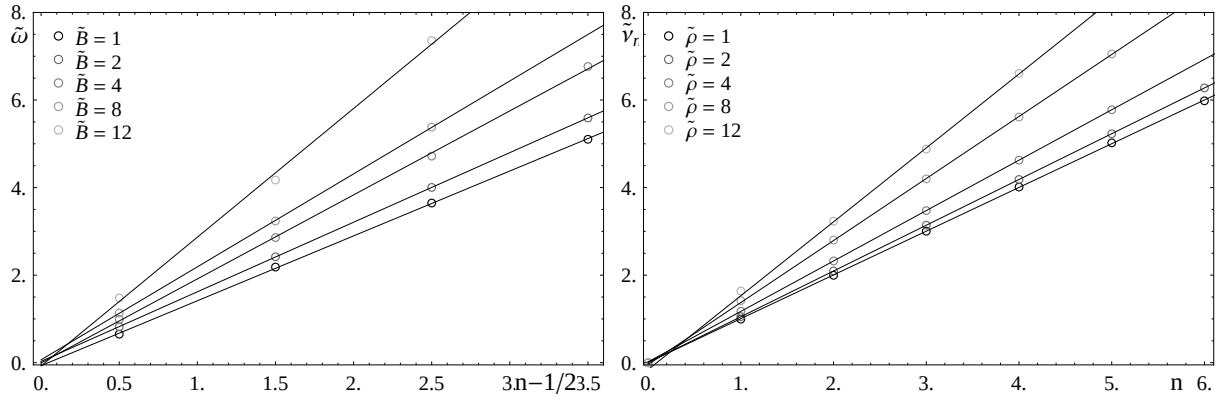

Figure 3.31: The real part $\tilde{\nu}_n$ of the location of the poles in the complex frequency plane as a function of the level number. The lines are linear fits. Left: Various values for $\tilde{B}$ at $f = 2$. Right: Varying $\tilde{\rho}$ at $f = 4$

Next, let us look at the spectrum of the resonances as a function of the resonance level n. In figure 3.31, we show the real part of the poles $\tilde{\nu}_n$ for various choices of $\tilde{\rho}$ and $\tilde{B}$ at $M_q = 0$. Because it is important to distinguish between behaviors that are, for example, of the kind $\sqrt{n(1+n)}$ from strictly linear behaviors, we used the direct search for poles in

order to obtain the highest accuracy. It turns out that the poles follow extremely closely a linear behavior $\tilde{\nu}_n = n\tilde{\nu}_0 + \delta\tilde{\nu}$ (or $\tilde{\nu}_n = (n-1/2)\tilde{\nu}_0 + \delta\tilde{\nu}$ in the case of a magnetic background field), with a small negative value for $\delta\tilde{\nu}$. The latter is easily explained from the behavior of the first pole that we found in the hydrodynamic regime. The constant separation implies that the spectrum of Landau levels is indeed the classical one for the finite mass case. This is slightly puzzling though, because one would have thought that if the collective excitations that carry the current have an effective mass, this mass would be finite. Then we should see a transition from the massive to the massless behavior at some frequency. Hence, either that mass must be large or frequency dependent, or some unusual mechanism gives rise to the Landau levels.

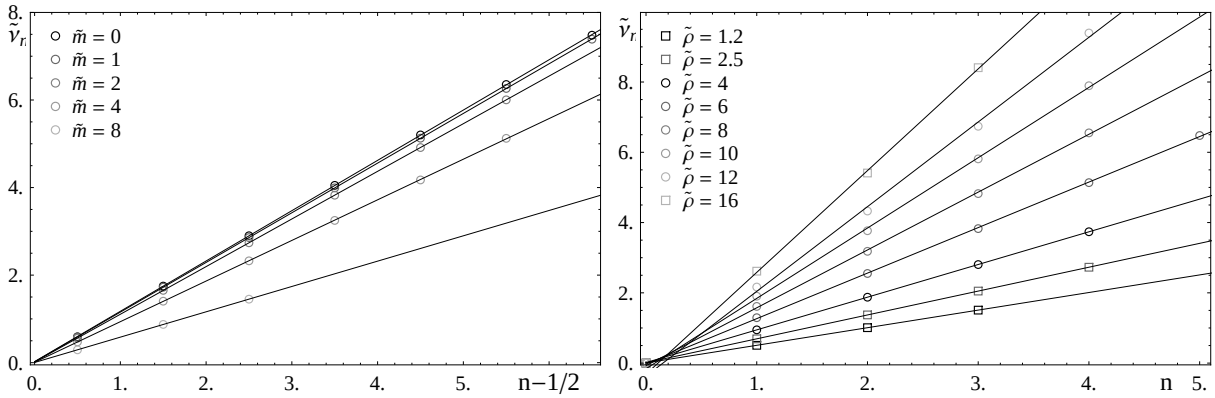

Figure 3.32: The real part $\tilde{\nu}_n$ of the location of the poles in the complex frequency plane as a function of the level number at finite quark mass. Left: Varying $\tilde{m}$ at $\tilde{B} = 4$ and $f = 4$. Right: Different values of $\tilde{\rho}$ at $\tilde{m} = 8$ and $f = 2$.

Looking at the case of finite quark mass in fig. 3.32, we find again no sign of a non-constant spacing between the poles, surprisingly even around the level of the quark mass. There is however a transition in the value of $\tilde{\nu}_0$ around that region, which we will follow up on later.

Finally looking at the behavior of the imaginary part of the poles, which reflects the inverse lifetime, in fig. 3.33, we find a small but significant deviation from the linear relation $\tilde{\gamma}_n = n\tilde{\gamma}_0 + \delta\tilde{\gamma}$ (and accordingly for the Landau levels). This small drift towards larger $\tilde{\gamma}_n$ for small n can again be explained from the non-trivial behavior of the first (hydrodynamic) poles and from the fact that we are in a finite temperature background, which renders the first few resonances that are close to the temperature scale less stable.

Finally, we can look at the resonances. Before looking at $\tilde{\nu}_0$, let us study the shift $\delta\tilde{\nu}$

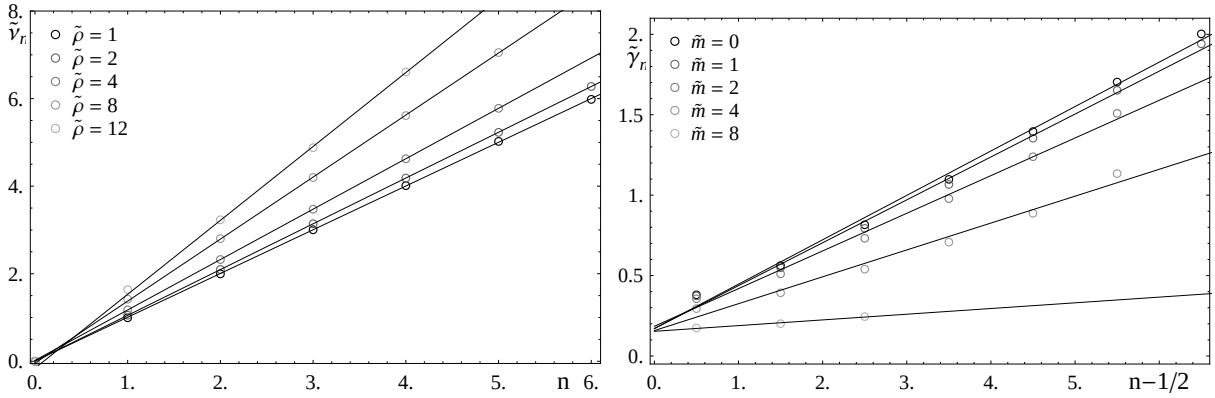

Figure 3.33: The imaginary parameter in the location of the poles, $\tilde{\omega}_n = \tilde{\nu}_n - i\tilde{\gamma}_n$. Left: Varying values of $\tilde{\rho}$ at $f = 4$. Right: Varying mass $\tilde{m}$ at $f = 4$ and $\tilde{B} = 4$.

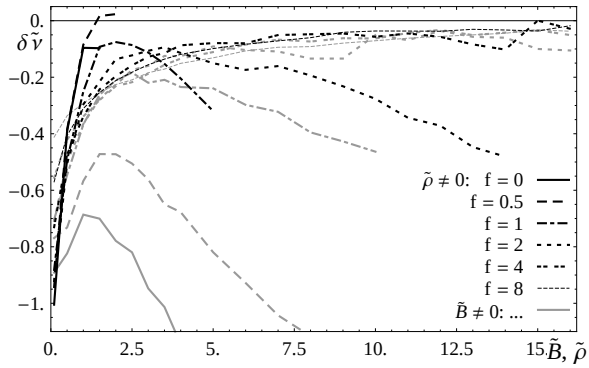

Figure 3.34: The overall shift in the poles $\delta\tilde{\nu}$ as a function of $\tilde{B}$ or $\tilde{\rho}$ for various values of f.

in fig. 3.34. We find that for large f, there is a universal behavior $\delta\tilde{\nu} \propto \tilde{B}^{-1}, \tilde{\rho}^{-1}$ with a proportionality constant that seems independent of f. A significantly different behavior exists only for small values of f and large values of $\tilde{B}$ or $\tilde{\rho}$. This may be simply due to the worse fitting because in those cases we found only the first two poles, and the second one has already a very low amplitude such that it is at the limit of what can be recognized as a resonance above the background. This overall behavior may be simply due to the fact that the first quasiparticle pole originates from the relaxation poles on the imaginary axis as we found in the previous section.

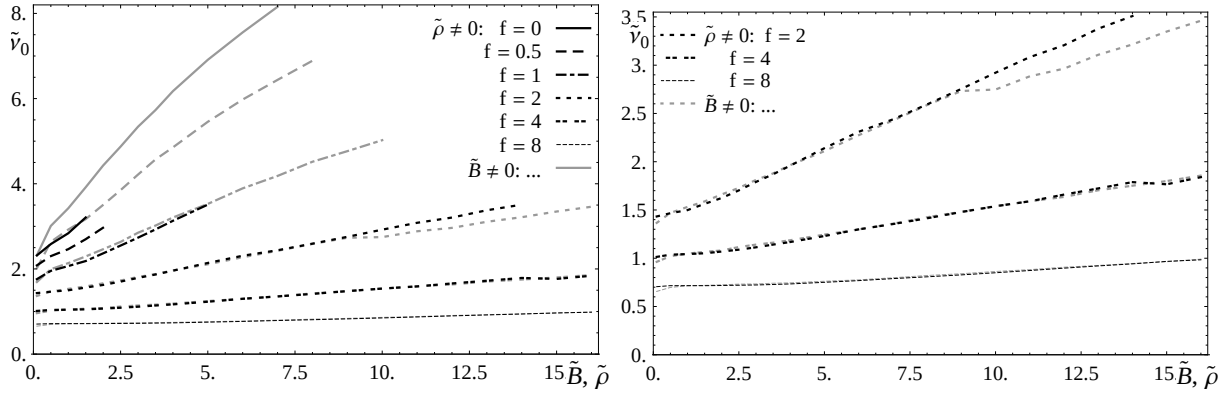

Figure 3.35: The separation $\tilde{\nu}_0$ in the spectrum of "plasmons" and "Landau levels" as a function of $\tilde{B}$ or $\tilde{\rho}$ for various values of f. The plot on a right only shows the highest f curves.

Next, let us look at the value of $\tilde{\nu}_0$ in fig. 3.35. There are two features to notice: Firstly the finite value of $\tilde{\nu}_0$ at vanishing magnetic field or density, and secondly the non-trivial dependence on $\tilde{B}$ or $\tilde{\nu}$ – both of which are quite different from what we would have naively expected for plasmons and Landau levels. It turns out that there are two equivalent ways to interpret this situation.

An interesting physical picture can be obtained by representing the data as $\tilde{\nu}_0^2$ as a function of the square of the magnetization $\tilde{M}$ or chemical potential $\tilde{\mu}$ that we compute in (E.2.26). As we see in fig. 3.36 the result are perfectly straight lines, such that the resonances are given by $\omega_c^2 = \omega_0^2 + \frac{M^2}{\alpha(f)^2}$ or $\omega_p^2 = \omega_0^2 + \frac{\mu^2}{\alpha(f)^2}$. Obviously, we could interpret the function $\alpha(f)$ as some kind of a mass scale that depends on f only, i.e. not on the width of the defect, but only its "topological" property. If we were – inappropriately – to look at the corresponding classical Schrödinger equation, we would see that then the magnetic and density perturbations are not independent, but mixes with some other potential. This

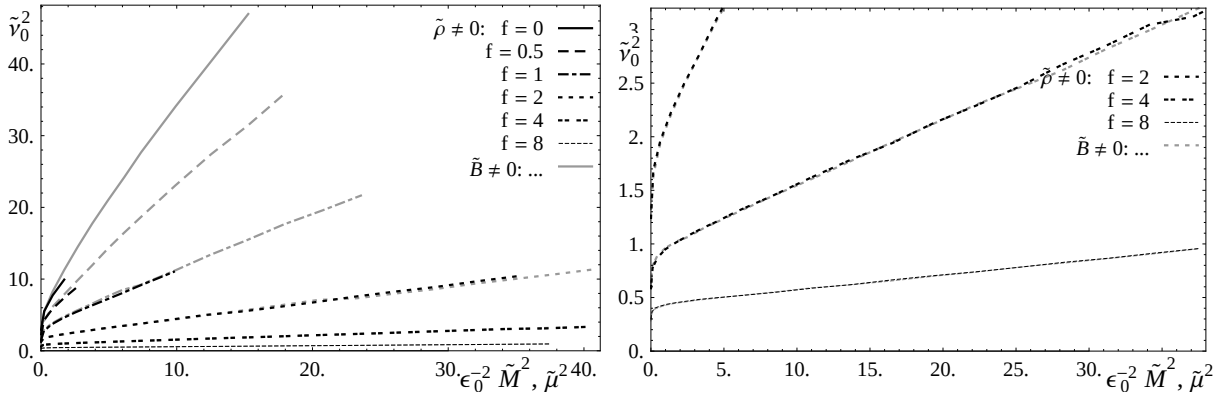

Figure 3.36: $\tilde{\nu}_0$ presented as $\tilde{\nu}^2$ as a function of the square of the magnetization or chemical potential $\tilde{M}^2$ or $\tilde{\mu}^2$ for various values of f. The plot on a right only shows the highest f curves.

is in contrast to the fact that the overall "amplitude" of the resonances, and hence the residue of the poles is at least for small fields proportional to the magnetic field. This is just what happens in the case of the classical Hall effect as discussed in section 3.3.1. In fact, we can check a few values for ω_0, and go back to fig. 2.12 to see that this resonance is precisely the one that we found in chapter 2 and interpreted as being resonances over the width of the defect.

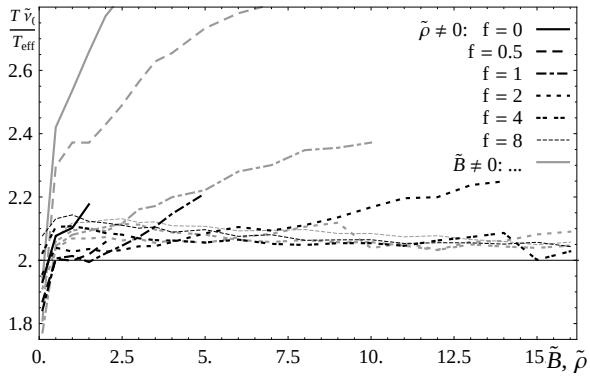

Figure 3.37: The ratio $\frac{\tilde{\nu}_0 T}{T_{eff}}$ as a function of $\tilde{B}$ or $\tilde{\rho}$ for various values of f.

Inspired by this, we can try to check the relation between the resonances and the length scale given by the effective temperature that we observed in fig. 3.36. To do so, we can plot the ratio $\frac{\tilde{\nu}_0 T}{T_{eff}}$ in fig. 3.37, where we see that it approaches within errors $\frac{\tilde{\nu}_0 T}{T_{eff}} \sim 2$. This is not a big surprise, as there is an underlying exact relation between $\frac{T_{eff}}{T}$ and μ (or M),

that we can easily verify numerically and may in principle be able to derive analytically.

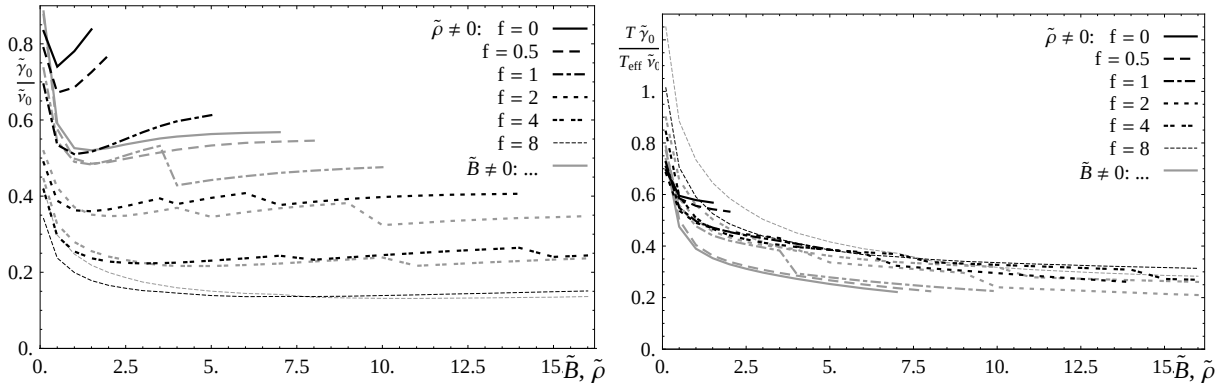

Figure 3.38: The "inverse lifetime to mass ratio" $\frac{\tilde{\gamma}_0}{\tilde{\nu}_0}$ for the magnetic and density resonances as a function of $\tilde{B}$ or $\tilde{\rho}$ for various values of f.

Before concluding the study of the parameters of the resonances, let us look at the ratio $\frac{\tilde{\gamma}_0}{\tilde{\nu}_0}$ in fig. 3.38. Firstly, we notice the steps in the curves, that happen to coincide with data sets at which the highest pole in the sequence of resonances drops out of the fit because of its decreasing amplitude. This indicates the limitations in fitting the parameters (that we expect to converge only asymptotically) accurately. Obviously, we could try to account for the non-linearity in $\tilde{\gamma}_n$ as in section 2.3.2, but this has the downside that fitting with more parameters makes the result less reliable and may simply hide the limitations of the numerical result. Secondly, we see that within those limitations and even though $\frac{\tilde{\gamma}_0}{\tilde{\nu}_0}$ itself seems to approach constants in $\tilde{\nu}$ or $\tilde{B}$, it seems to be best described as being proportional to $\frac{T_{eff}}{T}$. Within the errors, it seems that the appropriate ratio is independent of f and becomes also approximately constant in $\tilde{\nu}$ and $\tilde{B}$.

Next, we can look at the location of the poles at a finite quark mass in fig. 3.39. If we look only at $\tilde{\nu}_0$ as a function of $\tilde{B}$, we see a surprise, as there is only an overall shift in the curves depending on the quark mass. On the other hand, if we plot $\tilde{\nu}_0^2$ as a function of the square of the magnetization $\tilde{M}^2$, we see clearly the scale $\tilde{M} \sim \tilde{m}$ that separates the massive and massless regime. Below $\tilde{M} \sim \tilde{m}$, $\tilde{\nu}_0$ is suppressed with increasing mass and above $\tilde{M} \sim \tilde{m}$, the behavior is similar to the massless case. If we compare $\tilde{\nu}_0$ to the effective temperature, we find that $\frac{\tilde{\nu}_0 T}{T_{eff}}$ is approximately constant around $2.04 \ldots 2.06$ with no apparent systematic trend, so even in this case the effective temperature sets the appropriate scale for the quasiparticle energy spectrum. In principle, it would be interesting

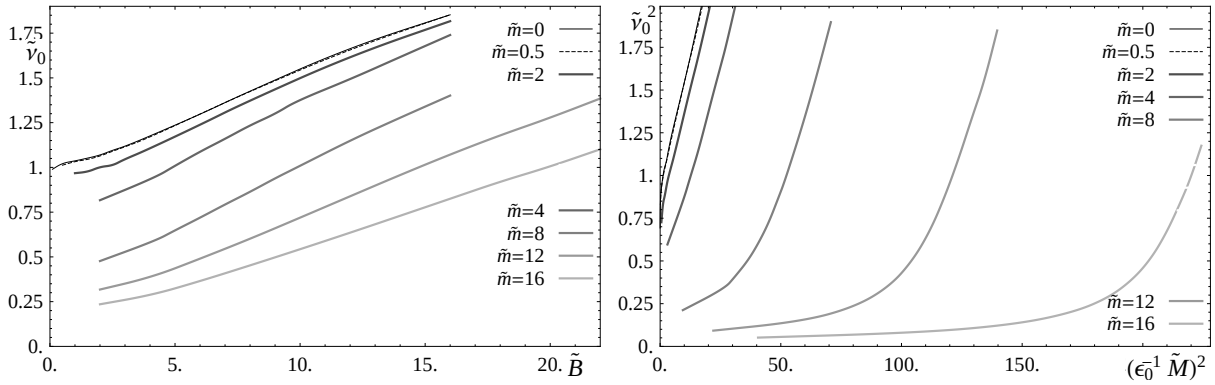

Figure 3.39: $\tilde{\nu}_0$ for various values of the quark mass parameter $\tilde{m}$ at $f = 4$. Left: As a function of the magnetic field. Right: $\tilde{\nu}_0^2$ as a function of the magnetization $\tilde{M}^2$.

to study also smaller values of f, however at smaller f and large masses, it is not possible to find reliably at least the first two or three poles.

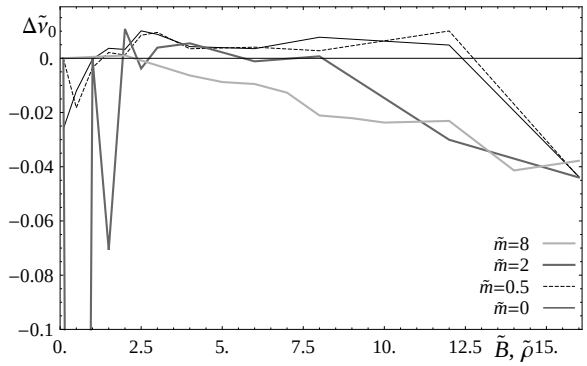

Figure 3.40: The difference in $\tilde{\nu}_0$ between the case of the magnetic field and density at $f = 4$ for various values of the quark mass as a function of $\tilde{\rho} = \tilde{B}$.

In principle, we expect that the results in the presence of the finite density and the magnetic field are different as we turn on the finite mass. Comparing $\tilde{\nu}$ for these cases in fig. 3.40, we see that the difference is very small, even as $\tilde{m} > \tilde{B}$. We are uncertain as to whether these deviations are significant. From the behavior at $\tilde{m} = 8$, it seems that there may be a small effect, which is suppressed in the quasiparticle regime. This question is resolved in 3.41, where we plot T_{eff}/T at finite mass. We see that there is indeed a small difference between the dependence on $\tilde{\rho}$ and $\tilde{B}$ at finite quark mass. Upon close inspection we also notice the separation between the regimes above and below the mass scale with the scalings $\frac{T_{eff}}{T} \propto \tilde{B}^{1/2}$ or $\frac{T_{eff}}{T} \propto \tilde{B}$, respectively, at least in the case of the magnetic field. It seems that there, the scale is $\tilde{B} \sim \tilde{m}$, whereas for the density it is $\tilde{\rho} \sim \tilde{m}^2$.

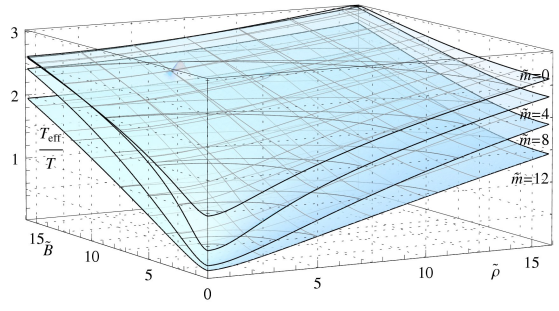

Figure 3.41: The scale T_{eff}/T at $f = 1$ and various values of the quark mass as a function of the net baryon density and magnetic field.

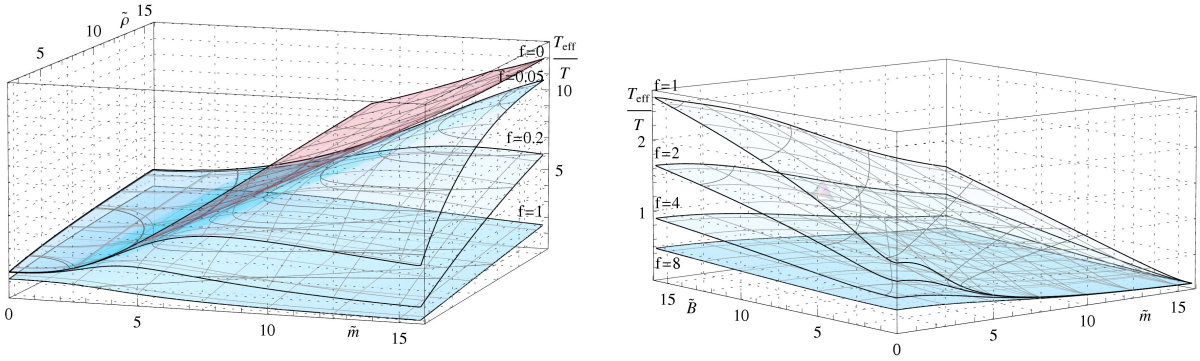

Figure 3.42: Left: $\frac{T_{eff}}{T}$ as a function of the mass and the net baryon density for various (small) values of f. We choose the lower bound of the range $2 \leq \tilde{\rho} \leq 16$ to avoid the phase transition at the critical mass and numerical problems near it. Right: $\frac{T_{eff}}{T}$ as a function of the mass and the magnetic field for various values of f.

Because of the very good agreement between the quasiparticle spectrum and T_{eff}, let us have one more look at the mass-dependence of $\frac{T_{eff}}{T}$ in fig. 3.42. Generically, the dependence on $\tilde{\rho}$ and $\tilde{B}$ is very similar at large values of f and differs very significantly at small values, hence our choice of plots. At small values of f, we see a very interesting behavior. It seems that at vanishing f, T_{eff} is essentially given by the mass, with only a subleading dependence on $\tilde{\rho}$ at large masses, which actually reduces T_{eff} with increasing $\tilde{\rho}$. As we turn on f, this behavior turns over into a more common behavior, starting first at small f at large masses and small densities. This may be some transition from a purely 2-dimensional system to a system that extends also in the third dimension. What makes this behavior so surprising is that normally, both in the mass dependence and also at $M_q = 0$, any dependence on f is subleading at large $\tilde{\rho}$. We should be careful with conclusions however, because we have not tested the dependence of the resonances on T_{eff} in this regime. Looking at the $\tilde{B}$ dependence at large f, we find that the behavior is more generic, with a $\sim \frac{\tilde{B}}{\tilde{m}}$ scaling of T_{eff} at $\tilde{m} \gg \tilde{B}$ and dependence approximately proportional to $\sqrt{\tilde{B}}$ at $\tilde{m} \ll \tilde{B}$. We also note that The transition between the two regimes becomes clearer at increasing f, i.e. as we widen the defect. Large f also suppress the $\tilde{B}$ dependence of T_{eff}.

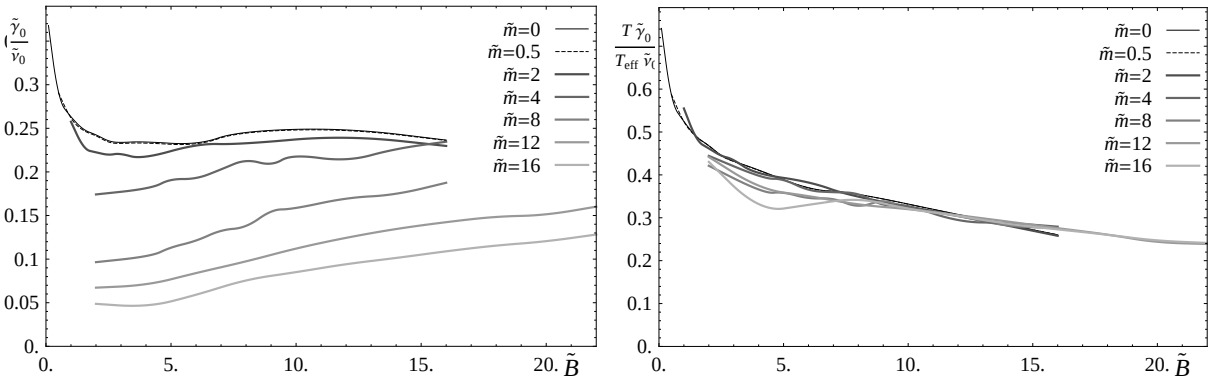

Figure 3.43: The "inverse lifetime to mass ratio" $\frac{\tilde{\gamma}_0}{\tilde{\nu}_0}$ for the magnetic resonances as a function of $\tilde{B}$ for $f = 4$ and various values of $\tilde{m}$.

To conclude, let us also in this case look at the ratio $\frac{\tilde{\nu}_0}{\tilde{\gamma}_0}$ which we show in fig. 3.43. Again, we see that $\frac{\tilde{\nu}_0}{\tilde{\gamma}_0}$ is approximately constant in $\tilde{B}$, however it seems to depend on the quark mass. If we divide by the effective temperature, the dependence on the quark mass is removed, however there seems to be some dependence on $\tilde{B}$.

Finally, we can look at how the poles split if we turn on the Hall effect. In fig. 3.44, we show the location of the poles for various values of f, $\tilde{\rho}$ and $\tilde{B}$. In black, we show the poles

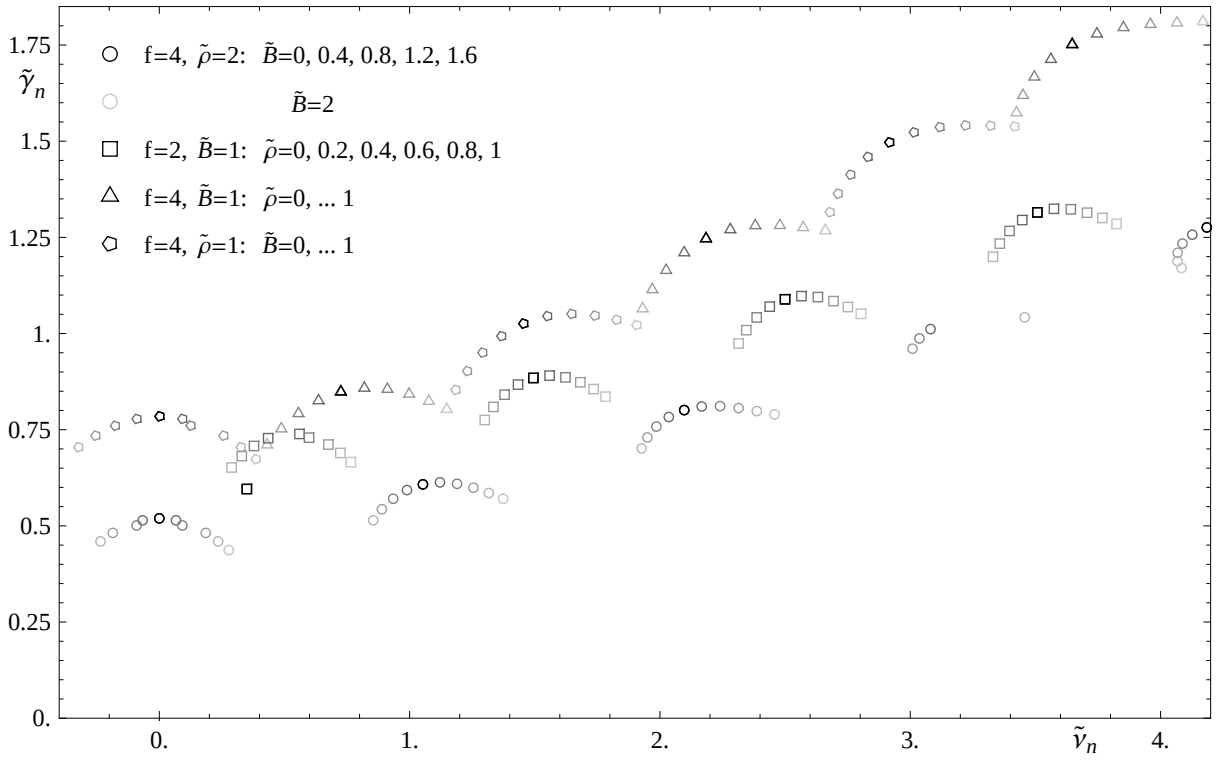

Figure 3.44: The splitting of the poles due to the Hall effect at various values of $\tilde{\rho}$, $\tilde{B}$ and f. The black symbols indicate the sequence of poles in the absence of the Hall effect for some choice of f and $\tilde{B}$ or $\tilde{\rho}$. With decreasing gray shade, we turn on the $\tilde{\rho}$ or $\tilde{B}$, respectively, causing the original pole to split in two poles.

in the absence of the Hall effect, and then we show the sequence of poles as we gradually turn on the "other" parameter. The most surprising result is that the total spacing $\tilde{\nu}_0$ of the pairs of poles remains approximately unchanged, with quadratic dependence on the "smaller" background quantity $\delta\tilde{\nu}_0(\tilde{B}) := \sqrt{\tilde{\nu}_0^2 - \tilde{\nu}_0(\tilde{B}=0)^2} \propto \tilde{B}$ that is within errors consistent with the behavior of the effective temperature. The splitting of the poles, $\tilde{\nu}_\Delta$ depends approximately linearly on the magnetic field or density that we turn on, however there seems to be no simple dependence of the proportionality coefficient on the obvious candidates such as the specific magnetic moment $\frac{\partial M}{\partial \rho_0}$, the density of states or the magnetic susceptibility. We show this in fig. 3.45

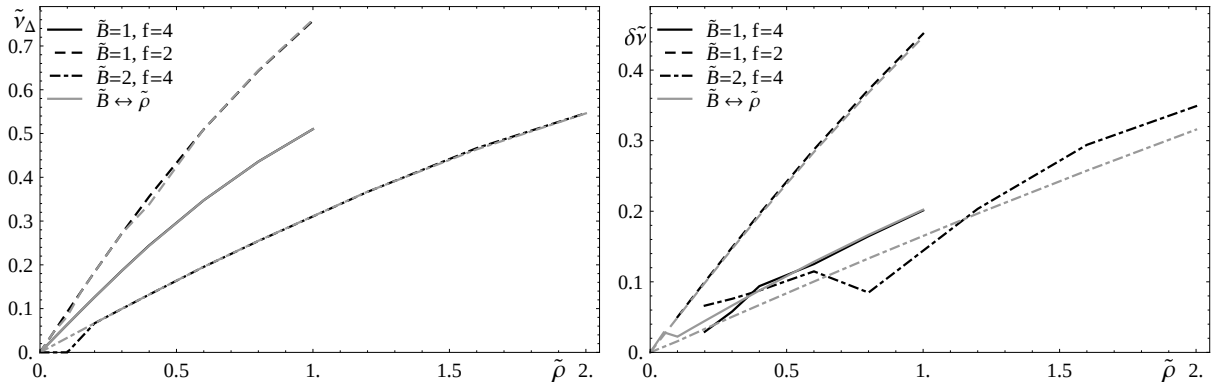

Figure 3.45: Left: The splitting of the energy of the quasiparticle poles due to the Hall effect, $\tilde{\nu}_\Delta$. Right: The shift in $\tilde{\nu}_0$ from turning on the second parameter, written as $\delta\tilde{\nu}_0(\tilde{B}) := \sqrt{\tilde{\nu}_0^2 - \tilde{\nu}_0(\tilde{B}=0)^2} \propto \tilde{B}$ (and $\tilde{\rho} \leftrightarrow \tilde{B}$).

The origin of the resonances on the gravity side is again straightforwardly explained in terms of quasinormal modes on the brane. Taking the same Ansatz as for the effective temperature, but now in terms of the variable s that we used in section 3.4.1.1 and computing the equation of motion for the Ansatz $A_y = A_0 e^{\int ds\zeta}$ as in (3.4.96), we obtain

$$\zeta^2 + \dot{\zeta} + \left(\left(\sqrt{-G}\, G^{tu} G^{xy}\right)'\right)^2 \frac{G^{uu}}{G^{tt}} - G G^{tt} G^{uu} G^{xx} G^{yy} \tilde{\omega}^2 = 0 \,. \tag{3.5.123}$$

Since we just want to have a brief picture, we will only work to leading order, i.e.. use $\zeta_0 := i\tilde{\omega}\sqrt{G G^{tt} G^{uu} G^{xx} G^{yy}}$ and the pertubation $\zeta = \zeta_0 + \epsilon$. Taking only the leading terms, we find the equation of motion

$$0 = \dot{\epsilon} - 2\epsilon\zeta_0 + \dot{\zeta}_0 =: \dot{\epsilon} - \epsilon\alpha(s) - \beta(s) \,, \tag{3.5.124}$$

again with the general solution $\epsilon = e^{\int_0^s d\bar{s}\,\alpha(\bar{s})}\left(\epsilon_0 + \int_0^s d\tilde{s}\, e^{-\int_0^{\tilde{s}} d\bar{s}\,\alpha(\bar{s})}\beta(\tilde{s})\right)$. Essentially what happens now is that the resonances arise from the inhomogeneous term. If we imagine that the source term β were a delta function at some position s_0 with amplitude ξ, then the result would be $\epsilon = \xi e^{\int_s^{s_0} d\bar{s}\alpha(\bar{s})}$. Setting $s = 0$ and taking the real part gives us the resonances we want as $\delta\sigma \sim \xi \cos 2\omega \int_0^{s_0} \sqrt{GG^{tt}G^{uu}G^{xx}G^{yy}}$.

To see where the resonances originate from in the geometry, we consider the high frequency limit $\tilde{\omega} \gg 1$ and remind ourselves that the integral of a periodic function vanishes, however the contribution to an integral of the type $\int F(x)e^{i\omega x}$ from some region around x_0 will be of the order $\frac{F'(x_0)}{\omega}$. In our case, the frequency in the exponent is also not constant, but we can take care of that by a coordinate change $s \to \int \zeta_0$. After taking the derivative and changing back to s, we find that the term that gives us the contribution in the integral is $ds\,\partial_s \frac{\dot{\zeta}(s)}{\zeta(s)}$. This expression already shows us straightforwardly that these resonances appear only in the presence of the background fields, since otherwise $\sqrt{-GG^{tt}G^{uu}G^{xx}G^{yy}} = 1$. In fig. 3.46, we show this term for various choices of the magnetic field, f and the density. We see how this length scale arises, and we see also the structure that gives rise to the line splitting in the Hall effect. It also demonstrated how the different phase between the magnetic and plasma resonances arises, essentially through flipping the sign in this term. The shape of this contribution gives rise to the amplitude of the oscillations, and the positive and negative sections tell us that there is a higher suppression by $\tilde{\omega}$. Note that at small $u \ll \sqrt{\tilde{B}}$, $\tilde{\rho}$ we have $s \sim u$ and $\zeta \sim \sqrt{1+f^2}$. Hence at small or $\mathcal{O}(1)$ values for $\tilde{B}$ and $\tilde{\rho}$, the spacing between resonances will be mostly controlled by the value of ζ, and not through s. The curves in the plot however control through their shape the nature and the stability of the resonances. Essentially, we can interpret this as scattering off a potential

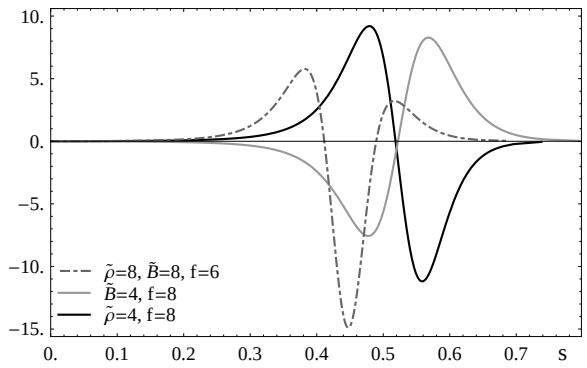

Figure 3.46: Coefficient giving an estimate of the contribution to the resonances as described in the text.

step, as we discussed around equation (2.2.90).

Chapter 4

Discussion and Conclusion

In this thesis, we used holographic techniques to investigate the transport properties of certain defect CFT's. In particular, we studied matter on a $(2+1)$-dimensional defect emersed in a heat bath. Most of our analysis covers two distinct defect CFTs. The first was realized by embedding $N_{\rm f}$ probe D5-branes in $\mathrm{AdS}_5 \times S^5$, as described in section 2.1.1 and in this case, the system (at $T = 0$) preserves eight supersymmetries. The second system involves embedding $N_{\rm f}$ probe D7-branes in the $\mathrm{AdS}_5 \times S^5$ background and the resulting defect CFT preserves no supersymmetries. In this case, it is however not quite sure in how far the setup persists in the light of gravitational backreaction. In both cases, the theory could be deformed by introducing an additional internal flux on the probe branes, a flux in the AdS and a deformation of the sphere. In the dual CFT, the defect in the presence of the internal flux separated regions where the rank of the SYM gauge group was different. As described in section 2.1.2, this flux was crucial to remove an instability which would otherwise appear with the D7-brane construction. Perhaps surprisingly, the transport properties of both defect CFT's were essentially identical in the massless case. Certainly, higher order effects might not be identical anymore.

4.1 Conformal effects

In the first part of this thesis, we focused on the presence of the internal flux parameter f, $f\, N_f \sqrt{\lambda}/\pi \in \mathbb{Z}$, in order to isolate the properties that appear to be due the defect nature of the system. Overall, our analysis revealed the expected diffusion-dominated hydrodynamic limit at small wave-numbers and we found a smooth crossover to a collisionless regime at the large wave-numbers. In the latter regime, the defect theory exhibits a conduction

threshold, given by the wave-number q of the current and the system is approximately described only in terms of the "rest-frame frequency" $\nu = \sqrt{\omega^2 - q^2}$.

In many respects, our results coincided with those in [49], where holographic techniques were used to study a purely $(2+1)$-dimensional system with sixteen supersymmetries. Hence maximal supersymmetry (or supersymmetry, in general) does not seem to be a key feature for producing the interesting behavior of these holographic models. Instead many properties seem to emerge from the infinite N_c and infinite λ limits, that are implicit in making a supergravity analysis of the AdS dual. In section 2.4, we elucidated one such effect that arises purely from the large-N_c and large-λ limits, namely the frequency independence of the conductivity, $\tilde{\sigma}(\tilde{\omega})$. In [49], this effect was described as a consequence of the electromagnetic duality of the gauge theory giving the dual description of the CFT currents. We were able to explicitly show that this duality is lost when stringy corrections are included in the worldvolume gauge field action and explicitly calculated the frequency dependence in $\tilde{\sigma}(\tilde{\omega})$ arising from the corresponding finite-λ corrections to the conductivity. As described in appendix B, one can well imagine that there will be other interactions which, although they appear to be of higher order in the α' expansion, provide further corrections to the conductivity with coefficients $f^n/\sqrt{\lambda}$, where $n > 2$. Hence, our results in section 2.4 are only the leading corrections when f is small but finite. There will also be curvature interactions to the worldvolume action of the probe branes [97, 98]. These will also produce finite-λ corrections but in contrast to the previous discussion, the latter will not be enhanced by factors of f and first appear only at order $1/\lambda$.

While certain aspects of charge transport were similar for the present defect CFT's and the maximally supersymmetric CFT studied in [49], we also found some profound differences. The most prominent one is the dependence of our results on the internal flux f – certainly a difference since no such parameter exists in the maximally supersymmetric case. For example then, with large f, strong quasiparticle peaks appeared in the spectral functions and conductivities. Similarly, certain phenomena in the defect CFT seemed to be controlled by a new dynamically generated scale in this regime, *i.e.,* a scale distinct from the temperature T. We denoted this scale as the effective temperature T_{eff} in section 2.2.2.1. For small f, $T_{eff} \sim T$ to within factors of order one. However, for large f, one finds that $\pi T/(2T_{eff}) \simeq k\sqrt{f}$ where $k = 4\Gamma(5/4)^2/\sqrt{\pi}$, as shown in (2.2.85). While this seems a curious way to present the ratio of T and T_{eff}, it was found in section 2.3.2 that precisely this combination played a role in fixing the spacing of the quasiparticle poles. Further, as also noted there, precisely the same behavior was found at large f for the diffusion constant: $\pi\, D\, T \simeq k\sqrt{f}$.

A more intuitive picture as to the origin of this dynamical scale comes from considering the probe brane geometry, as in section 2.1. Recall that when f is non-vanishing, the defect

separates a region where the SYM has gauge group $U(N_c + q)$ from one where the gauge group is $U(N_c)$. However, on the side where the rank of the gauge group is enhanced, the defect also excites a non-commutative configuration of adjoint scalars in a $U(q)$ subgroup of the full $U(N_c + q)$. At $T = 0$, this configuration extends to infinity with $\mathrm{Tr}(\Phi^2) = \frac{q^2}{4N_f}\frac{1}{z^2}$. In particular, this configuration preserves the conformal symmetry, *i.e.,* does not introduce a new scale. The scalar profile is reflected in the radial profile of the probe D-branes which also extends out to $z \to \infty$ when $T = 0$ and f is non-vanishing. However, when the temperature is non-vanishing, the probe branes fall into the horizon at a finite value of z. For large f, one finds

$$z_{max}\, T = k\,\sqrt{f}\,, \tag{4.1.1}$$

where k is precisely the same constant found above. The natural interpretation of this profile is that at finite temperature, thermal fluctuations decohere the scalar fields at some distance away from the defect. That is, at finite T, the defect can only excite a coherent configuration of scalars out to z_{max}. However, at small f, z_{max} vanishes whilst the dynamical length scale doesn't vanish. We can interpret that by some extra contribution to the width that arises from excitations in the bulk fields that are induced at strong coupling from the presence of the charged matter degrees of freedom on the defect.

One interpretation then is that the defect effectively acquires a finite width when T is non-vanishing. This intuitive picture may seem more reasonable, if we recall that the system is at (extremely) strong coupling and so any probe exciting of the defect fields will actually excite a complicated mixture of defect fields and "bulk" SYM fields. This picture of finite-width for the defect seems to match well with the results for the quasiparticle spectrum on the defect. In particular, we found that both the conduction threshold and the resonance peaks are well-described by a quasiparticle "tower" with equally spaced "rest frame" energy and constant "mass to inverse lifetime ratio". The length scale that is suggested from this spectrum is very similar to πDT and $\pi T/(2T_{eff})$ (and at large f also similar to z_{max}) plus a small constant.

In terms of the effective Schrödinger analysis, *e.g.,* see appendix C, the quasinormal spectrum arises in the gravity side from interference on a potential barrier in the asymptotic region. From the profile of the brane, this translates into an interference or resonance in the region around the defect. These two dual pictures of the origin of the spectrum seem orthogonal. The intuitive CFT picture involves a width and implicitly, a potential, in the space transverse to the defect, while the effective Schrödinger analysis constructs an effective potential in the radial or "energy scale" direction. It would certainly be interesting to have a clearer connection between these two descriptions.

The hydrodynamic and collisionless regimes are cleanly separated at a critical wave-

number where the diffusion pole disappears, as observed in section 2.3.3. There, we found that the diffusion mode is partnered with another dissipative mode on the imaginary axis. These two poles coalesce at the critical wave-number and move out into the complex plane for larger q. Hence precisely at the critical wave-number q_c, the corresponding thermal correlator will exhibit a curious double pole on the imaginary axis. Interestingly, q_c has a similar qualitative f dependence as the other (inverse) length scales and is also quantitatively close, as $q_c/(\pi T) \sim 0.67/(k\sqrt{f})$. This supports again the concept that the properties of the defect are controlled by one fundamental length scale, that can be related to the effective width of the defect.

In section 2.5, we outlined a topological Hall conductivity, which is induced when the defect is coupled to the SYM gauge theory with a topological θ-term. Of course, it is also interesting to study the Hall conductivity induced by a background magnetic field on the defect as we do in the second part of this thesis.

4.2 Condensed matter effects

In the second part of this thesis, we added to our analysis the presence of a finite background magnetic field, finite quark mass and net baryon number density. This allowed us on the one hand to enlarge the class of theories that we are studying, and on the other hand it allowed us to compare the rich structure of our results to known phenomena in condensed matter physics, that are based either on generic considerations or on physics in the weakly coupled regime. We tried to distinguish between a) generic properties that seem to be independent of physical details of particular models, b) intuition that carries over from the weak coupling regime and c) properties that are specific to the strong coupling regime and allow us to build some new intuition that is generic in the strong coupling regime.

In section 3.1.1, we looked at the gravitational setup that corresponds to turning on the various parameters in the field theory side. We looked both at supersymmetric field theories with the D3-D5 embedding and at non-supersymmetric D3-D7 setups. The latter is of particular interest to condensed matter physics because the the spectrum of charged matter contains only fermions on the massless level. Furthermore it is curious that the only change is a Chern-Simons term with non-constant coupling at finite "quark" mass. However, we did not pursue this avenue at the massive level, since the results would be unreliable as an attempt to to stabilize the branes with a large internal flux f produces an inconsistency due to gravitational backreaction. We deferred a more detailed discussion of the phase diagram to appendix E, where we found results that are similar to the ones found previously in 3+1 dimensional field theories [45], and we found that the blackhole

embeddings that we use to compute the transport properties are always thermodynamically preferred.

We then went on to provide a few analytic results in section 3.2. In 3.2.1, we studied how the field theory outcome of the EM duality in gravity side changes in the case of the extra parameters. We found the very interesting result, that the transport properties are now related under a simultaneous exchange of the dimensionless magnetic field and density and the transverse and longitudinal coordinate, while interchanging the complex 2-dimensional conductivity tensor with its inverse. From a condensed matter point of view, this relates completely distinct parameters of the theory for a large class of 2+1 dimensional theories whose gravity dual obeys EM duality. This duality also became apparent in appendix E, where we studied the thermodynamics, and in the massless case, there was a degeneracy between the density and magnetic field. Throughout chapter 3.5 and appendix E, we saw how this duality gets broken as we consider a finite mass. However, still, this breaking appears gradually, with the parameter M_q/T.

In chapter 3.4, we then discussed several regimes. In the DC limit, we found the Drude conductivity at finite density, a magnetoresistance effect and a Hall conductivity. They can be parametrized under the Drude model, obviously giving a new description to the "Drude-parameters" in terms of the parameters of the theory, as the underlying microscopic physics is different. However, the overall scalings in the limit of large density and magnetic field are the familiar ones. Coincidentally, if we assume that the form of this DC conductivity has a high degree of generality, this could address the minimum quantum conductivity in Graphene [109]. There, it is known that at the neutrality point, which corresponds in our case to vanishing net baryon density, there is a minimum in the conductivity of e^2/h per carrier type, and this has apparently been of significant interest in the community [108]. Under an appropriate translation of the parameters, this is precisely what we observe in our case, as we also find an increasing conductivity as we move away from the neutrality point, which goes beyond the results in [49]. However, for example from the observed magnetic resonances, our defects seem to be quite different from the chiral nature of graphene [89]. We then studied the small-frequency limit, in which we reproduce the existence of a Drude peak and the minimum in the magnetoresitance. We could also identify a relaxation time, and accurately reproduce a relation between the frequency dependence of the diagonal conductivity and the hall conductivity, in the limit of large densities. In general, the structure of the frequency dependence resembled the generic prediction from the Drude model. We also found however, that the particular behavior of the parameters that depend on a particular model changes – for example the relaxation time receives a dependence on the magnetic field.

When we compared the relaxation time to the location of the purely dissipative poles

in the hydrodynamic regime that we studied numerically in section 3.5.2, we found that there was a disagreement with the dominant "relaxation pole" only at small densities. This can be explained by the remarkable constant DC conductivity from the EM duality at vanishing density (2.4.98), that is obviously not considered in the Drude model. In this regime and also in general, we observed that there is always a total finite quark density in thermal equilibrium (which we can't control) that influences the transport properties even at vanishing net density. Beyond the dominant relaxation pole, that showed an unusual dependence on the density, which we attributed to the strong coupling, there was a second relaxation pole, that shows a more classical behavior, but has no significant contribution to the charge transport. We were able to reproduce the transition to the quasiparticle regime that we found in the first part, and also found another transition in which the relaxation poles merge and turn into the first Landau level at some critical magnetic field, rather than the diffusion pole merging with the first relaxation pole. This transition can be attributed to strong coupling and is absent in free particle models. Overall, there is an interesting interplay between those relaxation poles and the diffusion pole as we tune the parameters, and there is a common theme that before poles move to large (imaginary) frequencies or leave their regime of validity, they either merge into quasiparticle poles or have decaying residue.

The diffusion pole also has an unusual dependence on the density, which can be motivated from the strong coupling properties. We verified that the numerically obtained diffusion constant agrees with the one obtained analytically from the membrane paradigm. We also computed the permittivity. This gives us what we called the "relative" permittivity, that depends on the mass, magnetic field, internal flux and density. The diffusion constant and permittivity reproduce precisely the DC conductivity from the diffusion behavior, i.e. the Einstein relation.

In the opposite regime, i.e. in the low temperature limit, we found again the conduction threshold at $\omega = q$. Our analytical approximations were focussed on the exponentially suppressed conductivity at small frequencies and large wavenumbers, $q \gg T \gg omega$, and extended the result for the diagonal conductivity that we found in the first part of the thesis. Now, the "effective temperature" that controls the exponential suppression however also depends on the other parameters of the theory. In particular, the density and magnetic field now raise that factor, i.e. reduce the exponential suppression. This is however not to be misunderstood as doping a semiconductor. At very large values of those parameters, of the order $\tilde{B}, \tilde{\rho} \gg \tilde{q}^2$, we were able to demonstrate that the conductivity turns into the DC result. Computing the Hall conductivity gave an interesting result as we obtained a finite value of the Hall conductivity even in the regime where the diagonal conductivity vanishes. This is however a common theme in condensed matter physics, for

example in semiconductors at low temperatures or on Hall plateaus in the quantum Hall effect.

The rest of the work in the quasiparticle regime was mostly numerics-based. In section 3.5.1, we gave an overview over the spectral curves, where we found the appearance of what one could describe as the strong-coupling equivalent of Landau levels and plasmons, and line splitting in the Hall effect. We also noticed that increasing the mass or the internal flux parameter f makes the results approach the low temperature limit, as we expect from our results on the effective temperature. Furthermore, we looked at how the resonances from the isotropic regime carry over to the finite-wavenumber regime in which we observed the resonances in chapter 2. In particular, we found that for the transverse correlator, the density resonances connect smoothly whereas the magnetic resonances connected less smoothly – which can be explained in terms of the localizing property of the magnetic field. The more quantitative approach to the quasiparticle regime was to extract the location of the poles in the correlator in order to obtain the quasiparticle spectrum. We found that the poles are exactly equally spaced, indicating that the mechanism underlying the magnetic resonances is just a quantum harmonic oscillator as in the classical generation of Landau levels. The length scales corresponding to the spectrum can be explained in two ways: On the one hand, they are just given by approximately 2 times the effective temperature, over essentially all the parameter range including the mass. On the other hand they can be related to the magnetization or chemical potential, which splits in the massive case into regimes below and above the quark mass. In this scenario, however, it seems that the Landau levels or plasmons are strongly coupled to the resonances over the "width" of the defect, as apparent from the minimum spacing of the resonances. This fits in nicely with the line splitting that we observed in the context of the Hall effect, where each pole splits in two, indicating that there are overall two types of resonances in the system. In a qualitative description, we discussed, as in the first part, how the quasiparticles arise from quasinormal modes in the scattering off a step in a potential in the gravity side.

Comparing our results to those obtained from field theory methods [57], we found that there were a few similarities as a resonance or threshold at $\omega = q$ is also generically obtained using field theory methods. Furthermore, our results can be expressed in terms of a universal function that depends on ω/T. Expressed in this way, this universal function depends on dimensionless quantities like ρ_0/T^2, and hence also depends on the temperature. Overall, it seems that using AdS/CFT, we could more straightforwardly obtain the very complex behavior of this universal function. Also, it seems that the methods in [57] do not find quasiparticle resonances, that seem to be an integral part of the defect that we studied.

For directions of future research, it would certainly be interesting to gain a better inter-

pretation of our results in terms of the microscopic theory beyond what we have attempted in this thesis. This reveals a big weakness in using the AdS/CFT correspondence, as it is in practice to some degree like performing an experiment; and the "microscopic" theory in AdS/CFT is not the field theory, but the gravitational configuration. Another interesting direction would be to study the problems of the D3-D7 defect more in detail, as having a purely fermionic system is very appealing, even if it is only in the sector of the fundamental representation on the defect and the 3+1 bulk is still SYM. It would be interesting to see what kind of effects may then appear in the "massive" case.

4.3 Closing remarks

Overall, we hope that this work demonstrates that there is great potential in string theory to produce tangible results that are of relevance for example to condensed matter physics. We think that we may have delivered a few starting points, that may be generic enough to be worth trying to pursue further and compare to the experimental condensed matter literature.

Also, we hope that this work may provide some use in generating intuition for strongly coupled field theories. Certainly, a new kind of intuition can be gained, which is based on the geometry on the gravity side. This is related to the fact that there is also some degeneracy in the concept of what one refers to as a "model" – the field theory that is translated in to the gravity setup under AdS/CFT, or the gravity setup itself in connection with the "rules" of AdS/CFT. In the end, it does not matter, as all we need are "risky predictions" [30] to make from our theory.

APPENDICES

Appendix A

Probe brane horizon

In this section, we want to elaborate on the induced geometry of the probe brane at the event horizon. The embeddings of the probe branes found in section 2.1 may seem somewhat surprising since the brane seems to cross the horizon at an angle, *i.e.,* , $\chi' \neq 0$ at the horizon, as shown in eq. (2.1.17). However, common arguments suggest that such a configuration could not be smooth or remain static – see, *e.g.,* [68]. Hence, we must explain here why our static brane embeddings cross the horizon 'at an angle' without any singularity.

We begin by considering the noncompact part of the brane geometry, which is common to both the D5-branes (2.1.7) and D7-branes (2.1.19):

$$ds^2 = \frac{r^2}{L^2}\left(-h(r)dt^2 + dx^2 + dy^2\right) + \left(\frac{L^2}{r^2 h(r)} + \frac{r^2}{L^2}z'^2\right)dr^2\,, \tag{A.0.1}$$

where z' is given in eq. (2.1.15). It is a straightforward exercise to calculate some of the curvature invariants for this geometry, *e.g.,*

$$\begin{aligned} R &= -\frac{12}{L^2(1+f^2)} - \frac{4f^2 r_0^8}{L^2(1+f^2)r^8} \text{ and} \\ R_{ab}R^{ab} &= \frac{36}{L^4(1+f^2)^2} + \frac{4}{L^4(1+f^2)^2 r^{16}}\left(r_0^8 r^8(1+8f^2+3f^4) + 4r_0^{12}r^4 f^2 + 7r_0^{16}f^4\right)\,. \end{aligned} \tag{A.0.2}$$

In both of these expressions, the first term corresponds to the result expected for an AdS_4 geometry with radius of curvature $L\sqrt{1+f^2}$. The subsequent terms arise because in general the induced geometry only approaches AdS_4 asymptotically. That is, these terms

originate from both the brane bending and the presence of background black hole. In any event, these expressions remain finite at the horizon indicating that the brane geometry remains smooth there. The probe brane's geometry can also be characterized by the extrinsic curvature, given the embedding in the AdS_5 black hole background. It is again a straightforward exercise to evaluate these curvatures and produce, *e.g.,* the following scalar invariants

$$K \;=\; -\frac{4f\sqrt{1+f^2(\frac{r_0}{r})^4}}{\sqrt{1+f^2}}\frac{r_0}{L^2}\,, \quad K_{ab}K^{ab} \;=\; \frac{4f^2\big(1+(\frac{r_0}{r})^8\big)}{1+f^2}\frac{r_0^2}{L^4}\,. \tag{A.0.3}$$

Again, evaluating either of these expressions at the horizon yields a finite result, indicating that the brane embedding is smooth there.

To study the probe brane geometry at the horizon in more detail, it is convenient to change to suitable Kruskal coordinates:

$$U = e^{-(r^\star+\frac{r_0}{L^2}\,t)}\;, \qquad V = e^{-(r^\star-\frac{r_0}{L^2}\,t)}\;; \qquad r^\star = r_0\int_r^\infty \frac{r'^2\,dr'}{r'^4-r_0^4}\;, \tag{A.0.4}$$

which puts the induced metric (A.0.1) in the form

$$ds^2 \;=\; r(U,V)^2\frac{L^2\mathfrak{h}}{r_0^2}dUdV \,+\, r(U,V)^6\frac{\mathfrak{h}^2z'^2}{r_0^2L^2}(VdU+UdV) \,+\, \frac{r(U,V)^2}{L^2}\big(dx^2+dy^2\big)\;, \tag{A.0.5}$$

where we defined for convenience $\mathfrak{h} = (1+\frac{r_0}{r})^2(1+(\frac{r_0}{r})^2)e^{2\tan^{-1}\frac{r_0}{r}} \in]1,4e^\pi]$. We note that ∂_U is only null at the part of the horizon where $V=0$ and vice-versa.

To see now whether the brane falls vertically into the horizon, we want to compute the tangent to the brane in the z direction, $t_z = v^\mu e^a_\mu \xi^\mu_z$, where ξ_z is the finite norm killing vector ∂_z on the horizon, v is any non-singular vector in the brane and we use the map $e^\mu_a = \partial_a x^\mu$ to compute it's push-forward. It is easy to see that the only relevant non-zero components are $e^z_U = Vz'$ and $e^z_V = Uz'$, so the brane falls vertically into the horizon only at the bifurcation surface.

Appendix B

Corrections to D5-brane action

The worldvolume action (2.1.4) is a low-energy effective action which captures the interactions of the massless open string modes supported on the D5-branes. The "stringy" nature of the underlying theory will in principle produce an infinite series of higher dimension terms that are suppressed at low energies by the inverse string tension, *i.e.,* $\alpha' \equiv \ell_{\rm s}^2$. However, in practice, one typically only includes a specific set of terms to a certain order in the α' expansion. In fact, the action (2.1.4) implicitly captures an infinite set of these stringy corrections, as can be seen by the explicit factor of $\ell_{\rm s}^2$ accompanying the gauge field strength in the DBI action. Further, we might add that this entire series of terms plays a role in our analysis, as the full square-root form of the action is used in (2.1.8) to normalize the DBI contributions. However, as already alluded to in section 2.1.2, the DBI action does not capture all of the higher dimension stringy interactions. Beyond the non-abelian commutator terms referred to there, the full low-energy action includes additional terms involving derivatives of the gauge field strength [95, 96], as well as higher derivative couplings to the bulk fields [97, 98]. In terms of the dual CFT, the contributions of these α' interactions will provide finite λ corrections to the leading supergravity results.

In the following and in section 2.4, we focus our attention on a particular new term involving derivatives of the field strength, which modifies the vector correlators on the D5-branes. Our results below give the leading $1/\lambda$ corrections when f is finite. Our calculations consider explicitly those leading contributions for the transverse correlator. As we discuss in section 2.4, the higher derivative interaction also upsets the electromagnetic duality on the AdS_4 part of the worldvolume.

An effective action to describe open string gauge fields at higher order in α' has been extensively studied in the literature, *e.g.,* see [95, 96]. However, since we consider only the

linearized equations of motion (or the quadratic action) to compute the correlators in the AdS_4 directions, the leading term at (α'^3) is [95]

$$-\frac{1}{4g_4^2}\frac{\zeta(3)}{16\pi^4}\frac{(2\pi\ell_s^2)^3}{L^2\sqrt{1+f^2}}\int d^6\sigma\sqrt{-g}\,\nabla_\mu F_{\alpha\beta}\nabla^\mu F^{\alpha\beta}\,F^2\ . \tag{B.0.1}$$

In fact, this term only becomes relevant for the calculation of the vector correlators because of the flux background on the compact S^2. After integrating over the internal two-sphere, this interaction reduces to

$$-\frac{1}{4g_4^2}\frac{\zeta(3)}{2\pi}\frac{\ell_s^2\,f^2}{\sqrt{1+f^2}}\int d^4\sigma\sqrt{-g}\,\nabla_\mu F_{\alpha\beta}\nabla^\mu F^{\alpha\beta}\ . \tag{B.0.2}$$

Note that the background flux (2.1.6) remains unmodified by this new interaction. When considering linearized fluctuations of the vector field, we can work with a perturbative expansion in $\ell_{\rm s}^2/L^2 = 1/\sqrt{\lambda}$. We begin with the Ansatz

$$F = F^{(0)} + \frac{\ell_{\rm s}^2}{L^2}\,F^{(1)} + \cdots\ . \tag{B.0.3}$$

The equations determining the leading 0^{th} order field are still the same Maxwell equations (2.2.34), while for $F^{(1)}$, we have

$$\nabla_\nu F^{(1)\,\nu\mu} \;=\; \frac{\zeta(3)}{2\pi}\frac{L^2\,f^2}{\sqrt{1+f^2}}\nabla_\nu\nabla_\alpha\nabla^\alpha F^{(0)\,\nu\mu}\,. \tag{B.0.4}$$

Writing this out explicitly for $\mu = y$ gives

$$\begin{aligned}
&\partial_u\frac{h}{\sqrt{H}}\partial_u A_y^{(1)} + \frac{\sqrt{H}}{h}(\tilde\omega^2 - h\tilde q^2)\partial_u A_y^{(1)} \qquad\qquad (B.0.5)\\
&\quad= \frac{\zeta(3)f^2}{2\pi\sqrt{1+f^2}}\left(\partial_u\,u^2\sqrt{\frac{h}{H}}\partial_u\,\frac{h}{u^2\sqrt{H}}\partial_u\,u^2\sqrt{\frac{h}{H}}\partial_u A_y^{(0)} \;+\; \partial_u\,\frac{u^2}{\sqrt{H}}(\tilde\omega^2 - \tilde q^2 h)\partial_u A_y^{(0)}\right.\\
&\qquad+\;\left.\frac{\tilde\omega^2 u^2}{\sqrt{h}}\partial_u\,\frac{h}{u^2\sqrt{H}}\partial_u\,\frac{u^2}{\sqrt{h}}A_y - \tilde q^2 u^2\partial_u\,\frac{h}{u^2\sqrt{H}}\partial_u\,u^2 A_y^{(0)} + \frac{u^2\sqrt{H}}{h^2}\left(\tilde\omega^2 - \tilde q^2 h\right)^2 A_y^{(0)}\right)\ .
\end{aligned}$$

Note that we adopt the convention above that the derivatives ∂_u act on all factors to their right. At the horizon, $u \to 1$, we again wish to impose infalling boundary conditions. If we substitute the expansion (2.2.52) for A_y as $u \to 1$, the right hand side of (B.0.5) diverges as $h^{i\tilde\omega/4-2}$ and hence we expect to find singular behaviour in $A_y^{(1)}$ there. Hence we

begin by isolating this singular behaviour in a particular solution to (B.0.5): $A_y^{(1),NHG} \sim h^{i\tilde{\omega}/4}(\frac{a}{h}+b+c\log h+d\,h\,\log h)$ with appropriate constants a,b,c,d. This particular solution is holds to order h^0 near $u\to 1$ and is well-behaved in the rest of the geometry. Implicitly, it also satisfies the desired infalling boundary conditions. Next we add to $A_y^{(1),NHG}$ a contribution which is regular at the horizon and takes the form on an infalling homogenous solution near $u\to 1$ as described by (2.2.52) and (2.2.53). That is, we use the Ansatz

$$A_y^{(1)} \;=\; A_y^{(1),NHG} + h^{i\tilde{\omega}/4}\left(1+\left(\frac{i\tilde{\omega}}{4}\frac{3+5f^2}{1+f^2}+\frac{\tilde{q}^2}{4+2i\tilde{\omega}}\right)(1-u)\right)\mathscr{F}(u)\;. \tag{B.0.6}$$

where $\partial_u\mathscr{F}(u)|_{u\to 1}=0$. This Ansatz is constructed so that $\mathscr{F}(u)$ is well behaved everywhere and we proceed by calculating this profile numerically. In practise, we apply the boundary condition at some small, but finite, $(1-u)$, so need we go one order higher in h and increase the accuracy for solving $A^{(0)}$.

The correlator is then found by substituting our original Ansatz (B.0.3) into (2.2.41),

$$C_{yy} \;=\; \frac{\varepsilon_0}{\sqrt{1+f^2}}\frac{\partial_u(A_y^{(0)}+\ell_{\rm s}^2/L^2\,A_y^{(1)})}{A_y^{(0)}+\ell_{\rm s}^2/L^2\,A_y^{(1)}} \;\simeq\; \frac{\varepsilon_0}{\sqrt{1+f^2}}\left[\frac{\partial_u A_y^{(0)}}{A_y^{(0)}}+\frac{\ell_{\rm s}^2}{L^2}\,\partial_u\left(\frac{A_y^{(1)}}{A_y^{(0)}}\right)\right]_{u\to 0}+\cdots\;. \tag{B.0.7}$$

From this expression, we can see that the normalization of any homogenous solution in $A_y^{(1)}$ does not effect the correlator, as we expect for a gauge-invariant quantity. The expressions for C_{tt} and C_{xx} following from (2.2.42) are similar to that above.

The second term on the right-hand side of (B.0.7) yields the correction to the correlator due to the fact that the solutions for the fluctuations $A_\mu(u)$ are modified. In addition, (B.0.2) also contributes to the overall value of the bulk action and hence provides an additional modification of the correlators. Proceeding as in (2.2.37), we now get two boundary terms at order $\ell_{\rm s}^2$, since $D_\mu F_{\alpha\beta}D^\mu F^{\alpha\beta} = D_\mu(F_{\alpha\beta}D^\mu F^{\alpha\beta}) - D_\alpha(A_\beta D_\mu D^\mu F^{\alpha\beta}) + A_\beta(e.o.m.)^\beta$, where the last term combines with contributions from the leading Maxwell term in the action to vanish by the equations of motion. These expressions lead to a number of new contributions to the flux (2.2.40), which in principle even contribute to off-diagonal correlators. We might add that there is a further ambiguity in these expressions because the effective action (B.0.2) was constructed from examining string scattering amplitudes [95] and so it is only determined up to total derivatives or boundary terms. Explicitly comparing [95] and [96], one finds that in fact their results differ by such a boundary term. However, this ambiguity does not contribute in our background (2.2.35) and in fact, of the myriad of potential boundary contributions, only a single term survives

$$\Delta C_{yy} \;=\; -\frac{\ell_{\rm s}^2\,f^2\zeta(3)}{2\pi\sqrt{1+f^2}}\,\frac{\varepsilon_0}{\sqrt{1+f^2}}\,\frac{\nabla^2\partial_u A_y}{A_y}\bigg|_{u\to 0}\;. \tag{B.0.8}$$

Similar expressions survive for C_{tt} and C_{xx} while the potential contributions to the off-diagonal correlators vanish. Combining the results in (B.0.7) and (B.0.8), we can write the total change to the correlator as

$$\delta C_{yy} \;=\; \frac{\ell_{\rm s}^2}{L^2}\,\frac{\varepsilon_0}{\sqrt{1+f^2}}\,\left[\partial_u\left(\frac{A_y^{(1)}}{A_y^{(0)}}\right) - \frac{L^2 f^2\zeta(3)}{2\pi\sqrt{1+f^2}}\frac{\nabla^2\partial_u A_y^{(0)}}{A_y^{(0)}}\right]_{u\to 0}\,. \tag{B.0.9}$$

Again similar expressions arise for δC_{tt} and δC_{xx}.

The two previous formulae, (B.0.8) and (B.0.9), still require a precise definition for $\nabla^2\partial_u A_y$. This expression should understood as the covariant tensor expression $\nabla^2 F_{uy}$ which when evaluated asymptotically yields a remarkably simple result:

$$\nabla^2\partial_u A_y = -\frac{2}{L^2}\,\frac{1}{1+f^2}\,\partial_u A_y + \cdots \tag{B.0.10}$$

where the implicit terms decay rapidly enough as $u\to 0$ that they will not contribute to the correlator. Hence (B.0.8) can be greatly simplified to

$$\Delta C_{yy} \;=\; \frac{\ell_{\rm s}^2}{L^2}\frac{f^2\zeta(3)}{\pi(1+f^2)^{3/2}}\frac{\varepsilon_0}{\sqrt{1+f^2}}\,\left.\frac{\partial_u A_y}{A_y}\right|_{u\to 0}\,. \tag{B.0.11}$$

The last factor has exactly the same form as the leading correlator (2.2.41) and so this contribution can be interpreted in terms of a rescaling of the pre-factor ε_0:

$$\varepsilon_0 \to \varepsilon_0\left(1+\frac{1}{\sqrt{\lambda}}\frac{f^2\,\zeta(3)}{\pi(1+f^2)^{3/2}}\right)\,, \tag{B.0.12}$$

where we have replaced $\ell_{\rm s}^2/L^2 = 1/\sqrt{\lambda}$. Remarkably our numerical calculations show that the first contribution to δC_{yy} in (B.0.9) also produces a shift of ε_0 with precisely the same f dependence – see figure 2.15.

At this point, several comments are in order. We already pointed out that the square-root form of the DBI action already incorporates an infinite set of stringy α' corrections. While this form was incorporated in our leading order calculations, *e.g.,* (2.1.8), it did not appear to introduce any $1/\lambda$ corrections. Of course, these factors are hidden in the definition (2.1.9) of f and for finite values of f, we are actually introducing a magnetic flux quantum number $q\sim O(\sqrt{\lambda})$. In this context, it is not quite correct to say the interaction (B.0.1) is the leading term to modify the correlators. One can well imagine that there will be other interactions which, although they appear to be of higher order in the α' expansion, will modify the correlator with contributions of order $f^n/\sqrt{\lambda}$ where $n>2$. Of course, these contributions will be suppressed in a regime where $f\ll 1$. Considering the possible tensor structure of the relevant higher order interactions, it seems that this class of contributions will always be arising from an equation of motion of the form (B.0.4).

Appendix C

Hyperbolic tangent potential

To get more insight into the appearance of the finite temperature effects in the frequency dependence of the conductivity, we can study a qualitatively similar problem that has an analytic solution.

C.1 Finding the spectral curves

Let us modify the effective Schrödinger equation in (2.2.90) to write it in terms of the complex frequency ν of section 2.3, *i.e.,* $\tilde{\nu} \equiv \sqrt{\tilde{\omega}^2 - \tilde{q}^2}$,

$$\left(-\partial_\rho^2 + V\right) A_y \;=\; \tilde{\nu}^2 A_y \tag{C.1.1}$$

$$\text{with} \qquad V = -\tilde{q}^2\, u^4 \quad \text{and} \quad \rho \;=\; \int_0^u d\tilde{u} \frac{\sqrt{H}}{h} \;.$$

Recall in terms of the new radial coordinate ρ, the asymptotic boundary is mapped to $\rho = 0$ and the horizon, to $\rho \to \infty$. In fact, it is straightforward to evaluate the integral above to find $\rho(u)$ in terms of incomplete elliptic integrals of the third kind or alternatively, in terms of the Appell hypergeometric function [106] $\rho = \sqrt{1+f^2}u\, F_1\left(\frac{1}{4}; \frac{1}{2}, 1; \frac{5}{4}; -f^2u^4, u^4\right)$. Note that the only difference between (2.2.90) and (C.1.1) is that we have subtracted $\tilde{q}^2\, A_y$ from both sides in the equation above. Hence in the present form, the effective potential V vanishes at $\rho = 0$ and approaches $-\tilde{q}^2$ as $\rho \to \infty$.

The equation of motion in the form of (C.1.1) can be examined in three distinct regions

which for $f \gg 1$, where the potential looks roughly like

$$\begin{aligned} V &\sim 0 &&: \quad \rho \lesssim f^{1/2} \\ V &\sim -\tilde{q}^2(2f^{1/2}-\rho)^{-4} &&: \quad f^{1/2} \lesssim \rho \lesssim 2f^{1/2}-1 \\ V &\sim -\tilde{q}^2 + \tilde{q}^2 e^{-4(\rho-2f^{1/2}+1)} &&: \quad 2f^{1/2}-1 \lesssim \rho \ . \end{aligned} \tag{C.1.2}$$

Of course, the full potential is smooth across these three regions.

To model the "smooth" step with a finite slope and a fast tailoff in the asymptotic regions, we will use

$$V_{app} = -\tilde{q}^2 \frac{1 + \tanh \mathfrak{n}(\rho-\rho_0)}{2} \ , \tag{C.1.3}$$

which allows us to find exact solution for (C.1.1). We fix the "step" position ρ_0 either as location where the the potential has half its minimum, *i.e.,* at $u^4_{half} = 1/2$ or the point where the slope of the potential is minimum, *i.e.,* at

$$u^4_{min} = \frac{5f^2 - 7 + \sqrt{(7-5f^2)^2 + 108f^2}}{18f^2} \ . \tag{C.1.4}$$

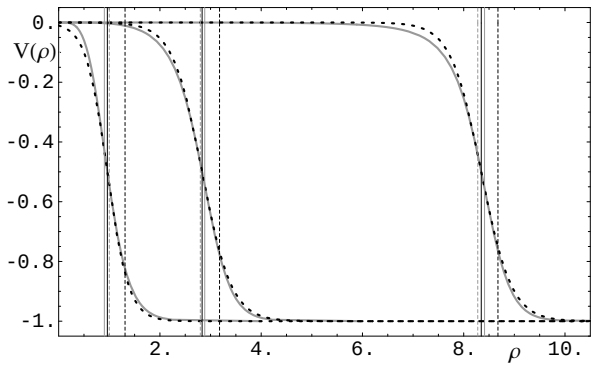

Figure C.1: The exact potential V (solid grey) and the tanh approximation V_{app} (black dotted), for $f \in \{0, 4, 25\}$ with $\tilde{q} = 1$. We also indicate a number of interesting values of ρ with narrow vertical lines: $\rho(u_{half})$, solid black; $\rho(u_{min})$, solid grey; $\rho = \frac{\pi T}{2T_{eff}}$, dashed black; and $\rho = \pi D T$, grey dashed.

To fix the parameter $\mathfrak{n}$ that we will use to characterize the slope of the step of the potential, we simply take the slope of the full potential at either of the corresponding points: $\mathfrak{n} \equiv -2\,\partial_\rho V|_{u_{half,min}} = 8\tilde{q}^2 u^3 h(u) H(u)^{-1/2}\big|_{u_{half,min}}$. Working with u_{half} or u_{min} will give V_{app} which is a good approximation of the full potential V. As shown in figure C.1, the potentials constructed with these two choices typically can not be distinguished. For comparison purposes, the figure also indicates two other interesting scales: $\rho = \pi T/2T_{eff}$ and $\pi D T$. There we see that both of these scales are close to the width of the effective potential but $\rho = \pi D T$ is particularly close to the center of the step.

Note that $V(\rho = 0) = 0$ and $\partial_\rho V(\rho = 0) = 0$ while neither of these properties holds for the approximation (C.1.3). We will take account of this fact simply by expanding around $\rho - \rho_0 \to -\infty$ and discarding higher order terms when computing the values at $\rho = 0$. One can expect this potential to be a good approximation for $\tilde{\nu} \gg 1$, where the result is

less sensitive to the details of the potential away from it's maximum slope and for large f, where the results should be dominated by the large flat part of the potential.

Using infalling boundary conditions at $\rho \to \infty$, the solution is

$$\begin{aligned} A_y &= A_{y0}\, {}_2F_1\Big(1+\tfrac{i\tilde{\nu}}{2\mathfrak{n}}(1-\sqrt{1+\tilde{q}^2/\tilde{\nu}^2}), \tfrac{i\tilde{\nu}}{2\mathfrak{n}}(1-\sqrt{1+\tilde{q}^2/\tilde{\nu}^2}); 1-\tfrac{i\tilde{\nu}}{\mathfrak{n}}\sqrt{1+\tilde{q}^2/\tilde{\nu}^2}; \tfrac{1}{1+e^{2\mathfrak{n}(\rho-\rho_0)}}\Big) \\ &\qquad (1-\tanh\,\mathfrak{n}(\rho-\rho_0))^{-\frac{i\tilde{\nu}}{2\mathfrak{n}}\sqrt{1+\tilde{q}^2/\tilde{\nu}^2}} (1+\tanh\,\mathfrak{n}(\rho-\rho_0))^{\frac{i\tilde{\nu}}{2\mathfrak{n}}} \end{aligned} \tag{C.1.5}$$

and the asymptotic expansion gives us

$$\begin{aligned} A_y &= A_{y0}\, e^{i\tilde{\nu}(\rho-\rho_0)} \left(\frac{\Big(\sqrt{1+\tilde{q}^2/\tilde{\nu}^2}-1\Big)\ \Gamma\Big(\frac{i\tilde{\nu}}{2\mathfrak{n}}(1-\sqrt{1+\tilde{q}^2/\tilde{\nu}^2})\Big)^2\ \Gamma\big(-\frac{i\tilde{\nu}}{\mathfrak{n}}\big)}{\Big(\sqrt{1+\tilde{q}^2/\tilde{\nu}^2}+1\Big)\ \Gamma\Big(-\frac{i\tilde{\nu}}{2\mathfrak{n}}(\sqrt{1+\tilde{q}^2/\tilde{\nu}^2}+1)\Big)^2\ \Gamma\big(\frac{i\tilde{\nu}}{\mathfrak{n}}\big)} \ +\ e^{-2i\tilde{\nu}(\rho-\rho_0)} \right) \\ &\equiv A_{y0}\, e^{i\tilde{\nu}(\rho-\rho_0)} \left(\aleph \ +\ e^{-2i\tilde{\nu}(\rho-\rho_0)}\right)\ , \end{aligned} \tag{C.1.6}$$

for which we redefined A_{y0}. In the opposite limit, as $\rho \to \infty$, the solution converges exponentially to $A_y \propto e^{-i\tilde{\nu}\rho\sqrt{1+\tilde{q}^2/\tilde{\nu}^2}}$, which is the desired infalling wave solution at the horizon.

The transverse conductivity can now be written in a compact suggestive form in terms of the implicitly defined $\aleph$:

$$\tilde{\sigma}_{yy} \ =\ \varepsilon_0\, \mathrm{Re}\ \frac{\tilde{\nu}}{\tilde{\omega}} \frac{\aleph \ -\ e^{2i\tilde{\nu}\rho_0}}{\aleph \ +\ e^{2i\tilde{\nu}\rho_0}}\,, \tag{C.1.7}$$

which is of the same form as the result (2.2.2.2), but with different coefficients. We again see how the oscillatory pattern arises from interference in the asymptotic region due to the potential "step", and how the effective temperature arises from tunnelling through the potential out of the "heat bath" in the near horizon region. For $|\tilde{\nu}| \gg \mathfrak{n}$, we find the limit

$$\aleph \ \overset{|\tilde{\nu}|\to\infty}{\longrightarrow}\ \frac{4\mathfrak{n}\tilde{\nu}}{\mathrm{sgn}(\mathrm{Re}\ \tilde{\nu})\,\pi\tilde{q}^2} e^{\mathrm{sgn}(\mathrm{Re}\ \tilde{\nu})\,\pi\tilde{\nu}/\mathfrak{n}} \left(1+\mathscr{O}\left(\tfrac{\tilde{q}}{\tilde{\nu}}\ \log\ \tilde{\nu}/\mathfrak{n}\right)\right)\ , \tag{C.1.8}$$

This result shows that the subleading term in the conductivity (beyond the low temperature limit (2.2.51)) has an exponential frequency dependence for $\tilde{\omega} > \tilde{q}$, as we found in section 2.2.2.1. We can also see how the results depend on $\mathfrak{n}$, *i.e.,* on the slope of the step in the potential. We compare the present results (C.1.7) for the conductivity to our numerical results and to the perturbative approximation in figure 2.9. There we can see that the various approaches are in very close agreement for $\tilde{\omega} \gtrsim \tilde{q}$.

C.2 Exact pole structure

We can look at the solutions (C.1.6) and identify the quasinormal modes by imposing the asymptotic boundary condition: $A_y(\rho = 0) = 0$. The quasinormal frequencies are then simply determined by the equation

$$e^{2i\tilde{\nu}\rho_0} \;=\; -\frac{\left(\sqrt{1+\tilde{q}^2/\tilde{\nu}^2}-1\right)\,\Gamma\Big(\frac{i\tilde{\nu}}{2\mathfrak{n}}(1-\sqrt{1+\tilde{q}^2/\tilde{\nu}^2})\Big)^2\,\Gamma\big(-\frac{i\tilde{\nu}}{\mathfrak{n}}\big)}{\left(\sqrt{1+\tilde{q}^2/\tilde{\nu}^2}-1\right)\,\Gamma\Big(-\frac{i\tilde{\nu}}{2\mathfrak{n}}(1+\sqrt{1+\tilde{q}^2/\tilde{\nu}^2})\Big)^2\,\Gamma\big(\frac{i\tilde{\nu}}{\mathfrak{n}}\big)} \tag{C.2.9}$$

which simplifies in the limit of $|\tilde{\nu}| \gg \mathfrak{n}, \tilde{q}$ to

$$e^{(2i\rho_0-\mathrm{sgn}(\mathrm{Re}\;\tilde{\nu})\,\pi/\mathfrak{n})\tilde{\nu}} \;\simeq\; -\frac{4\mathfrak{n}\tilde{\nu}}{\mathrm{sgn}(\mathrm{Re}\;\tilde{\nu})\,\pi\tilde{q}^2}\;. \tag{C.2.10}$$

These quasinormal frequencies also give the location of the poles in the spectral function [82, 107], with the exception of the asymptotically constant solution, $\tilde{\nu} = 0$. In the terminology of section 2.3, the present approximation yields:

$$\tilde{\nu}_0 = \frac{4\pi\rho_0}{4\rho_0^2+\pi^2/\mathfrak{n}^2}\;, \qquad \frac{\tilde{\gamma}_0}{\tilde{\nu}_0} = \frac{\pi}{2\rho_0\mathfrak{n}}\;. \tag{C.2.11}$$

Further as mentioned in section 2.3, the subleading contributions are logarithmic in n, giving us

$$\delta\tilde{\nu}_n = \frac{\tilde{\gamma}_0 - i\tilde{\nu}_0}{2\pi}\big(\ln n + \ln\frac{4\mathfrak{n}(i\gamma_0-\tilde{\nu}_0)}{\pi\tilde{q}^2}\big)\;, \tag{C.2.12}$$

in contrast to the constant shift as the largest subleading term for the full correlator.

The residues in the Green's function, before taking the imaginary part, are given by

$$\mathscr{R}^{(n)}_{yy} \;\equiv\; \frac{\varepsilon_0}{\sqrt{1+f^2}}\operatorname*{Res}_{\tilde{\nu}=\tilde{\nu}_n}\frac{\partial_u A_y}{A_y}\bigg|_{u\to 0^+} \;=\; \varepsilon_0\,\frac{-2i\tilde{\nu}_n}{2i\rho_0-\partial_{\tilde{\nu}}\log\gamma|_{\tilde{\nu}=\tilde{\nu}_n}}\;. \tag{C.2.13}$$

One finds that $\partial_{\tilde{\nu}}\log\gamma$ can be expressed in terms of digamma functions, and asymptotes to

$$\frac{\varepsilon_0}{\sqrt{1+f^2}}\operatorname*{Res}_{\tilde{\nu}=\tilde{\nu}_n}\frac{\partial_u A_y}{A_y}\bigg|_{u\to+0} \;\simeq\; \varepsilon_0\,\frac{-2\tilde{\nu}_n}{2\rho_0+i\pi/\mathfrak{n}}\;, \tag{C.2.14}$$

where we used implicitly $n \in \mathbb{Z}$ to label all the poles.

We can use the knowledge of the poles to verify that the spectral function is indeed approximated extremely well by the regularized sum of poles plus the term linear in $\tilde{\omega}$ as given in (2.3.94),

$$\begin{aligned} C_{yy} &= \varepsilon_0 \sum_{n\neq 0} \mathscr{R}_{yy}^{(n)} \frac{\tilde{\nu}_n \operatorname{sgn}(\operatorname{Re}\,\tilde{\nu}_n)}{\left(\tilde{q}^2+\tilde{\nu}_n^2\right)^{1/2}} \left(\frac{1}{\tilde{\omega} - \operatorname{sgn}(\operatorname{Re}\,\tilde{\nu}_n)\left(\tilde{q}^2+\tilde{\nu}_n^2\right)^{1/2}} + \frac{\operatorname{sgn}(\operatorname{Re}\,\tilde{\nu}_n)}{\left(\tilde{q}^2+\tilde{\nu}_n^2\right)^{1/2}} \right) \\ &+ \varepsilon_0 \lim_{n\to+\infty} \frac{\tilde{\omega}}{\pi} \log \frac{\tilde{\nu}_n - \tilde{\nu}_{n+1}}{\tilde{\nu}_{-(n+1)} - \tilde{\nu}_{-n}} \,, \end{aligned} \tag{C.2.15}$$

or from (2.3.95)

$$C_{xx} = \varepsilon_0 \sum_{n\neq 0} \left(\mathscr{R}_{xx}^{(n)} \frac{\tilde{\nu}_n \operatorname{sgn}(\operatorname{Re}\,\tilde{\nu}_n)}{\left(\tilde{q}^2+\tilde{\nu}_n^2\right)^{1/2}} \frac{\mathscr{R}_{xx}^{(n)}}{\tilde{\nu} - \operatorname{sgn}(\operatorname{Re}\,\tilde{\nu}_n)\left(\tilde{q}^2+\tilde{\nu}_n^2\right)^{1/2}} \right) \,, \tag{C.2.16}$$

which we show in figure 2.9. We also use the exact location of the poles to check how well the algorithm from section 2.3 finds the location and residue of the poles, which we show in figure 2.11 and discuss in section 2.3.

Appendix D

Components of the metric

In this appendix, we write out the components of the metric in the most convenient combination, including the implicit effective coupling in $\sqrt{-G} := \frac{\sqrt{(1-\Psi^2)^2+f^2}}{\sqrt{1+f^2}}\sqrt{-\det G}$:

$$\sqrt{-G}G^{xx}G^{yy} = \frac{(f^2+(1-\Psi(u)^2)^2)\sqrt{(1-\Psi^2)+u^2(1-u^4)\Psi'(u)^2}}{\left(1+\frac{\tilde{B}^2u^4}{1+f^2}\right)\sqrt{1-\Psi(u)^2}\sqrt{(f^2+\tilde{\rho}^2+\tilde{B}^2)u^4+1-\left(1+\frac{\tilde{B}^2u^4}{1+f^2}\right)(1-(1-\Psi(u)^2)^2)}}$$

$$\sqrt{-G}G^{uu}G^{yy} = \frac{(1-u^4)\sqrt{1-\Psi(u)^2}\sqrt{(f^2+\tilde{\rho}^2+\tilde{B}^2)u^4+1-\left(1+\frac{\tilde{B}^2u^4}{1+f^2}\right)(1-(1-\Psi(u)^2)^2)}}{\left(1+\frac{\tilde{B}^2u^4}{1+f^2}\right)\sqrt{(1-\Psi^2)+u^2(1-u^4)\Psi'(u)^2}}$$

$$\sqrt{-G}G^{tt}G^{yy} = -\frac{\left((1-\Psi(u)^2)^2+f^2+(\tilde{\rho}^2+\tilde{B}^2)u^4-\frac{\tilde{B}^2u^4}{1+f^2}(1-(1-\Psi(u)^2)^2)\right)\sqrt{(1-\Psi^2)+u^2(1-u^4)\Psi'(u)^2}}{(1-u^4)\left(1+\frac{\tilde{B}^2u^4}{1+f^2}\right)\sqrt{1-\Psi(u)^2}\sqrt{(f^2+\tilde{\rho}^2+\tilde{B}^2)u^4+1-\left(1+\frac{\tilde{B}^2u^4}{1+f^2}\right)(1-(1-\Psi(u)^2)^2)}}$$

$$\sqrt{-G}G^{tt}G^{uu} = \sqrt{(f^2+\tilde{\rho}^2+\tilde{B}^2)u^4+1-\left(1+\frac{\tilde{B}^2u^4}{1+f^2}\right)(1-(1-\Psi(u)^2)^2)}\ \times$$
$$\frac{\sqrt{1-\Psi(u)^2}\left((1-\Psi(u)^2)^2+f^2+(\tilde{\rho}^2+\tilde{B}^2)u^4-\frac{\tilde{B}^2u^4}{1+f^2}(1-(1-\Psi(u)^2)^2)\right)}{\left(1+\frac{\tilde{B}^2u^4}{1+f^2}\right)(f^2+(1-\Psi(u)^2)^2)\sqrt{(1-\Psi^2)+u^2(1-u^4)\Psi'(u)^2}}$$

$$\sqrt{-G}G^{tu}G^{xy} = \frac{\tilde{B}\tilde{\rho}}{1+\frac{\tilde{B}^2u^4}{1+f^2}}\ .$$

At $M_q = 0$, i.e. $\Psi(u) = 0$, these simplify to:

$$\begin{aligned}
\sqrt{-G}G^{xx}G^{yy} &= \frac{1+f^2}{\left(1+\frac{\tilde{B}^2u^4}{1+f^2}\right)\sqrt{1+(f^1+\tilde{\rho}^2+\tilde{B}^2)u^4}} \\
\sqrt{-G}G^{uu}G^{yy} &= \frac{(1-u^4)\sqrt{1+(f^1+\tilde{\rho}^2+\tilde{B}^2)u^4}}{1+\frac{\tilde{B}^2u^4}{1+f^2}} \\
\sqrt{-G}G^{tt}G^{yy} &= -\frac{1+f^2+(\tilde{\rho}^2+\tilde{B}^2)u^4}{(1-u^4)\left(1+\frac{\tilde{B}^2u^4}{1+f^2}\right)\sqrt{1+(f^1+\tilde{\rho}^2+\tilde{B}^2)u^4}} \\
\sqrt{-G}G^{tt}G^{uu} &= -\frac{\left(1+f^2+(\tilde{\rho}^2+\tilde{B}^2)u^4\right)\sqrt{1+(f^1+\tilde{\rho}^2+\tilde{B}^2)u^4}}{\left(1+\frac{\tilde{B}^2u^4}{1+f^2}\right)} \\
\sqrt{-G}G^{tu}G^{xy} &= \frac{\tilde{B}\tilde{\rho}}{1+\frac{\tilde{B}^2u^4}{1+f^2}} \ .
\end{aligned}$$

Appendix E

Thermodynamics of the defect

In this appendix, we compute the contribution of the defect to the extrinsic thermodynamic quantities that are localized on and around the defect. This allows us to study the phase diagram of the matter on the defect and tells us in which regime we can trust our analysis and in which regime the black hole embeddings that we consider may be unstable or metastable. Obviously it is also of interest on its own to study what states the matter on the defect takes in various regimes, and also how the nature of the defect affects the thermodynamic properties.

Naturally, we will implicitly consider the density of these quantities per unit area of the defect in terms of the boundary metric, which removes the divergence from the infinite volume factor of the integral. We will miss however any contribution to possible changes to the asymptotic characteristics of the 3+1 SYM. Since such asymptotic properties however should only depend on the topological properties, i.e. the flux parameter f and not the local properties of the embedding, this is still sufficient to argue about the phase diagram and stability, in the sense of which phases are thermodynamically preferred.

As in chapter 2, we will limit our discussion to the massive embeddings to the D5 case.

E.1 Free Energy and Thermodynamic Variable

As a starting point, we can straightforwardly compute the free energy via the standard procedure from the Euclidean energy, I_e, using

$$F \;=\; TI_e \;, \quad I_e \;=\; \int_{u_{min}}^{u_{max}} \mathcal{L}_e \;+\; I_{bdy} \;, \tag{E.1.1}$$

where the boundary terms

$$I_{bdy.} \;=\; -\frac{1}{3}\sqrt{\gamma}+\frac{1}{2}\Psi^2 \tag{E.1.2}$$

are dictated to us by consistency [111]. The other boundary terms of [111] do not contribute in our case because of isotropy in the flat directions and rotational symmetry on the sphere. Since the determinant on the boundary metric, γ, vanishes on the horizon, only the asymptotic boundary contributes. In the case of non-blackhole (Minkowski) embeddings there is only one (i.e. the asymptotic) boundary, provided the action is consistent at u_{min} and the point at u_{min} is included, as will be discussed below.

In the next step, one can construct other thermodynamic quantities, such as the entropy, $S=-\frac{\partial F}{\partial T}\big|_V$, the energy $E=-F+TS$ or the heat capacity $c_V=\frac{\partial E}{\partial T}\big|_V$. Since the defect is in thermal equilibrium with the bulk, and also the extrinsic curvature of the horizon in the brane geometry is the same as in the bulk theory, the choice for the temperature is obviously the bulk temperature $T=\frac{r_0}{\pi L^2}$. There is a slight ambiguity as to what one considers to be the thermodynamic volume V. One could either consider the defect as an isolated thermodynamic system, embedded in the SYM heat bath, or as part of an overall system. In the former case the volume is either the 2-dimensional volume $\int dx\,dy$ with the effective width of the defect considered to be an "internal" degree of freedom or alternatively the 3-dimensional volume $\int dx\,dy\,dz$ over a finite width Δz, e.g. $\Delta z=\int z'(u)\,du$, with $z'(u)$ given in (3.1.10). In the latter case, however, one considers a large volume of 3d SYM plus the defect, and the quantities that we are studying are just the contributions that are extrinsic in the two dimensions of the defect, and independent of the extension of the volume in the z-direction – in the limit of placing the boundary of the volume far away from the defect. To make this more explicit, we can look at the variation of the euclidean action, which gives

$$\delta I_e \;=\frac{\partial\mathcal{L}_e}{\partial\Psi'}\delta\Psi+\frac{\partial\mathcal{L}_e}{\partial A_t'}\delta A_t+\frac{\partial\mathcal{L}_e}{\partial\chi'}\delta\chi\ , \tag{E.1.3}$$

or in terms of field theory quantities

$$\delta F \;=\; 2C\delta M_q \;+\; \rho_0\delta\mu \;+\; F_f\delta z_{max}\ . \tag{E.1.4}$$

In principle we might expect a term $\propto m\delta m$ that would be divergent. This term however cancels because of the renormalization. Also the variation of the magnetic field does not contribute because of its tensor structure. F_f is just defined as the change of the 3+1 free energy density F_{SYM} due to varying $N_c\to N_c+q$, in dimensionful units:

$$F_f \;=\; \frac{\delta F_{SYM}}{\delta N_c}q \;=\; -2\frac{\pi^2}{8}N_cqT^4 \;=\; -\frac{\pi}{4}N_cN_f\sqrt{\lambda}fT^4. \tag{E.1.5}$$

If $f \sim \mathcal{O}(1)$, then term is suppressed by a factor $\lambda^{-1/2}$ compared to F_{SYM}. Noting the fact that the SYM background is isotropic such that the pressure equals the free energy, $F_{SYM} = P_{SYM}$, we could interpret $F_f \delta \Delta z$ as a work term for the case of the isolated defect. This demonstrates nicely that this case is inconsistent, since want to consider the defect system "on-shell" and study thermodynamic processes obviously with a fixed gauge group, i.e. at constant f, and hence we can't use z_{max} as an independent thermodynamic variable. Hence, we need to do a change of variables in the thermodynamic potentials, corresponding to a Legendre transformation of the action. Since we also want to consider processes at fixed baryon density on the defect, rather than at fixed chemical potential, we do Legendre transformations in χ and A_t:

$$\tilde{\mathcal{L}}_e \;=\; \mathcal{L}_e \;+\; \rho_0 A_t' \;-\; f\chi' \;\text{ or }\quad \tilde{I}_e \;=\; I_e \;+\; \rho_0 A_t \;-\; f\chi \;. \tag{E.1.6}$$

Now, the variation of the free energy is

$$\delta F \;=\; 2C\delta M_q \;+\; \mu\delta\rho_0 \;+\; z_{max}\delta F_f \;, \tag{E.1.7}$$

which implies $F = F(M_q, n_q, f, T)$. Obviously we consider f fixed, even though it is not inconceivable to have processes in condensed matter physics that change the effective gauge group.

In the case of Minkowski embeddings, the significance of the Legendre transformation can be seen nicely from the brane tension in the z direction at the endpoint of the brane u_{max} that can be straightforwardly computed from

$$\tau_z \;=\; g_{zz}\frac{\delta\mathcal{L}^{(D5)}}{\delta g_z z} \;=\; g_{zz}z'^2\frac{\delta\mathcal{L}^{(D5)}}{\delta g_r r} \;, \tag{E.1.8}$$

where g is here the D3 background metric. upon substitution of (3.1.10) and the boundary condition $\Psi \sim 1-(u_{max}-u)\frac{1}{u_{max}(1+u_{max}^4)}$ to match precisely the tension of qN_f D3 branes.

In particular, we can look at the source term that corresponds to attaching an appropriate stack of D3 branes in the flat directions at the endpoint of the probe branes and balances this tension to allow for a consistent static embedding,

$$\mathcal{L}_{source}(u) \;=\; -f\; z(u)\delta(u_{max}-u) \;. \tag{E.1.9}$$

After integration in the radial direction, this term gives precisely the same contribution to the action as the term $-\,f\chi'$ that we added for the Legendre transform. An interesting comment to add is that in this Minkowski embedding, the radial tension τ_r vanishes at the endpoint, and entirely generated by the 5-form flux acting on the brane.

E.2 Derived quantities

As some physical quantities of relevance, we will obtain the entropy $S = -\frac{\partial F}{\partial T}\big|_V$, the total energy $E = F + TS$, heat capacity $c_V = \frac{\partial E}{\partial T}\big|_V = -\frac{\partial^2 F}{\partial T^2}\Big|_V$, baryon number chemical potential $\mu = \frac{\partial F}{\partial \rho}\Big|_{T,V}$ and magnetization $M = \frac{\partial F}{\partial B}\big|_{T,V}$.

The latter two quantities are straightforward, since we only need to keep in mind the temperature scaling and normalization, such that

$$\mu = \frac{\partial F}{\partial \rho_0} = \frac{1}{2\pi^2(\pi T)^2\varepsilon_0}\frac{\partial F}{\partial \tilde{\rho}} =: \frac{1}{2\pi^2(\pi T)^2}\tilde{\mu} \quad \text{and} \tag{E.2.10}$$

$$M = \frac{\partial F}{\partial B} = \frac{1}{(\pi T)^2}\frac{\partial F}{\partial \tilde{B}} = \frac{\varepsilon_0}{(\pi T)^2}\tilde{M} \ . \tag{E.2.11}$$

In principle, there would also be a contribution from the variation of the embedding $\Psi(u)$ via a term $\frac{\delta I_e}{\delta \Psi}\partial_{\rho_0,B}\Psi$, however, it turns out that it does not contribute for the following reason: Since we did a Legendre transform in (A_t', ρ) and (χ', f), the variation $\frac{\delta}{\delta\Psi}$ at constant f, B and ρ_0 is on-shell, i.e. only a boundary term contributes:

$$\frac{\delta I_e}{\delta \Psi}\delta\Psi = \left[\left(\frac{\partial \mathcal{L}_e}{\partial \Psi'} + \frac{\partial I_{bdy}}{\partial \Psi}\right)\delta\Psi\right]_{bdy.} \ . \tag{E.2.12}$$

In principle, this term depends on $\tilde{m}$ and $\tilde{c}$, and keeping $\tilde{m}$ fixed. $\tilde{c}$ will generically depend on B and ρ, and hence $\delta\Psi = \partial_{\tilde{\rho},\tilde{B}}\,\tilde{c}\,u^2\delta(\tilde{\rho},\tilde{B})$. However, it turns out that in an expansion around $u = 0$ and ignoring overall factors, $\frac{\partial \mathcal{L}_e}{\partial \Psi'} + \frac{\partial I_{bdy}}{\partial \Psi} \sim \frac{\tilde{c}}{u} + \tilde{m}^2$, such that any such term will not contribute in the limit $u \to 0$. For black hole embeddings, there is obviously also the second boundary at the horizon, but this contribution vanishes since $\gamma \to 0$ and $\Psi \to 0$ as $u \to 0$. In the case of Minkowski embeddings, there exists only one boundary (the asymptotic one), as we learned above that the Legendre-transformed action is consistent at the endpoint u_{max} and corresponds to including this point in the integral. To demonstrate that there is indeed no contribution from the region at u_{max}, we can use the expansion of Ψ near u_{max},

$$\Psi = 1 - \frac{u_{max} - u}{u_{max}(1 + u_{max}^4)} + \frac{(u_{max} - u)^2 u_{max}^2(3 + 13u_{max}^4)}{6(1 - u_{max}^4)(1 + u_{max}^4)^2} + \mathcal{O}(u_{max} - u)^3 \ . \tag{E.2.13}$$

This relates any change $u_{max} \to u_{max} + \delta u_{max}$. If we then were to exclude the point at u_{max} and evaluate the integral only up to some $u_\epsilon = u_{max} - \epsilon$, then the contribution from

any on-shell variation of the scalar Ψ, $-\frac{\partial \mathcal{L}_e}{\partial \Psi'}\big|_{u=u_\epsilon}\delta\Psi(u_\epsilon)$ cancels the corresponding extra contribution to the integral, $\mathcal{L}_e(u_\epsilon)\frac{\delta\Psi(u_\epsilon)}{\Psi'(u_\epsilon)}$ as we take $\epsilon \to 0$.

Computing the entropy requires a few more steps. In order to compute the temperature derivative, we proceed by computing the integral (E.1.1) in terms of the dimensionless versions of the coordinates and fields. We then consider only the indirect temperature dependence of the terms in the integral and an overall explicit temperature factor which we find by dimensional analysis to be T^3. Keeping ρ_0, B, M_q and f fixed, the temperature dependencies that we will need are given by $\frac{\partial\tilde{\rho}}{\partial T}\big|_{\rho_0} = 2\frac{\tilde{\rho}}{T}$, $\frac{\partial\tilde{B}}{\partial T}\Big|_B = 2\frac{\tilde{B}}{T}$ and $\frac{\partial\tilde{m}}{\partial T}\big|_{M_q} = -\frac{\tilde{m}}{T}$. The variation of the action with respect to $\tilde{\rho}$ and $\tilde{B}$ are straightforward and defined in (E.2.10) and (E.2.11), and the variation with respect to Ψ gives on-shell

$$\delta\Psi\frac{\delta I_e}{\delta\Psi} \;=\; \frac{\partial\mathcal{L}_e}{\partial\Psi'}\delta\Psi \;+\; \int E_\Psi\delta\Psi \;+\; \frac{\partial I_{bdy}}{\partial\Psi}\delta\Psi \;=\; -\frac{2^{2/3}}{\sqrt{\lambda}T}\frac{c}{u_{min}}\delta\Psi|_{u_{min}} \tag{E.2.14}$$

where E_Ψ is the equation of motion for Ψ. Hence, in the limit $u_{min} \to 0$, we don't have to worry about the non-trivial temperature dependence of the condensate. Finally, we have to worry about the temperature dependence of the boundary of the integral. The boundary at the horizon is fixed in terms of the dimensionless coordinate at $u = 1$, so there is no contribution from the horizon. For the asymptotic boundary, we can compute, in dimensionless variables and ignoring overall factors:

$$\frac{\partial I_e}{\partial u_{min}}\bigg|_{u=u_{min}} \;=\; \mathcal{L}_e \;+\; \partial_{u_{min}} I_{bdy.} \;=\; -\frac{1}{6} + \frac{1}{2}\left(\tilde{\rho}^2 + \tilde{B}^2 + f^2 + c^2 - \frac{\tilde{m}^4}{4}\right) + \mathcal{O}(u_{min}) \tag{E.2.15}$$

Since we take the limit $u_{min} \to 0$, any temperature dependence at maximum dimensionful radius r_{max} is $\partial_T u_{min} = \frac{u_m in}{T}$ and hence, there is no contribution from this boundary either. Putting all the non-vanishing contributions together, we arrive with

$$S \;=\; -\frac{3F}{T} \;-\; \frac{2}{T}\left(\frac{\partial F}{\partial\tilde{\rho}}\tilde{\rho} + \frac{\partial F}{\partial\tilde{B}}\tilde{B}\right) \;+\; \frac{\delta I_e}{\delta\Psi}\Psi_{bdy.} \quad \text{or} \tag{E.2.16}$$

$$T\,S \;=\; -3F \;-\; 2\mu\rho_0 \;-\; 2M\,B \;+\; M_q\,C\;. \tag{E.2.17}$$

Finally, we can compute the total energy, $E = F + TS$ and the heat capacity

$$c_V \;=\; \frac{\partial E}{\partial T}\bigg|_V \;=\; -T\,\frac{\partial^2 F}{\partial T^2}\bigg|_V\;. \tag{E.2.18}$$

The second temperature derivative is again computed straightforwardly like the first derivative for the entropy. The most straightforward way is to take the temperature derivative

of the entropy. Keeping in mind that the total temperature derivative of the implicitly present equations of motion E_Ψ vanishes, the remaining terms are:

$$\frac{d^2 F}{d\,T^2}\equiv\left(\partial_T+\frac{2\tilde{\rho}}{T}\partial_{\tilde{\rho}}+\frac{2\tilde{B}}{T}\partial_{\tilde{B}}+\frac{d\,\Psi}{d\,T}\frac{\delta}{\delta\Psi}\right)\left(\partial_T+\frac{2\rho_0}{T}\partial_{\rho_0}+\frac{2\tilde{B}}{T}\partial_{\tilde{B}}\right)F\;-\;\frac{d}{d\,T}\frac{M_q\,C}{T} \tag{E.2.19}$$

$$=\left(\partial_T+\frac{2\tilde{\rho}}{T}\partial_{\tilde{\rho}}+\frac{2\tilde{B}}{T}\partial_{\tilde{B}}\right)^2 F-3\frac{M_q\,C}{T^2}+\left(\frac{2\tilde{\rho}}{T}\partial_{\tilde{\rho}}+\frac{2\tilde{B}}{T}\partial_{\tilde{B}}\right)\int E_\Psi\frac{d\Psi}{d\,T}\;-\;\frac{d}{d\,T}\frac{M_q\,C}{T}\;.$$

Here, we find that we cannot avoid computing the temperature dependence of the embedding Ψ and the condensate. This can be done in closed form, without resorting to numerical derivatives. To do so, we expand the temperature derivative of the equations of motion for Ψ and the boundary conditions on the horizon or at the endpoint of the brane to first order in temperature, obviously keeping the appropriate dimensionful quantities fixed. This term then gives us an inhomogeneous linear second order equation for $\frac{d\,\Psi}{d\,T}$, and a boundary condition fixing $\left(\frac{d\,\Psi}{d\,T}\right)^{-1}\partial_u\left(\frac{d\,\Psi}{d\,T}\right)$ - both of which are not very illuminating and we do not explicitly write them out here. Finally, we choose the boundary condition

$$\partial_u\left[\frac{d\,\Psi}{d\,T}\right]_{u_{min}}\;=\;-\,\Psi'|_{u_{min}} \tag{E.2.20}$$

at the asymptotic boundary to account for the temperature derivative of the dimensionless mass parameter - giving the problem numerically slightly non-trivial mixed boundary conditions. Alternatively, the heat capacity can also be written in a more systematic way,

$$\begin{aligned} c_v &= -T\left(\partial_T\,+\,2\frac{B}{T}\frac{d}{d\,B}\,+\,2\frac{\rho_0}{T}\frac{d}{d\,\rho_0}\,-\,\frac{M_q}{T}\frac{d}{d\,M_q}\right)^2 F \qquad\qquad (E.2.21)\\ &= -4B^2\frac{\chi_B}{T}\,-\,4\frac{\rho^2}{\epsilon\,T}\,-\,8\rho B\frac{m}{T}\,+\,\frac{M}{T}\left(4B\frac{d}{d\,B}\,+\,4\rho_0\frac{d}{d\,\rho+0}\,-\,M_q\frac{d}{d\,M_q}\right)C\,-\,6\frac{F}{T}\;, \end{aligned}$$

where we identified the magnetic susceptibility, density of states, and mean magnetic moment:

$$\chi_B \;=\; \tfrac{d\,M}{d\,B}\big|_{T,V,\rho_0} \;=\; \frac{1}{(\pi T)^2}\int\left(\partial_{\tilde{B}}^2\mathcal{L}_e+\partial_{\tilde{B}}E_\Psi\frac{d\Psi}{d\tilde{B}}\right) \tag{E.2.22}$$

$$\epsilon^{-1} \;=\; \tfrac{d\,\mu}{d\,\rho_0}\Big|_{T,V,B} \;=\; \frac{1}{\left(2\pi^2(\pi T)^2\varepsilon_0\right)^2}\int\left(\partial_{\tilde{\rho}}^2\mathcal{L}_e+\partial_{\tilde{\rho}}E_\Psi\frac{d\Psi}{d\tilde{\rho}}\right) \tag{E.2.23}$$

$$m \;=\; \tfrac{d\,M}{d\,\rho_0}\Big|_{T,V,B} \;=\; \frac{1}{2\pi^2(\pi T)^4\varepsilon_0}\int\left(\partial_{\tilde{B}}\partial_{\tilde{\rho}}\mathcal{L}_e+\partial_{\tilde{\rho}}E_\Psi\frac{d\Psi}{d\tilde{B}}\right)\;. \tag{E.2.24}$$

The derivatives of the scalar, $\frac{d\Psi}{d\tilde{B}}$ and $\frac{d\Psi}{d\tilde{\rho}}$ can be computed in an equivalent fashion as the derivative $\frac{d\Psi}{dT}$ described above.

E.2.1 Massless case

In the massless case, the free energy can be integrated straightforwardly analytically and becomes

$$\begin{aligned} F &= -4\pi T_5 r_0^3 \int_0^1 du \left(\frac{u^4-3}{3u^4\sqrt{1-u^4}} + \frac{\sqrt{1+\left(f^2+\tilde{\rho}^2+\tilde{B}^2\right)u^4}}{u^4} \right) \\ &= -\sqrt{\lambda}T^3 N_c \frac{1}{3}\left(\sqrt{1+f^2+\tilde{\rho}^2+\tilde{B}^2} \right. \\ &\qquad \left. + 2\left(-\left(f^2+\tilde{\rho}^2+\tilde{B}^2\right)\right)^{3/4} \mathcal{F}\left(\sinh^{-1}\left(-\left(f^2+\tilde{\rho}^2+\tilde{B}^2\right)\right)^{1/4}\Big|-1\right)\right) , \end{aligned} \tag{E.2.25}$$

where the first term in the integral cancels the divergence of the second term at $u \to 0$; we substituted field theory quantities in the dimensionful factor in the second line and $\mathcal{F}(\cdot|\cdot)$ is the incomplete elliptic integral of the first kind. For convenience, we give the asymptotic expansion $\mathcal{F}\left(\sinh^{-1}(-X)^{1/4}\,\big|-1\right) = i\mathcal{K}(2) - (-X)^{-1/4} + \mathcal{O}(X)^{-5/4}$ and the expansion at small values $\mathcal{F}\left(\sinh^{-1}(-X)^{1/4}\,\big|-1\right) = (-X)^{1/4}\left(1-\frac{X}{10}\right) + \mathcal{O}(-X)^{9/4}$, where $\mathcal{K}(.)$ is the complete elliptic integral of the first kind and $\mathcal{K}(2) \sim 1.854e^{i\pi/4}$. These asymptotic approximations are indicated in fig. E.1. We also note again the effect of the electric-magnetic duality, which relates quantities under the interchange of density and magnetic field, such that in the following we only need to show e.g. either the chemical potential or the magnetization.

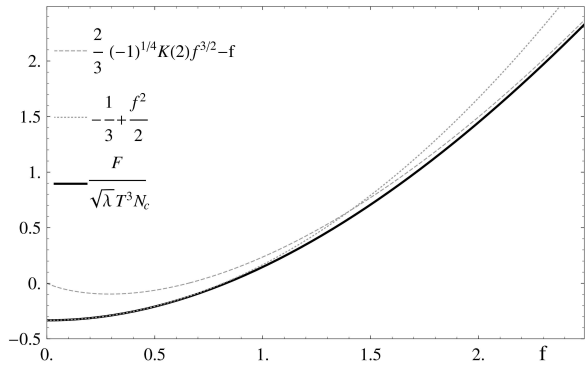

Figure E.1: The free energy density of the as a function of $\sqrt{f^2+\tilde{\rho}^2+\tilde{\nu}^2}$ (denoted for simplicity as "f".

Now, we can simply verify the relations (E.2.10) and (E.2.11):

$$\mu = \left.\frac{\partial F}{\partial \rho}\right|_T = (\pi T)^2 \frac{\partial F}{\partial \rho_0} \tag{E.2.26}$$
$$= \sqrt{\lambda} T^3 N_c \rho_0 \frac{\mathcal{F}\left(\sinh^{-1}\left(-\left(f^2+\rho_0^2/(\pi T)^2+B^2/(\pi T)^2\right)\right)^{1/4}\Big|-1\right)}{\left(-\left(f^2+\rho_0^2/(\pi T)^2+B^2/(\pi T)^2\right)\right)^{1/4}} = \sqrt{\lambda} T^3 N_c \int_0^1 du A_t'$$

$$z_{max} = \left.\frac{\partial F}{\partial F_f}\right|_T = \frac{4}{\pi N_c N_f \sqrt{\lambda} T^4}\frac{\partial F}{\partial f} \tag{E.2.27}$$
$$= \frac{1}{\pi T} f \frac{\mathcal{F}\left(\sinh^{-1}\left(-\left(f^2+\rho_0^2/(\pi T)^2+B^2/(\pi T)^2\right)\right)^{1/4}\Big|-1\right)}{\left(-\left(f^2+\rho_0^2/(\pi T)^2+B^2/(\pi T)^2\right)\right)^{1/4}} = \pi T \int_0^1 d\,u\,\chi' \ .$$

This is shown in fig. E.2, and we note that the dominant dependence of μ on ρ_0 or

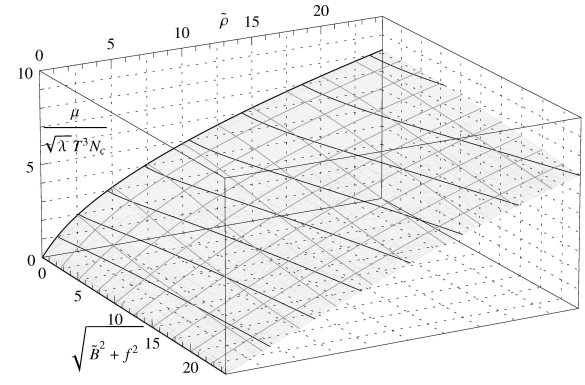

Figure E.2: The chemical potential as a function of $\tilde{\rho}$ and $\sqrt{\tilde{B}^2+f^2}$. Note that, due to electromagnetic duality, this is the same as the magnetization as a function of $\tilde{B}$ and $\sqrt{\tilde{\rho}^2+f^2}$, upon an appropriate scaling with a dimensionful constant.

M on B, with an apparent saturation behavior as the scaling power changes from 1 to

1/2. The behavior on the subleading quantities is a small suppression, which goes slightly against classical intuition Further more, we can straightforwardly give the contribution of the defect to the entropy, which is

$$\begin{aligned} S &= \sqrt{\lambda}T^2N_c\left(\sqrt{1+f^2+\rho^2/(\pi T)^2+B^2/(\pi T)^2}\right. \\ &\quad \left. + 2f^2\frac{\mathcal{F}\left(\sinh^{-1}\left(-\left(f^2+\rho^2/(\pi T)^2+B^2/(\pi T)^2\right)\right)^{1/4}\Big|-1\right)}{\left(-\left(f^2+\rho^2/(\pi T)^2+B^2/(\pi T)^2\right)\right)^{1/4}}\right) \quad , \end{aligned} \tag{E.2.28}$$

which is indicated in fig. E.3. Now, we can notice that for large values of f, this ex-

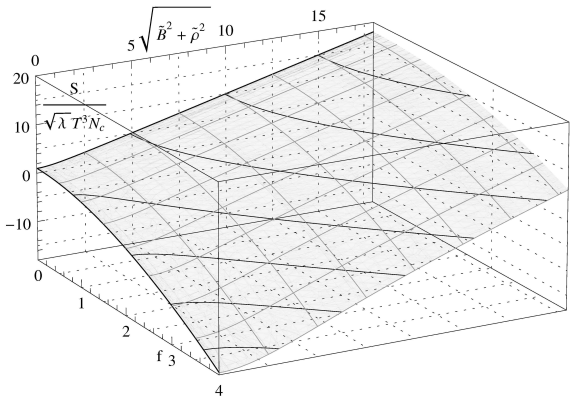

Figure E.3: The contribution of the defect to the entropy as a function of $\sqrt{\tilde{\rho}^2+\tilde{B}^2}$ and f.

pression turns negative. Since the thermodynamic quantities that we derive here are only contributions to the overall quantities of the system "defect+background", and the defect is certainly strongly coupled to the background and hence always in thermal equilibrium, this is not troublesome, as we can demonstrate:

First, we assume that the defect effectively extends roughly homogeneously over a region up to z_{max} in the normal direction. This is suggested by (3.1.10), (E.2.26) and at large f also by the results from chapter 2. Then, we consider the entropy density over this region,

$$\frac{S^{\Delta z}}{z_{max}} = 2\sqrt{\lambda}\pi T^3N_c\left(\frac{\left(-\left(f^2+\rho_0^2/(\pi T)^2+B^2/(\pi T)^2\right)\right)^{1/4}\sqrt{1+f^2+\rho_0^2/(\pi T)^2+B^2/(\pi T)^2}}{f\mathcal{F}\left(\sinh^{-1}\left(-\left(f^2+\rho_0^2/(\pi T)^2+B^2/(\pi T)^2\right)\right)^{1/4}\Big|-1\right)}-2f\right) , \tag{E.2.29}$$

where we look in particular at the density of the negative term, $-2\pi\sqrt{\lambda}T^3N_cf$. In our limit of large N_c and $N_c \gg f^2$, this term is precisely (minus) the contribution $q\frac{\delta S_{SYM}}{\delta N_c}$. This

can be interpreted simply in the way that the extra degrees of freedom due to changing $N_c \to N_c + \delta N_c$ become fully available only after the brane falls into the horizon, and the positive term in the entropy of the defect describes the extra degrees of freedom contributed by the defect inside that region. Furthermore, there is no region in which the total entropy of the combined system is negative.

At large densities or magnetic fields, the contribution to the entropy is just $\sqrt{\lambda}N_c\frac{\rho_0}{\pi}$ or $\sqrt{\lambda}N_c\,2\pi\varepsilon_0 B$, respectively - indicating that the number of degrees of freedom is independent of the temperature, and proportional to the number of quarks or magnetic states.

We can also straightforwardly compute the heat capacity:

$$c_V = 2\sqrt{\lambda}TN_c\left(\frac{1}{\sqrt{1+f^2+\rho_0^2/(\pi T)^2+B^2/(\pi T)^2}}\left(1+2f^2-\frac{f^4}{f^2+\rho_0^2/(\pi T)^2+B^2/(\pi T)^2}\right)\right.$$
$$\left.-\frac{f^2\mathcal{F}\left(\sinh^{-1}\left(-\left(f^2+\rho_0^2/(\pi T)^2+B^2/(\pi T)^2\right)\right)^{1/4}\middle|-1\right)}{\left(-\left(f^2+\rho_0^2/(\pi T)^2+B^2/(\pi T)^2\right)\right)^{1/4}}\left(3-\frac{f^2}{f^2+\rho_0^2/(\pi T)^2+B^2/(\pi T)^2}\right)\right) \quad \text{(E.2.30)}$$

which we show in figure E.4. Again, we notice that the heat capacity is negative for large f,

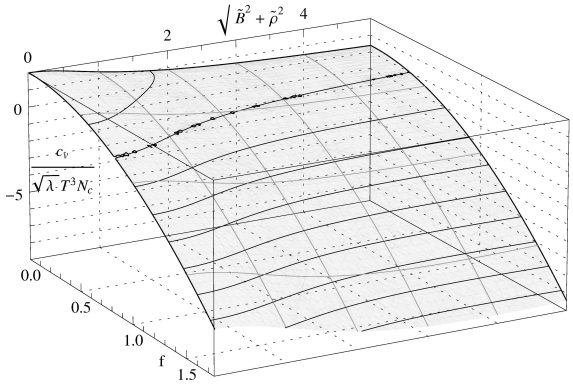

Figure E.4: The contribution of the defect to the specific heat as a function of $\sqrt{\tilde{\rho}^2+\tilde{B}^2}$ and f.

but as in the case with the entropy, this does not signify an instability, as the contribution is much smaller than the heat capacity of the background SYM in the appropriate region around the defect, and the negative contribution to the heat capacity simply indicates that the additional degrees of freedom only turn on gradually over some region $\sim z_{max}$ away from the defect. At small f, the heat capacity is just $c_V = 2\sqrt{\lambda}TN_c\frac{1}{\sqrt{1+\rho^2/(\pi T)^4+B^2/(\pi T)^4}}+\mathcal{O}(f^2)$. This is somewhat counter-intuitive, as one normally expects an increasing heat capacity with increasing density. However, since this system is strongly coupled, this is not too

surprising, as $\tilde{\rho}_0$ is obviously only the net baryon number density, but there is always a plasma of quarks and gluons in thermal equilibrium, so there is always a finite total density. As we increase the net quark density, beyond the normal equilibrium total quark density, we are changing the equilibrium, and it may happen that the density of gluons decreases.

Finally, we can look at magnetic the susceptibility,

$$\begin{aligned}\chi_B &= \frac{\sqrt{\lambda}N_c T}{2}\left(\frac{B^2}{(f^2+\rho_0^2/(\pi T)^2+B^2/(\pi T)^2)\sqrt{1+f^2+\rho_0^2/(\pi T)^2+B^2/(\pi T)^2}}\right. \\ &+ \left.(\pi T)^4\left(2-\frac{B^2}{\rho^2+B^2+f^2(\pi T)^4}\right)\frac{\mathcal{F}\left(\sinh^{-1}\left(-\left(f^2+\rho-0^2/(\pi T)^2+B^2/(\pi T)^2\right)\right)^{1/4}\Big|-1\right)}{\left(-\left(f^2+\rho_0^2/(\pi T)^2+B^2/(\pi T)^2\right)\right)^{1/4}}\right).\end{aligned} \tag{E.2.31}$$

This expression is always less than $\chi_B^{(0)}\sqrt{\lambda}N_c\pi^2T^3$ - the susceptibility of the defect without any of the parameters turned on as shown in fig. E.5 - and behaves asymptotically as $\chi_B^{(0)}\frac{(-1)^{1/4}\mathcal{K}(2)}{\sqrt{f}}$, $\chi_B^{(0)}\frac{(-1)^{1/4}\mathcal{K}(2)}{\sqrt{\rho/(\pi T)^2}}$ or $\chi_B^{(0)}\frac{(-1)^{1/4}\mathcal{K}(2)}{2\sqrt{B/(\pi T)^2}}$, respectively. Hence, the defect is diamagnetic. Again, we can blame this on the strong coupling, which may increase the spin-spin interactions. In the case of the equivalent density of states, this becomes more obvious, since asymptotic freedom should have the effect of lowering the energy density of the plasma as we increase the quark density.

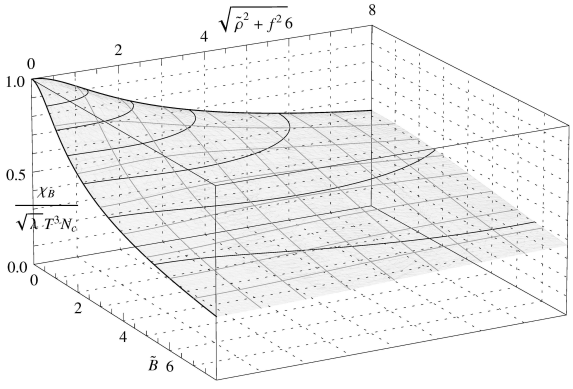

Figure E.5: The magnetic susceptibility of the defect as a function of $\tilde{B}$ and $\sqrt{\tilde{\rho}^2+f^2}$. This is the same as the density of states as a function of $\tilde{\rho}$ and $\sqrt{\tilde{B}^2+f^2}$.

E.2.2 Numerical results

Now, let us look at the phase diagram in fig. E.6. Looking at the different kinds of embeddings, we find that in the case of vanishing ρ and f, there are three phases: the stable

phases of the blackhole embedding at small masses $M_q < M_{max}^{(BH)}$ (or large temperatures), denoted as "**B**" and of the Minkowski embedding at large masses $M_q > M_{min}^{(flat)}$ (**M**). In principle, these connect via 2^{nd} order phase transition to an unstable phase with $M_{max}^{(BH)} > M_q > M_{min}^{(flat)}$ (**C**), but in practice, this phase is not realized and there will just be a first order phase transition from **B** to **M**. At finite f or ρ, the mass diverges at $u_{max} = 0$ or $\Psi_0 = 1$, so we find two additional phases, each one for the blackhole (**B1**) and Minkowski (**M1**) embeddings. We interpret this **B1** embedding as a phase with free quarks, but also a high density of mesons. In many situations, the phase transition between those phases will disappear, as we will see below. Using the condensate as an order parameter to identify different phases, we demonstrate the various phases in figs. E.6 - E.8. In order to demonstrate the phase transitions, and the disappearance of the blackhole phase **M** and the transition phase **C** in the presence of strong magnetic fields, we plot the results at fixed temperature with varying $M/(\pi T)$, rather than fixed mass and varying T/M. Obviously, in a thermodynamic process $M/(\pi T) = 0$ cannot be attained. In fig. E.6, we find that the critical masses decreases approximately linearly with the increasing magnetic field, there is a critical magnetic field, above which the blackhole phase **B** disappears. This indicates that the magnetic field catalyzes meson formation. This behavior is similar to what was observed in 3+1 dimensional systems in [110]. Rigorously speaking, however, there exists at all magnetic fields a continuation of the **B** phase at zero mass. Also, we find how the phase **C**, that is suppressed at finite density or f re-appears at large magnetic fields. The condensate is large in the blackhole phase **B1** and in the Minkowski phases and grows approximately proportional to the magnetic field – indicating chiral symmetry breaking. As indicated above, these phases have a very similar behavior. The reader is reminded however that at finite density, the Minkowski embedding is not physical within string theory. It is interesting though that turning on f reverses the linear mass dependence of the condensate when interpreted as the conjugate potential of the mass - meaning that if we increase the mass or lower the temperature, the free energy will "saturate". In the blackhole phase **B** in which the mesons are dissociated and we have only free quarks, the condensate vanishes and is independent of mass and magnetic field. This indicates to us that the $SU(N_f)$ is not broken.

In fig. E.7, we see that a finite net baryon density increases the critical masses, suppresses the blackhole phase **B** and the connecting phase and separates the two Minkowski phases. The phase **M** is left approximately unchanged by turning on the finite density, sitting still at $\tilde{c} \sim 0$ with unbroken chiral symmetry, but the condensate of the **M1** and **B1** phases is negative for $M_q \neq 0$ and approximately proportional to the mass. Turning on a finite magnetic field has the expected effect of lowering the critical masses, increasing phase space volume of the phases **C** and **B** and shifting the overall condensate - breaking also

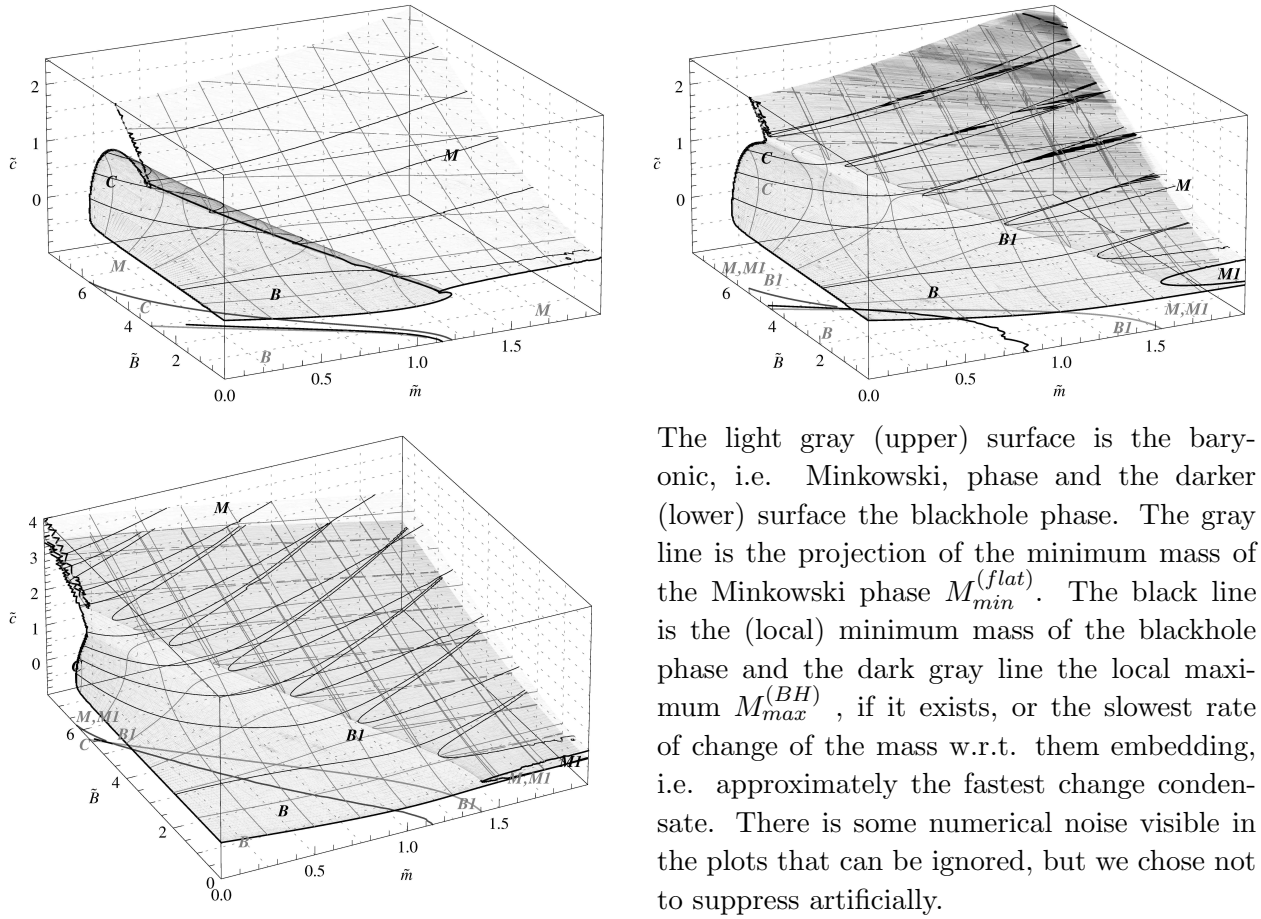

The light gray (upper) surface is the baryonic, i.e. Minkowski, phase and the darker (lower) surface the blackhole phase. The gray line is the projection of the minimum mass of the Minkowski phase $M_{min}^{(flat)}$. The black line is the (local) minimum mass of the blackhole phase and the dark gray line the local maximum $M_{max}^{(BH)}$, if it exists, or the slowest rate of change of the mass w.r.t. them embedding, i.e. approximately the fastest change condensate. There is some numerical noise visible in the plots that can be ignored, but we chose not to suppress artificially.

Figure E.6: Value of the condensate as a function of the dimensionless mass, $\tilde{m}$ and magnetic field, $\tilde{B}$ at fixed temperature. Top left: Vanishing density and magnetic field. The light and dark gray lines identify the transition between **B** and **C** and **M**, respectively. Top right: Density $\tilde{\rho} = 0.5$. The dark gray line is now the transition between **B** and **C**, or **B** and **B1** and the black line between **C** and **B1**. The light gray line is the transition between **M** and **M1**. Bottom left: $f = 0.25$. More details are explained in the bottom right.

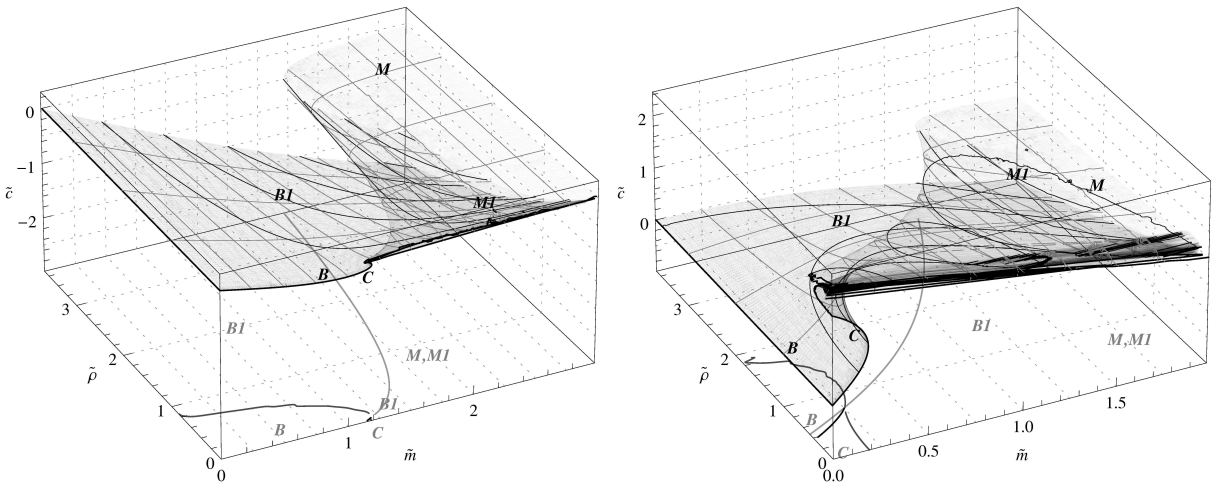

Figure E.7: Value of the condensate as a function of the dimensionless mass and density, at fixed temperature. Left: $\tilde{B} = 0$, right $\tilde{B} = 4$.

the symmetry of the **M** phase. Interestingly, this persists even at relatively large densities. To understand this behavior we recall that there is always a finite total baryon density, and the polarizing an localizing effect of the magnetic field is not affected by changing the ratio of quarks and anti-quarks. The parameter f, not surprisingly form the gravity point of view, but surprisingly from the field theory point of view, has a very similar effect to turning on a finite density as we show in fig. E.8.

In order to determine which phases are thermodynamically preferred, i.e. stable, we can look at the entropy. Before studying the data, we should notice that there is a trade-off between numerical accuracy and noisiness. This arises because a significant contribution to the entropy comes from the UV regime, i.e. small values of u. On the other hand, however, the solution for Ψ becomes unstable and noisy in this regime, so we usually choose a cutoff of the order of 10^{-5}, which causes usually no significant errors in the result – except for the case of the entropy. Even if we try to extrapolate at small u, the cancellation of the boundary term in (E.2.16) will not be accurate, so we need to push the minimum value for u as far as possible and we will notice some noise. Eventually, the qualitative result will not be affected in any event, and we can further check whether some apparent "effect" is due to numerical errors or not.

We use quantities that are made dimensionless using the mass as we consider the system at fixed mass. For example, we have $\bar{T} = \frac{1}{\tilde{m}}$ and $\bar{B} = \frac{\tilde{B}}{\tilde{m}^2}$. We chose this combination,

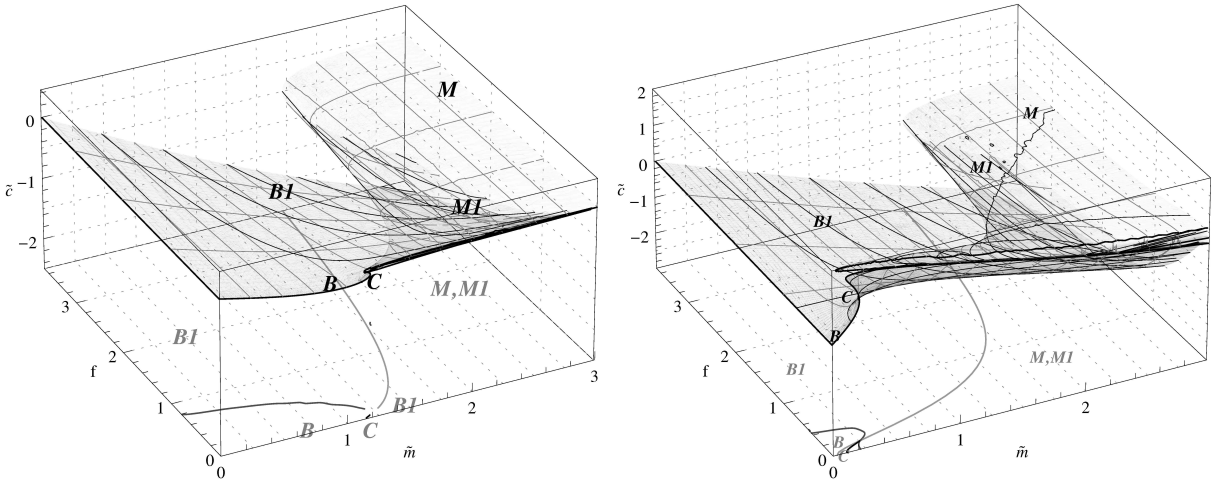

Figure E.8: Condensate as a function of the dimensionless mass and f, at fixed temperature. Left: $\tilde{B} = 0$, right $\tilde{B} = 4$.

because these are parameters that naturally arise in the computations. Notice however, that $\tilde{m}$ contains a factor of $\sqrt{\lambda}$, i.e. $\bar{T} = \sqrt{\lambda}\frac{T}{2^{3/2}M_q}$ and $\bar{B} = \frac{\tilde{B}}{\tilde{m}^2} = \lambda\frac{B}{8\pi^2 M_q^2}$.

If we now look at the entropy in fig. E.9, we see that in all cases, the blackhole embedding is preferred. In the case of having only the magnetic field non-vanishing, we actually notice the cusp-like behavior at the point where the blackhole and Minkowski phases meet, as it was observed in [45]. In the plot on the top right, at $f = 1/2$, we there is some numerical error which causes the entropy of the lower branch of the Minkowski embedding not to go to zero at vanishing temperature. In the bottom-left, we "cut out" the region of small temperatures and densities, as it was dominated by noise. We also notice again in the bottom right, which shows the plot "from behind", that f causes a negative entropy contribution, as discussed in the context of fig. E.3. Note that the hint of the entropy of the phases crossing around $\bar{T} \sim 0.25$ can be shown to be due to numerical errors.

Let us finally just take a quick look at the other first derivatives of the free energy. In fig. E.10, we show the magnetization and we notice that the magnetization is higher in the blackhole phase, where we expect more free quarks, and lower in the Minkowski phase where we expect more mesons. In the case of small finite f (qualitatively the same happens also for $\bar{\rho}$) however, the difference is highly suppressed and both phases have essentially the same magnetization.

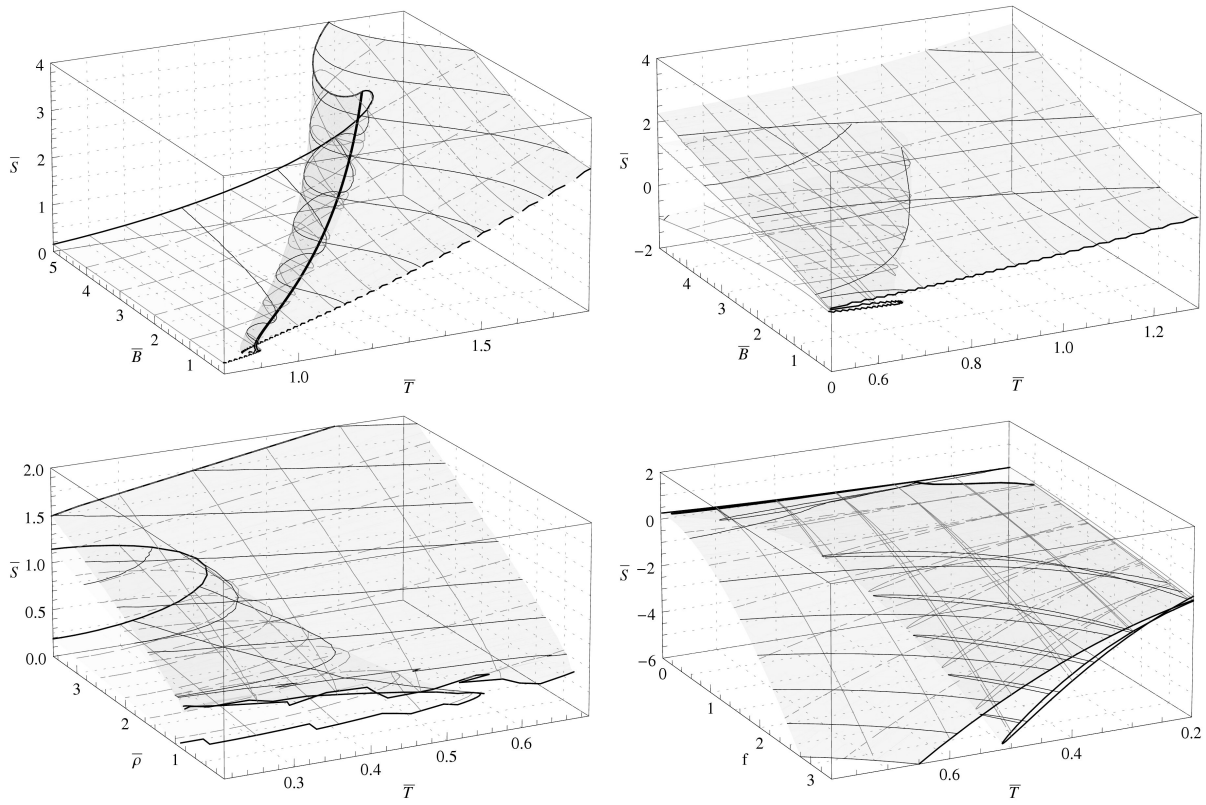

Figure E.9: The dimensionless entropy $\bar{S} = \frac{S}{8M_q^2 N_c}$ as a function of $\bar{T} = \sqrt{\lambda}\frac{T}{2^{3/2}M_q}$ and $\bar{B} = \lambda\frac{B}{8\pi^2 M_q^2}$ for $f = 0 = \bar{\rho}$ (top left) and $f = 1/2$, $\bar{\rho} = 0$ (top right) or as a function of $\bar{T}$ and $\bar{\rho}$ (bottom left) or f (bottom right).

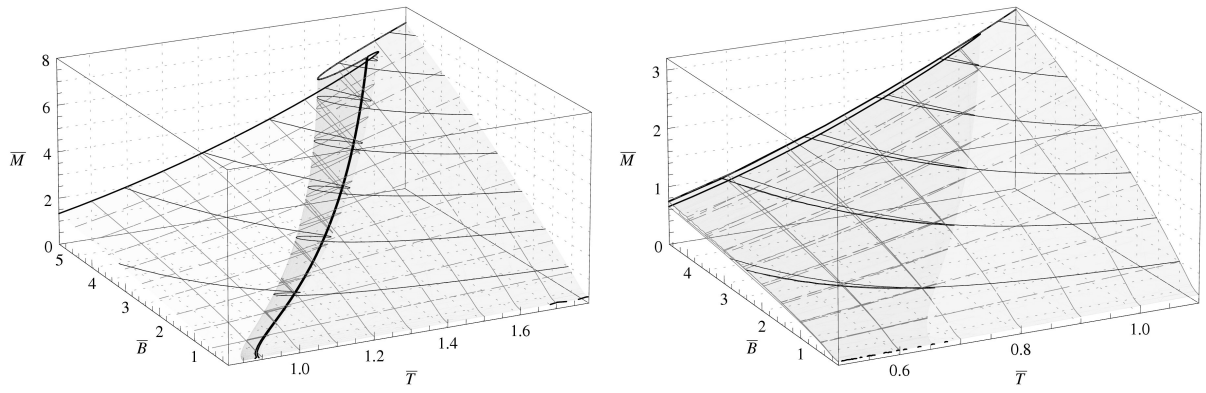

Figure E.10: The magnetization $\bar{M}$ as a function of the temperature-mass ratio $\bar{T}$ and the magnetic field $\bar{B}$ at $\bar{\rho} = 0 = f$ (left) and $f = 0$ (right).

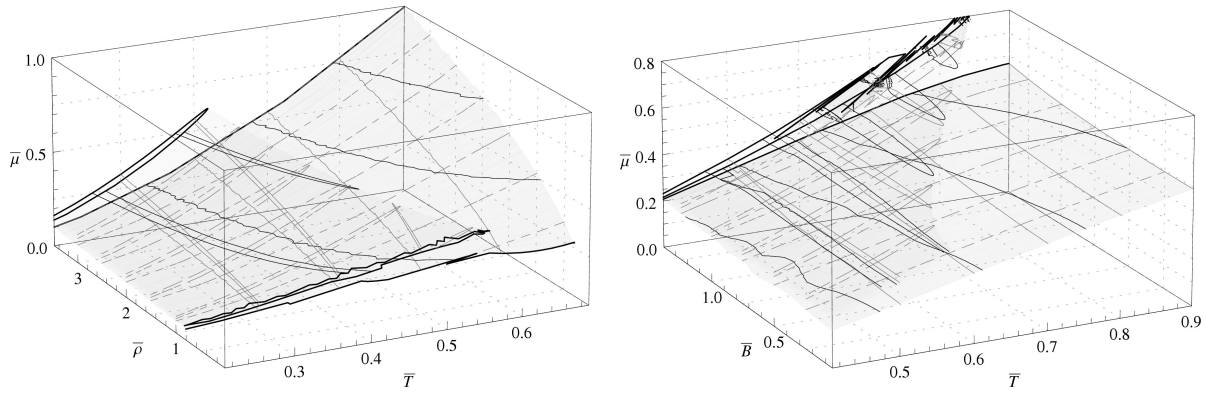

Figure E.11: The chemical potential $\bar{\mu}$ as a function of the temperature-mass ratio $\bar{T}$ and the density $\bar{\rho}$ at $\bar{B} = 0 = f$ (left) and as a function of $\bar{B}$ at $\bar{\rho} = 1/2$ (right).

In figure E.11, we look at the chemical potential. In contrast to the magnetization, there is a a significant difference in the chemical potential, that persists in all cases, and the chemical potential of the Minkowski phase is higher. Hence, inducing a difference in the density of baryons and anti-baryons requires more energy in the Minkowski phase. Intuitively, this would be the case if the Minkowski phase is dominated by mesons. It might also be related to the fact that in string theory, there should be no finite net baryon density in the Minkowski phase.

Bibliography

[1] G. Veneziano, "AN INTRODUCTION TO DUAL MODELS OF STRONG INTERACTIONS AND THEIR PHYSICAL MOTIVATIONS," Phys. Rept. **9**, 199 (1974). 1

[2] L. Brink, P. Di Vecchia and P. S. Howe, "A Locally Supersymmetric And Reparametrization Invariant Action For The Spinning String," Phys. Lett. B **65**, 471 (1976); S. Deser and B. Zumino, "A Complete Action For The Spinning String," Phys. Lett. B **65**, 369 (1976). 2

[3] A. M. Polyakov, "Quantum geometry of fermionic strings," Phys. Lett. B **103**, 211 (1981). 2

[4] D. J. Gross and F. Wilczek, "ULTRAVIOLET BEHAVIOR OF NON-ABELIAN GAUGE THEORIES," Phys. Rev. Lett. **30**, 1343 (1973); H. D. Politzer, "RELIABLE PERTURBATIVE RESULTS FOR STRONG INTERACTIONS?," Phys. Rev. Lett. **30**, 1346 (1973); G. 't Hooft, talk at *Marseille conference on renormalization of Yang-Mills fields and applications to particle physics* (1972), unpublished 2

[5] J. Scherk and J. H. Schwarz, "Dual Models For Nonhadrons," Nucl. Phys. B **81**, 118 (1974). 2

[6] P. Goddard and C. B. Thorn, "Compatibility of the Dual Pomeron with Unitarity and the Absence of Ghosts in the Dual Resonance Model," Phys. Lett. B **40**, 235 (1972); C. Lovelace, "Pomeron Form-Factors And Dual Regge Cuts," Phys. Lett. B **34**, 500 (1971). 2

[7] A. Neveu and J. H. Schwarz, "Factorizable dual model of pions," Nucl. Phys. B **31**, 86 (1971); P. Ramond, "Dual Theory for Free Fermions," Phys. Rev. D **3**, 2415 (1971). 2

[8] F. Gliozzi, J. Scherk and D. I. Olive, "Supersymmetry, Supergravity Theories And The Dual Spinor Model," Nucl. Phys. B **122**, 253 (1977). 2

[9] M. B. Green and J. H. Schwarz, "Supersymmetrical Dual String Theory," Nucl. Phys. B **181**, 502 (1981). 2

[10] M. B. Green and J. H. Schwarz, "Anomaly Cancellation In Supersymmetric D=10 Gauge Theory And Superstring Theory," Phys. Lett. B **149**, 117 (1984). 2

[11] J. Polchinski, "String theory. Vol. 2: Superstring theory and beyond," *Cambridge, UK: Univ. Pr. (1998) 531 p* 3

[12] T. Kaluza, Theodor, "Zum Unitätsproblem in der Physik", Sitzungsber. Preuss. Akad. Wiss. Berlin. (Math. Phys.) **1921**, 966972 (1921); O. Klein, "Quantentheorie und fünfdimensionale Relativitätstheorie", Zeitschrift für Physik a Hadrons and Nuclei, **37**, 895906 (1926) 3

[13] S. B. Giddings, S. Kachru and J. Polchinski, "Hierarchies from fluxes in string compactifications," Phys. Rev. D **66**, 106006 (2002) [arXiv:hep-th/0105097]. 4

[14] See, for example: M. R. Douglas and S. Kachru, "Flux compactification," Rev. Mod. Phys. **79** (2007) 733 [arXiv:hep-th/0610102]. 4

[15] S. Kachru, R. Kallosh, A. Linde and S. P. Trivedi, "De Sitter vacua in string theory," Phys. Rev. D **68**, 046005 (2003) [arXiv:hep-th/0301240]. 4

[16] M. R. Douglas, "The statistics of string/M theory vacua," JHEP **0305**, 046 (2003) [arXiv:hep-th/0303194]. 4

[17] F. Denef and M. R. Douglas, "Computational complexity of the landscape. I," Annals Phys. **322**, 1096 (2007) [arXiv:hep-th/0602072]. 4

[18] F. Gmeiner, R. Blumenhagen, G. Honecker, D. Lust and T. Weigand, "One in a billion: MSSM-like D-brane statistics," JHEP **0601**, 004 (2006) [arXiv:hep-th/0510170]. 4

[19] R. Bousso, "Holographic probabilities in eternal inflation," Phys. Rev. Lett. **97**, 191302 (2006) [arXiv:hep-th/0605263]. 4

[20] J. Polchinski, "Dirichlet-Branes and Ramond-Ramond Charges," Phys. Rev. Lett. **75**, 4724 (1995) [arXiv:hep-th/9510017]. 4

[21] M. Born and L. Infeld, "Foundations Of The New Field Theory," Proc. Roy. Soc. Lond. A **144**, 425 (1934). 5

[22] L. Randall and R. Sundrum, "A large mass hierarchy from a small extra dimension," Phys. Rev. Lett. **83**, 3370 (1999) [arXiv:hep-ph/9905221];L. Randall and R. Sundrum, "An alternative to compactification," Phys. Rev. Lett. **83**, 4690 (1999) [arXiv:hep-th/9906064]. 5

[23] D. Lust, "Intersecting brane worlds: A path to the standard model?," Class. Quant. Grav. **21**, S1399 (2004) [arXiv:hep-th/0401156]. 5

[24] C. V. Johnson, "D-Branes," *Cambridge, USA: Univ. Pr. (2003) 548 p* 6

[25] K. Becker, M. Becker and J. H. Schwarz, "String theory and M-theory: A modern introduction," *Cambridge, UK: Cambridge Univ. Pr. (2007) 739 p* 6

[26] See, for example:
T. Ortin *Gravity and Strings*, (Cambridge University Press, 2004) 6, 67

[27] S. W. Hawking and D. N. Page, "Thermodynamics Of Black Holes In Anti-De Sitter Space," Commun. Math. Phys. **87**, 577 (1983). 6

[28] G. R. Dvali and S. H. H. Tye, "Brane inflation," Phys. Lett. B **450**, 72 (1999) [arXiv:hep-ph/9812483]. 6

[29] J. C. Breckenridge, R. C. Myers, A. W. Peet and C. Vafa, "D-branes and spinning black holes," Phys. Lett. B **391**, 93 (1997) [arXiv:hep-th/9602065]. 6

[30] K. R. Popper, "Conjectures and Refutations: The Growth of Scientific Knowledge", Routledge, London (1963) 6, 139

[31] G. 't Hooft, "Dimensional reduction in quantum gravity," arXiv:gr-qc/9310026. 6

[32] L. Susskind, "The World As A Hologram," J. Math. Phys. **36**, 6377 (1995) [arXiv:hep-th/9409089]. 6

[33] J.M. Maldacena, "The large N limit of superconformal field theories and supergravity," Adv. Theor. Math. Phys. **2** (1998) 231 [arXiv:hep-th/9711200]. 6, 61

[34] O. Aharony, S.S. Gubser, J.M. Maldacena, H. Ooguri and Y. Oz, "Large N field theories, string theory and gravity," Phys. Rept. **323** (2000) 183 [arXiv:hep-th/9905111]. 7, 61, 63

[35] S.S. Gubser, I.R. Klebanov and A.M. Polyakov, "Gauge theory correlators from non-critical string theory," Phys. Lett. B **428** (1998) 105 [arXiv:hep-th/9802109];
E. Witten, Adv. Theor. Math. Phys. **2** (1998) 253 [arXiv:hep-th/9802150]. 8, 61

[36] K. Peeters, P. Vanhove and A. Westerberg, "Towards complete string effective actions beyond leading order," Fortsch. Phys. **52**, 630 (2004) [arXiv:hep-th/0312211]. 7

[37] N. Drukker and J. Plefka, "The structure of n-point functions of chiral primary operators in N=4 super Yang-Mills at one-loop," JHEP **0904**, 001 (2009) [arXiv:0812.3341 [hep-th]]. 7

[38] A. A. Tseytlin, arXiv:hep-th/0409296. 7

[39] J. A. Minahan and K. Zarembo, "The Bethe-ansatz for N = 4 super Yang-Mills," JHEP **0303**, 013 (2003) [arXiv:hep-th/0212208]. 7

[40] N. Itzhaki, J. M. Maldacena, J. Sonnenschein and S. Yankielowicz, Phys. Rev. D **58**, 046004 (1998) [arXiv:hep-th/9802042]. 8

[41] A. Karch and L. Randall, "Localized gravity in string theory," Phys. Rev. Lett. **87** (2001) 061601 [arXiv:hep-th/0105108]; JHEP **0106** (2001) 063 [arXiv:hep-th/0105132]. 8, 13, 17, 19, 20

[42] A. Karch and E. Katz, "Adding flavor to AdS/CFT," JHEP **0206** (2002) 043 [arXiv:hep-th/0205236];
O. Aharony, A. Fayyazuddin and J. M. Maldacena, JHEP **9807** (1998) 013 [arXiv:hep-th/9806159]. 8, 15

[43] T. Albash, V. Filev, C.V. Johnson and A. Kundu, "A topology-changing phase transition and the dynamics of flavour," arXiv:hep-th/0605088;
T. Albash, V. Filev, C.V. Johnson and A. Kundu, "Global currents, phase transitions, and chiral symmetry breaking in large N_c gauge theory," arXiv:hep-th/0605175;
V.G. Filev, C.V. Johnson, R.C. Rashkov and K.S. Viswanathan, "Flavoured large N gauge theory in an external magnetic field," arXiv:hep-th/0701001;
A. Karch and A. O'Bannon, "Chiral transition of N=4 super Yang-Mills with flavor on a 3-sphere," Phys. Rev. D **74** (2006) 085033 [arXiv:hep-th/0605120]. 8, 16

[44] J. Babington, J. Erdmenger, N.J. Evans, Z. Guralnik and I. Kirsch, "Chiral symmetry breaking and pions in non-supersymmetric gauge/gravity duals," Phys. Rev. D **69** (2004) 066007 [arXiv:hep-th/0306018];
I. Kirsch, "Generalizations of the AdS/CFT correspondence," Fortsch. Phys. **52**

(2004) 727 [arXiv:hep-th/0406274].
8, 13, 16, 63, 64, 65

[45] D. Mateos, R.C. Myers and R.M. Thomson, "Holographic phase transitions with fundamental matter," Phys. Rev. Lett. **97** (2006) 091601 [arXiv:hep-th/0605046];
D. Mateos, R. C. Myers and R. M. Thomson, JHEP **0705** (2007) 067 [arXiv:hep-th/0701132]. iii, 8, 13, 16, 63, 64, 65, 135, 168

[46] M. Kruczenski, D. Mateos, R.C. Myers and D.J. Winters, "Meson spectroscopy in AdS/CFT with flavour," JHEP **0307** (2003) 049 [arXiv:hep-th/0304032]. 8, 16

[47] See, for example:
W. Zajc, "Quark Gluon Plasma at RHIC (and in QCD and String Theory)," presented at PASCOS 08 — see http://pirsa.org/08060040/;
K. Rajagopal, "Quark Gluon Plasma in QCD, at RHIC, and in String Theory," presented at PASCOS 08 — see http://pirsa.org/08060041/;
D. Mateos, "String Theory and Quantum Chromodynamics," Class. Quant. Grav. **24** (2007) S713 [arXiv:0709.1523 [hep-th]];
S. S. Gubser, "Heavy ion collisions and black hole dynamics," Gen. Rel. Grav. **39** (2007) 1533 [Int. J. Mod. Phys. D **17** (2008) 673];
D. T. Son, "Gauge-gravity duality and heavy-ion collisions," AIP Conf. Proc. **957** (2007) 134. 8, 9

[48] A. Buchel, J. T. Liu and A. O. Starinets, "Coupling constant dependence of the shear viscosity in N=4 supersymmetric Yang-Mills theory," Nucl. Phys. B **707**, 56 (2005) [arXiv:hep-th/0406264]. 9

[49] C. P. Herzog, P. Kovtun, S. Sachdev and D. T. Son, "Quantum critical transport, duality, and M-theory," Phys. Rev. D **75** (2007) 085020 [arXiv:hep-th/0701036]. iii, 9, 12, 23, 25, 26, 28, 29, 52, 53, 68, 133, 136

[50] S.A. Hartnoll and P. Kovtun, "Hall conductivity from dyonic black holes," arXiv:0704.1160 [hep-th]; 9, 59, 63

[51] See, for example:
S. A. Hartnoll, P. K. Kovtun, M. Muller and S. Sachdev, "Theory of the Nernst effect near quantum phase transitions in condensed matter, and in dyonic black holes," Phys. Rev. B **76** (2007) 144502 [arXiv:0706.3215 [cond-mat.str-el]]; 9

[52] S. A. Hartnoll and C. P. Herzog, "Ohm's Law at strong coupling: S duality and the cyclotron resonance," Phys. Rev. D **76** (2007) 106012 [arXiv:0706.3228 [hep-th]]; A. O'Bannon, "Holographic Thermodynamics and Transport of Flavor Fields," arXiv:0808.1115 [hep-th]; N. Evans and E. Threlfall, "R-Charge Chemical Potential in the M2-M5 System," arXiv:0807.3679 [hep-th];
E. I. Buchbinder, A. Buchel and S. E. Vazquez, "Sound Waves in (2+1) Dimensional Holographic Magnetic Fluids," arXiv:0810.4094 [hep-th]; S. A. Hartnoll and C. P. Herzog, "Impure AdS/CFT," Phys. Rev. D **77** (2008) 106009 [arXiv:0801.1693 [hep-th]]; M. Fujita, Y. Hikida, S. Ryu and T. Takayanagi, "Disordered Systems and the Replica Method in AdS/CFT," arXiv:0810.5394 [hep-th]. 9

[53] [fermi] S. S. Lee, "A Non-Fermi Liquid from a Charged Black Hole: A Critical Fermi Ball," arXiv:0809.3402 [hep-th];

[54] C. P. Herzog, P. K. Kovtun and D. T. Son, "Holographic model of superfluidity," arXiv:0809.4870 [hep-th]; S. S. Gubser and F. D. Rocha, "The gravity dual to a quantum critical point with spontaneous symmetry breaking," arXiv:0807.1737 [hep-th]; S. A. Hartnoll, C. P. Herzog and G. T. Horowitz, "Building an AdS/CFT superconductor," arXiv:0803.3295 [hep-th]; M. M. Roberts and S. A. Hartnoll, "Pseudogap and time reversal breaking in a holographic superconductor," arXiv:0805.3898 [hep-th]; K. Maeda and T. Okamura, "Characteristic length of an AdS/CFT superconductor," arXiv:0809.3079 [hep-th]; M. M. Roberts and S. A. Hartnoll, "Pseudogap and time reversal breaking in a holographic superconductor," JHEP **0808**, 035 (2008) [arXiv:0805.3898 [hep-th]]; S. S. Gubser and S. S. Pufu, "The gravity dual of a p-wave superconductor," arXiv:0805.2960 [hep-th]; D. Minic and J. J. Heremans, "High Temperature Superconductivity and Effective Gravity," arXiv:0804.2880 [hep-th]; S. S. Gubser, "Colorful horizons with charge in anti-de Sitter space," arXiv:0803.3483 [hep-th]; M. Ammon, J. Erdmenger, M. Kaminski and P. Kerner, "Superconductivity from gauge/gravity duality with flavor," arXiv:0810.2316 [hep-th]; P. Basu, A. Mukherjee and H. H. Shieh, "Supercurrent: Vector Hair for an AdS Black Hole," arXiv:0809.4494 [hep-th]; S. A. Hartnoll, C. P. Herzog and G. T. Horowitz, "Holographic Superconductors," arXiv:0810.1563 [hep-th]; 9

[55] T. Albash and C. V. Johnson, "A Holographic Superconductor in an External Magnetic Field," JHEP **0809**, 121 (2008) [arXiv:0804.3466 [hep-th]]; E. Nakano and W. Y. Wen, "Critical Magnetic Field In A Holographic Superconductor," Phys. Rev. D **78**, 046004 (2008) [arXiv:0804.3180 [hep-th]]; W. Y. Wen, "Inhomogeneous magnetic field in AdS/CFT superconductor," arXiv:0805.1550 [hep-th]; 9

[56] See, for example:
D. T. Son, "Toward an AdS/cold atoms correspondence: a geometric realization of the Schrödinger symmetry," Phys. Rev. D **78** (2008) 046003 [arXiv:0804.3972 [hep-th]]; K. Balasubramanian and J. McGreevy, "Gravity duals for non-relativistic CFTs," Phys. Rev. Lett. **101**, 061601 (2008) [arXiv:0804.4053 [hep-th]]; W. D. Goldberger, "AdS/CFT duality for non-relativistic field theory," arXiv:0806.2867 [hep-th]; J. L. B. Barbon and C. A. Fuertes, "On the spectrum of nonrelativistic AdS/CFT," JHEP **0809** (2008) 030 [arXiv:0806.3244 [hep-th]]; C. P. Herzog, M. Rangamani and S. F. Ross, "Heating up Galilean holography," arXiv:0807.1099 [hep-th]; J. Maldacena, D. Martelli and Y. Tachikawa, "Comments on string theory backgrounds with non-relativistic conformal symmetry," JHEP **0810** (2008) 072 [arXiv:0807.1100 [hep-th]]; A. Adams, K. Balasubramanian and J. McGreevy, "Hot Spacetimes for Cold Atoms," arXiv:0807.1111 [hep-th]; D. Minic and M. Pleimling, "Non-relativistic AdS/CFT and Aging/Gravity Duality," arXiv:0807.3665 [cond-mat.stat-mech]; J. W. Chen and W. Y. Wen, "Shear Viscosity of a Non-Relativistic Conformal Gas in Two Dimensions," arXiv:0808.0399 [hep-th]; S. Kachru, X. Liu and M. Mulligan, arXiv:0808.1725 [hep-th]; P. Kovtun and D. Nickel, "Black holes and non-relativistic quantum systems," arXiv:0809.2020 [hep-th]; C. Duval, M. Hassaine and P. A. Horvathy, "The geometry of Schrödinger symmetry in gravity background/non-relativistic CFT," arXiv:0809.3128 [hep-th]; D. Yamada, "Thermodynamics of Black Holes in Schrödinger Space," arXiv:0809.4928 [hep-th]; S. A. Hartnoll and K. Yoshida, "Families of IIB duals for nonrelativistic CFTs," arXiv:0810.0298 [hep-th]. 9

[57] See, for example: S. Sachdev, *Quantum Phase Transitions*, Cambridge University Press (1999). 9, 65

[58] K. Damle and S. Sachdev, "Nonzero-temperature transport near quantum critical points," Phys. Rev. B **56**, 8714 (1997). 9, 138

[59] A. Sen, "Entropy Function and AdS(2)/CFT(1) Correspondence," JHEP **0811**, 075 (2008) [arXiv:0805.0095 [hep-th]]. 9, 11

[60] D. Gaiotto, A. Strominger and X. Yin, "From AdS(3)/CFT(2) to black holes / topological strings," JHEP **0709**, 050 (2007) [arXiv:hep-th/0602046]. 10

10

[61] D. R. Nelson, "Defects and Geometry in Condensed Matter Physics," Cambridge University Press (2002). 11

[62] M. Pleimling, "Critical phenomena at perfect and non-perfect surfaces," J. Phys. A **387**, R79 (2004); T. C. Lubensky and M. H. Rubin, "Critical phenomena in semi-infinite systems. 2. Mean-field theory," Phys. Rev. B **12**, 3885 (1975). 11

[63] O. DeWolfe, D.Z. Freedman and H. Ooguri, "Holography and defect conformal field theories," Phys. Rev. D **66** (2002) 025009 [arXiv:hep-th/0111135]. 13, 17, 19

[64] J. Gomis and C. Romelsberger, "Bubbling defect CFT's," JHEP **0608** (2006) 050 [arXiv:hep-th/0604155];
E. D'Hoker, J. Estes and M. Gutperle, "Exact half-BPS type IIB interface solutions. II: Flux solutions and multi-janus," JHEP **0706** (2007) 022 [arXiv:0705.0024 [hep-th]]. 13, 19

[65] S.Y. Rey, "Quantum Phase Transitions from String Theory," talk at Strings 2007 — see: http://www.ift.uam.es/strings07/010_marco.htm 13, 16

[66] J. L. Davis, P. Kraus and A. Shah, "Gravity Dual of a Quantum Hall Plateau Transition," arXiv:0809.1876 [hep-th]. 13, 59, 67

[67] S. Kobayashi, D. Mateos, S. Matsuura, R.C. Myers and R.M. Thomson, "Holographic phase transitions at finite baryon density," JHEP **0702** (2007) 016 [arXiv:hep-th/0611099];
D. Mateos, S. Matsuura, R. C. Myers and R. M. Thomson, "Holographic phase transitions at finite chemical potential," JHEP **0711** (2007) 085 [arXiv:0709.1225 [hep-th]]. 13, 63, 64

[68] R. Emparan, G.T. Horowitz and R.C. Myers, "Black holes radiate mainly on the brane," Phys. Rev. Lett. **85** (2000) 499 [arXiv:hep-th/0003118]. 13, 20, 63, 64, 141

[69] E. Keski-Vakkuri and P. Kraus, "Quantum Hall Effect in AdS/CFT," arXiv:0805.4643 [hep-th]. 59, 66

[70] D. Arean and A.V. Ramallo, "Open string modes at brane intersections," JHEP **0604** (2006) 037 [arXiv:hep-th/0602174];
D. Arean, A. V. Ramallo and D. Rodriguez-Gomez, "Mesons and Higgs branch in defect theories," Phys. Lett. B **641** (2006) 393 [arXiv:hep-th/0609010]. 16, 20

[71] R.C. Myers and R.M. Thomson, "Holographic mesons in various dimensions," [arXiv:hep-th/0605017]. 16, 24

[72] E. Witten, "Anti-de Sitter space, thermal phase transition, and confinement in gauge theories," Adv. Theor. Math. Phys. **2** (1998) 505 [arXiv:hep-th/9803131]. 16

[73] J. Erdmenger, Z. Guralnik and I. Kirsch, "Four-dimensional superconformal theories with interacting boundaries or defects," Phys. Rev. D **66** (2002) 025020 [arXiv:hep-th/0203020]. 19

[74] A. Kapustin and S. Sethi, "The Higgs branch of impurity theories," Adv. Theor. Math. Phys. **2** (1998) 571 [arXiv:hep-th/9804027]. 19

[75] N. R. Constable, R. C. Myers and O. Tafjord, "The noncommutative bion core," Phys. Rev. D **61** (2000) 106009 [arXiv:hep-th/9911136]. 20, 21, 66

[76] P. Breitenlohner and D.Z. Freedman, "Positive Energy In Anti-De Sitter Backgrounds And Gauged Extended Supergravity," Phys. Lett. B **115** (1982) 197;
L. Mezincescu and P.K. Townsend, "Stability At A Local Maximum In Higher Dimensional Anti-De Sitter Space And Applications To Supergravity," Annals Phys. **160** (1985) 406. 20, 22, 62

[77] R. C. Myers, "Dielectric-branes," JHEP **9912** (1999) 022 [arXiv:hep-th/9910053];
W. Taylor and M. Van Raamsdonk, "Multiple Dp-branes in weak background fields," Nucl. Phys. B **573** (2000) 703 [arXiv:hep-th/9910052]. 21

[78] A. A. Tseytlin, "On non-abelian generalisation of the Born-Infeld action in string theory," Nucl. Phys. B **501** (1997) 41 [arXiv:hep-th/9701125]. 21

[79] R. C. Myers, "Nonabelian phenomena on D-branes," Class. Quant. Grav. **20** (2003) S347 [arXiv:hep-th/0303072]. 21

[80] A. Hashimoto and W. Taylor, "Fluctuation spectra of tilted and intersecting D-branes from the Born-Infeld action," Nucl. Phys. B **503** (1997) 193 [arXiv:hep-th/9703217];
P. Bain, "On the non-Abelian Born-Infeld action," arXiv:hep-th/9909154. 21

[81] N. R. Constable, R. C. Myers and O. Tafjord, "Non-Abelian brane intersections," JHEP **0106** (2001) 023 [arXiv:hep-th/0102080]. 21, 22, 66, 67

[82] D.T. Son and A.O. Starinets, "Minkowski-space correlators in AdS/CFT correspondence: Recipe and applications," JHEP **0209**, 042 (2002) [arXiv:hep-th/0205051]. 25, 26, 150

[83] P.K. Kovtun and A.O. Starinets, "Quasinormal modes and holography," Phys. Rev. D **72**, 086009 (2005) [arXiv:hep-th/0506184]. 25

[84] L.P. Kadanoff and P.C. Martin, "Hydrodynamic Equations and Correlation Functions," Ann. Phys. **24** (1963) 419. 32

[85] See, for example:
P. M. Chaikin and T. C. Lubensky *Principles of condensed matter physics*, (Cambridge University Press, 1995) 33, 53, 90

[86] See, for example:
L. D. Landau and E. M Lifshitz *Statistical Physics, Part 1*, (Butterworth-Heinemann, 1980) 33, 90

[87] See, for example:
M. P. Marder *Condensed Matter Physics*, (Wiley, 2000); D. W. Snoke *Solid State Physics*, (Pearson, 20009); N. W. Marmin and N. D. Ashcroft *Solid State Physics*, (Brooks Cole, 1976) 72

[88] N. Nagaosa *Quantum Field Theory in Condensed Matter Physics*, (Springer, 1995) 76

[89] G. Li and E. Y. Andrei *Observation of Landau levels of Dirac fermions in graphite* Nature Physics **3** (2007) 623 75, 76, 100, 136

[90] For example, see: http://mathworld.wolfram.com/ConfluentHypergeometricLimitFunction.html 36

[91] R. C. Myers, A. O. Starinets and R. M. Thomson, "Holographic spectral functions and diffusion constants for fundamental matter," JHEP **0711** (2007) 091 [arXiv:0706.0162 [hep-th]]. 39, 40

[92] A. Nunez and A. O. Starinets, "AdS/CFT correspondence, quasinormal modes, and thermal correlators in N = 4 SYM," Phys. Rev. D **67** (2003) 124013 [arXiv:hep-th/0302026];
A. O. Starinets, "Quasinormal modes of near extremal black branes," Phys. Rev. D **66** (2002) 124013 [arXiv:hep-th/0207133]. 39

[93] R. C. Myers and A. Sinha, "The fast life of holographic mesons," JHEP **0806** (2008) 052 [arXiv:0804.2168 [hep-th]]. 39, 40, 41

[94] A. S. Miranda, J. Morgan and V. T. Zanchin, "Quasinormal modes of plane-symmetric black holes according to the AdS/CFT correspondence," arXiv:0809.0297 [hep-th]. 52

[95] Y. Kitazawa, "Effective lagrangian for open superstring from five point function," Nucl. Phys. B **289** (1987) 599. 53, 143, 144, 145

[96] P. Koerber and A. Sevrin, "The non-Abelian Born-Infeld action through order α'^3," JHEP **0110** (2001) 003 [arXiv:hep-th/0108169]; "Testing the α'^3 term in the non-abelian open superstring effective action," JHEP **0109** (2001) 009 [arXiv:hep-th/0109030]. 53, 143, 145

[97] C. P. Bachas, P. Bain and M. B. Green, "Curvature terms in D-brane actions and their M-theory origin," JHEP **9905** (1999) 011 [arXiv:hep-th/9903210]. 53, 133, 143

[98] M. Wijnholt, "On curvature-squared corrections for D-brane actions," arXiv:hep-th/0301029. 53, 133, 143

[99] E. Witten, "SL(2,Z) action on three-dimensional conformal field theories with Abelian symmetry," arXiv:hep-th/0307041. 59, 70, 96

[100] C. P. Burgess and B. P. Dolan, "Particle-vortex duality and the modular group: Applications to the quantum Hall effect and other 2-D systems," arXiv:hep-th/0010246. 70

[101] P. Kovtun, D.T. Son and A.O. Starinets, "Holography and hydrodynamics: Diffusion on stretched horizons," JHEP **0310**, 064 (2003) [arXiv:hep-th/0309213]. 30, 31, 88

[102] G. Policastro, D.T. Son and A.O. Starinets, "From AdS/CFT correspondence to hydrodynamics," JHEP **0209**, 043 (2002) [arXiv:hep-th/0205052]. 30

[103] A. O. Starinets, "Quasinormal spectrum and the black hole membrane paradigm," arXiv:0806.3797 [hep-th]; see, also: http://pirsa.org/06060018 30

[104] C.P. Herzog, "The hydrodynamics of M-theory," JHEP **0212** (2002) 026 [arXiv:hep-th/0210126]. 32

[105] C. P. Herzog and D. T. Son, "Schwinger-Keldysh propagators from AdS/CFT correspondence," JHEP **0303**, 046 (2003) [arXiv:hep-th/0212072]. P. Kovtun, D. T. Son and A. O. Starinets, "Viscosity in strongly interacting quantum field theories from black hole physics," Phys. Rev. Lett. **94**, 111601 (2005) [arXiv:hep-th/0405231].

[106] For example, see: http://mathworld.wolfram.com/AppellHypergeometricFunction.html 147

[107] D. Birmingham, I. Sachs and S. N. Solodukhin, "Conformal field theory interpretation of black hole quasi-normal modes," Phys. Rev. Lett. **88** (2002) 151301 [arXiv:hep-th/0112055]. 150

[108] P. Giacconi, R. Soldati "On the mystery of the missing pie in Graphene," [arXiv:0906.2856v1 [cond-mat.mes-hall]] 136

[109] A. K. Geim and K. S. Novoselov, "The rise of graphene", Nature Materials **6**, 183 (2007). 136

[110] V. G. Filev, C. V. Johnson, R. C. Rashkov and K. S. Viswanathan, "Flavoured large N gauge theory in an external magnetic field," JHEP **0710**, 019 (2007) [arXiv:hep-th/0701001]; T. Albash, V. G. Filev, C. V. Johnson and A. Kundu, "Finite Temperature Large N Gauge Theory with Quarks in an External Magnetic Field," JHEP **0807**, 080 (2008) [arXiv:0709.1547 [hep-th]]. 63, 165

[111] A. Karch, A. O'Bannon and K. Skenderis, "Holographic renormalization of probe D-branes in AdS/CFT," JHEP **0604**, 015 (2006) [arXiv:hep-th/0512125]. 155